

REDUCTION OF QUANTUM FLUCTUATIONS BY
ANISOTROPY FIELDS IN HEISENBERG
FERRO- AND ANTIFERROMAGNETS

Dissertation
zur Erlangung des Doktorgrades
des Departments Physik
der Universität Hamburg

vorgelegt von
Björn Vogt
aus Hildesheim

Hamburg
2009

Gutachter der Dissertation:	Prof. Dr. Stefan Kettemann Prof. Dr. Michael Potthoff
Gutachter der Disputation:	Prof. Dr. Stefan Kettemann Prof. Dr. Georges Bouzerar
Datum der Disputation:	20. August 2009
Vorsitzender des Prüfungsausschusses:	PD Dr. Alexander Chudnovskiy
Vorsitzender des Promotionsausschusses:	Prof. Dr. Robert Klanner
MIN-Dekan der Fakultät für Mathematik, Informatik und Naturwissenschaften:	Prof. Dr. Heinrich Graener
Departmentleiter:	Prof. Dr. Jochen Bartels

Kurzzusammenfassung

Das anisotrope Heisenberg-Modell $H = \pm \sum_{\langle ij \rangle} \mathbf{S}_i \cdot \mathbf{S}_j - h_p \sum_i (S_i^z)^p$, mit geradzahligem p , wird sowohl durch thermische als auch durch quantenmechanische Fluktuationen grundlegend beeinflusst. Dabei kann das quantenmechanische Heisenberg-Modell durch die Variation zweier Parameter auf ein System mit rein klassischen Fluktuationen reduziert werden: Es ist bereits länger bekannt, dass sowohl große Spinquantenzahlen $S \gg 1$ als auch große Anisotropiefelder $h_p \gg 1$ die Quantenfluktuationen komplett zerstören können und damit zu einem klassischen Limes führen, der für $h_p > 0$ ein Ising-artiges System zurücklässt. Diese Studie untersucht nun das Einsetzen klassischer Tendenzen, die durch vergleichsweise kleine Werte für S und h_p hervorgerufen werden. Die damit einhergehende und einsetzende Unterdrückung der Quantenfluktuationen steht dabei in direktem Zusammenhang zu aktuellen Experimenten, die mithilfe spinpolarisierter Rastertunnelmikroskopie an der Universität Hamburg durchgeführt werden: Entsprechende spinaufgelöste Messungen, die magnetische Strukturen auf der Nanoskala sichtbar machen, werden durch nicht vernachlässigbare Anisotropiefelder beeinflusst und wurden mithilfe eines klassischen Heisenberg-Modells interpretiert. Die theoretische Untersuchung in der vorliegenden Arbeit überprüft und bewertet nun den Gültigkeitsbereich dieser klassischen Beschreibung; zu diesem Zweck werden die Auswirkungen der Anisotropiefelder auf die typisch quantenmechanischen Eigenschaften des Heisenbergmodells näher unter die Lupe genommen. Hierzu bestimmen wir die kritischen Temperaturen für Ferro- und Antiferromagnete und die Untergitter-Magnetisierung in Antiferromagneten. Die resultierende Abhängigkeit von der Dimension, der Spinquantenzahl und dem Anisotropiefeld wird für einen umfassenden Wertebereich ausgewertet und dargestellt. Wir vergleichen dabei die Ergebnisse aus folgenden Methoden: Klassisches Mean-Field (CMF), Quanten-Mean-Field (QMF), Lineare Spinwellen-Approximation (LSWA), Random-Phase-Approximation (RPA) und numerische Quanten-Monte-Carlo-Verfahren (QMC).

Schlussendlich erhalten wir hierüber konsistente Ansichten über die einsetzenden klassischen Tendenzen und die damit verbundene Unterdrückung der Quantenfluktuationen. Letztere stellen sich dabei als außergewöhnlich empfindlich auf die Anwesenheit selbst kleinster Anisotropiefelder heraus, was wir durch die Einführung der Anisotropie-Suszeptibilität explizit quantifizieren können. Diese starke Einflussnahme selbst kleinster Anisotropiefelder stellt ein bedeutendes Ergebnis der vorliegenden Arbeit dar. Im Endeffekt ermöglicht diese Studie eine fundierte Bewertung über die klassische Modellierung der oben erwähnten experimentellen Messungen, die zurzeit in Hamburg durchgeführt werden.

Abstract

The anisotropic Heisenberg model $H = \pm \sum_{\langle ij \rangle} \mathbf{S}_i \cdot \mathbf{S}_j - h_p \sum_i (S_i^z)^p$, with p even, is influenced by thermal as well as by quantum fluctuations. Thereby, the quantum Heisenberg system can be profoundly changed towards a classical system by tuning two parameters: It is well-known that both large spin quantum numbers $S \gg 1$ and large anisotropy fields $h_p \gg 1$ destroy the quantum fluctuations completely and lead to a classical limit that renders the system Ising-like in the easy-axis case $h_p > 0$. This study aims to elucidate the incipience of these classical trends that is induced by relatively small values for the parameters h_p and S . The accompanied incipient suppression of quantum fluctuations for relatively small h_p and S is thereby closely related to modern experiments that are currently performed in Hamburg: Corresponding SP-STM measurements, which reveal magnetic structures at the nanoscale, are influenced by non-negligible anisotropy fields and have been modelled by classical Heisenberg systems. This theoretical study reveals the validity of this classical approach by investigating the impact of the anisotropy fields on the quantum properties of the Heisenberg model.

In order to illustrate the resulting effects by the anisotropy fields h_p , we determine the critical temperature for ferro- and antiferromagnets and the ground state sublattice magnetization for antiferromagnets. The outcome depends on the dimension d , the spin quantum number S and the anisotropy field h_p and is studied for a widespread range of these parameters. We compare these quantities with the use of the following theories: Classical Mean Field (CMF), Quantum Mean Field (QMF), Linear Spin Wave Approximation (LSWA) and Random Phase Approximation (RPA). Our findings will be confirmed and quantitatively improved by numerical Quantum Monte Carlo (QMC) simulations. If provided by the respective method, we will investigate the differences between the ferromagnet (FM) and antiferromagnet (AFM).

We finally find a consistent picture of the classical trends and elucidate, thereby, the suppression of quantum fluctuations in anisotropic spin systems. We further reveal that the quantum fluctuations are extraordinarily sensitive to the presence of small anisotropy fields. This sensitivity can be quantified by the introduction of a quantity we want to refer to as anisotropy susceptibility. As an important result, we conclude that even tiny anisotropy fields lead to a strong reduction of quantum fluctuations. In the end, this study enables us to validate the classical modelling of the experiments performed at the University of Hamburg.

“Phase transitions are all around us, whether we boil a kettle or make some ice [...]”

A.J. Schofield [1]

Contents

1	Introduction	1
1.1	Physical Motivation	1
1.2	Classical and Quantum Spin Systems	1
1.2.1	Overview of Models	2
1.2.2	Anisotropy Fields and Conventions	4
1.3	Positioning of Our Studies	5
1.3.1	Experimental Point of View	5
1.3.2	Theoretical Point of View	6
1.4	Outline of this Thesis	7
1.5	Toy Models	8
2	Classical Mean Field	10
2.1	Mean Field Strategies	10
2.2	Isotropic Systems	12
2.3	Heisenberg Model with Anisotropy Fields	15
2.3.1	Free Energy and Critical Temperatures	15
2.3.2	Crossover Phenomenon	21
2.4	Excursion I: XY Model with Z_p -Anisotropy	25
2.4.1	Overview of Primal Renormalization Group Considerations	25
2.4.2	Mean Field Free Energy Landscapes	26
2.4.3	Phase Diagram	38
2.5	Excursion II: Semiclassical Models and Quantum-Classical Mapping	39
2.6	Retrospect and Outlook	42
3	Quantum Mean Field	43
3.1	Isotropic Systems	43
3.2	Modifications for Anisotropy Fields	45
3.3	Relevance of Higher-Order Fields	47
3.4	Retrospect and Outlook	48
4	Linear Spin Wave Approximation	49
4.1	Overview: Two Methods - One Message	49
4.2	Isotropic Systems	50
4.2.1	Method I: Bosonic Operators	50

4.2.2	Method II: Approximating Fluctuations	52
4.2.3	FM vs. AFM	54
4.2.4	Excursion: Ground State Energy of FM and AFM	55
4.3	Anisotropy Modifications	57
4.3.1	Method I: Additional Bosonic Terms	57
4.3.2	Method II: Additional Fluctuation Terms	60
4.3.3	FM vs. AFM	61
4.4	Sublattice Magnetization	63
4.4.1	Method I - Derivation	64
4.4.2	Method II - Derivation	65
4.4.3	FM vs. AFM	67
4.4.4	Results and Discussion	68
4.5	Staggered and Uniform Fields	74
4.5.1	Uniform Magnetic Field	74
4.5.2	Staggered Magnetic Field	77
4.5.3	Fields on a Single Sublattice	77
4.6	Anisotropy Susceptibility	78
4.7	Retrospect and Outlook	80
5	Random Phase Approximation	81
5.1	Overview	81
5.2	Technical Preparations: Green's Functions and their Properties	82
5.3	Isotropic Systems	83
5.3.1	Ferromagnet	83
5.3.2	Antiferromagnet	90
5.4	Consequences for Magnetic Fields	95
5.4.1	Ferromagnet	95
5.4.2	Antiferromagnet	95
5.5	Modifications for Quadratic Anisotropy Fields	97
5.5.1	Ferromagnet	98
5.5.2	Antiferromagnet	101
5.6	Higher-Order Anisotropy Fields	110
5.7	Retrospect and Outlook	112
6	Quantum Monte Carlo	114
6.1	Introduction to ALPS	114
6.1.1	Handling and Features	114
6.1.2	Overview of the Algorithms	117
6.2	Simulation Setups and Benchmarks	117
6.2.1	Literature Values for Benchmarking	118
6.2.2	Procedures and Analyses	118
6.2.3	$S = \frac{1}{2}$ -Heisenberg Model in Three Dimensions	119
6.2.4	Classical Heisenberg Model in Three Dimensions	120
6.2.5	Ising Model in Three Dimensions	121
6.2.6	Ising Model in Two Dimensions	121
6.3	Numerical Results for the $S=1$ -Heisenberg FM	122
6.4	Numerical Results for the $S=1$ -AFM	125

6.5	Comparison of FM and AFM	126
6.5.1	FM vs. AFM I - Entropy vs. Quantum Fluctuations	126
6.5.2	FM vs. AFM II - Spin Wave Dispersion	129
6.5.3	Reducing $T_C^{\text{AFM}} - T_C^{\text{FM}}$ by Anisotropy Fields	129
6.5.4	Reducing $T_C^{\text{AFM}} - T_C^{\text{FM}}$ by Large Spin Quantum Numbers	130
6.6	Numerical Results for $S=3/2$	131
6.6.1	$S=3/2$ -FM	131
6.6.2	$S=3/2$ -AFM	133
6.7	Numerical Results for the $S=2$ -FM	134
6.7.1	$p=2$: Quadratic Fields	134
6.7.2	$p=4$: Quartic Fields	134
6.8	Numerical Results for Two-Dimensional Systems	136
6.8.1	$S=1$ -FM in Two Dimensions	136
6.8.2	$S=1$ -AFM in Two Dimensions	138
6.9	Comparison to the Analytical RPA Results	139
6.10	Retrospect and Outlook	142
7	Outlook: Extension to Disordered Systems	143
7.1	Dilution - Motivation for Ongoing Research	143
7.2	Monte Carlo on Diluted Lattices	144
7.3	Self-Consistent Local RPA for Disordered Systems	146
7.3.1	Basic Idea	146
7.3.2	Code Implementation	148
7.3.3	Successful Benchmarks	151
7.3.4	Further Prospect	156
8	Résumé	157
A	Binder Cumulants	161
A.1	$S=1$ - Heisenberg FM	161
A.2	$S=1$ - Heisenberg AFM	165
A.3	$S=3/2$ - Heisenberg FM	168
A.4	$S=3/2$ - Heisenberg AFM	171
A.5	$S=2$ - Heisenberg FM with $p=2$	175
A.6	$S=2$ - Heisenberg FM with $p=4$	178
A.7	Two Dimensions: $S=1$ -FM	182
A.8	Two Dimensions: $S=1$ -AFM	185
B	List of Abbreviations - Glossary	188
	Bibliography	190

Chapter 1

Introduction

1.1 Physical Motivation

The exploration of magnetism has been fascinating mankind for centuries and millennia: Having started to attract philosophers' interest in ancient times, with the city of Magnesia in Asia Minor giving its name for this phenomenon [2], the first scientific essay on magnetism of the modern era was given by William Gilbert in 1600 [3]. In the course of time, these primal considerations have been further refined: The rise of statistical methods in the 19th and 20th century allowed to develop an innovative understanding of the magnetic properties based on theoretical models at the atomic scale. These theoretical insights inspired generations of physicists and engineers and gave rise to inventions vital for our daily life: Nowadays, magnetism represents a widely applied phenomenon used for navigation, electricity generation, etc. and not least for digital data storage devices in the information technology. Modern hard disk drives store information via the orientation of magnetic domains that are written and read out with the use of the Giant Magnetoresistance Effect, whose discovery was awarded with the Nobel prize in 2007 [4].

The current trend of miniaturization gives rise to the combination of magnetic phenomena and the nanotechnology, which is justifiably regarded as the key technology of the 21st century. The University of Hamburg is well positioned for this challenge: Modern and state-of-the-art experiments on magnetism at the atomic scale are performed with the use of spin-polarized scanning tunneling microscopes [5, 6]. This thesis will investigate according theoretical spin models and will study the possibilities to affect their quantum properties by the presence of anisotropy fields.

1.2 Classical and Quantum Spin Systems

The history of Statistical Physics has been greatly influenced by the use of appropriate models. The following section gives a brief overview on the models that are related to this study.

1.2.1 Overview of Models

The investigations of this thesis will be mainly based on the Heisenberg spin model, which was first set up and explored by Werner Heisenberg in 1928 [7]. Its classical version describes the spin \mathbf{S}_i by a three-dimensional spherical vector,

$$H^{\text{class}} = \pm \sum_{\langle ij \rangle} J_{ij} \mathbf{S}_i \cdot \mathbf{S}_j \quad \text{with} \quad \mathbf{S}_i = S \begin{pmatrix} \sin \vartheta_i \cos \varphi_i \\ \sin \vartheta_i \sin \varphi_i \\ \cos \vartheta_i \end{pmatrix}, \quad (1.1)$$

and is characterized by the complete absence of commutation relations. The upper sign refers throughout to the AFM, and the lower one to the FM.

The quantum Heisenberg model, on the contrary, incorporates all of the commutation relations for quantum spins:

$$H = \pm \sum_{\langle ij \rangle} J_{ij} \mathbf{S}_i \cdot \mathbf{S}_j \quad \text{with} \quad [S_i^\alpha, S_j^\beta] = i \delta_{ij} \varepsilon_{\alpha\beta\gamma} S_i^\gamma \quad (\hbar = 1). \quad (1.2)$$

Thereby, the Heisenberg model is characterized by the appearance of three spin components and, accordingly, three spin dimensions: The classical version exhibits the $O(3)$ -symmetry of the spherical vector in (1.1), whereas the quantum model shows the $SU(2)$ -symmetry for quantum spins associated with the quantization condition in (1.2).

The Heisenberg model, in its classical as well as quantum version, has been widely studied: According to the Mermin-Wagner theorem [8], its continuous spin symmetry prevents the emergence of long-range order in two spatial dimensions and causes consequently the vanishing of the critical temperature in two dimensions. Therefore, the isotropic Heisenberg model exhibits finite critical temperatures only for dimensions $d > 2$. For large spin quantum numbers S , the classical Heisenberg model (1.1) will represent an important classical limit and reference point for the quantum model in (1.2).

The XY model is closely related to the Heisenberg model and is characterized by two spin dimensions:

$$\text{classical:} \quad H_{XY}^{\text{class}} = \pm \sum_{\langle ij \rangle} J_{ij} \mathbf{S}_i \cdot \mathbf{S}_j \quad \text{with} \quad \mathbf{S}_i = S \begin{pmatrix} \cos \varphi_i \\ \sin \varphi_i \end{pmatrix} \quad (1.3)$$

$$= \pm \sum_{\langle ij \rangle} J_{ij} S^2 \cos(\varphi_i - \varphi_j), \quad (1.4)$$

$$\text{quantum:} \quad H_{XY} = \pm \sum_{\langle ij \rangle} J_{ij} [S_i^x S_j^x + S_i^y S_j^y] \quad \text{with} \quad [S_i^x, S_i^y] \neq 0 \quad (1.5)$$

$$= \pm \sum_{\langle ij \rangle} \frac{J_{ij}}{2} [S_i^+ S_j^- + S_i^- S_j^+] \quad \text{with} \quad [S_i^+, S_i^-] \neq 0. \quad (1.6)$$

In the classical case the planar spins are described by the $O(2)$ -symmetry. The appearance of two spin dimensions gives rise to a very special and intriguing phenomenon: In concordance with the Mermin-Wagner theorem [8],

there is no finite critical temperature and no second order phase transition at finite temperatures in the spatially two-dimensional XY model that would induce an ordered magnetic phase. Nonetheless, Kosterlitz and Thouless found a topological phase transition by concerning vortices that become bound at low temperatures [9, 10, 11]. Thereby, this Kosterlitz-Thouless transition turned out to be restricted to two spin dimensions: There have been extensive studies [12, 13, 14] that tried to recover a topological phase transition in the Heisenberg system in two spatial dimensions, but failed to prove it ever since. Nowadays, it is commonly accepted that the Heisenberg model exhibits no topological phase transition, in contrast to the XY model. The search for this insight has puzzled the scientific community over decades, as Blöte et al. pointed out [15]:

“The two-dimensional Heisenberg and XY models are such close relatives that it has taken a long history of efforts before their properties could be told apart.”

In one spin dimension, the corresponding reference model is given by the probably most famous model in Statistical Physics: The Ising model has been invented and primally explored by Ernst Ising at the University of Hamburg in the 1920s [16, 17]. This model, which was accordingly named after him, contains just one single spin component with two possible orientations:

$$H_{\text{Ising}} = \pm \sum_{\langle ij \rangle} J_{ij} S_i^z S_j^z \quad \text{with } S_i^z \in \{-S, +S\}. \quad (1.7)$$

As a consequence, the Ising model prefers the spin alignment along a denoted axis, e.g. the z -axis, and exhibits the corresponding discrete Z_2 -symmetry. Due to this discrete symmetry, the Ising model circumvents the Mermin-Wagner theorem and shows a second order phase transition at finite temperatures in two dimensions, as Onsager [18, 19] proved in his famous exact analytical treatment in the 1940s. An overview of the efforts and progresses on the Ising model is given in [17, 20]. Since the Ising model exhibits only one spin dimension, it is per definition a classical model that is not influenced by any quantum fluctuations.

The classical Ising model will represent an important reference point and benchmark for our studies, since the different spin dimensions of the Heisenberg, XY and Ising model can be linked by anisotropy fields, which we introduce in the coming paragraph.

The model overview of this section is summarized in fig. 1.1. Please note the indicated location of the Ising model on the classical side, which provides the basis for intriguing phenomena that are related to the suppression of quantum fluctuations.

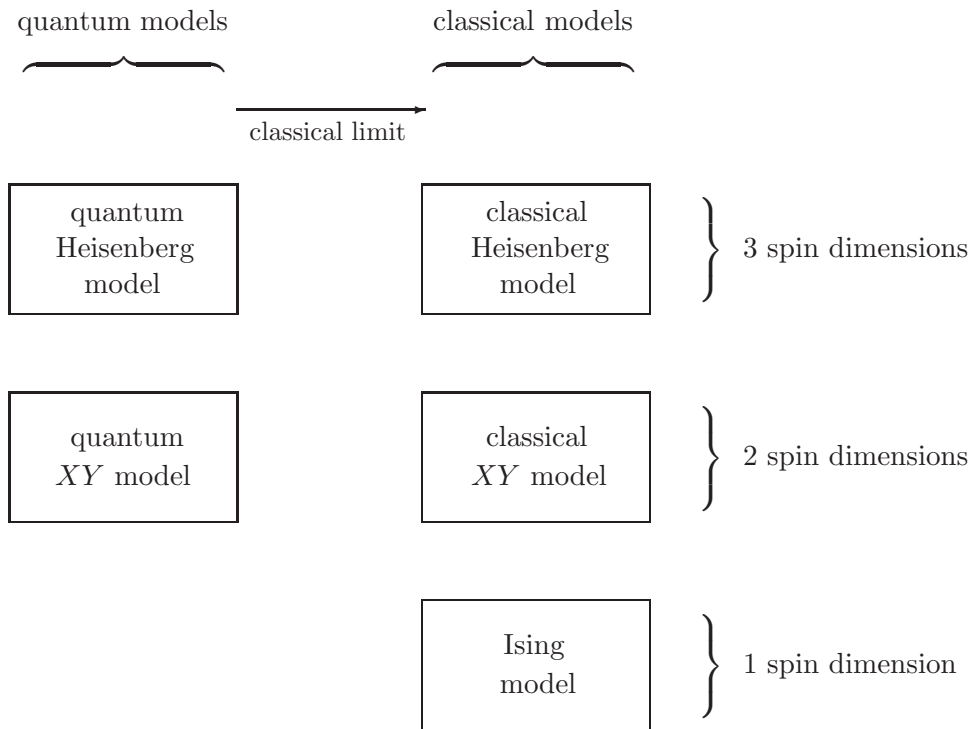


Figure 1.1: Overview of the models that are related to this study.

1.2.2 Anisotropy Fields and Conventions

In this thesis we will study the outcome of anisotropy fields that mark preferred spin orientations and subsequently reduce the symmetry of the spin space.

The complete quantum Heisenberg Hamiltonian, which contains the single-site anisotropy fields h_p with even p , reads

$$H = \pm \sum_{\langle ij \rangle} \mathbf{S}_i \cdot \mathbf{S}_j - h_p \sum_i (S_i^z)^p. \quad (1.8)$$

The kind of magnetism is determined by the sign in (1.8): The upper sign refers to the antiferromagnet (AFM), the lower one to the ferromagnet (FM). Thereby, we will restrict ourselves to models exhibiting nearest-neighbour interactions,

$$J_{ij} = \begin{cases} J > 0 & \text{for the lattice sites } i \text{ and } j \text{ being nearest neighbours,} \\ 0 & \text{otherwise,} \end{cases} \quad (1.9)$$

as suggested by the sum $\sum_{\langle ij \rangle}$, with each pair counted only once. Throughout this thesis, we impose periodic boundary conditions and focus on simple lattice structures (simple cubic, square lattice and chain).

In general, we will focus on the anisotropy case with even p and especially $p \in \{2, 4, 6\}$. Fields with odd p , on the contrary, represent a linear magnetic

field for $p = 1$ and its higher-order versions for odd $p \geq 3$. From time to time, if explicitly mentioned, we will study the outcome of the latter.

We will refer to h_p as the anisotropy field itself and to p as the order of the anisotropy. In order to avoid any confusion, we want to emphasize that not all of the possible combinations of S and p lead to a new kind of physics. A prominent example is the quadratic anisotropy term $-h_2 \sum_i (S_i^z)^2$, which has no effect for $S = \frac{1}{2}$, since it is just adding the trivial constant $-\sum_i h_2/4$ to the Hamiltonian. For a given spin quantum number, we can find only a finite number of integer values of p , whose anisotropy terms cannot be reduced to lower p . We will call the corresponding h_p irreducible anisotropy fields. For general S the reduction formula is given by

$$\prod_{m=-S}^{+S} (S_i^z - m) = 0. \quad (1.10)$$

According to (1.10), anisotropy terms $-h_p \sum_i (S_i^z)^p$ are irreducible for $S \geq \frac{p}{2}$. For any $S < \frac{p}{2}$ the reduction formula (1.10) allows to reduce $(S_i^z)^p$ to lower-order fields containing no new physical constellation. Throughout this thesis we will concentrate exclusively on irreducible anisotropy fields.

The presence of positive anisotropies $h_p > 0$ induces now an easy-axis (EA) along the z -axis: As a consequence, the system is rendered Ising-like. Therefore, the original $O(3)$ -symmetry (in the classical case), respectively the $SU(2)$ -symmetry (in the quantum case), is consequently reduced to the discrete Z_2 -symmetry of the Ising model. As a major consequence, this reduction implies the suppression of quantum fluctuations: The original quantum system is driven towards a classical system in the Ising limit $h_p \gg 1$. In the course of this thesis, we will investigate in detail the emergence of this limit and the accompanied reduction of quantum fluctuations.

Negative anisotropy fields, on the contrary, induce an easy-plane (EP) and lead to a planar symmetry, i.e. to the $O(2)$ -symmetry in the classical case.

Further consequences are reviewed in the theoretical section of the following paragraph.

1.3 Positioning of Our Studies

The investigations presented in this thesis close a gap in the theoretical treatment of anisotropic Heisenberg spin systems, but also include important conclusions concerning modern experiments currently performed at the University of Hamburg that reveal magnetic properties at the nanoscale.

1.3.1 Experimental Point of View

The investigation of magnetism at the atomic scale is greatly influenced by the experimental technique of the spin-polarized scanning tunneling microscopy (SP-STM), which has been explored by Wiesendanger [21, 22]. Recent overviews on the experimental setups and subsequent results are given in [5, 6].

In the course of these experimental studies, single spins on surfaces as well as two-dimensional films on substrates have been intensely studied at the University of Hamburg [23]-[31]. In order to explain these intriguing measurements, the experimental samples have been theoretically modelled by classical Heisenberg systems that are affected by anisotropy fields (see especially [29]).

Our theoretical study aims now to validate this classical modelling: Therefore, we will elucidate the quantum character of Heisenberg spin models of the kind (1.8). We will demonstrate in detail that quantum effects are consequently reduced and suppressed by the emergence of anisotropy fields. Our final results will highlight the extreme sensitivity of quantum fluctuations to the fields h_p .

We want to emphasize that those experimental samples exhibit spin quantum numbers $S > \frac{1}{2}$ and can, therefore, be profoundly influenced by the presence of anisotropy fields. $S = \frac{1}{2}$ - samples, on the contrary, remain unaffected by h_p -fields with even p ; their quantum properties could be alternatively influenced by magnetic fields h_1 or coupling anisotropies, which have been widely investigated as we will point out in the following paragraph.

1.3.2 Theoretical Point of View

Since theoretical studies on Heisenberg spin systems started, it has been well established that anisotropies can have a profound influence on the thermodynamic properties of the corresponding systems [32]-[49]. Many investigations, on both FMs and AFMs as well as on classical and quantum systems, revealed the general consequences on the phase transitions and their respective critical temperatures due to the presence of anisotropies [32, 33]. Several of these studies were inspired by exact treatments and presented mathematically rigorous proofs [34, 35, 36, 37].

The case of two spatial dimensions attracted special interest: The presence of easy-axis anisotropies, rendering the system Ising-like, allows to circumvent the Mermin-Wagner theorem and consequently leads to a finite critical temperature [33, 38, 39]. Several studies on two-dimensional easy-axis systems consistently found a logarithmic dependence of the critical temperature [38, 40]. Investigations on easy-plane Heisenberg models [41, 42, 43, 44, 45], on the contrary, successfully recovered the Kosterlitz-Thouless behaviour.

In recent years, a lot of impressing properties of thin film systems have been discovered revealing incipient Kosterlitz-Thouless and 2nd order phase transitions [46, 47, 48, 49]. One of the fascinating properties found in those layered systems are crossover phenomena, which manifest the change of the spin symmetry due to the presence of anisotropies [43, 46, 47, 49].

These theoretical findings have been confirmed from the experimental point of view [50, 51] and were so persuasive that measurements of non-vanishing critical temperatures in low-dimensional samples left the only conclusion that Ising-like anisotropies have to be present to explain the experimental results [52].

Most of the studies mentioned above focused on coupling anisotropies of the kind $\pm \sum_{\langle ij \rangle} \left[J_{xy} \left(S_i^x S_j^x + S_i^y S_j^y \right) + J_z S_i^z S_j^z \right]$ with $J_{xy} \neq J_z$, but anisotropy

fields $(S_i^z)^p$ have not gained that attention. Nevertheless, successful studies [53, 54, 55, 56, 57] on anisotropy fields, published recently, highlight the still ongoing research interest on this fascinating as well as challenging topic.

Therefore, in our view, a comprehensive treatment reviewing the effects of anisotropy fields on the suppression of quantum fluctuations is still missing. We consequently investigate, for a widespread range of parameters, the interplay of the classical trends and limits that are provided by increasing spin quantum numbers S and anisotropy fields h_p .

1.4 Outline of this Thesis

In this paragraph we briefly highlight the topics of each chapter and the reader might use this outline as a quick guide to this thesis.

In order to gain a survey of the involved effects, we start by applying a classical Mean Field (CMF) approach in chapter 2. Thereby, we can estimate the influence of the anisotropy fields on the critical temperature, respectively on purely thermal fluctuations. We further visualize the free energy landscapes for various classes of models and anisotropy fields that illustrate the preference of certain spin components for non-zero anisotropies $h_p \neq 0$. The careful study of this incipient preference exhibits the crossover phenomena mentioned in paragraph 1.3.2. The following Quantum Mean Field (QMF) treatment in chapter 3 extends this Mean Field concept by including quantum effects that give rise to an interplay with thermal fluctuations. The comparison of the relevance of higher-order anisotropy fields (distinct even p) will point out a surprising effect that can be explained by the rise of anisotropy gaps.

Based on this illustrative picture we refine our analytical procedures in the following chapters and improve the reliability of these qualitatively convincing results: We apply the Linear Spin Wave Approximation (LSWA) in chapter 4 and the Random Phase Approximation (RPA) in chapter 5 and modify them appropriately to include the effects of the anisotropy fields h_p . Both theories incorporate quantum effects on an approximative analytical level and provide a more detailed understanding of the suppression of quantum fluctuations: For that purpose, we determine the critical temperature $T_C(h_p)$ in RPA and, for antiferromagnets in LSWA and RPA, the sublattice magnetization $M_{T=0}^{\text{sl}}$ for a comprehensive set of the parameters S , h_p and the dimension d . The results exhibit a strong influence of the anisotropy fields, which consequently transform the original quantum systems rapidly into a classical one. We highlight the sensitivity to anisotropy fields by considering a quantity we want to refer to as anisotropy susceptibility. In the end, these investigations enable us to assess the classical modelling of the SP-STM experiments performed in Hamburg. As a numerical and quantitatively very reliable counterpart to these analytical studies we performed several Quantum Monte Carlo (QMC) simulations presented in chapter 6 and appendix A. Our numerical measurements result in various phase diagrams $T_C(h_p, S)$ that persuasively complement our analytical findings. In chapter 7 we present a detailed outlook to disordered sys-

tems containing impurity spins on diluted lattices. We present the completely implemented generalization to disordered systems on the RPA level and show successful numerical benchmarks. Therefore, these developments open the way for future studies that could be directly based on this thesis. The closing chapter 8 reviews the results of this thesis and highlights the physical conclusions.

Most of the chapters end with a summarizing overview headlined ‘Retrospect and Outlook’: The reader might use these sections as quick guides to the chapters; additionally, each chapter is self-contained and can thus be read separately.

To keep the describing text focused on the physical contents, we abbreviate the most frequently repeated expressions. The list of abbreviations in appendix B explains these terms and acts, thereby, as a glossary.

1.5 Toy Models

In order to point out the typical quantum fluctuations in antiferromagnets, this paragraph deals with small systems that illustrate pure quantum effects at $T=0$ in an exact analytical treatment. Although staying far off the thermodynamical limit, basic properties appear we will also find by more sophisticated approximation schemes in the following chapters.

We consider two quantum Heisenberg spins with $S = 1/2$ and the corresponding Hamiltonian

$$H = \pm 2J \mathbf{S}_1 \cdot \mathbf{S}_2 = \pm J (\mathbf{S}_{\text{tot}}^2 - \mathbf{S}_1^2 - \mathbf{S}_2^2), \quad (1.11)$$

with the total spin \mathbf{S}_{tot} determined by the usual spin addition. The upper sign refers to the AFM and the lower one to the FM. From the energy eigenvalues $E = \pm J[S_{\text{tot}}(S_{\text{tot}}+1) - \frac{3}{2}]$ with $S_{\text{tot}} \in \{0, 1\}$, we can directly identify the ground states at $T=0$: Whereas the ground state of the FM is given by the triplets with $S_{\text{tot}} = 1$ with a non-zero magnetization for $m_{S_{\text{tot}}} = \pm 1$, the ground state of the AFM is determined by the singlet with $S_{\text{tot}} = 0$ that leads to a vanishing sublattice magnetization $M_{T=0}^{\text{sl}}$ due to $m_{S_{\text{tot}}} = 0$. Beyond that, it is well-known that the ground state of the one-dimensional FM exhibits long-range order, whereas the AFM turns out to show no long-range order at all [58]. In higher dimensions the ground state of the AFM yet exhibits long-range order, but at a reduced level compared to the FM [59]. Therefore, the quantum fluctuations in the AFM manifest themselves by singlet formations that are capable of destroying or at least reducing the long-range order in the system.

These singlet formations in AFMs can be further illustrated by a Heisenberg ring consisting of four spins with $S = 1/2$: The resulting singlet state, known as a resonant valence bond state, is itself formed up by the possible two-spin-singlets.

In order to study the trend that is induced by quadratic anisotropy fields, we have to increase the spin quantum number S : In the two-spin system (1.11)

with $S=1$, we accordingly find the shift of the ground state energy $\Delta E \sim -h_2$. Thereby, due to the use of the S^z -eigenstates, the energy is further lowered for the easy-axis scenario $h_p > 0$, showing that the easy-axis is indeed energetically preferred, whereas for $h_p < 0$ the easy-plane is preferred.

In certain coming paragraphs the use of specified fields will highlight the singlet character of the involved antiferromagnetic quantum fluctuations.

Chapter 2

Classical Mean Field

The Mean Field (MF) theory allows to perform analytical calculations with manageable effort. Although this theory is well-known in the literature [60, 61, 62, 63, 64] for certain shortcomings, the Mean Field approach offers strong qualitative insights: After including appropriate adaptations, our classical Mean Field (CMF) treatment will reveal and impressively illustrate the basic effects that are induced by the presence of anisotropy fields.

Since we are concerning classical systems in this chapter, the FM and AFM will exhibit no essential differences. Therefore, we will restrict our following considerations to ferromagnetic Hamiltonians.

2.1 Mean Field Strategies

There exist several theoretical approaches, which share the same name “Mean Field”. Among all these approaches, we will refer in this thesis to variational approaches as the Mean Field method. The basis for this particular Mean Field ansatz is given by the free energy functional

$$F[\rho] = \text{Tr}[\rho H] + T \text{Tr}[\rho \ln \rho] , \quad (2.1)$$

which represents an upper limit to the non-approximated free energy [61]. Thereby, $\text{Tr}[\dots]$ denotes the trace over the corresponding spin spaces of all the N spins on the lattice. Due to (2.1), the following MF technique is sometimes called “ $\text{Tr}[\rho \ln \rho]$ ansatz” as well [61].

The essential nature of the MF ansatz becomes apparent by the vital MF assumption of a factorized density matrix:

$$\rho = \prod_{i=1}^N \rho_i . \quad (2.2)$$

The single-spin density matrices ρ_i have further to fulfill

$$\rho_i \geq 0 \quad \forall i \quad \text{and} \quad \text{Tr}_i[\rho_i] = 1 \quad \forall i \quad \Rightarrow \quad \text{Tr}[\rho] = \prod_{i=1}^N \text{Tr}_i[\rho_i] = 1 , \quad (2.3)$$

with $\text{Tr}_i[\dots]$ denoting the trace over the spin space of a single spin.

There are now two different strategies how to obtain the density matrix (2.2) with its properties (2.3).

The first, more general strategy does not further specify the kind of factorization in (2.2) and regards the density matrix ρ itself as a variational parameter. According to the upper bound that is provided by the free energy functional in (2.1), we pursue its minimization via the functional derivative

$$\frac{\delta F[\rho]}{\delta \rho_i} = H_{\text{MF}}^{(i)} + T [\ln[\rho_i] + 1] \stackrel{!}{=} \zeta_i \quad \text{for } i = 1, \dots, N. \quad (2.4)$$

The Lagrange multipliers ζ_i have been introduced to fulfill the conditions $\text{Tr}_i[\rho_i] = 1$ for $i = 1, \dots, N$, and we consequently yield

$$\rho_i = \frac{1}{Z_i} \exp \left[-\beta H_{\text{MF}}^{(i)} \right] \quad \text{for } i = 1, \dots, N, \quad (2.5)$$

with the inverse temperature $\beta = 1/T$ ($k_B = 1$), the resulting MF Hamiltonian

$$H_{\text{MF}} = \sum_{i=1}^N H_{\text{MF}}^{(i)} \quad (2.6)$$

and the single-spin partition function

$$Z = Z_i = \text{Tr}_i \left[\exp \left[-\beta H_{\text{MF}}^{(i)} \right] \right] \quad \forall i = 1, \dots, N. \quad (2.7)$$

Please note that the form of the approximated MF Hamiltonian in (2.6) is not chosen by hand, but represents the outcome of this variational approach. As a consequence, this particular MF method preserves the most general expression for the approximative Hamiltonian on the MF level.

The magnetization \mathbf{M} , which represents the according order parameter, is subsequently determined self-consistently via the expectation value

$$\mathbf{M} = \langle \mathbf{S} \rangle = \langle \mathbf{S}_i \rangle = \text{Tr}_i [\rho_i \mathbf{S}_i] \quad \forall i = 1, \dots, N. \quad (2.8)$$

The second, less general MF strategy is appropriately described by the name “trial density matrix approach”: We choose (by hand) a concretely specified factorized density matrix

$$\rho = \prod_{i=1}^N \rho_i = \rho \left(\{ \langle S_i^\alpha \rangle \} \right), \quad (2.9)$$

with $\{ \langle S_i^\alpha \rangle \}$ denoting the set of order parameters (i : lattice site; α : spin component), which is self-consistently determined by $\langle S_i^\alpha \rangle = \text{Tr}_i [\rho_i S_i^\alpha]$. In this alternative variational approach the order parameters $\{ \langle S_i^\alpha \rangle \}$ represent the variational parameters; for an appropriate choice of the trial density matrix ρ , the

minimization condition $\partial F/\partial S_i^\alpha \stackrel{!}{=} 0$ is subsequently fulfilled. In consequence of its less general ansatz, this trial density matrix approach may not contain all of the spin components α .

In textbooks, the trial density matrix approach is often misleadingly referred to as *the* Mean Field theory. Since most textbooks deal merely with isotropic systems, the use of a reduced number of spin components does not represent a severe shortcoming due to the symmetry in spin space. For the appropriate description of anisotropic systems, on the contrary, the incorporation of all the spin components represents a vital step for the understanding of the underlying mechanisms. Therefore, we will use, throughout this chapter, density matrices containing all of the spin components, which will exhibit and illustrate the thermal privileging of certain spin components in anisotropic spin systems.

Thus, we will either use the first, more general variational strategy in order to include automatically all of the spin components, or make use of the second strategy with an ably chosen trial density matrix containing all of the spin components.

2.2 Isotropic Systems

We start by demonstrating our procedure for isotropic systems, and will extend our considerations to anisotropic systems in the following section.

The Mean Field approaches explained above that take into account all of the spin components, lead for the classical isotropic FM Heisenberg model (1.1) to the effective Hamiltonian substitution

$$H = - \sum_{\langle ij \rangle} J_{ij} \mathbf{S}_i \cdot \mathbf{S}_j \xrightarrow{\text{MF}} H_{\text{MF}} = -zJ \sum_{i=1}^N \mathbf{M} \cdot \mathbf{S}_i, \quad (2.10)$$

$$\text{with } \mathbf{M} = \mathbf{M}_i = S \begin{pmatrix} \langle \sin \vartheta_i \cos \varphi_i \rangle \\ \langle \sin \vartheta_i \sin \varphi_i \rangle \\ \langle \cos \vartheta_i \rangle \end{pmatrix} \quad \forall i = 1, \dots, N, \quad (2.11)$$

and $z=2d$ denoting the coordination number for simple lattices (simple cubic, square and chain lattices). For the free energy we get the expression

$$F = -\frac{1}{2} zJ N \mathbf{M}^2 + T \sum_{i=1}^N \text{Tr}_i [\rho_i \ln \rho_i], \quad (2.12)$$

$$\text{with } \rho_i = \frac{1}{Z_i} \exp [\beta zJ \mathbf{M} \cdot \mathbf{S}_i]. \quad (2.13)$$

Applying the properties (2.3) of the density matrix $\rho = \prod_i \rho_i$, we yield the free energy per spin

$$f = \frac{1}{2} zJ \mathbf{M}^2 - T \ln Z, \quad (2.14)$$

$$\text{with } Z = Z_i = \int_{-\pi}^{+\pi} d\varphi_i \int_0^{+\pi} d\vartheta_i \sin \vartheta_i \exp [\beta zJ \mathbf{M} \cdot \mathbf{S}_i] \quad \forall i = 1, \dots, N. \quad (2.15)$$

After expanding (2.14) up to the quartic order in the magnetization \mathbf{M} , the conclusive functional form of the free energy reads

$$f = \frac{3}{2} \frac{1}{S^2} [T - T_C^{\text{iso}}] \mathbf{M}^2 + \frac{1}{180} (\beta_C^{\text{iso}})^3 (zJ)^4 S^4 \mathbf{M}^4 + \mathcal{O}[\mathbf{M}^6] , \quad (2.16)$$

which enables us to identify the critical temperature of the isotropic classical Heisenberg model:

$$T_C^{\text{iso}} = \frac{zJ}{3} S^2 . \quad (2.17)$$

This functional form for the free energy is closely related to the phenomenological Landau theory [61]. The graphical plot of (2.16) in fig. 2.1 accordingly recovers the famous “Mexican hat” potential for temperatures below the critical temperature T_C^{iso} . The corresponding plots for anisotropic systems will, later on, beautifully elucidate the impact of the anisotropy fields.

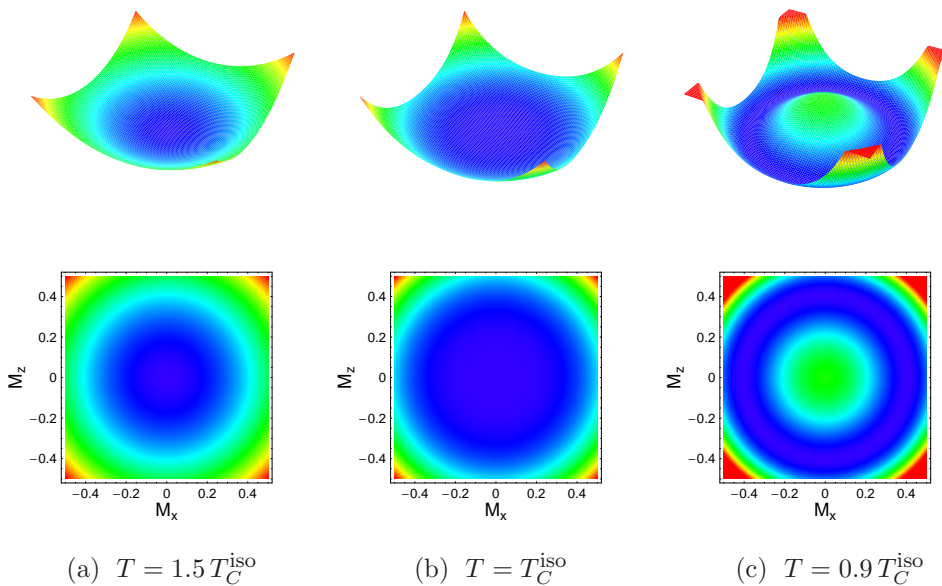


Figure 2.1: Plots of the analytical free energy expression (2.16) for different temperatures T ; T_C^{iso} denotes the critical temperature (2.17); for the sake of simplicity, we set $zJ = 1$ and $S = 1$; the blue colour indicates the minima of the free energy landscape (since the absolute value of the free energy is given in arbitrary units and is non-fixed anyway, we omitted the colour legend).

For the classical XY model (1.3) we find by the same procedure the resulting free energy per spin

$$f^{XY} = \frac{1}{S^2} [T - T_C^{XY}] \mathbf{M}^2 + \frac{1}{64} (\beta_C^{XY})^3 (zJ)^4 S^4 \mathbf{M}^4 + \mathcal{O}[\mathbf{M}^6] , \quad (2.18)$$

$$\text{with } \mathbf{M} = \mathbf{M}_i = S \begin{pmatrix} \langle \cos \varphi_i \rangle \\ \langle \sin \varphi_i \rangle \end{pmatrix} \quad \forall i = 1, \dots, N , \quad (2.19)$$

and the corresponding critical temperature

$$T_C^{XY} = \frac{zJ}{2} S^2 . \quad (2.20)$$

Last but not least, we find for the Ising model (1.7)

$$f^{\text{Ising}} = \frac{1}{2} \frac{1}{S^2} [T - T_C^{\text{Ising}}] M^2 + \frac{1}{12} (\beta_C^{\text{Ising}})^3 (zJ)^4 S^4 M^4 + \mathcal{O}[M^6] , \quad (2.21)$$

$$\text{with } M = M_i = \langle S_i^z \rangle \quad \forall i = 1, \dots, N , \quad (2.22)$$

$$\text{and } T_C^{\text{Ising}} = zJS^2 . \quad (2.23)$$

The results for the isotropic systems are summarized in table 2.1.

Model	Critical temperature
Heisenberg	$\frac{zJ}{3} S^2$
XY	$\frac{zJ}{2} S^2$
Ising	zJS^2

Table 2.1: Critical temperatures of various isotropic spin models determined by the classical Mean Field approach.

In the end, the critical temperatures show an inverse proportionality to the number of spin dimensions n : $T_C = zJS^2/n$. This finding is thermodynamically quite persuasive since it is well-known that the appearance of multiple spin dimensions raises the capability of enlarged thermal fluctuations.

Please note that the spatial dimension d affects the critical temperatures in table 2.1 solely via the coordination number $z=2d$. Therefore, the Mean Field theory is not capable to comply with the Mermin-Wagner theorem [8] due to the simplicity of its underlying factorization approach (2.2). Nonetheless, the MF approach enables us, for a start, to illustrate the basic effects on a qualitative level, and we will remove this MF-specific shortcoming by more sophisticated techniques in the subsequent chapters.

Alternative trial density matrix approaches, which merely take into account certain spin components, yield for isotropic systems identical results for the critical temperature. This ambiguity exhibits that none of the spin components is thermodynamically preferred to each other. Anisotropy fields, on the contrary, will induce preferred axes and planes, as we will point out in the coming paragraph.

2.3 Heisenberg Model with Anisotropy Fields

This section deals with the MF treatment of the classical FM Heisenberg model (1.1) that is affected by anisotropy fields h_p with $p \in \{2, 4, 6\}$:

$$H = - \sum_{\langle ij \rangle} J_{ij} \mathbf{S}_i \cdot \mathbf{S}_j - h_p S^p \sum_{i=1}^N \cos^p \vartheta_i. \quad (2.24)$$

An appropriate Mean Field ansatz, which takes into account all of the spin components, reads

$$H \longrightarrow H_{\text{MF}} = -zJ \sum_{i=1}^N \mathbf{M} \cdot \mathbf{S}_i - h_p S^p \sum_{i=1}^N \cos^p \vartheta_i, \quad (2.25)$$

and is achieved by the density matrix

$$\rho_i = \frac{1}{Z_i} \exp \left[\beta z J \mathbf{M} \cdot \mathbf{S}_i + \beta h_p S^p \cos^p \vartheta_i \right] \quad \text{for } i = 1, \dots, N, \quad (2.26)$$

$$\text{with } Z = Z_i = \int_{-\pi}^{+\pi} d\varphi_i \int_0^{+\pi} d\vartheta_i \sin \vartheta_i \exp \left[\beta z J \mathbf{M} \cdot \mathbf{S}_i + \beta h_p S^p \cos^p \vartheta_i \right] \quad (2.27)$$

$$\text{and } \mathbf{M} = \begin{pmatrix} M_x \\ M_y \\ M_z \end{pmatrix} = \mathbf{M}_i = S \begin{pmatrix} \langle \cos \varphi_i \sin \vartheta_i \rangle \\ \langle \sin \varphi_i \sin \vartheta_i \rangle \\ \langle \cos \vartheta_i \rangle \end{pmatrix} \quad \forall i = 1, \dots, N. \quad (2.28)$$

A similar MF ansatz has been proposed by Udvardi et al. for the description of reorientation phase transitions in thin magnetic films [65, 66].

2.3.1 Free Energy and Critical Temperatures

By expanding the free energy expression

$$f = \frac{1}{2} z J \mathbf{M}^2 - T \ln Z \quad (2.29)$$

up to the fourth order in the magnetization components M_α , $\alpha \in \{x, y, z\}$, and up to the first order in the anisotropy field h_p , we get the resulting Landau-like free energy

$$\begin{aligned}
 f &= \frac{3}{2} \frac{1}{S^2} \left[T - T_C^{\text{iso}} (1 + a_p^z \beta_C^{\text{iso}} h_p S^p) \right] M_z^2 \\
 &+ \frac{3}{2} \frac{1}{S^2} \left[T - T_C^{\text{iso}} (1 - a_p^{x/y} \beta_C^{\text{iso}} h_p S^p) \right] (M_x^2 + M_y^2) \\
 &+ \frac{1}{180} (\beta_C^{\text{iso}})^3 (zJ)^4 S^4 \mathbf{M}^4 + \mathcal{O}[h_p \cdot M_\alpha^4] + \mathcal{O}[\mathbf{M}^6] , \quad (2.30)
 \end{aligned}$$

with T_C^{iso} given by (2.17) and the prefactors $a_p^\alpha > 0$ summarized in table 2.2. Thereby, we considered the influence of the anisotropy fields h_p solely for the quadratic order of the magnetization. In the end, these h_p -corrections for the M_α^2 -terms represent the decisive shifts of the critical temperatures: From (2.30), we can conclude the occurrence of a single second order phase transition with the critical temperature

$$T_C^z = T_C^{\text{iso}} \left[1 + a_p^z \beta_C^{\text{iso}} h_p S^p \right] \quad \text{for } h_p > 0, \quad (2.31)$$

$$T_C^{x/y} = T_C^{\text{iso}} \left[1 - a_p^{x/y} \beta_C^{\text{iso}} h_p S^p \right] \quad \text{for } h_p < 0. \quad (2.32)$$

Although we find distinct values for T_C^α with $\alpha \in \{x, y, z\}$, the entire spin system exhibits just one single critical temperature: Those components α , which show the highest value of all T_C^α , are consequently thermodynamically preferred. Therefore, we recover an easy-axis (EA) in z -direction with $T_C^{EA} = T_C^z$ for $h_p > 0$, and an easy-plane (EP) on the x - y -plane with $T_C^{EP} = T_C^x = T_C^y$ for $h_p < 0$. This finding is, of course, not a surprising one, but we could derive this resulting behaviour without demanding it a priori. According to the remaining effective spin dimensions (EA: 1, EP: 2) we find for all investigated even p the characteristic ratio $a_p^z / a_p^{x/y} = 2$.

a_p^α	$p = 2$	$p = 4$	$p = 6$
z - component	$a_2^z = \frac{4}{15}$	$a_4^z = \frac{8}{35}$	$a_6^z = \frac{4}{21}$
x/y - component	$a_2^{x/y} = \frac{2}{15}$	$a_4^{x/y} = \frac{4}{35}$	$a_6^{x/y} = \frac{2}{21}$

Table 2.2: Analytically determined prefactors a_p^α , with $\alpha \in \{x, y, z\}$ and $p \in \{2, 4, 6\}$; a_p^α is decisive for the shift of the critical temperatures T_C^α in (2.30)-(2.32).

Furthermore, the multiple-spin-component Mean Field approach enables us to illustrate the preference of certain spin components in fig. 2.2 - 2.4 by plotting the analytical function (2.30). For the sake of simplicity, we restricted our illustrations to the magnetization components M_x and M_z , since M_y behaves identically to M_x , as we can see from (2.30) and (2.32). The appearance of specifically located minima in the distorted free energy landscapes clearly demonstrates the privileging of the M_z -axis for $h_2 > 0$ in fig. 2.2 - 2.3 and the preferring of the M_x -component (resp. the M_x - M_y -plane) for $h_2 < 0$ in fig. 2.4. This anisotropic behaviour is to be contrasted with the isotropic “Mexican hat” potential in fig. 2.1.

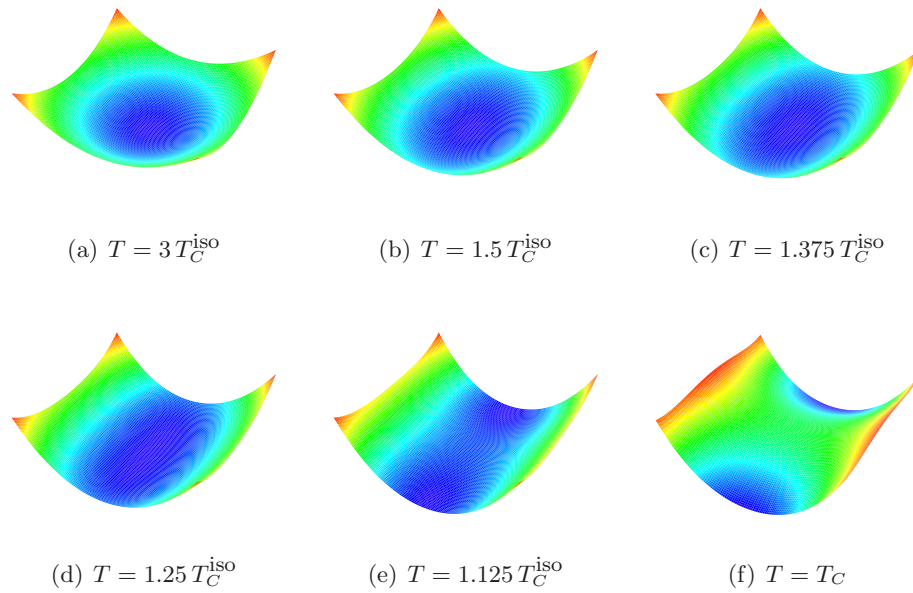
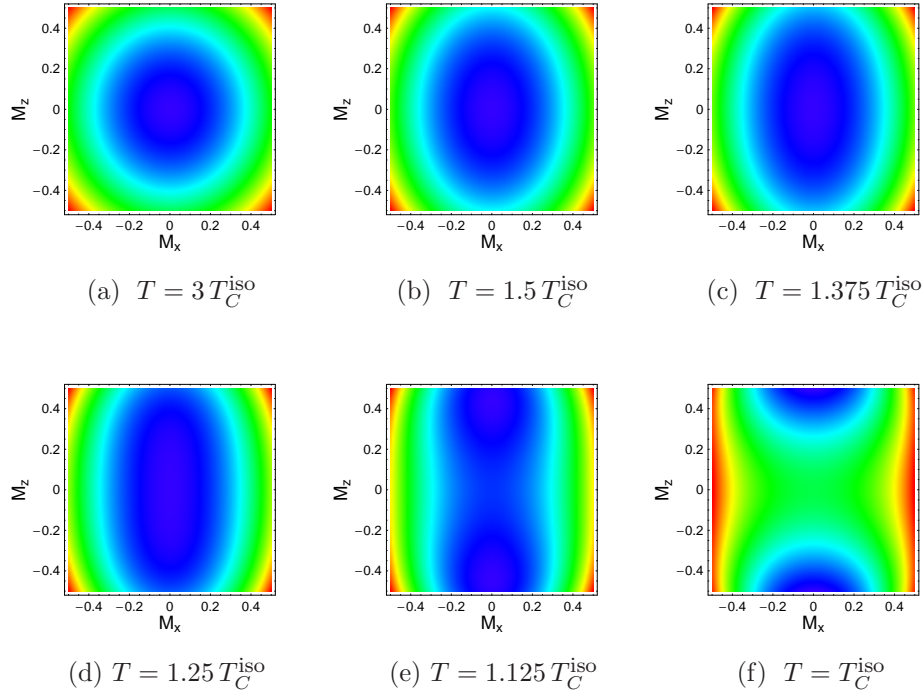


Figure 2.2: Free energy landscape (2.30) in the M_x - M_z -plane (M_y set to zero) of the classical anisotropic Heisenberg model (2.24) with fixed quadratic ($p = 2$) anisotropy field $h_2 = +0.3$ for various temperatures T ; $T_C^{\text{iso}} = \frac{zJ}{3} S^2$ denotes the critical temperature of the isotropic system; we set $zJ = 1$ and $S = 1$.

The emergence of privileged spin components is thereby accompanied by the change of the underlying spin symmetry: For $h_2 > 0$ we recover the familiar Z_2 -symmetry of the Ising model along the z -axis of the magnetization, whereas for $h_2 < 0$ the $O(2)$ -symmetry of the XY model emerges on the M_x - M_y -plane.


 Figure 2.3: Two-dimensional version of fig. 2.2 for $h_2 = +0.3$.

We can check our results by an alternative determination of the critical temperature: For that purpose, we determine the magnetization self-consistently via

$$\mathbf{M} = \frac{1}{Z_i} \int_{-\pi}^{+\pi} d\varphi_i \int_0^{+\pi} d\vartheta_i \sin \vartheta_i \mathbf{S}_i \exp \left[\beta z J \mathbf{M} \cdot \mathbf{S}_i + \beta h_p S^p \cos^p \vartheta_i \right] \quad (2.33)$$

$\forall i = 1, \dots, N$. In the limits

$$T \lesssim T_C \quad \text{and} \quad M \gtrsim 0, \quad (2.34)$$

we can expand the right-hand side of (2.33) up to the first order in $(\lim_{M \gtrsim 0} M)$ and up to the first order in h_p , and may subsequently cancel $(\lim_{M \gtrsim 0} M)$ on both sides of the resulting equation. The resulting outcome confirms our results in (2.31) and (2.32). In the course of this thesis, we will make repeated use of this particular procedure for the determination of the critical temperatures. A similar technique, in order to extract the critical temperatures of anisotropic spin systems, has been applied by Udvardi et al. in finite-size systems [65, 66].

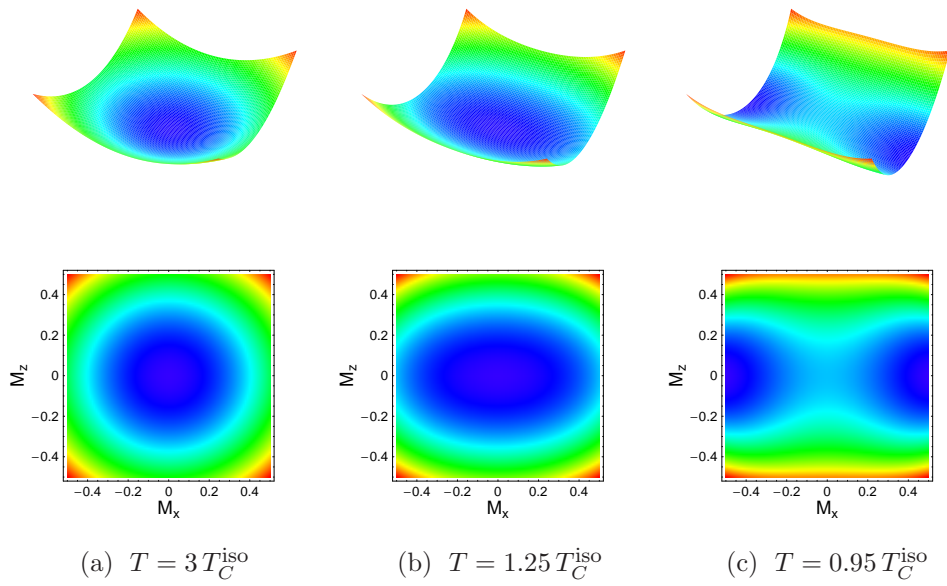


Figure 2.4: Free energy landscape (2.30) of the classical anisotropic Heisenberg model in the M_x - M_z -plane (M_y set to zero) for negative anisotropy $h_2 = -0.3$ at various temperatures T .

The creation of EA and EP and the accompanied change of the underlying spin symmetry is reflected by the limits of the critical temperatures for large anisotropy fields $|h_p| \gg 1$: Via the self-consistent calculation of the magnetization, we numerically determined the critical temperature, which is characterized by the vanishing of the magnetization $M \xrightarrow{z} 0$. For positive $h_p \gg 1$, we consistently found the numerical Ising limit

$$T_C^{\text{EA}} = T_C^z(h_p) \xrightarrow{h_p \gg 1} T_C^{\text{Ising}} = zJS^2 \quad \text{for } h_p > 0, \quad (2.35)$$

whereas negative anisotropies $h_p < 0$ give rise to the XY limit for $|h_p| \gg 1$:

$$T_C^{\text{EP}} = T_C^{x/y}(h_p) \xrightarrow{|h_p| \gg 1} T_C^{\text{XY}} = \frac{zJ}{2} S^2 \quad \text{for } h_p < 0. \quad (2.36)$$

The resulting phase diagram for $p = 2$ is shown in fig. 2.5. For small h_2 , we find an excellent agreement with the analytical approximations (2.31) and (2.32), which incorporate the linear order $\mathcal{O}[h_p]$.

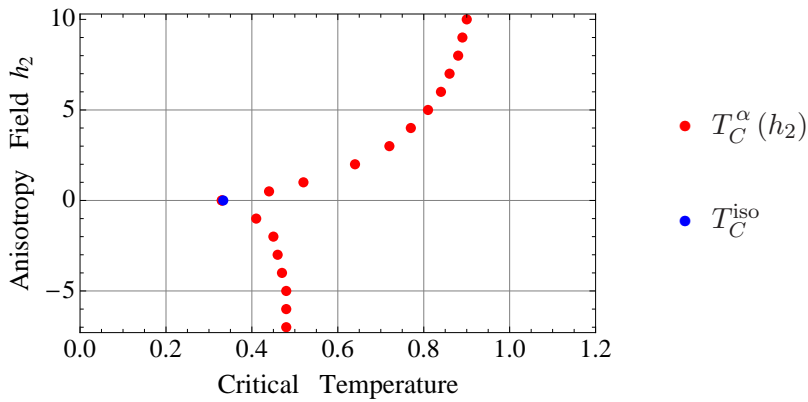


Figure 2.5: Numerically determined critical temperatures $T_C^\alpha(h_2)$ for the classical Heisenberg model (2.24) influenced by quadratic ($p = 2$) anisotropy fields h_2 ; for $h_2 > 0$ the component α of T_C^α is given by $\alpha = z$, whereas for $h_2 < 0$ $\alpha \in \{x, y\}$; for the numerical treatment we set $zJ = 1$ and $S = 1$; starting from the isotropic value $T_C^{\text{iso}} = 1/3$, we recover the Ising limit $T_C \rightarrow 1$ for large positive anisotropy fields $h_2 \gg 1$, and the XY limit $T_C \rightarrow 1/2$ for large negative fields $h_2 < 0$, $|h_2| \gg 1$; the numerical errors are smaller than the size of the symbols.

Finally, we pass a vital comment on the scaling of the anisotropy term $\sim S^p$ in (2.24), which stems from the length S of the classical spin vectors: Since T_C^{iso} scales itself $\sim S^2$, we have to rescale the higher-order fields with $p > 2$ by S^{p-2} in order to compare their relative relevance for an arbitrary spin length S . As a consequence, the rescaled anisotropy term appropriately scales $\sim S^2$ like the coupling term in (2.24). We will revisit this rescaling scheme repeatedly in the course of this thesis. For the classical Heisenberg model we clearly find from table 2.2 the hierarchy

$$a_2^\alpha > a_4^\alpha > a_6^\alpha, \quad (2.37)$$

for both the EA ($\alpha = z$) and the EP ($\alpha \in \{x, y\}$) scenario. Therefore, we find a stronger relevance for fields h_p of lower order p . We will study the hierarchy of relevance in more detail in the following chapter.

For any finite odd p , we find linear terms $\sim h_p M_z$ in the free energy expansions and consequently conclude a first order transition scenario for $h_p \neq 0$.

2.3.2 Crossover Phenomenon

The observation of the free energy landscape in fig. 2.2-2.4 reveals another intriguing phenomenon, which manifests the change of symmetry that is induced by the presence of anisotropies: Whereas the free energy remains unaffected by anisotropy fields at very large temperatures $T \gg h_p$, we can clearly observe the incipient distortion of the free energy that is accompanied by the privileging of certain spin components. This distortion demonstrates the commencing change of the underlying spin symmetries above the critical temperature. Since this change is not accompanied by any discontinuities or divergencies in the thermodynamic quantities, we conclude a crossover scenario, which was found in related studies [43, 46, 47, 49]. In order to quantify this crossover, we could consider direction-dependent free energies, but, in order to deal with experimentally accessible quantities, we examine the magnetic susceptibilities of the anisotropic system. Due to the direction-dependency for $h_p \neq 0$, we consider the component-wise defined magnetic susceptibilities

$$\chi^\alpha(T) = \frac{\partial M_\alpha}{\partial \pi_\alpha} \quad \text{with } \alpha \in \{x, y, z\}, \quad (2.38)$$

and with the uniform magnetic field $\boldsymbol{\pi} = (\pi_x, \pi_y, \pi_z)$.

For that purpose, we introduce this external field $\boldsymbol{\pi}$ in the free energy

$$\bar{f} = -\boldsymbol{\pi} \cdot \mathbf{M} + b_p^{x/y} (M_x^2 + M_y^2) + b_p^z M_z^2 + c \mathbf{M}^4 + \mathcal{O}[\mathbf{M}^6], \quad (2.39)$$

$$\text{with } b_p^{x/y} = \frac{3}{2} \frac{1}{S^2} \frac{T_C^{\text{iso}}}{T} \left[T - T_C^{\text{iso}} \left(1 - a_p^{x/y} \frac{h_p S^p}{T} \right) \right], \quad (2.40)$$

$$b_p^z = \frac{3}{2} \frac{1}{S^2} \frac{T_C^{\text{iso}}}{T} \left[T - T_C^{\text{iso}} \left(1 + a_p^z \frac{h_p S^p}{T} \right) \right], \quad (2.41)$$

$$c = \frac{1}{180} \beta^3 (zJ)^4 S^4 + \mathcal{O}[h_p], \quad (2.42)$$

and a_p^α given in table 2.2. In contrast to the Landau-like expression in (2.30) that is approximated for $T \approx T_C^{\text{iso}}$, we now take into account the explicit temperature dependence of the coefficients b_p^α and c , which stems from the original free energy expansion for arbitrary temperatures. From (2.39)-(2.42), we subsequently extract the susceptibilities χ^z and $\chi^x = \chi^y$ by suitable derivatives.

Let us demonstrate this procedure in detail for $h_p > 0$: We start with the preferred component M_z . In order to find the minimum of (2.39) along the M_z -axis, which represents the global minimum for $h_p > 0$, we set $M_x = M_y = 0$ and calculate the derivative with respect to M_z :

$$\frac{\partial \bar{f}}{\partial M_z} = -\pi_z + 2b_p^z M_z + 4c M_z^3 \stackrel{!}{=} 0. \quad (2.43)$$

The subsequent derivative with respect to π_z yields

$$2b_p^z \chi^z + 12c M_z^2 \chi^z = 1. \quad (2.44)$$

For the remaining expression M_z^2 we insert temperature-dependent values: For the high-temperature region $T > T_C^z$ we insert $M_z = 0$, whereas its value in the low-temperature region $T < T_C^z$ is determined by the derivative $\partial f / \partial M_z = 0$, which yields

$$M_z^2 = -\frac{b_p^z}{2c} \quad \text{for } T < T_C^z. \quad (2.45)$$

These substitutions give

$$\chi^z = \begin{cases} +\frac{1}{2b_p^z} & \text{for } T > T_C^z, \\ -\frac{1}{4b_p^z} & \text{for } T < T_C^z. \end{cases} \quad (2.46)$$

For the non-preferred magnetization component M_x (representing M_y as well, which we set to zero for the sake of simplicity), we have to adapt this procedure slightly: In the high-temperature region $T > T_C^z$ we may set $M_z = 0$ and may simply change the indices $z \rightarrow x$ to obtain

$$\chi^x = +\frac{1}{2b_p^x} \quad \text{for } T > T_C^z. \quad (2.47)$$

In the low-temperature region $T < T_C^z$, on the contrary, we have to bear in mind the non-zero value of $M_z^2 = -b_p^z/2c$. The derivative of \bar{f} with respect to M_x is consequently given by

$$\frac{\partial \bar{f}}{\partial M_x} = -\pi_x + 2b_p^x M_x + 4c M_x (M_x^2 + M_z^2) \stackrel{!}{=} 0. \quad (2.48)$$

The subsequent derivative with respect to π_x gives with (2.45)

$$2[b_p^x - b_p^z] \chi^x + 12c M_x^2 \chi^x = 1. \quad (2.49)$$

By inserting the minimum value $M_x = 0$, we finally yield the low-temperature susceptibility along the x -component of the magnetization:

$$\chi^x = +\frac{1}{2[b_p^x - b_p^z]} \quad \text{for } T < T_C^z. \quad (2.50)$$

For χ^y we find the identical outcome with $x \rightarrow y$ and $b_p^y = b_p^x$.

The resulting susceptibilities χ^z , χ^x and their ratios are depicted in fig 2.6-2.7 for $p = 2$.

For $h_p < 0$, we have to substitute all of the indices $x \leftrightarrow z$. Please pay regard to the asymmetry between the EA and EP scenario characterized by $b_p^x (\pm h_p) \neq b_p^z (\mp h_p)$.

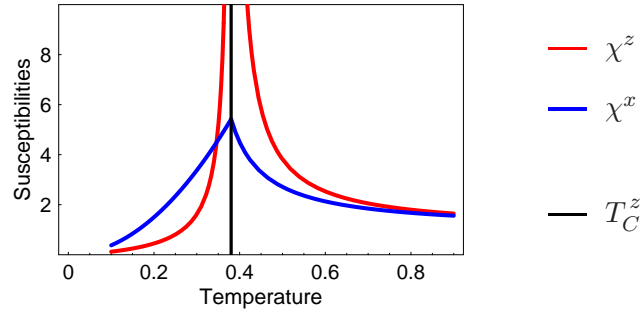


Figure 2.6: Temperature dependency of the susceptibilities χ^x and χ^z for fixed positive quadratic anisotropy field $h_2 = +0.2$; for the sake of simplicity, we set $zJ = 1$ and $S = 1$.

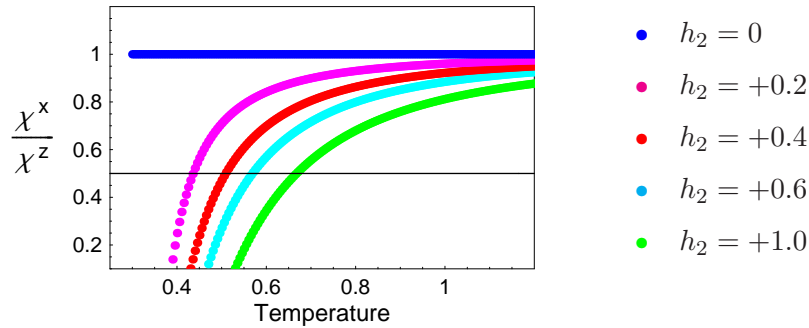


Figure 2.7: Temperature dependency of the susceptibility ratio χ^x/χ^z for various positive quadratic anisotropy fields $h_2 \geq 0$; we set $zJ = 1$ and $S = 1$.

In order to concretize the crossover point, we constitute the following reasonable crossover criterion: As suggested by the figures above, we define the crossover temperature T_{CO} by

$$\frac{\chi^x(T_{CO})}{\chi^z(T_{CO})} \stackrel{!}{=} \frac{1}{2} \quad \text{for } h_p > 0, \quad (2.51)$$

$$\frac{\chi^z(T_{CO})}{\chi^x(T_{CO})} \stackrel{!}{=} \frac{1}{2} \quad \text{for } h_p < 0. \quad (2.52)$$

The resulting, numerically determined phase diagrams of the anisotropic Heisenberg model, including the crossovers, are shown in fig. 2.8 for $p \in \{2, 4, 6\}$. Although the critical temperatures are shifted to a lesser extent for higher-order anisotropy fields h_p with $p \in \{4, 6\}$, we still find the crossover occurring at relatively large temperatures. For small anisotropy fields h_p , we find an excellent agreement with the analytical expressions (2.31)-(2.32).

- ① $O(3)$ -symmetry, non-ordered
- ② Z_2 -symmetry (Ising-like), non-ordered
- ③ Z_2 -symmetry (Ising-like), ordered
- ④ $O(2)$ -symmetry, non-ordered
- ⑤ $O(2)$ -symmetry, ordered

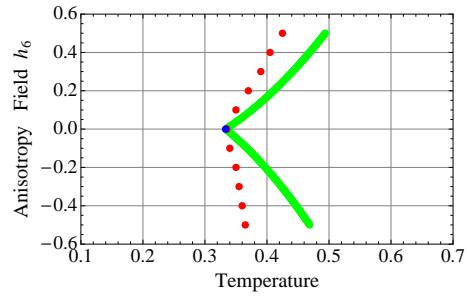
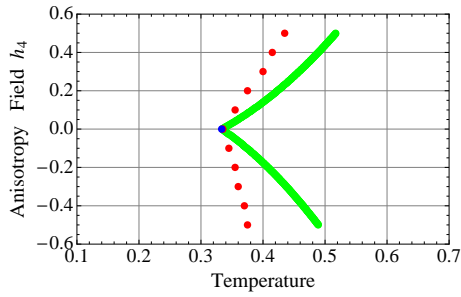
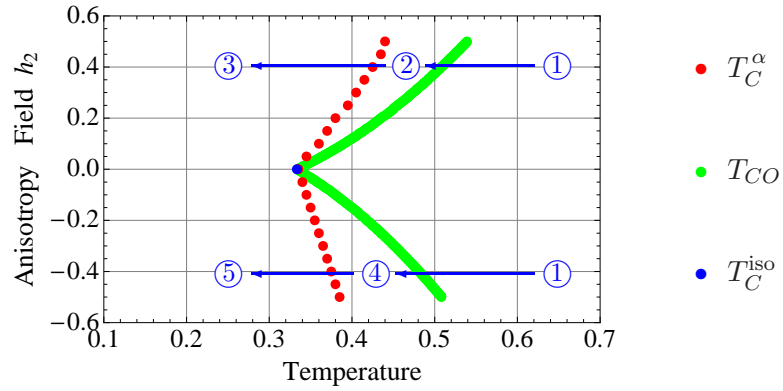


Figure 2.8: Phase diagrams of the anisotropic Heisenberg model (2.24) including the critical temperatures T_C^α ($\alpha = z$ for $h_p > 0$ and $\alpha \in \{x, y\}$ for $h_p < 0$) and the crossover temperatures T_{CO} defined by (2.51)-(2.52) for $p = 2$ (a), $p = 4$ (b) and $p = 6$ (c); T_C^{iso} denotes the critical temperature of the isotropic system; we set $zJ = 1$ and $S = 1$.

The following two paragraphs present extended considerations demonstrating the potency of this Mean Field approach especially for classical systems: Whereas section 2.4 highlights the capability of the multiple-spin-component Mean Field approach for the anisotropic XY model, section 2.5 shows up the embedding of semiclassical models that are related to our classical models via the Quantum-Classical Mapping. The reader, who is solely interested in the results on the Heisenberg systems, may therefore omit these specialized paragraphs and continue directly with section 2.6, resp. chapter 3.

2.4 Excursion I: XY Model with Z_p -Anisotropy

In order to demonstrate the powerful graphical illustrations that are provided by an appropriate multi-spin-component Mean Field approach, we further investigate the ferromagnetic classical XY model (1.3)-(1.4) influenced by the Z_p -anisotropy $\cos [p \varphi_i]$ [67, 68]:

$$H = -J \sum_{\langle i,j \rangle} \mathbf{S}_i \cdot \mathbf{S}_j - h_p \sum_{i=1}^N \cos [p \varphi_i] \quad \text{with } \mathbf{S}_i = \begin{pmatrix} \cos \varphi_i \\ \sin \varphi_i \end{pmatrix} \quad (2.53)$$

$$= -J \sum_{\langle i,j \rangle} \cos (\varphi_i - \varphi_j) - h_p \sum_{i=1}^N \cos [p \varphi_i]. \quad (2.54)$$

Since we will not deal with S -dependent phenomena in this subchapter, we set, for the sake of simplicity, the classical spin length $S = 1$.

2.4.1 Overview of Primal Renormalization Group Considerations

In the late 1970s Jose, Kadanoff, Kirkpatrick and Nelson [67] revealed in a pioneering breakthrough the relevance of these anisotropy fields h_p in the sense of the renormalization group: With the use of the particular spin wave approximation $\cos (\varphi_i - \varphi_j) \rightarrow [\varphi_i - \varphi_j]^2$, they found for the anisotropy fields in (2.54) the following recursion relation in two dimensions:

$$h_p \rightarrow b^{\lambda_p(T)} h_p \quad \text{with } \lambda_p(T) = 2 - \frac{T}{4\pi J} p^2. \quad (2.55)$$

Thereby, $b > 1$ denotes the increase of the lattice spacing a under the renormalization group transformation according to $a \rightarrow b \cdot a$. From (2.55), they concluded that the anisotropy fields h_p are strongly relevant at sufficiently low temperatures guaranteeing $\lambda_p(T) > 0$. For large temperatures, on the contrary, the anisotropy fields turn out to be irrelevant according to $\lambda_p(T) < 0$. The corresponding borderline of marginality ($\lambda_p(T) = 0$) is given by

$$T_{\text{marginal}} = \frac{8\pi J}{p^2}. \quad (2.56)$$

As a consequence, fields of the type (2.54) with a higher order p' are clearly less relevant than those of lower orders $p'' < p'$.

Such renormalization group investigations on the relevance of anisotropy fields are thereby closely related to our studies on the anisotropic Heisenberg model: The corresponding renormalization group treatment for the Heisenberg model with quadratic anisotropy fields can be found in [62]. Therefore, we adopt, from time to time, the word “relevance”, which originally stems from renormalization group considerations, to describe the strength of anisotropy fields.

Jose et al. further pursued the calculation of $\lambda_p(T)$ with the use of the Migdal recursion scheme, which results in the phase diagram h_p vs. T/J that contains the curves $T_C(h_p)$ describing the phase transitions into ordered phases (see fig. 13 in [67]). We will explicitly compare their renormalization group phase diagram with the corresponding one achieved by the following Mean Field approach. By this comparison, we will reveal the underestimated sensitivity to the anisotropy fields in the Mean Field framework.

The impact of this pioneering work by Jose, Kadanoff, Kirkpatrick and Nelson [67] is highlighted by the number of citations: By now, their original article has been cited over 1200 times according to [69].

We will supplement this work by impressive illustrations of the corresponding free energy landscapes achieved by analytical power expansions. Related studies [70] on extended “non-linear models” describe similar free energy landscapes in words, but did neither plot nor visualize them. Therefore, this section represents a natural supplement to these studies.

2.4.2 Mean Field Free Energy Landscapes

For the Hamiltonian (2.54), we expect the following privileged orientations:

$$h_p > 0 : \quad \varphi_n = \frac{2\pi}{p} \cdot n \quad \text{with } n \in \{1, \dots, p\}, \quad (2.57)$$

$$h_p < 0 : \quad \varphi_n = \frac{(2n-1)\pi}{p} \quad \text{with } n \in \{1, \dots, p\}. \quad (2.58)$$

In the following, we will present the analytical results from the expansion of the free energy and the corresponding plots of the free energy landscapes, which ultimately confirm the preferred directions in (2.57)-(2.58) a posteriori. Thereby, we will have to perform more elaborate expansion schemes for increasing anisotropy orders p , as we will point out in the following.

The appropriate Mean Field ansatz, which takes into account both of the spin components $S_i^x = \cos \varphi_i$ and $S_i^y = \sin \varphi_i$, reads

$$H \rightarrow H_{\text{MF}} = -zJ \sum_{i=1}^N \mathbf{M} \cdot \mathbf{S}_i - h_p \sum_{i=1}^N \cos [p \varphi_i] \quad (2.59)$$

$$= -zJ \sum_{i=1}^N [M_x \cos \varphi_i + M_y \sin \varphi_i] - h_p \sum_{i=1}^N \cos [p \varphi_i], \quad (2.60)$$

$$\text{with } \mathbf{M} = \begin{pmatrix} M_x \\ M_y \end{pmatrix} = \mathbf{M}_i = \begin{pmatrix} \langle \cos \varphi_i \rangle \\ \langle \sin \varphi_i \rangle \end{pmatrix} \quad \forall i = 1, \dots, N, \quad (2.61)$$

and is achieved by the density matrix

$$\rho_i = \frac{1}{Z_i} \exp \left[\beta z J \mathbf{M} \cdot \mathbf{S}_i + \beta h_p \cos [p \varphi_i] \right] \quad \text{for } i = 1, \dots, N, \quad (2.62)$$

with the partition function

$$Z = Z_i = \int_{-\pi}^{+\pi} d\varphi_i \exp \left[\beta z J \mathbf{M} \cdot \mathbf{S}_i + \beta h_p \cos [p \varphi_i] \right] \quad \forall i = 1, \dots, N. \quad (2.63)$$

The free energy per spin is accordingly given by

$$f = +\frac{1}{2} z J \mathbf{M}^2 - T \ln Z. \quad (2.64)$$

In the following, we will expand this free energy, with the use of (2.63), for each $p \in \{1, 2, 3, 4, 5, 6\}$ separately.

$h_p = 0$

For the benchmarking isotropic case $h_p = 0$, we recover the “Mexican hat” potential described by

$$f_{h_p=0} = [T - T_C^{\text{XY}}] \mathbf{M}^2 + \frac{1}{64} (\beta_C^{\text{XY}})^3 (zJ)^4 \mathbf{M}^4 + \mathcal{O}[\mathbf{M}^6] \quad (2.65)$$

$$\text{with } T_C^{\text{XY}} = \frac{1}{\beta_C^{\text{XY}}} = \frac{zJ}{2}, \quad (2.66)$$

which is depicted in fig. 2.9.

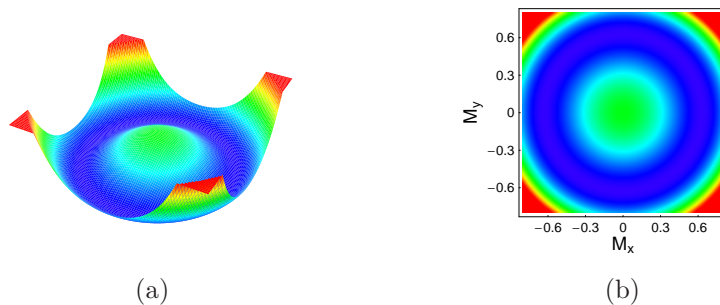


Figure 2.9: Three- and two-dimensional plot of the isotropic ($h_p = 0$) free energy landscape (2.65) in the M_x - M_y -plane at $T = 0.8 T_C^{\text{XY}}$; we set $zJ = 1$.

$$p = 1$$

For the case of the magnetic field h_1 with $p = 1$, we find the according expansion of the free energy up to the first order in h_1

$$f_{p=1} = -h_1 M_x + [T - T_C^{XY}] \mathbf{M}^2 + \frac{1}{64} (\beta_C^{XY})^3 (zJ)^4 \mathbf{M}^4 + \mathcal{O}[h_1 \cdot M_\alpha^3] + \mathcal{O}[\mathbf{M}^6]. \quad (2.67)$$

The graphical plots of (2.67) in fig. 2.10-2.11 clearly illustrate the preference of $\pm M_x$ for $h_1 \gtrless 0$. From the appearance of linear terms in (2.67) we explicitly conclude that a first order phase transition takes place.

$$h_1 > 0$$

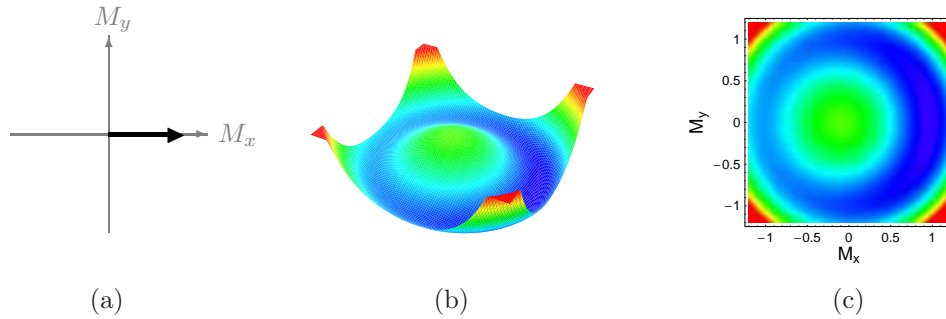


Figure 2.10: Three- and two-dimensional plot of the free energy landscape (2.67) in the M_x - M_y -plane for $h_1 = +0.05$ at $T = \frac{1}{2} T_C^{XY}$ (we set $zJ = 1$); subfigure (a) illustrates the preferred spin direction according to (2.57).

$$h_1 < 0$$

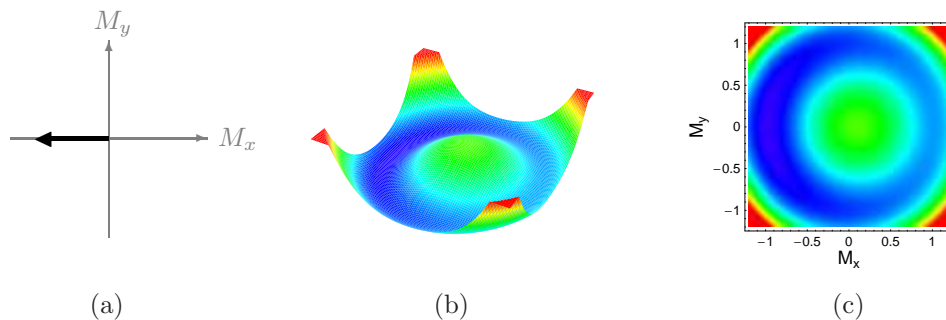


Figure 2.11: Plot of (2.67) for $h_1 = -0.05$ at $T = \frac{1}{2} T_C^{XY}$ ($zJ = 1$); subfigure (a) illustrates the preferred spin direction according to (2.58).

$p = 2$

For quadratic anisotropy fields h_2 , we find the expanded free energy

$$f_{p=2} = \left(T - T_C^{\text{XY}} \left[1 + \frac{1}{2} \beta_C^{\text{XY}} h_2 \right] \right) M_x^2 + \left(T - T_C^{\text{XY}} \left[1 - \frac{1}{2} \beta_C^{\text{XY}} h_2 \right] \right) M_y^2 + \frac{1}{64} (\beta_C^{\text{XY}})^3 (zJ)^4 \mathbf{M}^4 + \mathcal{O} [h_2 \cdot M_\alpha^4] + \mathcal{O} [\mathbf{M}^6], \quad (2.68)$$

which is depicted in fig. 2.12 for $h_2 > 0$ and in fig. 2.13 for $h_2 < 0$.

$h_2 > 0$

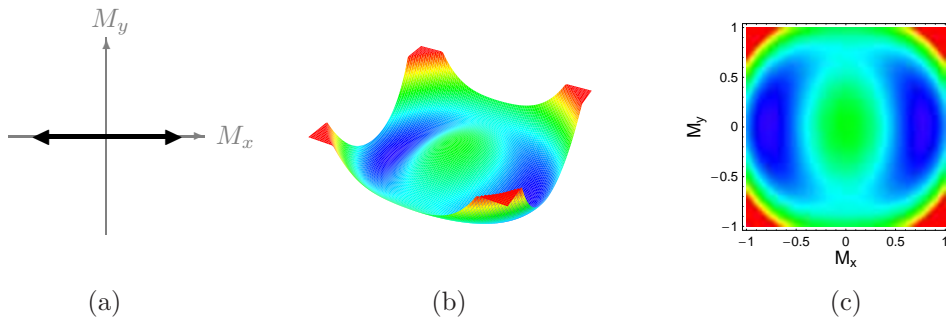


Figure 2.12: Plot of (2.68) for $h_2 = +0.1$ at $T = 0.7 T_C^{\text{XY}}$ ($zJ = 1$); subfigure (a) illustrates the preferred spin directions according to (2.57).

$h_2 < 0$

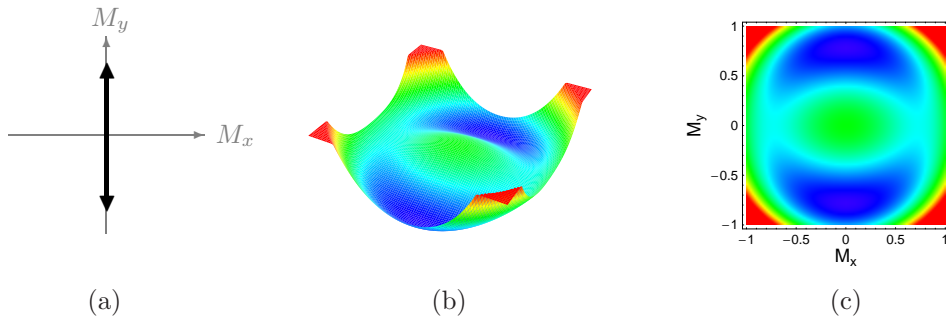


Figure 2.13: Plot of (2.68) for $h_2 = -0.1$ at $T = 0.7 T_C^{\text{XY}}$ ($zJ = 1$); subfigure (a) illustrates the preferred spin directions according to (2.58).

The appearance of solely even powers of M_α signifies the occurrence of a second order transition scenario. The symmetrically shifted critical temperatures read

$$T_C^x = T_C^{XY} \left[1 + \frac{1}{2} \beta_C^{XY} h_2 \right] \quad \text{for } h_2 > 0, \quad (2.69)$$

$$T_C^y = T_C^{XY} \left[1 - \frac{1}{2} \beta_C^{XY} h_2 \right] \quad \text{for } h_2 < 0. \quad (2.70)$$

As before, we can extract a crossover phenomenon from considering direction-dependent magnetic susceptibilities $\chi^\alpha = \partial M_\alpha / \partial \pi_\alpha$, with π_α denoting the components of the magnetic field $\boldsymbol{\pi} = (\pi_x, \pi_y)$ with $\alpha \in \{x, y\}$. We accordingly define the crossover temperature T_{CO} by

$$\frac{\chi^y(T_{CO})}{\chi^x(T_{CO})} \stackrel{!}{=} \frac{1}{2} \quad \text{for } h_2 > 0, \quad (2.71)$$

$$\frac{\chi^x(T_{CO})}{\chi^y(T_{CO})} \stackrel{!}{=} \frac{1}{2} \quad \text{for } h_2 < 0. \quad (2.72)$$

The anisotropy-dependent crossovers and second order transitions are depicted in the resulting phase diagram fig. 2.14 for $p = 2$. The data points have been numerically determined as in the foregoing subchapter. For small values of the anisotropy fields h_2 , the analytical expressions (2.69)-(2.70) are in excellent concordance with the numerical data points.

- ① $O(3)$ -symmetry, non-ordered
- ② Z_2 -symmetry (Ising-like), non-ordered
- ③ Z_2 -symmetry (Ising-like), ordered

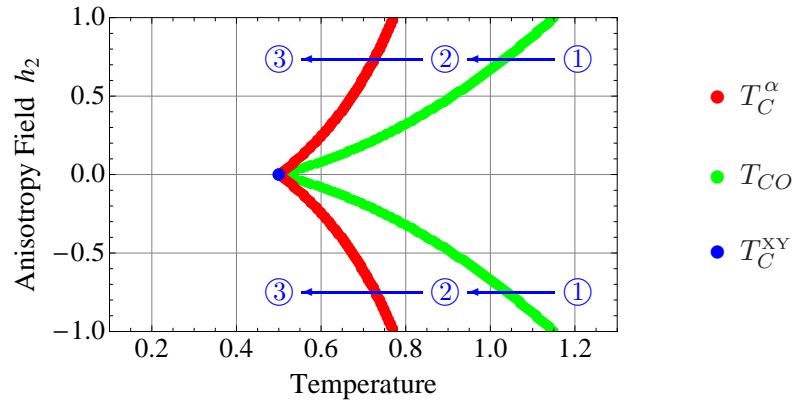


Figure 2.14: Phase diagram of the XY model (2.54) with the twofold anisotropy $p = 2$, including the critical temperatures T_C^α ($\alpha = x$ for $h_2 > 0$ and $\alpha = y$ for $h_2 < 0$) and the crossover temperatures T_{CO} defined by (2.71)-(2.72); we set $zJ = 1$.

For large quadratic anisotropy anisotropy fields $|h_2| \gg 1$, we find the Ising limit $T_C^{\text{Ising}} = zJ$, for positive ($h_2 > 0$) as well as negative ($h_2 < 0$) anisotropy fields. The numerically determined Ising limits are depicted in fig. 2.15.

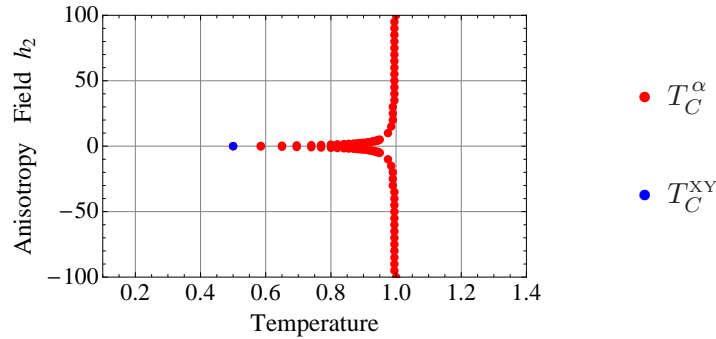


Figure 2.15: Phase diagram of the XY model (2.54) with $p=2$ demonstrating the Ising limits $T_C^\alpha \rightarrow T_C^{\text{Ising}}$ for $|h_2| \gg 1$, with the spin components $\alpha = x$ for $h_2 > 0$ and $\alpha = y$ for $h_2 < 0$; we set $zJ = 1$.

$p = 3$

In the according free energy expansion for $p = 3$, the threefold anisotropy field h_3 appears first in the cubic magnetization order:

$$f_{p=3} = [T - T^*] \mathbf{M}^2 - w(T) (M_x^3 - 3M_x M_y^2) + u(T) \mathbf{M}^4 + \mathcal{O}[h_3 M_\alpha^5] + \mathcal{O}[\mathbf{M}^6], \quad (2.73)$$

$$\text{with } T^* = \frac{zJ}{2}, \quad w(T) = \frac{1}{48} \beta^3 (zJ)^3 h_3 \quad (2.74)$$

$$\text{and } u(T) = \frac{1}{64} \beta^3 (zJ)^4. \quad (2.75)$$

The corresponding plots are shown in fig. 2.16 for $h_3 > 0$ and in fig. 2.17 for $h_3 < 0$.

Due to the presence of the cubic term in the expansion of the free energy in (2.73), the quadratic term does no longer include the critical temperature, but the supercooling temperature T^* , which represents the lower temperature limit of metastability for a first order transition scenario [61]. From (2.73)-(2.75), we can directly identify the supercooling temperature $T^* = zJ/2$, which turns out to be identical with the isotropic transition temperature $T^* = T_C^{\text{xy}}$.

$h_3 > 0$

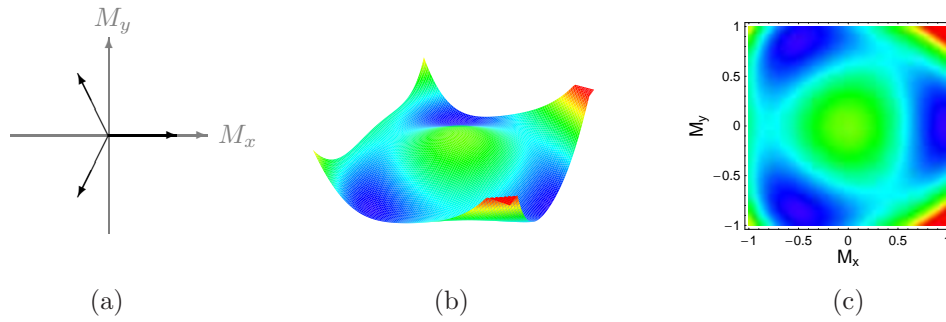


Figure 2.16: Plot of the free energy (2.73)-(2.75) for $h_3 = +0.2$ at $T = 0.6 T_C^{XY}$ ($zJ = 1$); subfigure (a) illustrates the preferred spin directions according to (2.57).

$h_3 < 0$

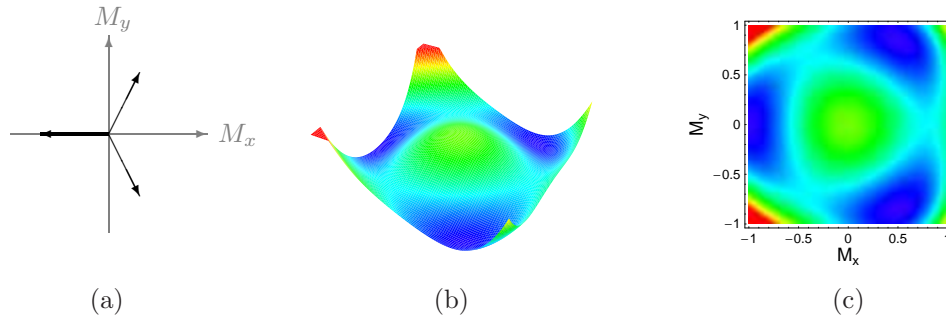


Figure 2.17: Plot of the free energy (2.73)-(2.75) for $h_3 = -0.2$ at $T = 0.6 T_C^{XY}$ ($zJ = 1$); subfigure (a) illustrates the preferred spin directions according to (2.58).

The transition temperature for $p = 3$ is consequently determined by

$$T_C = T^* + \frac{w^2(T^*)}{4u(T^*)} = T^* + \frac{1}{18} \frac{h_3^2}{zJ}. \quad (2.76)$$

The upper limit of metastability is given by the superheating temperature

$$T^{**} = T_C + \frac{w^2(T_C)}{32u(T_C)} = T_C + \frac{1}{144} \frac{h_3^2}{zJ} \approx T_C. \quad (2.77)$$

The resulting phase diagram for $p = 3$ is shown in fig. 2.18. The data points for the transition temperature T_C have been determined numerically and are for small h_3 in excellent coincidence with the analytical expression (2.76).

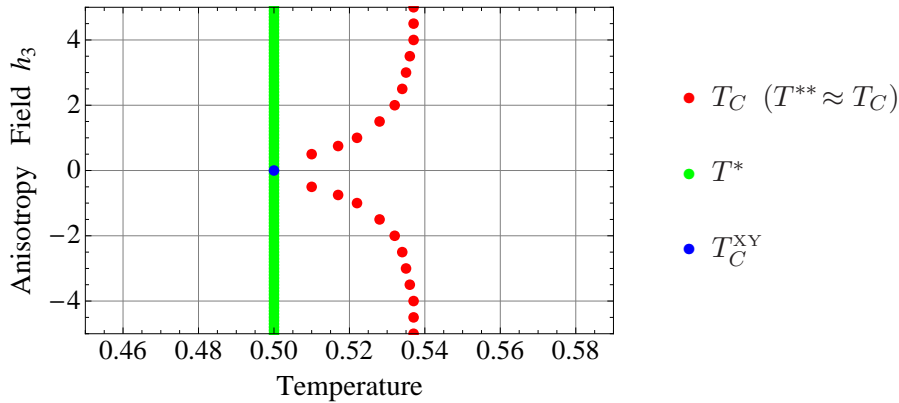


Figure 2.18: Phase diagram of the anisotropic XY model (2.54) with three-fold anisotropy ($p = 3$); T^* and T^{**} denote the supercooling and superheating temperatures, which signify the limits of metastability; we set $zJ = 1$.

We highlight the emergence of a first order transition for $h_3 \neq 0$ by considering two typical quantities: For the latent heat Q we obtain the quadratic dependence on the anisotropy field h_3

$$Q = T_C \left[\frac{w(T_C)}{2u(T_C)} \right]^2 = \frac{2}{9} \frac{h_3^2}{zJ}. \quad (2.78)$$

We further observe a discontinuity $\sim h_3$ in the magnetization:

$$M_{\text{dis}} = \frac{w(T_C)}{2u(T_C)} = \frac{2}{3} \frac{h_3}{zJ}. \quad (2.79)$$

Therefore, we clearly conclude a first order transition scenario for $h_3 \neq 0$, which reduces to a second order phase transition in the isotropic limit $h_3 \rightarrow 0$.

$p = 4$

For the fourfold anisotropies h_4 , we find their first emergence in the quartic order of the magnetization in the corresponding free energy expansion:

$$\begin{aligned} f_{p=4} = & [T - T_C^{\text{XY}}] \mathbf{M}^2 + \frac{1}{64} (\beta_C^{\text{XY}})^3 (zJ)^4 \mathbf{M}^4 \\ & - \frac{1}{384} (\beta_C^{\text{XY}})^4 (zJ)^4 h_4 \left(M_x^4 + M_y^4 - 6M_x^2 M_y^2 \right) + \mathcal{O}[h_4 M_\alpha^6]. \end{aligned} \quad (2.80)$$

The plots of (2.80) for $h_4 > 0$ in fig. 2.19 and for $h_4 < 0$ in fig. 2.20 consistently confirm the appearance of four privileged magnetization directions a posteriori.

$h_4 > 0$

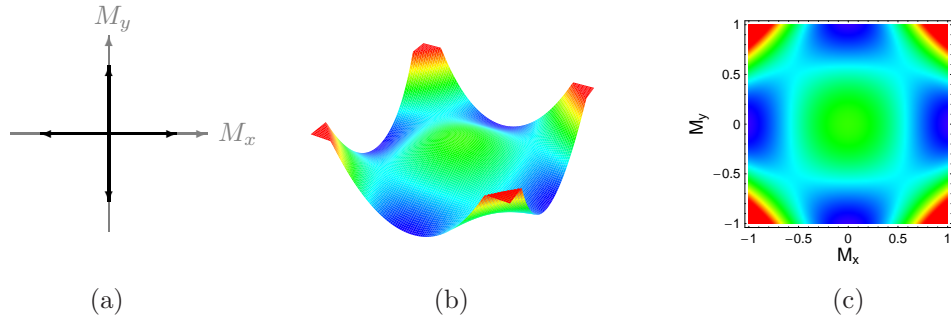


Figure 2.19: Plot of the free energy (2.80) for $h_4 = +1.0$ at $T = 0.6 T_C^{XY}$ ($zJ = 1$); subfigure (a) illustrates the preferred spin directions according to (2.57).

$h_4 < 0$

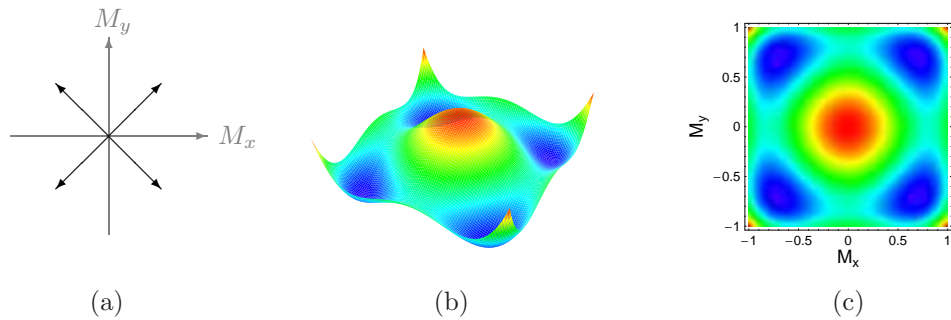


Figure 2.20: Plot of the free energy (2.80) for $h_4 = -0.6$ at $T = 0.6 T_C^{XY}$ ($zJ = 1$); subfigure (a) illustrates the preferred spin directions according to (2.58).

We presented these illustrating free energy landscapes in September 2007 on the RTN Nano Meeting in Portoroz, Slovenia [71]. An independent publication [72] in November 2007 in Physical Review Letters highlights the topical interest in such illustrations: Their magnetization histogram, found by a classical Monte Carlo simulation, shows a conclusive resemblance to our fig. 2.19.

From the occurrence of solely even powers in (2.80), we clearly conclude a second order phase transition with the non-shifted critical temperature

$$T_C(p=4) = T_C^{XY}. \quad (2.81)$$

$p = 5$

For the fivefold anisotropy field h_5 , we have to extend our previous expansion scheme: Since the first appearance of h_5 occurs in the fifth order of the magnetization, we have to expand at least up to the sixth magnetization order; the latter, however, includes a negative sign, so we consequently have to expand up to the positive eighth order to stabilize the free energy potential. The resulting free energy expression reads

$$\begin{aligned}
 f_{p=5} = & [T - T_C^{\text{XY}}] \mathbf{M}^2 + \frac{1}{64} (\beta_C^{\text{XY}})^3 (zJ)^4 \mathbf{M}^4 \\
 & - \frac{1}{3840} (\beta_C^{\text{XY}})^5 (zJ)^5 h_5 \left(M_x^5 - 10 M_x^3 M_y^2 + 5 M_x M_y^4 \right) \\
 & - \frac{1}{576} (\beta_C^{\text{XY}})^5 (zJ)^6 \mathbf{M}^6 + \mathcal{O}[h_5 M_\alpha^7] \\
 & + \frac{11}{49152} (\beta_C^{\text{XY}})^7 (zJ)^8 \mathbf{M}^8 + \mathcal{O}[h_5 M_\alpha^9] + \mathcal{O}[\mathbf{M}^{10}] . \quad (2.82)
 \end{aligned}$$

Due to the first appearance of h_5 in the fifth magnetization order of (2.82), we have to insert relatively large values for h_5 in order to visualize the preferred magnetization orientations in fig. 2.21-2.22.

$h_5 > 0$

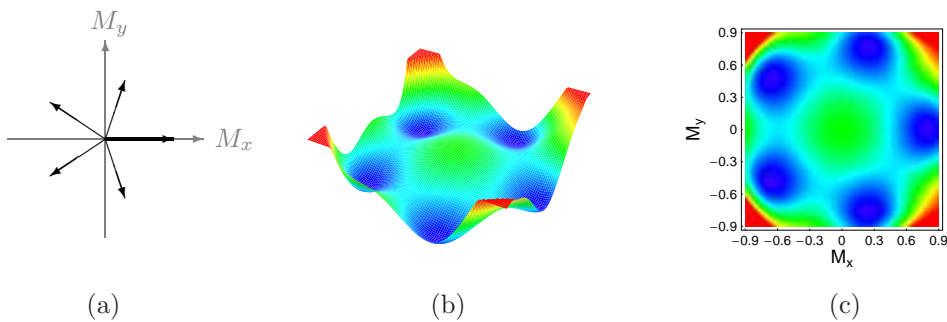


Figure 2.21: Plot of the free energy (2.82) for $h_5 = +10.0$ at $T = 0.8 T_C^{\text{XY}}$ ($zJ = 1$); subfigure (a) illustrates the preferred spin directions according to (2.57).

Due to the first emergence of h_5 in the fifth order term, we are dealing with a first order transition scenario. Nevertheless, the appearance of a fifth magnetization order merely represents a weak signal of a first order transition. Therefore, corresponding experimental and numerical measurements would correspondingly find vanishingly small latent heats and magnetization discontinuities. Thus, the

first order character of this particular transition is strongly disguised, and may be equally regarded as a continuous phase transition in practice. Nonetheless, these fifth order terms are vital for recovering the Z_5 -symmetry, as the plots in fig. 2.21-2.22 impressively point out.

$$\boxed{h_5 < 0}$$

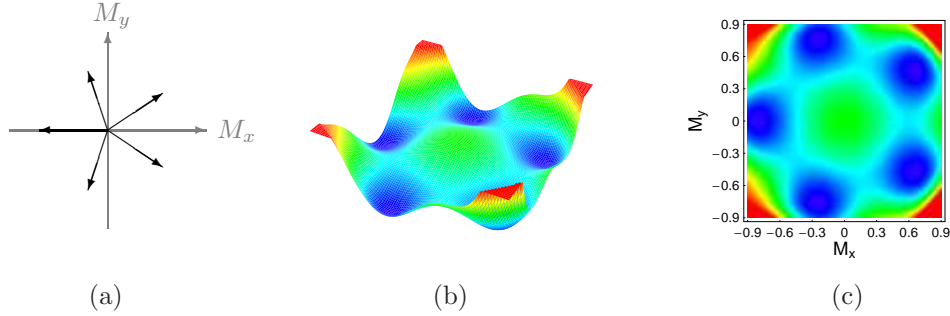


Figure 2.22: Plot of the free energy (2.82) for $h_5 = -10.0$ at $T = 0.8 T_C^{\text{XY}}$ ($zJ = 1$); subfigure (a) illustrates the preferred spin directions according to (2.58).

Thereby, the transition temperature turns out to be identical with its isotropic value $T_C(p = 5) = T_C^{\text{XY}}$.

$$\boxed{p = 6}$$

The sixfold anisotropy field h_6 first appears in the sixth order of the magnetization. Due to the negative sign of the unperturbed sixth order term, we consequently have to expand the free energy up to the positive eighth order:

$$\begin{aligned} f_{p=6} = & [T - T_C^{\text{XY}}] \mathbf{M}^2 + \frac{1}{64} (\beta_C^{\text{XY}})^3 (zJ)^4 \mathbf{M}^4 - \frac{1}{576} (\beta_C^{\text{XY}})^5 (zJ)^6 \mathbf{M}^6 \\ & - \frac{1}{46080} (\beta_C^{\text{XY}})^6 (zJ)^6 h_6 \left(M_x^6 - 15 M_x^4 M_y^2 + 15 M_x^2 M_y^4 - M_y^6 \right) \\ & + \frac{11}{49152} (\beta_C^{\text{XY}})^7 (zJ)^8 \mathbf{M}^8 + \mathcal{O}[h_6 M_\alpha^8] + \mathcal{O}[\mathbf{M}^{10}] . \end{aligned} \quad (2.83)$$

The plots of (2.83) in fig. 2.23-2.24 consistently confirm the six distinct preferred magnetization orientations, for positive as well as negative fields h_6 . As before, we have to insert relatively large values for h_6 in order to visualize the involved effects.

$h_6 > 0$

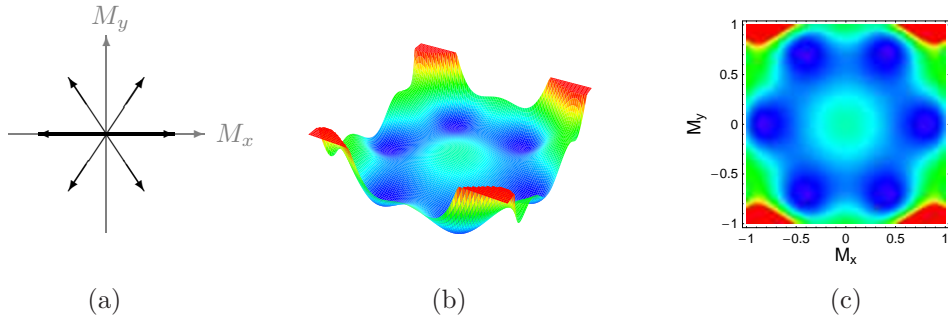


Figure 2.23: Plot of the free energy (2.83) for $h_6 = +70.0$ at $T = 0.8 T_C^{\text{XY}}$ ($zJ = 1$); subfigure (a) illustrates the preferred spin directions according to (2.57).

$h_6 < 0$

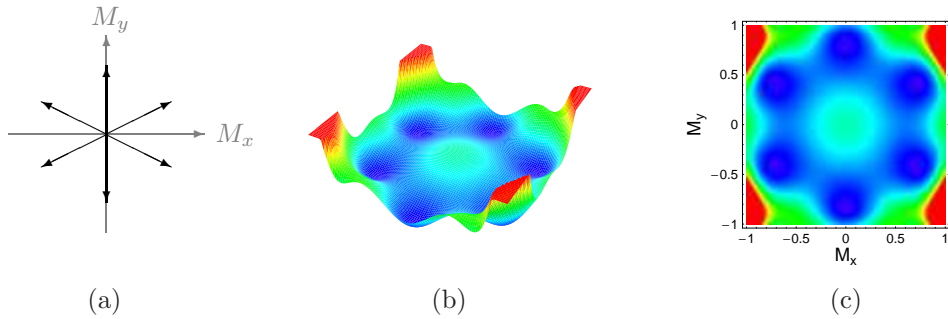


Figure 2.24: Plot of the free energy (2.83) for $h_6 = -70.0$ at $T = 0.8 T_C^{\text{XY}}$ ($zJ = 1$); subfigure (a) illustrates the preferred spin directions according to (2.58).

The occurrence of solely even powers in (2.83) leads to a second order phase transition with the non-shifted critical temperature $T_C(p=6) = T_C^{\text{XY}}$.

2.4.3 Phase Diagram

The resulting MF phase diagram is shown in fig. 2.25. For large anisotropy fields $|h_p| \gg 1$, we consistently find complete concordance with the Mean Field treatment of the Z_p -clock model [61, 73, 74]:

$$H_{\text{clock}} = -J_{\text{clock}} \sum_{\langle ij \rangle} \cos [\varphi_i - \varphi_j]$$

with $\varphi_i = \frac{2\pi n_i}{p}$ and $n_i \in \{1, \dots, p\}$,

(2.84)

$\forall i = 1, \dots, N$. Thereby, the Z_p -clock model [61] may not be mistaken for the p -state Potts model [75], which merely scans the full spin alignment:

$$H_{\text{Potts}} = -J_{\text{Potts}} \sum_{\langle ij \rangle} [p \delta_{\sigma_i, \sigma_j} - 1] \quad \text{with } \sigma_i \in \{1, \dots, p\} \quad \forall i. \quad (2.85)$$

As a consequence, the limits of the critical temperatures $T_C (h_p \rightarrow \pm\infty)$ are consistent with the MF critical temperatures of the Z_p -clock model (2.84), but deviate from those of the Potts model (2.85).

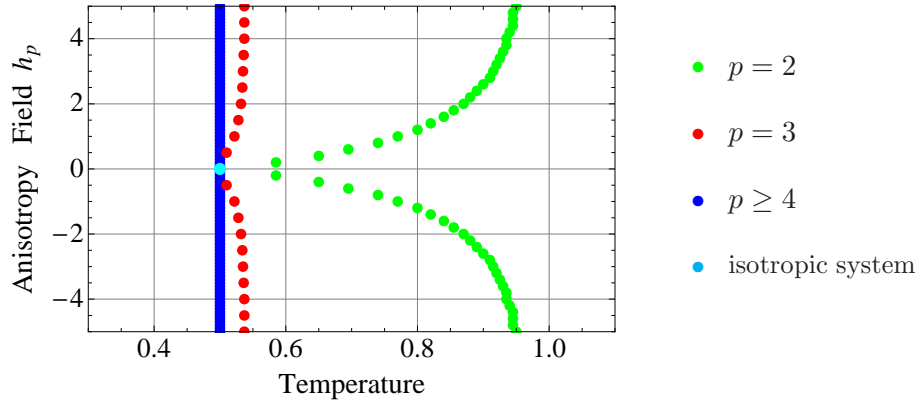


Figure 2.25: Phase diagram: Transition temperatures $T_C (h_p)$ of the XY model (2.54) with Z_p -anisotropies for $p \geq 2$ ($zJ = 1$).

From the comparison to the phase diagram gained by the renormalization group treatment (fig. 13 in [67]), we clearly conclude that the Mean Field treatment strongly underestimates the overall relevance of the anisotropy fields.

Therefore, the need arises to apply more sophisticated techniques in order to elucidate the role of the anisotropy fields to the full extent. In the coming chapters, which deal again with anisotropic Heisenberg systems, we will therefore extend our applied methods and will eventually remove this typical shortcoming of the Mean Field framework.

2.5 Excursion II: Semiclassical Models and Quantum-Classical Mapping

In this section we extend our model overview of section 1.2.1 summarized in fig. 1.1: There exist as well semiclassical versions of the Heisenberg and XY model that are located between the classical and quantum models.

The $O(n)$ quantum rotors [76]

$$H = \pm \sum_{\langle ij \rangle} J_{ij} \mathbf{S}_i \cdot \mathbf{S}_j + \begin{cases} \frac{g}{2} \sum_{i=1}^N (L_i^z)^2 & \text{for } n = 2, \\ \frac{g}{2} \sum_{i=1}^N \mathbf{L}_i^2 & \text{for } n = 3, \end{cases} \quad (2.86)$$

$$\text{with } [S_i^\alpha, L_i^\beta] = -i \varepsilon_{\alpha\beta\gamma} S_i^\gamma \quad \text{and} \quad [S_i^\alpha, S_i^\beta] = 0 \quad \forall \alpha, \beta, \quad (2.87)$$

consist of $O(n)$ spin vectors \mathbf{S}_i that are influenced by non-commuting terms $\sim g$; the latter are formulated in terms of the $O(n)$ generators

$$[L_i^\alpha, L_i^\beta] = i \varepsilon_{\alpha\beta\gamma} L_i^\gamma. \quad (2.88)$$

The non-vanishing commutation relations in (2.87) give subsequently rise to quantum fluctuations for $g \neq 0$. The strength of these quantum fluctuations is accordingly tuned by the so-called quantum parameter g . Nonetheless, the Hamiltonians (2.86) neglect the commutation relations between the distinct spin components ($[S_i^\alpha, S_i^\beta] = 0 \quad \forall \alpha, \beta$), which explains the naming ‘‘semiclassical’’. The extended model overview is summarized in fig. 2.26.

Thereby, the quantum rotors represent a vital ingredient to the theory of quantum phase transitions that are solely driven by quantum fluctuations: In the 1970s, Hertz [77] set up the corresponding theory that d -dimensional semiclassical systems at $T = 0$ with a quantum parameter $g > 0$ are closely related to $(d+1)$ -dimensional classical ($g = 0$) systems at a finite temperature $T > 0$.

This idea offers an illustrative understanding of the quantum phase transitions that are merely driven by quantum instead of pure thermal fluctuations: As it is well-known for classical phase transitions that thermal fluctuations are capable to suppress and destroy the long range order for high temperatures $T \gtrsim J$, so can quantum fluctuations suppress and destroy the long range order for large quantum parameters $g \gtrsim J$, even at $T = 0$. As we distinguish for classical phase transitions the regions of the ordered ($T < T_C$) and non-ordered ($T > T_C$) phases separated by the critical temperature T_C , we can classify the same regions for quantum phase transitions at $T = 0$: For small quantum parameters $g < g_C$, the system is in its quantum ordered phase, whereas strong quantum fluctuations with $g > g_C$ lead to the quantum disordered phase. Thereby, g_C denotes the critical quantum parameter signifying the quantum phase transition. These plausible and catchy analogies are summarized in table 2.3.

Thereby, the theory of quantum phase transitions has been accompanied by experimental successes in the recent past that represent milestones of low-temperature physics [78, 79, 80].

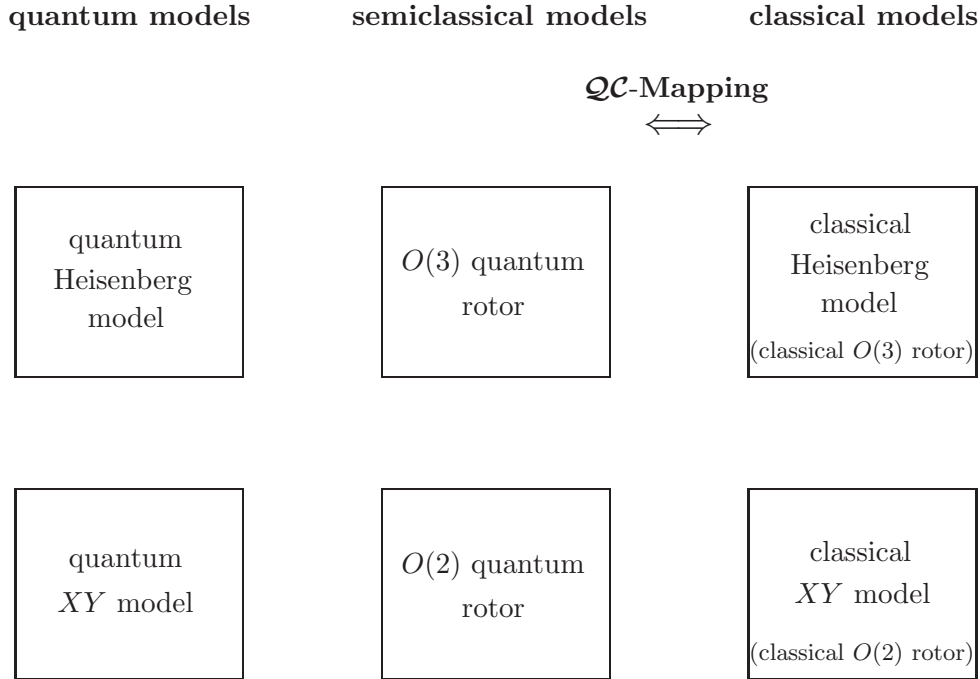


Figure 2.26: Extended model overview including the semiclassical $O(n)$ quantum rotors (2.86) with n referring to the number of spin dimensions: The upper line refers to $n = 3$, and the lower one to $n = 2$.

	$(d+1)$ - dimensional classical systems <small>($g = 0, T > 0$)</small>	d - dimensional semiclassical systems <small>(at $T = 0, g > 0$)</small>
ordered phase <small>(order parameter > 0)</small>	$T < T_C$	$g < g_C$
non-ordered phase <small>(order parameter = 0)</small>	$T > T_C$	$g > g_C$

Table 2.3: Analogies between d -dimensional semiclassical systems and their $(d+1)$ -dimensional classical counterparts provided by the QC-Mapping.

The corresponding mathematical mapping is performed with the use of the quantum mechanical path integral [76, 81, 82, 83, 84, 85] and turns out to be closely related to the path integral formulation of the quantum harmonic oscillator [86]. This method is called Quantum-Classical Mapping (*QC*-Mapping) and represents a widely used approach for quantum systems at the absolute zero of temperature.

In our case, the d -dimensional semiclassical $O(n)$ quantum rotors at $T=0$ can be directly mapped onto the $(d+1)$ -dimensional classical $O(n)$ rotors [76, 81, 82, 83, 84, 85], which are better known as the classical XY ($n = 2$) and the classical Heisenberg ($n = 3$) model, as indicated in fig. 2.26. Thereby, the value for the critical quantum parameter g_C can be directly adopted from the critical temperature T_C of the $(d+1)$ -dimensional classical system.

In the end, the *QC*-mapping enables us to predict the impact of the anisotropy fields h_p on quantum phase transitions at $T = 0$: The critical quantum parameter $g_C(h_p)$ will consequently exhibit a vital dependence on h_p , which leads to shifts in the critical quantum parameter $g_C(h_p > 0) > g_C(h_p = 0)$ and eventually to the preference of certain spin components. At the crossover $g_{CO} > g_C$, we consequently observe the adopted distortion of the free energy and the incipient change of the symmetry in spin space.

Despite the advantages of the *QC*-Mapping according to Hertz [77], which was successfully set up in the 1970s and is found nowadays in most modern textbooks [76, 85], there have been experimental breakthroughs in the recent past [87, 88], which demand either an appropriate extension of Hertz' theory or require the direct inclusion of genuine quantum effects and properties.

In the following chapters we will investigate pure quantum models and will extract genuine quantum effects that are influenced by thermal as well as by quantum fluctuations. Thereby, the presence of anisotropy fields will profoundly affect this genuine quantum effects.

At this point, we close our excursion subchapters and return to our primary topic of interest, namely investigating the impact of anisotropy fields on the properties of the Heisenberg model.

2.6 Retrospect and Outlook

In the course of this chapter we elucidated the impact of anisotropy fields on the critical temperatures of classical spin models: With the use of a multiple-spin-component Mean Field approach, we could illustrate the increased shifts of the critical temperatures for the privileged spin components. Thereby, we confirmed a posteriori the EA case for $h_p > 0$ and the EP scenario for $h_p < 0$ in the Heisenberg model (2.24).

The graphical plots of the analytically derived free energy landscape impressively underlined the preference of certain spin components. These graphical illustrations further suggested the emergence of a crossover that manifests the change of the underlying spin symmetry: By a careful analysis of the direction-dependent magnetic susceptibilities, we could set up an appropriate crossover criterion and find the corresponding crossovers well above the critical temperatures.

We pursued these analytical considerations for the anisotropic Heisenberg model as well as for an XY model with Z_p -anisotropy.

Despite several evident advantages presented in this chapter, the Mean Field ansatz has to face certain shortcomings: Due to its strongly simplified approach, the Mean Field outcome for the critical temperatures does particularly not comply with the Mermin-Wagner theorem [8]. This severe shortcoming will be removed in the subsequent chapters with the use of more sophisticated techniques.

In the coming chapter we will extend our Mean Field considerations to the inclusion of quantum effects: The incorporation of the spin quantum number as a further non-trivial parameter will reveal an intriguing effect.

Chapter 3

Quantum Mean Field

In order to include quantum effects on a qualitative level, we treat the Heisenberg system further on by a MF approach, but now take into account the quantization of the spin. Although the derivation of the basic quantum Mean Field (QMF) equations is similar to the classical case, the outcome will be quite a different one. Since the quantum formulation is given in terms of the S^z -eigenstates, we will restrict the quantum treatment from here on to the easy-axis case and to the z -components of the spins and the magnetization $M = M_z$. Therefore, we omit some of the sub- and superscripts ‘ z ’ and ‘EA’ in the following. Due to its simplicity, the QMF approach is not capable of distinguishing FMs and AFMs. Nevertheless, the comparison with its classical counterpart will reveal a surprising effect.

3.1 Isotropic Systems

The derivation of the basic MF equations for the quantum case follows the same procedure as in the classical case [61]. As before, the MF free energy represents an upper bound to its non-approximative version. We will concentrate on the FM case, but the following treatment can be easily altered to the AFM case with a staggered magnetization on a sublattice structure, which yields in the end identical results for the critical temperature.

In order to focus on the easy-axis case, we choose a trial density matrix ρ_i that merely contains the z -components of the spins:

$$\rho_i = \frac{1}{Z_i} \exp [+ \beta z J M m_i] \quad \text{for } i = 1, \dots, N, \quad (3.1)$$

with $m_i \in \{-S, -S + 1, \dots, +S\}$ denoting the magnetic quantum number of the i th spin, $M = M_i = \langle S_i^z \rangle \forall i$ representing the magnetization and N denoting the total number of spins on the lattice. This density matrix fulfills the conditions

$$\text{Tr}_i[\rho_i] = \sum_{m_i=-S}^{+S} \rho_i = 1 \quad \forall i \quad \Rightarrow \quad \text{Tr}[\rho] = \left(\prod_{i=1}^N \text{Tr}_i \right) \left[\prod_{i=1}^N \rho_i \right] = 1, \quad (3.2)$$

and corresponds to the Hamiltonian substitution

$$H = - \sum_{\langle ij \rangle} J_{ij} \mathbf{S}_i \cdot \mathbf{S}_j \quad \xrightarrow{\text{MF}} \quad H_{\text{MF}} = -zJM \sum_{i=1}^N S_i^z. \quad (3.3)$$

Instead of an integration over continuous angles as in the classical case, the trace in the quantum case is given by the sum over the discrete S^z -eigenstates. The partition function correspondingly reads

$$Z = Z_i = \sum_{m_i=-S}^{+S} \exp[+\beta zJM m_i] \quad \forall i = 1, \dots, N. \quad (3.4)$$

In order to determine the critical temperature T_C^{iso} of the isotropic system, we calculate the magnetization self-consistently via the expectation value $\langle S_i^z \rangle = \langle S^z \rangle = M \quad \forall i$:

$$M = \frac{1}{Z} \sum_{m=-S}^{+S} m \exp[+\beta zJM m]. \quad (3.5)$$

The expansion in the limits $T \lesssim T_C^{\text{iso}}$ and $M \gtrsim 0$ yields

$$\lim_{M \rightarrow 0} M = \frac{zJ}{3} S(S+1) \beta_C^{\text{iso}} \lim_{M \rightarrow 0} M \quad \text{with} \quad \beta_C^{\text{iso}} = \frac{1}{T_C^{\text{iso}}}, \quad (3.6)$$

and we may cancel $\lim_{M \rightarrow 0} M$ on both sides of the equation. The resulting critical temperature for the isotropic system is consequently given by

$$T_C^{\text{iso}} = \frac{zJ}{3} S(S+1). \quad (3.7)$$

The appearance of the squared quantum spin length $S(S+1)$ is a clear indication for the continued inclusion of quantum effects. In the classical limit $S(S+1) \rightarrow S^2$ we recover our CMF result (2.17).

This outcome for the critical temperature can be persuasively checked by the expansion of the free energy. Since the free energy turns out to be particularly S -dependent in the quantum case, we start in this section with the easiest case represented by the isotropic system, whose free energy can be formulated for general S , and we will pursue the calculation for the more sophisticated anisotropic system for explicit spin quantum numbers S in the following paragraph. The free energy per spin for the isotropic Heisenberg model reads for general S up to non-relevant constants

$$f = \frac{1}{2} zJM^2 - T \ln Z \quad (3.8)$$

$$\begin{aligned} &= \frac{3}{2} \frac{1}{S(S+1)} (T - T_C^{\text{iso}}) M^2 + \\ &+ \frac{(zJ)^4}{360} (\beta_C^{\text{iso}})^3 S(1 + 3S + 4S^2 + 2S^3) M^4 + \mathcal{O}[M^6], \quad (3.9) \end{aligned}$$

with T_C^{iso} consistently given by (3.7). In the classical limit of large spin quantum numbers $S \gg 1$, both the quadratic and the quartic term in (3.9) reduce to the corresponding terms of the classical free energy (2.16).

Please note that this MF approach is immune to unphysical anisotropy fields, e.g. $(S^z)^2$ for $S = \frac{1}{2}$: In such cases, the free energy simply contains trivial additive terms, which shift the zero point of the free energy, which is not specified anyway. As a consequence, the physically relevant free energy terms and the according critical temperature remain unchanged.

3.2 Modifications for Anisotropy Fields

In this section we extend our QMF concept to the inclusion of irreducible anisotropy fields

$$H = - \sum_{\langle ij \rangle} J_{ij} \mathbf{S}_i \cdot \mathbf{S}_j - h_p \sum_{i=1}^N (S_i^z)^p \quad \text{with even } p \leq 2S. \quad (3.10)$$

The trial density matrix ansatz

$$\rho_i = \frac{1}{Z_i} \exp [+ \beta z J M m_i + \beta h_p m_i^p] \quad \text{for } i = 1, \dots, N \quad (3.11)$$

fulfills (3.2) and leads to the partition function

$$Z = Z_i = \sum_{m_i=-S}^{+S} \exp [+ \beta z J M m_i + \beta h_p m_i^p] \quad \forall i = 1, \dots, N. \quad (3.12)$$

By applying the same expansion as in the classical case, we get the resulting free energy

$$\begin{aligned} f(S, h_p) &= \frac{3}{2} \frac{1}{S(S+1)} \left[T - T_C^{\text{iso}} (1 + a_p(S) \beta_C^{\text{iso}} h_p) \right] M^2 + \\ &+ b(S) M^4 + \mathcal{O}[h_p \cdot M^4], \end{aligned} \quad (3.13)$$

with $b(S) > 0$ denoting the S -dependent prefactors of the quartic term, which have been analytically determined for each S and p , but are omitted here for the sake of straightforwardness. From (3.13), we can identify the shifted critical temperature of the anisotropic system

$$T_C(h_p, S) = T_C^{\text{iso}} \left[1 + a_p(S) \beta_C^{\text{iso}} h_p \right], \quad (3.14)$$

with T_C^{iso} denoting the critical temperature of the isotropic system (3.7). The decisive prefactors $a_p(S)$ are determined analytically for each spin quantum number S and each degree p of the anisotropy field h_p . The results are summarized in table 3.1 and fig. 3.1.

Thereby, we need to rescale the fields for $p = 4$ and $p = 6$: In order to compare the effects of higher-order anisotropies, we have to bear in mind that the anisotropy term $-h_p \sum_i (S_i^z)^p$ scales $\sim S^p$. Therefore, we have to rescale the quantum prefactors of the higher-order fields with $p > 2$ by S^{p-2} :

$$\tilde{a}_p(S) = \frac{a_p}{S^{p-2}}. \quad (3.15)$$

Please note that this rescaling scheme appropriately leaves over the scaling of squared spin operators as in the coupling term and that correspondingly $\tilde{a}_2 = a_2$.

S	$\tilde{a}_2 = a_2$	\tilde{a}_4	\tilde{a}_6
$\frac{1}{2}$	reducible	reducible	reducible
1	$\frac{1}{3}$	reducible	reducible
$\frac{3}{2}$	$\frac{4}{5}$	reducible	reducible
2	$\frac{7}{5} = 1.4$	$\frac{31}{20} = 1.55$	reducible
$\frac{5}{2}$	$\frac{32}{15} \approx 2.13$	$\frac{1216}{525} \approx 2.32$	reducible
3	3	$\frac{67}{21} \approx 3.19$	$\frac{607}{189} \approx 3.21$
$\frac{7}{2}$	4	$\frac{1432}{343} \approx 4.17$	$\frac{9964}{2401} \approx 4.15$
4	$\frac{77}{15} \approx 5.13$	$\frac{253}{48} \approx 5.27$	$\frac{19877}{3840} \approx 5.18$
$\frac{9}{2}$	$\frac{32}{5} = 6.4$	$\frac{2624}{405} \approx 6.48$	$\frac{206432}{32805} \approx 6.29$
5	$\frac{39}{5} = 7.8$	$\frac{39}{5} = 7.8$	$\frac{23439}{3125} \approx 7.50$
$\frac{11}{2}$	$\frac{28}{3} \approx 9.33$	$\frac{3352}{363} \approx 9.23$	$\frac{386548}{43923} \approx 8.80$
6	11	$\frac{2717}{252} = 10.78$	$\frac{13211}{1296} \approx 10.19$
$\frac{13}{2}$	$\frac{64}{5} = 12.8$	$\frac{14720}{1183} \approx 12.44$	$\frac{11675968}{999635} \approx 11.68$
7	$\frac{221}{15} \approx 14.73$	$\frac{73151}{5145} \approx 14.22$	$\frac{477581}{36015} \approx 13.26$
$\frac{15}{2}$	$\frac{84}{5} = 16.8$	$\frac{1208}{75} \approx 16.11$	$\frac{1260148}{84375} \approx 14.94$
8	19	$\frac{1159}{64} \approx 18.11$	$\frac{68419}{4096} \approx 16.70$
10	$\frac{437}{15} \approx 29.13$	$\frac{57247}{2100} \approx 27.26$	$\frac{25960859}{1050000} \approx 24.72$

Table 3.1: Rescaled prefactors $\tilde{a}_p = a_p/S^{p-2}$ ($\tilde{a}_2 = a_2$) of the anisotropy fields h_p according to (3.14)-(3.15); the comment ‘reducible’ refers to fields h_p with $p > 2S$, which can be reduced by (1.10) and consequently contain no new physical constellation.

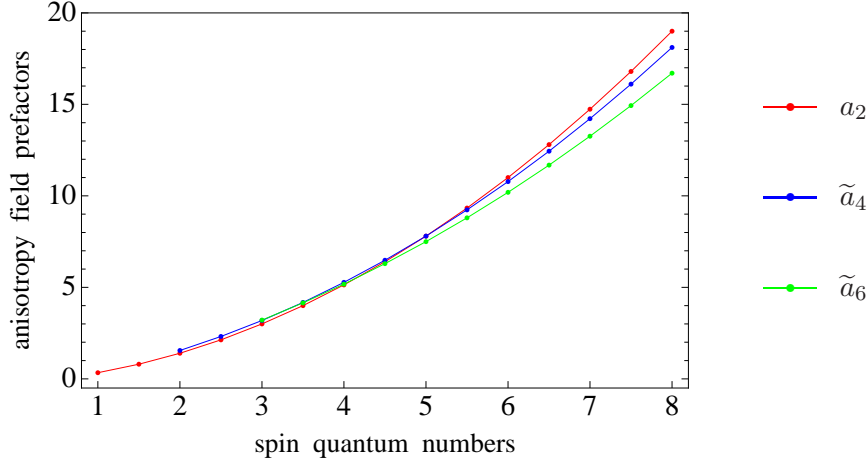


Figure 3.1: Graphical illustration of the rescaled prefactors $\tilde{a}_p = a_p/S^{p-2}$ ($\tilde{a}_2 = a_2$) of the irreducible anisotropy fields h_p according to (3.14)-(3.15).

We further checked the results in table 3.1 by calculating the expectation value $\langle S_i^z \rangle = \langle S^z \rangle = M \quad \forall i$ in the limits $T \xrightarrow{\leq} T_C$ and $M \xrightarrow{\geq} 0$, as explained in the foregoing paragraph, and found complete concordance.

3.3 Relevance of Higher-Order Fields

In contrast to their classical counterparts, the prefactors $a_p(S)$, which are decisive for the shift of the critical temperature, include now an S -dependence. After the rescaling $a_p \rightarrow \tilde{a}_p$ (3.15), we find the following surprising behaviour for irreducible fields h_p : For small spin quantum numbers $S \leq 3$, the anisotropy fields h_p of higher order p are clearly more relevant,

$$\tilde{a}_2(S) < \tilde{a}_4(S) < \tilde{a}_6(S) \quad \text{for } S \leq 3, \quad (3.16)$$

in contrast to the classical prediction (2.37). In the region $\frac{7}{2} \leq S \leq 5$ a reordering of relevance takes place, until for large spins $S \geq \frac{11}{2}$ the lower-order anisotropy fields have regained a stronger relevance:

$$\tilde{a}_2(S) > \tilde{a}_4(S) > \tilde{a}_6(S) \quad \text{for } S \geq \frac{11}{2}. \quad (3.17)$$

This latter finding is again consistent with the classical result we expect for $S \rightarrow \infty$.

The key for understanding this at first glance puzzling behaviour is given by the anisotropy gaps that are provided by the anisotropy term $-h_p \sum_i (S_i^z)^p$: In the classical case, we were dealing with a continuous angle and, therefore, with an effective anisotropy field $h_p^{\text{eff}} = \int_0^\pi d\vartheta \sin \vartheta \cos^p(\vartheta)$, which is clearly stronger for lower p and, therefore, capable of explaining the classical hierarchy

in (2.37).

In the quantum case, on the contrary, the quantization of the spin gives rise to gaps in the anisotropy term: The larger the order p of the anisotropy, the larger is the resulting anisotropy gap in $\sum_i (S_i^z)^p$. Due to these increased energy gaps for larger p , the system consequently suppresses thermal and quantum fluctuations to a larger extent and leads thereby to a larger $T_C(h_p)$. This underlying mechanism explains the switched around hierarchy of relevance (3.16) for higher-order anisotropy fields in the quantum case at small spin quantum numbers S . For larger S , the spin quantization becomes again less important, and we consistently recover the classical relevance (3.17) and (2.37).

As a consequence, the value of the spin quantum number S is crucial for the relevance of higher-order anisotropy fields.

3.4 Retrospect and Outlook

The quantum version of the Mean Field approach enabled us to describe the impact of the anisotropy fields h_p on the critical temperatures $T_C(h_p, S)$ of the quantum Heisenberg model.

Thereby, we revealed the S -dependence of the relevance for the anisotropy fields h_p with $p \in \{2, 4, 6\}$: Whereas we can consistently refer back to our classical results of the foregoing chapter 2 for large spin quantum numbers $S \gg 1$, we find the hierarchy switched around by tuning the spin quantum number S towards smaller values $S \leq 3$. This decisive S -dependence is summarized in table 3.1 and fig. 3.1 and could be explained by the S -dependent anisotropy gaps that are provided by the anisotropy term $-h_p \sum_i (S_i^z)^p$.

In the following chapters, we will further refine our findings how the presence of anisotropy fields affects the critical temperatures, and we will study the shifts of $T_C(h_p)$ in detail. Our numerical Quantum Monte Carlo simulations, performed in chapter 6, will clearly confirm the predicted larger relevance of the higher-order fields h_p with $p > 2$ for $S = 2$.

Whereas the MF approaches have been too simple to incorporate the genuine differences between the FM and AFM, the following more sophisticated treatments will enable us to extract and distinguish their typical properties, which go beyond the classical $J \rightarrow -J$ - symmetry.

Chapter 4

Linear Spin Wave Approximation

4.1 Overview: Two Methods - One Message

The spin wave analysis, originating from Felix Bloch's primal considerations in the 1930s [89], is a well-known and appreciated semiclassical approximation technique. Based on assumptions that are valid for large spin quantum numbers $S \gg 1$, it still includes quantum phenomena and yields astonishingly good results even for $S = 1/2$ [59, 90, 91]. We will make use of its linear version, which turns out to be identical with the regime of non-interacting magnons.

There are two slightly differing approaches for the Linear Spin Wave Approximation (LSWA): Kubo [59] applied the Holstein-Primakoff transformation [92] and transformed the spin system into a bosonic one. We will refer to this approach as Method I or as Kubo-Manousakis method, due to Manousakis' wonderful and comprehensive review article for isotropic and coupling-anisotropic systems [91]. On the contrary, Anderson [90] used an approximative semiclassical expansion for the spin fluctuations that maps the spin system onto decoupled harmonic oscillators and circumvents the Holstein-Primakoff transformation. Anderson's method will be referred to as method II. We will outline the basic and the modified treatment for anisotropy fields by making use of both methods in parallel. Thereby, we will point out their similarities and differences. Both methods will turn out to show a slightly different S -dependence in special cases, but their differences vanish for large S , which is, therefore, again consistent with the basic LSWA assumptions. As a consequence, this parallel treatment will be a powerful validation tool on the LSWA level. The reader, who yet might to choose to focus on method I, may leave out the subsections that contain 'Method II' in the headlines, or vice versa, without missing the main points.

We will focus on antiferromagnets (AFMs), but will, from time to time, compare to the less complicated ferromagnetic (FM) case. By comparing to the FM, we will be able to extract the quantum fluctuations, which are still present and typical for the AFM ground states. Although we will not determine critical temperatures in this chapter, since LSWA assumes an ordered state right from

the beginning, our investigation on the ground state sublattice magnetization will reveal the amount of the remnant quantum fluctuations in the system.

Although the idea of quadratic anisotropy fields was touched upon in the original articles [59, 90], only infinitesimal fields have been included in order to mark a preferred direction and to stabilize the system. Our study of finite anisotropies, on the other hand, combined with the investigation on the suppression of quantum fluctuations, will yield quite a different interpretation and reveal the sensitivity to anisotropy fields for a widespread range of parameters.

4.2 Isotropic Systems

We start by outlining the basic treatment for the isotropic AFM Hamiltonian

$$H = +J \sum_{\langle ij \rangle} \mathbf{S}_i \cdot \mathbf{S}_j . \quad (4.1)$$

The presence of anisotropy fields leads to additional terms, whose impact will be discussed in the next section.

In the AFM the nearest neighbours stem from different sublattices, i.e.

$$\left\{ \begin{array}{l} i \in A \\ j \in B \end{array} \right\} , \quad (4.2)$$

with A and B denoting the sublattices of the bipartite lattice structure.

4.2.1 Method I: Bosonic Operators

After rewriting the isotropic Hamiltonian,

$$H = +J \sum_{\langle ij \rangle} \left[S_i^z S_j^z + \frac{1}{2} (S_i^+ S_j^- + S_i^- S_j^+) \right] , \quad (4.3)$$

we apply the Holstein-Primakoff transformation [59, 91, 92]:

for $i \in A$:

$$S_i^+ = \sqrt{2S} f_S(n_i^A) a_i , \quad S_i^- = \sqrt{2S} a_i^\dagger f_S(n_i^A) , \quad S_i^z = S - n_i^A , \quad (4.4)$$

$$\text{with } f_S(n_i^A) = \sqrt{1 - \frac{n_i^A}{2S}} , \quad n_i^A = a_i^\dagger a_i . \quad (4.5)$$

for $j \in B$:

$$S_j^+ = \sqrt{2S} b_j^\dagger f_S(n_j^B) , \quad S_j^- = \sqrt{2S} f_S(n_j^B) b_j , \quad S_j^z = -S + n_j^B , \quad (4.6)$$

$$\text{with } f_S(n_j^B) = \sqrt{1 - \frac{n_j^B}{2S}} , \quad n_j^B = b_j^\dagger b_j . \quad (4.7)$$

As a result, we get, due to the sublattice structure, two distinct sorts of creation and annihilation operators $\{a_i^\dagger, a_i\}_{i \in A}$, $\{b_j^\dagger, b_j\}_{j \in B}$, both obeying the bosonic commutation relations, with all of the mixed commutators vanishing.

The recasted Hamiltonian reads

$$\begin{aligned}
 H = & -dJS^2N + 2dJS \left[\sum_{i \in A} n_i^A + \sum_{j \in B} n_j^B \right] - J \sum_{\langle ij \rangle} n_i^A n_j^B \\
 & + JS \sum_{\langle ij \rangle} \left[f_S(n_i^A) a_i f_S(n_j^B) b_j + a_i^\dagger f_S(n_i^A) b_j^\dagger f_S(n_j^B) \right], \quad (4.8)
 \end{aligned}$$

with the dimension d , and is valid for simple lattices having the coordination number $z = 2d$ and containing N spins in total. The linear version of the spin wave analysis (LSWA) takes into account all of the operators up to their bilinear order. Therefore, the term $-J \sum_{\langle ij \rangle} n_i^A n_j^B$ is neglected and

$$f_S(n^{A/B}) \approx 1 - \frac{n^{A/B}}{4S} - \frac{(n^{A/B})^2}{32S^2}, \quad \text{for } S \gg 1, \quad (4.9)$$

is approximated by $f_S \approx 1$:

$$H_{\text{LSWA}} = -dJS^2N + 2dJS \left[\sum_{i \in A} n_i^A + \sum_{j \in B} n_j^B \right] + JS \sum_{\langle ij \rangle} \left[a_i b_j + a_i^\dagger b_j^\dagger \right]. \quad (4.10)$$

With the use of the Fourier transformation

$$a_i = \sqrt{\frac{2}{N}} \sum_{\mathbf{q}} \exp[-i\mathbf{q}\mathbf{r}_i] a_{\mathbf{q}}, \quad a_i^\dagger = \sqrt{\frac{2}{N}} \sum_{\mathbf{q}} \exp[+i\mathbf{q}\mathbf{r}_i] a_{\mathbf{q}}^\dagger, \quad (4.11)$$

$$b_j = \sqrt{\frac{2}{N}} \sum_{\mathbf{q}} \exp[+i\mathbf{q}\mathbf{r}_j] b_{\mathbf{q}}, \quad b_j^\dagger = \sqrt{\frac{2}{N}} \sum_{\mathbf{q}} \exp[-i\mathbf{q}\mathbf{r}_j] b_{\mathbf{q}}^\dagger, \quad (4.12)$$

thereby $\sum_{\mathbf{q}} = N/2$ due to the sublattices, we get

$$\begin{aligned}
 H_{\text{LSWA}} = & -dJS^2N + 2dJS \sum_{\mathbf{q}} \left[a_{\mathbf{q}}^\dagger a_{\mathbf{q}} + b_{\mathbf{q}}^\dagger b_{\mathbf{q}} \right] \\
 & + 2dJS \sum_{\mathbf{q}} \gamma_{\mathbf{q}} \left[a_{\mathbf{q}} b_{\mathbf{q}} + a_{\mathbf{q}}^\dagger b_{\mathbf{q}}^\dagger \right], \quad (4.13)
 \end{aligned}$$

$$\text{with } \gamma_{\mathbf{q}} = \frac{1}{d} \sum_{i=1}^d \cos q_i, \quad (4.14)$$

for simple lattices (simple cubic, square lattice and chain), with their lattice constant set equal to one and their d -dimensional wave vector denoted by \mathbf{q} . Since the last term of (4.13) is yet non-diagonal in $\{a_{\mathbf{q}}^\dagger, a_{\mathbf{q}}\}$ and $\{b_{\mathbf{q}}^\dagger, b_{\mathbf{q}}\}$, we apply the Bogoliubov transformation

$$a_{\mathbf{q}} = \alpha_{\mathbf{q}} \cosh \theta_{\mathbf{q}} - \beta_{\mathbf{q}}^\dagger \sinh \theta_{\mathbf{q}}, \quad a_{\mathbf{q}}^\dagger = \alpha_{\mathbf{q}}^\dagger \cosh \theta_{\mathbf{q}} - \beta_{\mathbf{q}} \sinh \theta_{\mathbf{q}}, \quad (4.15)$$

$$b_{\mathbf{q}} = \beta_{\mathbf{q}} \cosh \theta_{\mathbf{q}} - \alpha_{\mathbf{q}}^\dagger \sinh \theta_{\mathbf{q}}, \quad b_{\mathbf{q}}^\dagger = \beta_{\mathbf{q}}^\dagger \cosh \theta_{\mathbf{q}} - \alpha_{\mathbf{q}} \sinh \theta_{\mathbf{q}}, \quad (4.16)$$

which maps onto new sets of boson operators $\{\alpha_{\mathbf{q}}^\dagger, \alpha_{\mathbf{q}}\}, \{\beta_{\mathbf{q}}^\dagger, \beta_{\mathbf{q}}\}$ obeying the bosonic commutation relations. The corresponding diagonalization condition

$$\tanh [2\theta_{\mathbf{q}}] = \gamma_{\mathbf{q}} \quad (4.17)$$

leads to the final Hamiltonian

$$H_{\text{LSWA}} = -dJS(S+1)N + 2dJS \sum_{\mathbf{q}} \sqrt{1-\gamma_{\mathbf{q}}^2} \left[1 + n_{\mathbf{q}}^\alpha + n_{\mathbf{q}}^\beta \right], \quad (4.18)$$

$$\text{with } n_{\mathbf{q}}^\alpha = \alpha_{\mathbf{q}}^\dagger \alpha_{\mathbf{q}} \quad \text{and} \quad n_{\mathbf{q}}^\beta = \beta_{\mathbf{q}}^\dagger \beta_{\mathbf{q}}, \quad (4.19)$$

which is diagonal in the boson number operators $n_{\mathbf{q}}^\alpha$ and $n_{\mathbf{q}}^\beta$.

From (4.18) we can now identify the ground state energy ($n_{\mathbf{q}}^\alpha = n_{\mathbf{q}}^\beta = 0$) and the spin wave excitation energy $\omega_{\mathbf{q}}$ of the isotropic system,

$$\omega_{\mathbf{q}} = 2dJS \sqrt{1-\gamma_{\mathbf{q}}^2}, \quad (4.20)$$

which is identical for both sorts of boson excitations ($n_{\mathbf{q}}^{\alpha/\beta} \neq 0$). Making use of the long wavelength approximation $|\mathbf{q}| \ll 1$, we recover the linear spin wave dispersion relation

$$\omega_{\mathbf{q}} \approx 2\sqrt{d}JS |\mathbf{q}| \sim |\mathbf{q}|, \quad (4.21)$$

which is typical for AFMs [93, 94]. As expected, there is no gap existing at $\mathbf{q} = \mathbf{0}$ in the isotropic system, since the spins may freely fluctuate into all of the directions provided by the underlying continuous symmetry. This picture is profoundly changed by inducing anisotropies we will deal with later on.

4.2.2 Method II: Approximating Fluctuations

Anderson's method [90], in contrast to the Kubo-Manousakis scheme, circumvents the Holstein-Primakoff transformation by performing an approximation for the remaining fluctuations of S_i^z and S_j^z ; the latter is motivated by the assumption of an ordered antiferromagnetic state:

$$S_i^z \sim +S \quad \text{for } i \in A, \quad S_j^z \sim -S \quad \text{for } j \in B. \quad (4.22)$$

Rewriting the z -component of the spins

$$S^z = \pm S_Q \sqrt{1 - \frac{(S^x)^2 + (S^y)^2}{S_Q^2}}, \quad \text{using } S_Q = \sqrt{S(S+1)}, \quad (4.23)$$

and expanding up to the quadratic order for $S \gg 1$ yields

$$S^z \approx \pm S_Q \mp \frac{(S^x)^2 + (S^y)^2}{2S_Q}, \quad (4.24)$$

with the upper sign referring to spins on sublattice A and the lower one to those on sublattice B . S_Q represents the quantum mechanical length of a single spin.

For the sake of clarification, we choose here to alter Anderson's notation [90], which is rather misleading in our view: He called, by referring to the zeroth order in the foregoing expansion, $S_C = \sqrt{S(S+1)}$ with C for 'classical', despite the fact that S_C is identical with the quantum spin length.

The resulting differences, in special cases hereinafter, between Anderson's method and that of Kubo and Manousakis will merely arise due to the difference between S_Q and S . For large spin quantum numbers these differences disappear according to $S_Q \approx S + \frac{1}{2} \approx S$.

In order to convert the original spin system into harmonic oscillators, the first step is to introduce the following position and momentum operators in Fourier space:

$$Q_{\mathbf{q}} = \sqrt{\frac{2}{NS}} \sum_{i \in A} \exp[-i\mathbf{q}\mathbf{r}_i] S_i^x, \quad P_{\mathbf{q}} = \sqrt{\frac{2}{NS}} \sum_{i \in A} \exp[+i\mathbf{q}\mathbf{r}_i] S_i^y, \quad (4.25)$$

$$R_{\mathbf{q}} = \sqrt{\frac{2}{NS}} \sum_{j \in B} \exp[+i\mathbf{q}\mathbf{r}_j] S_j^x, \quad S_{\mathbf{q}} = -\sqrt{\frac{2}{NS}} \sum_{j \in B} \exp[-i\mathbf{q}\mathbf{r}_j] S_j^y, \quad (4.26)$$

with the d -dimensional wave vector \mathbf{q} and N spins in total, half of them on each sublattice. Due to the minus sign in $S_{\mathbf{q}}$, stemming from the opposite alignment on the distinct sublattices, we get two independent sets $\{Q_{\mathbf{q}}, P_{\mathbf{q}}\}$, $\{R_{\mathbf{q}}, S_{\mathbf{q}}\}$ of position and momentum operators obeying the usual commutation relations

$$[Q_{\mathbf{q}}, P_{\mathbf{q}'}] = i\delta_{\mathbf{q}, \mathbf{q}'}, \quad [R_{\mathbf{q}}, S_{\mathbf{q}'}] = i\delta_{\mathbf{q}, \mathbf{q}'}, \quad (4.27)$$

with all of the remaining mixed commutators vanishing. Making use of these new operators, the Hamiltonian reads in Fourier space:

$$\begin{aligned} H_{\text{LSWA}} &= -dJS(S+1)N + dJS \sum_{\mathbf{q}} [Q_{\mathbf{q}}^2 + P_{\mathbf{q}}^2 + R_{\mathbf{q}}^2 + S_{\mathbf{q}}^2] \\ &\quad + 2dJS \sum_{\mathbf{q}} \gamma_{\mathbf{q}} [Q_{\mathbf{q}}R_{\mathbf{q}} - P_{\mathbf{q}}S_{\mathbf{q}}], \end{aligned} \quad (4.28)$$

$$\text{with } \gamma_{\mathbf{q}} = \frac{1}{d} \sum_{i=1}^d \cos q_i.$$

Since the last term of (4.28) is yet non-diagonal, we introduce, as a second step, the superpositions

$$x_{\mathbf{q}}^1 = \frac{1}{\sqrt{2}} (Q_{\mathbf{q}} + R_{\mathbf{q}}), \quad p_{\mathbf{q}}^1 = \frac{1}{\sqrt{2}} (P_{\mathbf{q}} + S_{\mathbf{q}}), \quad (4.29)$$

$$x_{\mathbf{q}}^2 = \frac{1}{\sqrt{2}} (Q_{\mathbf{q}} - R_{\mathbf{q}}), \quad p_{\mathbf{q}}^2 = \frac{1}{\sqrt{2}} (P_{\mathbf{q}} - S_{\mathbf{q}}), \quad (4.30)$$

which still represent two independent sorts $\{x_{\mathbf{q}}^1, p_{\mathbf{q}}^1\}$, $\{x_{\mathbf{q}}^2, p_{\mathbf{q}}^2\}$ of position and momentum operators:

$$[x_{\mathbf{q}}^1, p_{\mathbf{q}}^1] = i, \quad [x_{\mathbf{q}}^2, p_{\mathbf{q}}^2] = i, \quad (4.31)$$

with all of the commutators with mixed superscripts 1 and 2 vanishing. These superpositions enable us to diagonalize the Hamiltonian and to reduce the system to two decoupled harmonic oscillators:

$$\begin{aligned}
 H_{\text{LSWA}} &= -dJS(S+1)N \\
 &+ dJS \sum_{\mathbf{q}} \left[(x_{\mathbf{q}}^1)^2 (1 + \gamma_{\mathbf{q}}) + (p_{\mathbf{q}}^1)^2 (1 - \gamma_{\mathbf{q}}) \right] \\
 &+ dJS \sum_{\mathbf{q}} \left[(x_{\mathbf{q}}^2)^2 (1 - \gamma_{\mathbf{q}}) + (p_{\mathbf{q}}^2)^2 (1 + \gamma_{\mathbf{q}}) \right] \quad (4.32)
 \end{aligned}$$

$$= -dJS(S+1)N + 2dJS \sum_{\mathbf{q}} \sqrt{1 - \gamma_{\mathbf{q}}^2} \left[1 + n_{\mathbf{q}}^1 + n_{\mathbf{q}}^2 \right] . \quad (4.33)$$

At this, $n_{\mathbf{q}}^1$ and $n_{\mathbf{q}}^2$ denote the occupation numbers of the harmonic oscillators. Contrasting (4.18) with (4.33), we find a perfect concordance of both methods for the isotropic system. Even so, the parallel comparison of these distinct schemes provides different points of view on this semiclassical technique.

As before, we can extract the linear spin wave dispersion $\omega_{\mathbf{q}} \approx 2\sqrt{d}JS|\mathbf{q}|$, which is identical for both sorts of oscillator excitations ($n_{\mathbf{q}}^1 \neq 0$ or $n_{\mathbf{q}}^2 \neq 0$). We also observe a vanishing energy gap at $\mathbf{q} = \mathbf{0}$, due to the unhampered spin fluctuations.

4.2.3 FM vs. AFM

The aim of this paragraph and the subsequent ones that are headlined alike is to contrast the foregoing AFM results with their FM counterparts in order to outline the particular properties of the AFMs. Thereby, the AFM turns out to require a more sophisticated treatment, but compensates this by revealing intriguing quantum effects.

For the FM version of method I by Kubo and Manousakis, it is adequate, due to the absence of any sublattice structures, to introduce a single sort of boson operators $\{a_i^\dagger, a_i\}$ according to (4.4)-(4.5). The recasted ferromagnetic Hamiltonian

$$\begin{aligned}
 H^{\text{FM}} &= -dJS^2N + 2dJS \sum_i n_i - J \sum_{\langle ij \rangle} n_i n_j \\
 &- JS \sum_{\langle ij \rangle} \left[f_S(n_i) a_i a_j^\dagger f_S(n_j) + a_i^\dagger f_S(n_i) f_S(n_j) a_j \right] \quad (4.34)
 \end{aligned}$$

reads in the linear spin wave approximation

$$H_{\text{LSWA}}^{\text{FM}} = -dJS^2N + 2dJS \sum_i n_i - JS \sum_{\langle ij \rangle} \left[a_i a_j^\dagger + a_i^\dagger a_j \right]. \quad (4.35)$$

After applying the Fourier transformation $a_i = \sqrt{1/N} \sum_{\mathbf{q}} \exp[-i\mathbf{q}\mathbf{r}_i] a_{\mathbf{q}}$, with $\sum_{\mathbf{q}} = N$, the resulting Hamiltonian reads with $n_{\mathbf{q}} = a_{\mathbf{q}}^\dagger a_{\mathbf{q}}$ and (4.14)

$$H_{\text{LSWA}}^{\text{FM}} = -dJS(S+1)N + 2dJS \sum_{\mathbf{q}} (1 - \gamma_{\mathbf{q}}) \left[n_{\mathbf{q}} + \frac{1}{2} \right], \quad (4.36)$$

and turns out to be directly diagonal. Therefore, no further Bogoliubov transformation is necessary.

For the adaption of method II, on the other hand, it is sufficient to introduce the position and momentum operators $Q_{\mathbf{q}} = 1/\sqrt{NS} \sum_i \exp[-i\mathbf{q}\mathbf{r}_i] S_i^x$, $P_{\mathbf{q}} = 1/\sqrt{NS} \sum_i \exp[+i\mathbf{q}\mathbf{r}_i] S_i^y$, with $[Q_{\mathbf{q}}, P_{\mathbf{q}'}] = i \delta_{\mathbf{q},\mathbf{q}'}$, to get directly a diagonal Hamiltonian in Fourier space

$$H_{\text{LSWA}}^{\text{FM}} = -dJS(S+1)N + dJS \sum_{\mathbf{q}} (1 - \gamma_{\mathbf{q}}) [Q_{\mathbf{q}}^2 + P_{\mathbf{q}}^2] \quad (4.37)$$

$$= -dJS(S+1)N + 2dJS \sum_{\mathbf{q}} (1 - \gamma_{\mathbf{q}}) \left[n_{\mathbf{q}} + \frac{1}{2} \right], \quad (4.38)$$

which is identical with the Kubo-Manousakis result (4.36).

The corresponding ferromagnetic spin wave excitation energy reads is both methods

$$\omega_{\mathbf{q}} = 2dJS(1 - \gamma_{\mathbf{q}}), \quad (4.39)$$

and, consequently, leads to a quadratic dispersion relation

$$\omega_{\mathbf{q}} \approx JS|\mathbf{q}|^2 \sim |\mathbf{q}|^2 \quad \text{for } |\mathbf{q}| \ll 1, \quad (4.40)$$

which is consistently expected for FMs [93, 94]; as in the AFM case, we recover a vanishing energy gap ($\Delta = 0$). According to a suitable definition in Fourier space [95], $\omega_{\mathbf{q}} = \Delta + D|\mathbf{q}|^2$, we can identify the spin wave stiffness $D = JS$. In the coming section headlined alike, we will compare the resulting stiffnesses for several sorts of anisotropies.

4.2.4 Excursion: Ground State Energy of FM and AFM

At this point, we review the ground state energies of isotropic FMs and AFMs. Their comparison demonstrates the typical quantum fluctuations, which influence the AFM ground state, and enables us to illustrate their dependence on the spin quantum number S .

As pointed out in the paragraph 1.5 on toy models, FM ground states are characterized by triplets, whereas AFM ground states form up singlets, which give rise to the quantum fluctuations. Since LSWA incorporates those singlet formations, as will be further demonstrated in section 4.5, we can extract the corresponding quantum correction terms that distinguish AFMs from FMs.

For that purpose, let us briefly focus on the details:

For the FM, due to $\sum_{\mathbf{q}} \gamma_{\mathbf{q}} = 0$, we can identify from (4.36), respectively from (4.38), the ground state energy

$$E_0^{\text{FM}} = -dJS^2N \quad (4.41)$$

we would expect for N classical spins in d dimensions [90]. Therefore, we conclude a completely ordered FM ground state, which is not affected by quantum fluctuations.

For the AFM, on the contrary, we find the ground state energy

$$E_0 = -dJS(S+1)N + 2dJS \sum_{\mathbf{q}} \sqrt{1 - \gamma_{\mathbf{q}}^2}, \quad (4.42)$$

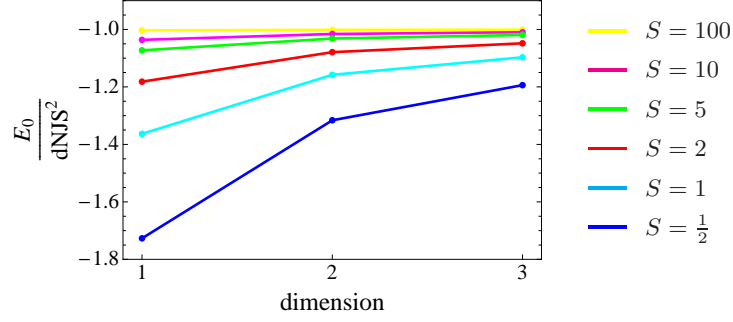


Figure 4.1: AFM ground state energy per spin for various dimensions d and spin quantum numbers S , normalized by d , J and S^2 . The lines are guides to the eyes.

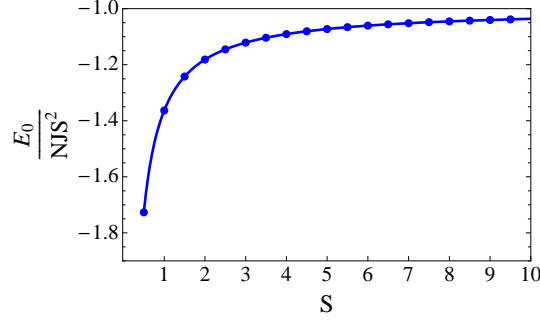


Figure 4.2: AFM ground state energy per spin in one dimension for various spin quantum numbers S , normalized by J and S^2 . The interpolation curve is taken from the numerical results for real values of S .

which explicitly reads for $d = 1$ [90]:

$$\begin{aligned}
 E_0 &= -JS^2N \left[1 + \frac{1}{S} - \frac{1}{2\pi S} \int_{-\pi}^{+\pi} |\sin q| dq \right] \\
 &= -JS^2N \left[1 + \frac{1 - \frac{2}{\pi}}{S} \right] = -JS^2N \left[1 + \frac{0.363}{S} \right]. \quad (4.43)
 \end{aligned}$$

The corresponding value for $S = \frac{1}{2}$, $E_0 = -1.73 JS^2N$, turns out to agree quite well with Bethe's exact solution of the antiferromagnetic chain giving $E_0 = -1.77 JS^2N$ [96]. In higher dimensions we find [90]

$$d = 2 : \quad E_0 = -2JS^2N \left[1 + \frac{0.158}{S} \right], \quad (4.44)$$

$$d = 3 : \quad E_0 = -3JS^2N \left[1 + \frac{0.097}{S} \right]. \quad (4.45)$$

From this, we recover consistently the well-known phenomenon of increased quantum fluctuations in low dimensions. In the limit of large spin quantum numbers, $S \rightarrow \infty$, we regain the classical value $E_0 \rightarrow -dJS^2N$. The rise of this classical trend as well as the enhanced quantum fluctuations in low dimensions are depicted in fig. 4.1. The case of one dimension, showing the strongest quantum fluctuations, is shown separately in fig. 4.2.

4.3 Anisotropy Modifications

In this section we will investigate the influence of anisotropy fields

$$-h_p \left[\sum_{i \in A} (S_i^z)^p + \sum_{j \in B} (S_j^z)^p \right] \quad (4.46)$$

with p even. The impact of odd p and particular fields, which are merely defined on one of the sublattices, will be discussed in the section after the next. The application of the two methods (I: Kubo and Manousakis, II: Anderson) will, bearing in mind their slight differences that disappear consistently for $S \gg 1$, mutually validate the final results.

Before we can start to study the physical impact of the anisotropy fields, we have to take special care of the order p . In contrast to QMF (chapter 3), LSWA fails to recover the reduction formula (1.10): Once having started with a reducible field, e.g. $(S_i^z)^2$ for $S=1/2$, it is erroneously raised to a physical relevance it is not supposed to have. Therefore, in order to avoid false impacts, we have to fix the order p by demanding $p \leq 2S$ right from the beginning.

4.3.1 Method I: Additional Bosonic Terms

Applying the Holstein-Primakoff transformation (4.4)-(4.7) and keeping the bosonic operators up to their bilinear order converts the anisotropy field (4.46) for p even to

$$-h_p \left[\sum_{i \in A} (S - n_i^A)^p + \sum_{j \in B} (-S + n_j^B)^p \right] \quad (4.47)$$

$$\xrightarrow{\text{LSWA}} -h_p S^p N + p h_p S^{p-1} \left[\sum_{i \in A} n_i^A + \sum_{j \in B} n_j^B \right]. \quad (4.48)$$

Due to the use of the binomial theorem in these approximations, the additional terms, which contain number operators, scale according to $\sim p h_p$. The emerging prefactor p will play a decisive role in the later discussion concerning the relevance of higher-order fields.

Thereby, the intermediate anisotropic linear spin wave Hamiltonian reads in real space

$$\begin{aligned} H_{\text{LSWA}} = & -dJS^2N - h_p S^p N + JS \sum_{\langle ij \rangle} [a_i b_j + a_i^\dagger b_j^\dagger] \\ & + 2dJS \left(1 + h_p \frac{p S^{p-2}}{2dJ} \right) \left[\sum_{i \in A} n_i^A + \sum_{j \in B} n_j^B \right], \end{aligned} \quad (4.49)$$

and in Fourier space with (4.14)

$$\begin{aligned}
 H_{\text{LSWA}} = & -dJS^2N - h_p S^p N + 2dJS \sum_{\mathbf{q}} \gamma_{\mathbf{q}} \left[a_{\mathbf{q}} b_{\mathbf{q}} + a_{\mathbf{q}}^{\dagger} b_{\mathbf{q}}^{\dagger} \right] \\
 & + 2dJS \left(1 + h_p \frac{p S^{p-2}}{2dJ} \right) \sum_{\mathbf{q}} \left[a_{\mathbf{q}}^{\dagger} a_{\mathbf{q}} + b_{\mathbf{q}}^{\dagger} b_{\mathbf{q}} \right] \quad , \quad (4.50)
 \end{aligned}$$

both carrying the additional h_p -terms. By comparing to (4.10) and (4.13), we observe that the essential operator structure is maintained, so we can apply the same Bogoliubov transformation (4.15)-(4.16) as before. Although the anisotropy fields merely seem to alter prefactors, it is indeed this change that creates all of the intriguing phenomena in the end.

The modified diagonalization condition reads instead of (4.17)

$$\tanh [2\theta_{\mathbf{q}}] = \gamma_{\mathbf{q}} \left[1 + h_p \frac{p S^{p-2}}{2dJ} \right]^{-1} . \quad (4.51)$$

Using the same notation (4.19) as before, we find the diagonal Hamiltonian

$$\begin{aligned}
 H_{\text{LSWA}} = & -dJS(S+1)N - h_p S^p N - h_p \frac{p}{2} S^{p-1} N \\
 & + 2dJS \sum_{\mathbf{q}} \sqrt{\left(1 + h_p \frac{p S^{p-2}}{2dJ} \right)^2 - \gamma_{\mathbf{q}}^2} \left[1 + n_{\mathbf{q}}^{\alpha} + n_{\mathbf{q}}^{\beta} \right] . \quad (4.52)
 \end{aligned}$$

To ensure a properly defined real square root, we will restrict ourselves from now on to the easy axis case $h_p > 0$.

From (4.52) we can directly identify the enlarged spin wave excitation energies

$$\omega_{\mathbf{q}}(h_p) = 2dJS \sqrt{\left(1 + h_p \frac{p S^{p-2}}{2dJ} \right)^2 - \gamma_{\mathbf{q}}^2} , \quad (4.53)$$

which read for long wavelengths $|\mathbf{q}| \ll 1$ and small positive anisotropy fields $h_p \ll 1$

$$\omega_{\mathbf{q}}(h_p) \approx 2dJS \sqrt{h_p \frac{p S^{p-2}}{dJ} + \frac{1}{2d} |\mathbf{q}|^2} . \quad (4.54)$$

The presence of the anisotropy field h_p inhibits now free spin fluctuations by marking a preferred axis along the z -component of the spins. Accordingly, an energy gap $\Delta > 0$ opens at $\mathbf{q} = \mathbf{0}$, which stabilizes the system:

$$\Delta(h_p) \approx \sqrt{4dJS^p p h_p} \sim \sqrt{p h_p} . \quad (4.55)$$

Such energy gaps in anisotropic antiferromagnets have been measured and confirmed experimentally by neutron spectroscopy [97], which is reviewed in [93]. Aside from that, we observe a deviation from the linear dispersion behaviour (4.21) induced by $h_p > 0$. All of the AFM dispersion properties are graphically summarized in fig. 4.3.

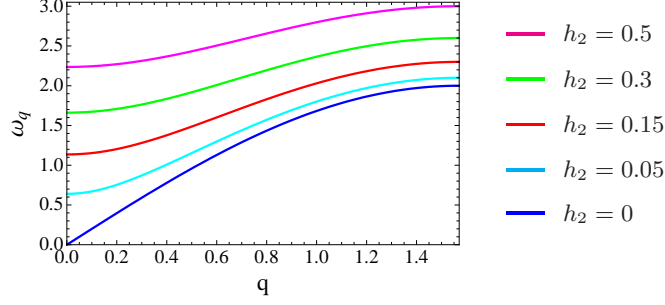


Figure 4.3: The AFM spin wave dispersion (4.53) in one dimension, influenced by various anisotropy fields $h_2 \geq 0$; the parameters J and S have been set equal to one; for $h_2 > 0$ we clearly realize the gap (4.55) and the deviation (4.54) from the isotropic linear behaviour (4.21) at $|\mathbf{q}| \ll 1$.

Due to the increasing gap $\Delta \sim \sqrt{p}$, we may already suggest a stronger relevance for anisotropies of higher order p . This issue will be pursued later on.

We may check our result (4.52) for $p=2$ by comparing to the field term used in the original articles [59, 90],

$$-\bar{h}_2 \sum_{r \in \{A, B\}} \left[(S_r^x)^2 + (S_r^y)^2 \right], \quad (4.56)$$

with r defined on both sublattices. Instead of (4.17) we get the diagonalization condition

$$\tanh [2 \theta_{\mathbf{q}}] = \gamma_{\mathbf{q}} \left[1 - \frac{\bar{h}_2}{dJ} \right]^{-1} \quad (4.57)$$

and the final Hamiltonian

$$\begin{aligned} H_{\text{LSWA}} &= -dJS(S+1)N \\ &+ 2dJS \sum_{\mathbf{q}} \sqrt{\left(1 - \frac{\bar{h}_2}{dJ}\right)^2 - \gamma_{\mathbf{q}}^2} \left[1 + n_{\mathbf{q}}^{\alpha} + n_{\mathbf{q}}^{\beta} \right]. \end{aligned} \quad (4.58)$$

The latter turns out to be identical to (4.52) for $\bar{h}_2 = -h_2$, after rewriting (4.56) as

$$-\bar{h}_2 \sum_r \left[S(S+1) - (S_r^z)^2 \right] = -\bar{h}_2 S(S+1)N + \bar{h}_2 \sum_r (S_r^z)^2. \quad (4.59)$$

Besides this further validation, we may point out the topics those previous studies have left out: Whereas the presence of an infinitesimal field $\bar{h}_2 < 0$ has been simply used to induce a preferred axis, the impact of finite anisotropy fields was completely neglected. We catch up on this issue in paragraph 4.4.4 by studying the outcome for a comprehensive set of parameters with a widespread range of their values. Furthermore, we extend our study to the cases $p > 2$ by choosing the more general anisotropy term $-h_p \sum_r (S_r^z)^p$ instead of (4.56).

4.3.2 Method II: Additional Fluctuation Terms

Approximating the anisotropy term (4.46) by the semiclassical expansion (4.24) up to the quadratic order in S_r^x and S_r^y , with $r \in \{A, B\}$, yields for p even

$$-h_p \sum_{r \in \{A, B\}} (S_r^z)^2 = -h_p S_Q^p N + h_p \frac{p}{2} S_Q^{p-2} \sum_{r \in \{A, B\}} \left[(S_r^x)^2 + (S_r^y)^2 \right]. \quad (4.60)$$

To convert the involved spin operators into position and momentum operators, we apply the transformation (4.25)-(4.26), which leads to the Hamiltonian

$$\begin{aligned} H_{\text{LSWA}} &= -dJS(S+1)N - h_p S_Q^p N \\ &\quad + dJS \left(1 + h_p \frac{p S_Q^{p-2}}{2dJ} \right) \sum_{\mathbf{q}} \left[Q_{\mathbf{q}}^2 + P_{\mathbf{q}}^2 + R_{\mathbf{q}}^2 + S_{\mathbf{q}}^2 \right] \\ &\quad + 2dJS \sum_{\mathbf{q}} \gamma_{\mathbf{q}} \left[Q_{\mathbf{q}} R_{\mathbf{q}} - P_{\mathbf{q}} S_{\mathbf{q}} \right], \end{aligned} \quad (4.61)$$

containing additional operator terms $\sim p h_p$. After decoupling with the use of (4.29)-(4.30), the diagonal Hamiltonian reads in Anderson's approximation scheme:

$$\begin{aligned} H_{\text{LSWA}} &= -dJS(S+1)N - h_p S_Q^p N \\ &\quad + dJS \sum_{\mathbf{q}} \left[(x_{\mathbf{q}}^1)^2 \left(1 + h_p \frac{p S_Q^{p-2}}{2dJ} + \gamma_{\mathbf{q}} \right) + (p_{\mathbf{q}}^1)^2 \left(1 + h_p \frac{p S_Q^{p-2}}{2dJ} - \gamma_{\mathbf{q}} \right) \right] \\ &\quad + dJS \sum_{\mathbf{q}} \left[(x_{\mathbf{q}}^2)^2 \left(1 + h_p \frac{p S_Q^{p-2}}{2dJ} - \gamma_{\mathbf{q}} \right) + (p_{\mathbf{q}}^2)^2 \left(1 + h_p \frac{p S_Q^{p-2}}{2dJ} + \gamma_{\mathbf{q}} \right) \right] \end{aligned} \quad (4.62)$$

$$\begin{aligned} \Rightarrow H_{\text{LSWA}} &= -dJS(S+1)N - h_p S_Q^p N \\ &\quad + 2dJS \sum_{\mathbf{q}} \sqrt{\left(1 + h_p \frac{p S_Q^{p-2}}{2dJ} \right)^2 - \gamma_{\mathbf{q}}^2} \left[1 + n_{\mathbf{q}}^1 + n_{\mathbf{q}}^2 \right]. \end{aligned} \quad (4.63)$$

From (4.63) we can identify the spin wave dispersion

$$\omega_{\mathbf{q}}(h_p) = 2dJS \sqrt{\left(1 + h_p \frac{p S_Q^{p-2}}{2dJ} \right)^2 - \gamma_{\mathbf{q}}^2}, \quad (4.64)$$

respectively for $|\mathbf{q}| \ll 1$ and $h_p \ll 1$

$$\omega_{\mathbf{q}}(h_p) \approx 2dJS \sqrt{h_p \frac{p S_Q^{p-2}}{dJ} + \frac{1}{2d} |\mathbf{q}|^2}, \quad (4.65)$$

and find the energy gap at $\mathbf{q} = \mathbf{0}$

$$\Delta(h_p) \approx \sqrt{4dJS^2 S_Q^{p-2} p h_p} \sim \sqrt{p h_p} > 0. \quad (4.66)$$

As before, we checked the case $p = 2$ by considering fields of the type (4.56).

For quadratic fields $p = 2$ we find a perfect concordance to the results (4.52)-(4.55) that are provided by the alternate Kubo-Manousakis method.

For $p > 2$, on the contrary, small differences between (4.52)-(4.55) and (4.63)-(4.66) occur: These arise, as mentioned before, due to the difference between S_Q and S . As LSWA is based on assumptions that are valid for large spin quantum numbers, we consequently find $S_Q \approx S$ for $S \gg 1$. Thereby, we can successfully reduce, even for $p > 2$, the outcome of the various techniques to a single result.

4.3.3 FM vs. AFM

In order to point out the specific character of the AFM, we contrast the foregoing findings to the FM case.

With the use of the Kubo-Manousakis boson operator approach (method I), the FM anisotropy field $-h_p \sum_i (S_i^z)^p$, with i defined on the entire lattice, is converted to

$$-h_p \sum_i (S_i^z)^p \approx -h_p S^p N + h_p p S^{p-1} \sum_i n_i. \quad (4.67)$$

As a consequence, the diagonal anisotropic Hamiltonian reads in Fourier space instead of (4.36)

$$\begin{aligned} H_{\text{LSWA}}^{\text{FM}} &= -dJS(S+1)N - h_p S^{p-1} \left(S + \frac{p}{2}\right) N \\ &\quad + 2dJS \sum_{\mathbf{q}} \left(1 + h_p \frac{p S^{p-2}}{2dJ} - \gamma_{\mathbf{q}}\right) \left[n_{\mathbf{q}} + \frac{1}{2}\right], \end{aligned} \quad (4.68)$$

which enables us to extract the ferromagnetic anisotropic dispersion relation

$$\omega_{\mathbf{q}} = 2dJS \left(1 + h_p \frac{p S^{p-2}}{2dJ} - \gamma_{\mathbf{q}}\right) \quad (4.69)$$

$$\approx p h_p S^{p-1} + JS |\mathbf{q}|^2 \quad \text{for } |\mathbf{q}| \ll 1. \quad (4.70)$$

As in the AFM case, we recognize for $h_p > 0$ the increase of the spin wave excitation energies and the opening of an energy gap $\Delta > 0$, which has been confirmed experimentally [98]. At that, the $|\mathbf{q}|^2$ -behaviour of the FM remains obviously unaffected by anisotropy fields, as illustrated in fig. 4.4.

For the sake of completeness, we compare these results to those from Anderson's scheme (method II). The application of the semiclassical approximation

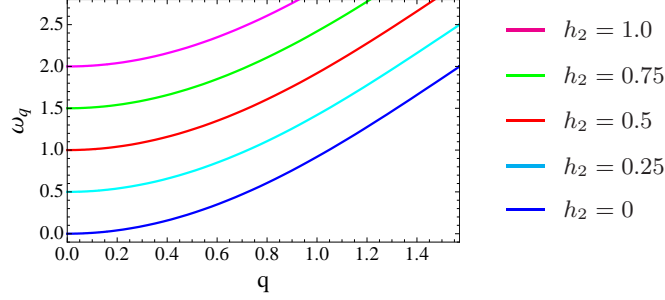


Figure 4.4: The FM spin wave dispersion (4.69) in one dimension, influenced by various anisotropy fields $h_2 \geq 0$; the parameters J and S have been set equal to one; for $h_2 > 0$ we clearly recognize the gap $\Delta > 0$; thereby, the $|\mathbf{q}|^2$ -behaviour remains manifestly unchanged by the presence of anisotropy fields.

(4.24) transforms the h_p -fields into

$$-h_p \sum_i (S_i^z)^p \approx -h_p S_Q^p N + h_p \frac{p}{2} S_Q^{p-2} \sum_i [(S_i^x)^2 + (S_i^y)^2]. \quad (4.71)$$

These additional terms alter (4.38) into

$$\begin{aligned} H_{\text{LSWA}}^{\text{FM}} &= -dJS(S+1)N - h_p S_Q^p N \\ &+ 2dJS \sum_{\mathbf{q}} \left(1 + h_p \frac{p S_Q^{p-2}}{2dJ} - \gamma_{\mathbf{q}} \right) \left[n_{\mathbf{q}} + \frac{1}{2} \right]. \end{aligned} \quad (4.72)$$

The corresponding dispersion relation reads

$$\omega_{\mathbf{q}} = 2dJS \left(1 + h_p \frac{p S_Q^{p-2}}{2dJ} - \gamma_{\mathbf{q}} \right) \quad (4.73)$$

$$\approx p h_p S S_Q^{p-2} + JS |\mathbf{q}|^2 \quad \text{for } |\mathbf{q}| \ll 1. \quad (4.74)$$

As in the AFM case, we find a perfect concordance of both methods for the case $p = 2$. We also checked this outcome by considering fields of the type $-\bar{h}_2 \sum_i [(S_i^x)^2 + (S_i^y)^2]$. For $p > 2$, again due to $S_Q \gtrsim S$, small differences occur that are negligible for large S and lead, therefore, to according results in the LSWA regime.

At this point, we take the chance to contrast our investigated anisotropy fields with coupling anisotropies. The LSWA treatment of coupling anisotropies of the kind $\pm \sum_{\langle ij \rangle} [J_z S_i^z S_j^z + J_{xy} (S_i^x S_j^x + S_i^y S_j^y)]$, with the anisotropy parameter $1 - \lambda = (J_z - J_{xy})/J_z$, has been reviewed by Manousakis [91].

In the FM, we find for both sorts of anisotropies a gap that is proportional to the respective anisotropy parameter:

$$\Delta(\lambda) = 2dJS(1 - \lambda), \quad (4.75)$$

$$\Delta(h_p) = p h_p S^{p-1}, \quad (4.76)$$

respectively $\Delta(h_p) = p h_p S S_Q^{p-2}$ in Anderson's scheme.

The \mathbf{q} -dependence, on the contrary, shows a completely differing behaviour. In order to express those differences, we make use of the spin wave stiffness [61], which we have defined in section 4.2.3 according to [95]:

$$D(\lambda) = \lambda JS , \quad (4.77)$$

$$D(h_p \neq 0) = D(h_p = 0) = JS . \quad (4.78)$$

Whereas the coupling anisotropy has a profound effect on the spin wave stiffness $D(\lambda) \sim \lambda$, the stiffness $D(h_p)$ stays constantly at its isotropic value regardless of the presence of fields $h_p > 0$, as we can see from (4.70) and fig. 4.4.

Therefore, we point out emphatically that anisotropy fields may not be confused with coupling anisotropies. Whereas mainly the latter have been intensely studied in the past (see chapter 1), such differing mechanisms motivate and demand to perform a comprehensive study that focuses on anisotropy fields.

4.4 Sublattice Magnetization

This section contains key results that reveal the amount of pure quantum fluctuations of AFMs at $T=0$, which can suppress or even destroy the long range order completely.

In order to express the quantum fluctuations quantitatively, we will take a closer look at the sublattice magnetization, also known as staggered magnetization: For an AFM we have a bipartite lattice structure, which can be divided into two distinct sublattices A and B , each of them showing a uniform spin alignment for a suitable parameter region; accordingly, the sublattice magnetization for the z -component is defined by

$$M^{\text{sl}} = \frac{1}{N} \left(\sum_{i \in A} \langle S_i^z \rangle - \sum_{j \in B} \langle S_j^z \rangle \right) . \quad (4.79)$$

At $T=0$ we can exclude the presence of thermal excitations and extract the mere quantum corrections that still affect the AFM ground state.

We will study in detail how the ground state sublattice magnetization $M_{T=0}^{\text{sl}}$ is influenced by the anisotropy field h_p and the spin quantum number S . For that purpose, we will examine the dependence $M_{T=0}^{\text{sl}}(h_p, S, d)$ for a widespread range of the parameters h_p and S in integer dimensions d . Thereby, we will demonstrate the rise of two classical trends: Both of the parameters h_p and S tend to make the system more and more classical for increasing values. For a suitable combination of both parameters, we may yet observe the fascinating interplay of these classical trends. Accordingly, we find the two classical limits $h_p \gg 1$ and $S \gg 1$. Nevertheless, even relatively small fields can have a profound influence: The outcome will further demonstrate that antiferromagnetic

Heisenberg systems turn out to be extremely sensitive to anisotropy fields. We will express this sensitivity by considering a quantity we want to introduce as anisotropy susceptibility. Before we start the discussion in section 4.4.4, we outline the derivation of the sublattice magnetization in both methods and point out the difference to the FM magnetization at $T = 0$.

4.4.1 Method I - Derivation

We start with the derivation of $M_{T=0}^{\text{sl}}$ based on the Kubo-Manousakis scheme (method I). Since a detailed description is missing in the literature review [91], we add those details in the following. The main part of this derivation can be performed in general, so we can insert the characteristics of isotropic and anisotropic systems afterwards.

In order to calculate the sublattice magnetization, we need to determine the expectation values of the summarized z -components of all the spins on the sublattices A and B .

The total z -component of the spins on sublattice A is given by

$$\left(S_{\text{tot}}^z\right)^{(A)} = \sum_{i \in A} S_i^z \stackrel{(4.4)}{=} \sum_{i \in A} (S - n_i^A) \stackrel{(4.11)}{=} \frac{SN}{2} - \sum_{\mathbf{q}} a_{\mathbf{q}}^\dagger a_{\mathbf{q}}, \quad (4.80)$$

and is converted, with the use of the Bogoliubov transformation (4.15)-(4.16), into

$$\begin{aligned} \left(S_{\text{tot}}^z\right)^{(A)} = \frac{SN}{2} - \sum_{\mathbf{q}} \left[\alpha_{\mathbf{q}}^\dagger \alpha_{\mathbf{q}} \cosh^2 \theta_{\mathbf{q}} + \beta_{\mathbf{q}}^\dagger \beta_{\mathbf{q}} \sinh^2 \theta_{\mathbf{q}} + \sinh^2 \theta_{\mathbf{q}} \right. \\ \left. - \left(\alpha_{\mathbf{q}}^\dagger \beta_{\mathbf{q}}^\dagger + \alpha_{\mathbf{q}} \beta_{\mathbf{q}} \right) \sinh \theta_{\mathbf{q}} \cosh \theta_{\mathbf{q}} \right]. \end{aligned} \quad (4.81)$$

The expectation values of the involved operators vanish at $T = 0$, since the system is in its ground state (denoted by the subscript '0'):

$$\langle \alpha_{\mathbf{q}}^\dagger \alpha_{\mathbf{q}} \rangle_0 = \langle n_{\mathbf{q}}^\alpha \rangle_0 = 0, \quad \langle \beta_{\mathbf{q}}^\dagger \beta_{\mathbf{q}} \rangle_0 = \langle n_{\mathbf{q}}^\beta \rangle_0 = 0, \quad (4.82)$$

$$\langle \alpha_{\mathbf{q}}^\dagger \beta_{\mathbf{q}}^\dagger \rangle_0 = \langle \alpha_{\mathbf{q}}^\dagger \rangle_0 \langle \beta_{\mathbf{q}}^\dagger \rangle_0 = 0, \quad \langle \alpha_{\mathbf{q}} \beta_{\mathbf{q}} \rangle_0 = \langle \alpha_{\mathbf{q}} \rangle_0 \langle \beta_{\mathbf{q}} \rangle_0 = 0. \quad (4.83)$$

Therefore, the resulting expectation value of (4.80) is given by

$$\begin{aligned} \left\langle \left(S_{\text{tot}}^z\right)^{(A)} \right\rangle_0 &= \frac{SN}{2} - \sum_{\mathbf{q}} \sinh^2 \theta_{\mathbf{q}} \\ &= \frac{SN}{2} - \frac{1}{2} \sum_{\mathbf{q}} \left[\frac{1}{\sqrt{1 - \tanh^2[2\theta_{\mathbf{q}}]}} - 1 \right]. \end{aligned} \quad (4.84)$$

On sublattice B we find

$$\left\langle \left(S_{\text{tot}}^z\right)^{(B)} \right\rangle_0 = -\frac{SN}{2} + \sum_{\mathbf{q}} \sinh^2 \theta_{\mathbf{q}} = -\left\langle \left(S_{\text{tot}}^z\right)^{(A)} \right\rangle_0, \quad (4.85)$$

and yield, therefore, the final expression for the ground state sublattice magnetization

$$\begin{aligned} M_{T=0}^{\text{sl}} &= \frac{1}{N} \left[\left\langle \left(S_{\text{tot}}^z \right)^{(A)} \right\rangle_0 - \left\langle \left(S_{\text{tot}}^z \right)^{(B)} \right\rangle_0 \right] \\ &= S + \frac{1}{2} - \frac{1}{N} \sum_{\mathbf{q}} \frac{1}{\sqrt{1 - \tanh^2[2\theta_{\mathbf{q}}]}}. \end{aligned} \quad (4.86)$$

The deviation from the maximal classical value S manifests the amount of quantum fluctuations that are still existing in the AFM at $T=0$. We will refer to this deviation as the quantum correction.

Depending on the diagonalization condition for $\tanh[2\theta_{\mathbf{q}}]$ we yield the results for isotropic and anisotropic systems. For isotropic systems, with $\tanh[2\theta_{\mathbf{q}}] = \gamma_{\mathbf{q}}$ (4.17), the sublattice magnetization reads

$$M_{T=0}^{\text{sl}} = S + \frac{1}{2} - \frac{1}{N} \sum_{\mathbf{q}} \frac{1}{\sqrt{1 - \gamma_{\mathbf{q}}^2}}. \quad (4.87)$$

Based on (4.87), we can now clearly conclude that the AFM is influenced by non-vanishing quantum fluctuations that give rise to a non-zero quantum correction, even at $T=0$. For an increasing spin quantum number S , we observe from (4.87) a decreasing quantum correction and, consistently, its vanishing in the classical limit $S \rightarrow \infty$ according to $M_{T=0}^{\text{sl}} \rightarrow S$.

The quantum fluctuations can also be profoundly influenced by anisotropy fields: For the anisotropic system, with $h_p > 0$, we find with (4.51)

$$M_{T=0}^{\text{sl}}(h_p) = S + \frac{1}{2} - \frac{1}{N} \sum_{\mathbf{q}} \left[1 - \frac{\gamma_{\mathbf{q}}^2}{\left(1 + h_p \frac{p S^{p-2}}{2dJ} \right)^2} \right]^{-1/2}. \quad (4.88)$$

Again, we successfully checked the case $p = 2$ of (4.88) by considering fields \bar{h}_2 of the type (4.56). From (4.88) we can extract another classical limit: For large anisotropy fields $h_p \rightarrow \infty$ the quantum correction tends to zero, as before for $S \rightarrow \infty$. Therefore, we are dealing with the combination of two classical limits: The quantum fluctuations can be totally suppressed either by $h_p \rightarrow \infty$ or by $S \rightarrow \infty$. The rise of these classical trends for relatively small fields will be illustrated in section 4.4.4. Thereby, we will investigate as well the interplay of these classical trends induced by a suitable combination of finite h_p and S .

4.4.2 Method II - Derivation

In order to derive the sublattice magnetization according to Anderson's method, we apply the semiclassical approximation (4.24) to the total z -component of the spins on sublattice A

$$\left(S_{\text{tot}}^z \right)^{(A)} = \sum_{i \in A} S_i^z = \frac{S_Q N}{2} - \sum_{i \in A} \frac{(S_i^x)^2 + (S_i^y)^2}{2 S_Q}, \quad (4.89)$$

which reads in Fourier space with the position and momentum operators (4.25)

$$\left(S_{\text{tot}}^z\right)^{(A)} = \frac{S_Q N}{2} - S \sum_{\mathbf{q}} \frac{Q_{\mathbf{q}}^2 + P_{\mathbf{q}}^2}{2 S_Q}. \quad (4.90)$$

The application of the superposition operators (4.29)-(4.30) yields

$$\begin{aligned} \left(S_{\text{tot}}^z\right)^{(A)} = \frac{S_Q N}{2} - \frac{S}{4 S_Q} \sum_{\mathbf{q}} \left[(x_{\mathbf{q}}^1)^2 + (x_{\mathbf{q}}^2)^2 + 2 x_{\mathbf{q}}^1 x_{\mathbf{q}}^2 \right. \\ \left. + (p_{\mathbf{q}}^1)^2 + (p_{\mathbf{q}}^2)^2 + 2 p_{\mathbf{q}}^1 p_{\mathbf{q}}^2 \right]. \end{aligned} \quad (4.91)$$

Please note that the prefactors of the terms with mixed superscripts are wrong in Anderson's paper [90]. Since their expectation values vanish according to

$$\langle x_{\mathbf{q}}^1 x_{\mathbf{q}}^2 \rangle_0 = \langle x_{\mathbf{q}}^1 \rangle_0 \langle x_{\mathbf{q}}^2 \rangle_0 = 0, \quad \langle p_{\mathbf{q}}^1 p_{\mathbf{q}}^2 \rangle_0 = \langle p_{\mathbf{q}}^1 \rangle_0 \langle p_{\mathbf{q}}^2 \rangle_0 = 0, \quad (4.92)$$

there was no resulting error in his article. Due to (4.92), the introduction of the superposition operators acts as a decoupling transformation for the sublattice magnetization as well as for the Hamiltonian (4.61)-(4.63).

For the calculation of the remaining expectation values of (4.91) we have to distinguish isotropic and anisotropic systems. In both cases we make use of the virial theorem

$$\left\langle \frac{1}{2 m_{\mathbf{q}}^{\delta}} (p_{\mathbf{q}}^{\delta})^2 \right\rangle_0 = \left\langle \frac{1}{2} m_{\mathbf{q}}^{\delta} (\overline{\omega}_{\mathbf{q}}^{\delta})^2 (x_{\mathbf{q}}^{\delta})^2 \right\rangle_0 = \left\langle \overline{\omega}_{\mathbf{q}}^{\delta} \left[n_{\mathbf{q}}^{\delta} + \frac{1}{2} \right] \right\rangle_0 = \frac{1}{4} \overline{\omega}_{\mathbf{q}}^{\delta}, \quad (4.93)$$

with $\delta \in \{1, 2\}$ referring to the superscripts used in (4.29)-(4.30). Subsequently, we identify $m_{\mathbf{q}}^{\delta}$ and $\overline{\omega}_{\mathbf{q}}^{\delta}$ from the Hamiltonians, which are expressed diagonal in $x_{\mathbf{q}}^{\delta}$ and $p_{\mathbf{q}}^{\delta}$, namely (4.32) for isotropic and (4.62) for anisotropic systems.

For the isotropic case, we extract with (4.93) from (4.32)

$$\left\langle (x_{\mathbf{q}}^1)^2 \right\rangle_0 = \left\langle (p_{\mathbf{q}}^2)^2 \right\rangle_0 = \frac{1}{2} \sqrt{\frac{1 - \gamma_{\mathbf{q}}}{1 + \gamma_{\mathbf{q}}}}, \quad (4.94)$$

$$\left\langle (x_{\mathbf{q}}^2)^2 \right\rangle_0 = \left\langle (p_{\mathbf{q}}^1)^2 \right\rangle_0 = \frac{1}{2} \sqrt{\frac{1 + \gamma_{\mathbf{q}}}{1 - \gamma_{\mathbf{q}}}}. \quad (4.95)$$

With the total z -component of the spins on sublattice B

$$\left\langle \left(S_{\text{tot}}^z\right)^{(B)} \right\rangle_0 = - \left\langle \left(S_{\text{tot}}^z\right)^{(A)} \right\rangle_0, \quad (4.96)$$

we get the isotropic sublattice magnetization

$$M_{T=0}^{\text{sl}} = S_Q - \frac{S}{S_Q} \frac{1}{N} \sum_{\mathbf{q}} \frac{1}{\sqrt{1 - \gamma_{\mathbf{q}}^2}}. \quad (4.97)$$

As before in method I, we conclude non-zero quantum corrections for the AFM ground state at $T = 0$. These quantum fluctuations can be suppressed by increasing spin quantum numbers S and we consistently recover the classical limit $M_{T=0}^{\text{sl}} \rightarrow S$ for $S \rightarrow \infty$.

For the anisotropic system, on the other hand, we use (4.93) and (4.62) to extract for $h_p > 0$

$$\langle (x_{\mathbf{q}}^1)^2 \rangle_0 = \langle (p_{\mathbf{q}}^2)^2 \rangle_0 = \frac{1}{2} \sqrt{\frac{1 + h_p \frac{p S_Q^{p-2}}{2dJ} - \gamma_{\mathbf{q}}}{1 + h_p \frac{p S_Q^{p-2}}{2dJ} + \gamma_{\mathbf{q}}}}, \quad (4.98)$$

$$\langle (x_{\mathbf{q}}^2)^2 \rangle_0 = \langle (p_{\mathbf{q}}^1)^2 \rangle_0 = \frac{1}{2} \sqrt{\frac{1 + h_p \frac{p S_Q^{p-2}}{2dJ} + \gamma_{\mathbf{q}}}{1 + h_p \frac{p S_Q^{p-2}}{2dJ} - \gamma_{\mathbf{q}}}}. \quad (4.99)$$

Therefore, the anisotropic sublattice magnetization reads in Anderson's formulation

$$M_{T=0}^{\text{sl}}(h_p) = S_Q - \frac{S}{S_Q} \frac{1}{N} \sum_{\mathbf{q}} \left[1 - \frac{\gamma_{\mathbf{q}}^2}{\left(1 + h_p \frac{p S_Q^{p-2}}{2dJ}\right)^2} \right]^{-1/2}, \quad (4.100)$$

which has been checked for $p=2$ by comparing to the fields \bar{h}_2 defined in (4.56). From (4.100) we extract, as before, another classical limit provided by $h_p \rightarrow \infty$. The implied classical trends that arise for combined S and h_p will be further pursued in section 4.4.4.

To compare (4.97) and (4.100) with the results (4.87)-(4.88) in the alternate Kubo-Manousakis scheme, we have to proceed carefully: Neglecting all of the contributions of the order $\mathcal{O}[1/S]$ for $S \gg 1$, we get

$$S_Q \approx S + \frac{1}{2} \quad \text{and} \quad \frac{S}{S_Q} \approx 1. \quad (4.101)$$

In order to achieve numerically consistent results, we emphasize that it is decisive to keep the second term in the $\frac{1}{S}$ -expansion of $S_Q \approx S + \frac{1}{2}$. By applying (4.101) to (4.97) and (4.100), we finally recover the same results in both approximations methods, for isotropic as well as for anisotropic systems with $h_p > 0$.

4.4.3 FM vs. AFM

The following comparison to the FM case will exhibit that the quantum corrections found in the foregoing sections are typical characteristics of the AFM ground state. The ground state magnetization of the FM is defined by

$$M_{T=0} = \frac{1}{N} \sum_i \langle S_i^z \rangle_0, \quad (4.102)$$

with the sites i defined on the entire lattice that contains N spins in total.

In the Kubo-Manousakis scheme (method I), we get with (4.4)-(4.5) and the Fourier transformation of section 4.2.3

$$M_{T=0} = S - \frac{1}{N} \sum_{\mathbf{q}} \langle n_{\mathbf{q}} \rangle_0 = S, \quad (4.103)$$

which coincides with the maximal classical value the magnetization can take on.

In Anderson's formulation (method II), the FM magnetization reads with the use of (4.24) and the operators $\{Q_{\mathbf{q}}, P_{\mathbf{q}}\}$ defined in section 4.2.3:

$$M_{T=0} = S_Q - \frac{S}{2S_Q} \frac{1}{N} \sum_{\mathbf{q}} \left[\langle Q_{\mathbf{q}}^2 \rangle_0 + \langle P_{\mathbf{q}}^2 \rangle_0 \right]. \quad (4.104)$$

From the corresponding virial theorem we take

$$\langle Q_{\mathbf{q}}^2 \rangle_0 = \langle P_{\mathbf{q}}^2 \rangle_0 = \frac{1}{2}, \quad (4.105)$$

and get the magnetization

$$M_{T=0} = S_Q - \frac{S}{2S_Q}. \quad (4.106)$$

In order to compare both methods, we have again to take special care of the approximation of S_Q for large S : With (4.101) we consistently regain $M_{T=0} = S$ as before.

In both methods, thereby, we recover the maximal classical value S and, accordingly, the absence of quantum corrections. Thus, the FM ground state is not affected at all by quantum fluctuations provided by singlet formations, which will be exposed in section 4.5. Due to its complete order, the FM ground state shows consequently no sensitivity to the presence of anisotropy fields.

4.4.4 Results and Discussion

This paragraph contains the graphical illustrations of the sublattice magnetization at $T=0$, which lead to the key messages of this thesis.

For the explicit calculation of the sublattice magnetization (4.88), we make use of the thermodynamical limit and replace the involved sums by integrals according to

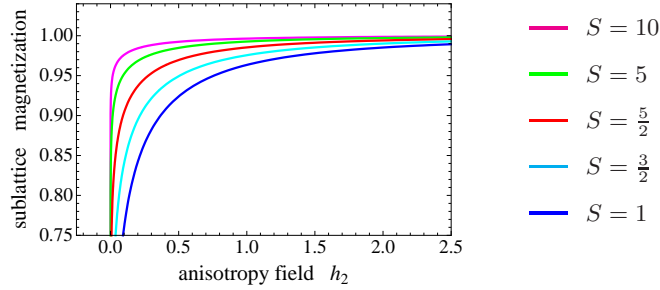
$$\frac{1}{N} \sum_{\mathbf{q}} \dots \rightarrow \frac{1}{2} \frac{1}{(2\pi)^d} \left(\prod_{i=1}^d \int_{-\pi}^{+\pi} dq_i \right) \dots, \quad (4.107)$$

and gain, based on (4.88), the following expression for general, but discretized dimensions d :

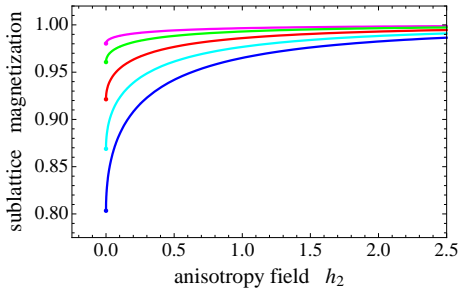
$$M_{T=0}^{\text{sl}}(h_p) = S + \frac{1}{2} - \frac{1}{2(2\pi)^d} \left(\prod_{i=1}^d \int_{-\pi}^{+\pi} dq_i \right) \left[1 - \left(\frac{\frac{1}{d} \sum_{i=1}^d \cos q_i}{1 + h_p \frac{p S^{p-2}}{2dJ}} \right)^2 \right]^{-1/2}. \quad (4.108)$$

To keep the graphical output manageable, we restrict the illustrations to the case $p=2$. General considerations will be pursued further on for general p , and the relevance of higher-order anisotropies with $p > 2$ will be discussed at the end of this section. During these calculations, the parameter J is set equal to one; the numerical value of h_2 can, therefore, be interpreted as the ratio h_2/J of the anisotropy field h_2 and the competing coupling constant J .

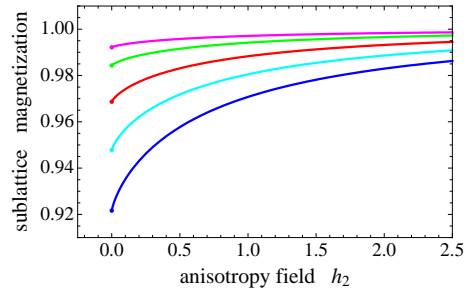
The sublattice magnetization and its dependence on the parameters h_2 and S is illustrated in fig.4.5 for various dimensions d . To depict the involved dependencies for a larger range of the parameter h_2 , we scaled the horizontal axis in fig.4.6 logarithmically.



(a) $d = 1$



(b) $d = 2$



(c) $d = 3$

Figure 4.5: Ground state sublattice magnetization $M_{T=0}^{\text{sl}}/S$ in one, two and three dimensions; in order to compare the results for various spin quantum numbers S , we normalized $M_{T=0}^{\text{sl}}$ by S .

These graphs clearly demonstrate the classical limits for $S \gg 1$ and $h_2 \gg 1$ and illustrate their implied interplay. In addition, these figures reveal the arising classical trend that is generated by increasing spin quantum numbers and anisotropy fields, respectively by a suitable combination of both. We can also observe from fig.4.5 that relatively small fields h_2 seem to induce profound changes of the sublattice magnetization. This observation will be quantified in section 4.6 by introducing the anisotropy susceptibility.

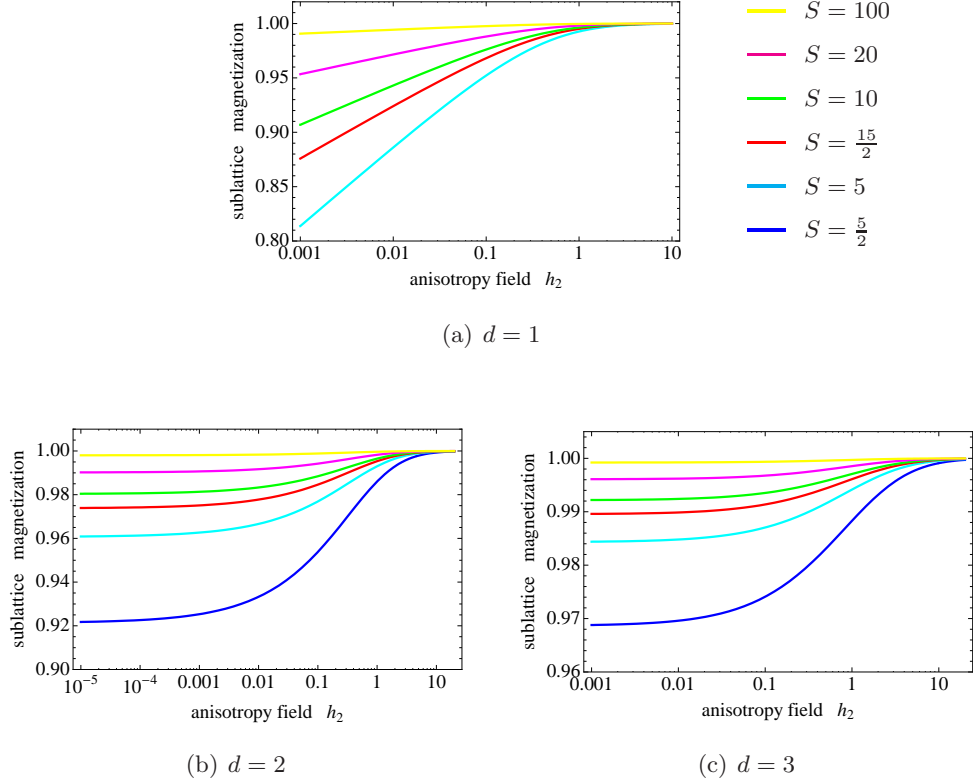


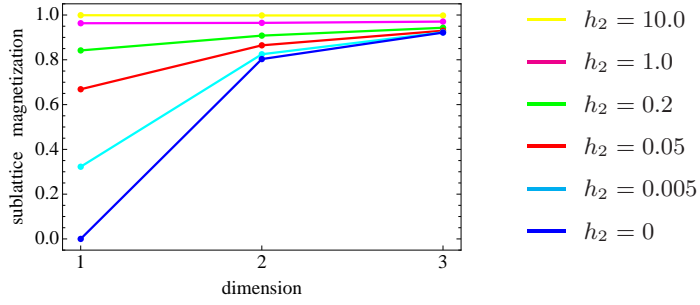
Figure 4.6: Logarithmically scaled counterpart to fig.4.5: Normalized ground state sublattice magnetization $M_{T=0}^{\text{sl}}/S$ in one, two and three dimensions.

The dimensional dependencies are emphasized in fig. 4.7 for fixed spin quantum numbers and various h_2 , and vice versa in fig. 4.8 and 4.9. We can clearly extract and, thereby, confirm the appearance of stronger quantum fluctuations in lower dimensions, as mentioned before. At this, the logarithmically divergent behaviour in one dimension,

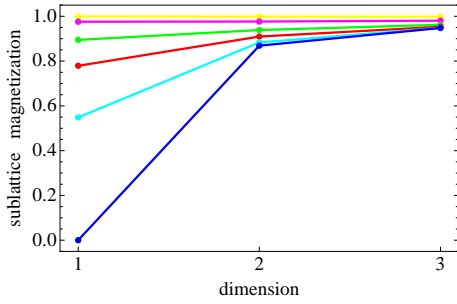
$$\lim_{h_p \rightarrow 0} M_{T=0}^{\text{sl}} \sim \lim_{h_p \rightarrow 0} \ln \left[\frac{p h_p}{J} \right] \rightarrow -\infty \quad \text{for } d = 1, \quad (4.109)$$

is artificial and has to be reinterpreted as an infinitely strong quantum correction for the isotropic system that leads to a vanishing long range order. The application of the Random Phase Approximation (RPA) in the next chapter will repair this incorrect behaviour.

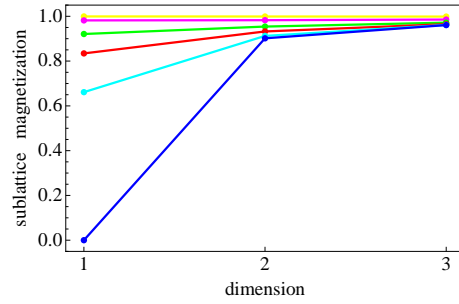
The well-known isotropic values in higher dimensions [59], giving e.g. the suppression to 80% of the classical value in $d = 2$ and 92% in $d = 3$ for $S = 1$, can be read from the figures, too.



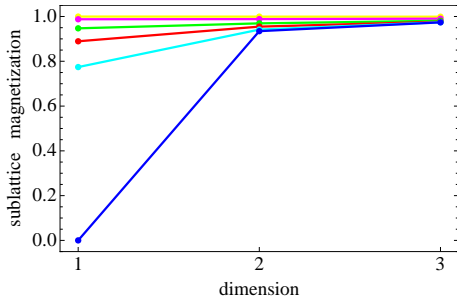
(a) $S = 1$



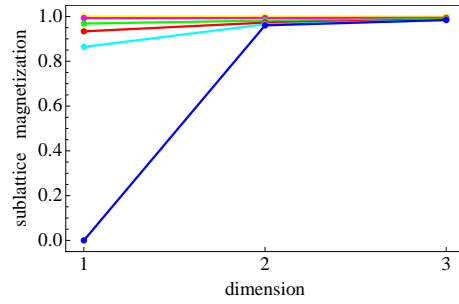
(b) $S = \frac{3}{2}$



(c) $S = 2$

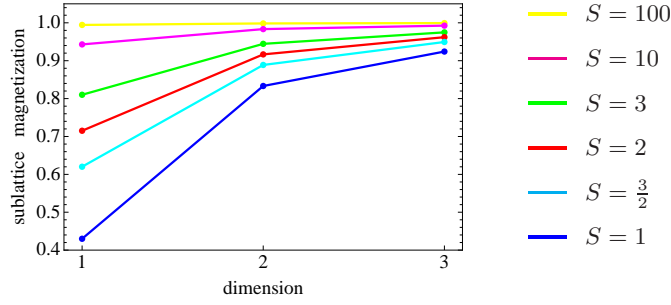


(d) $S = 3$

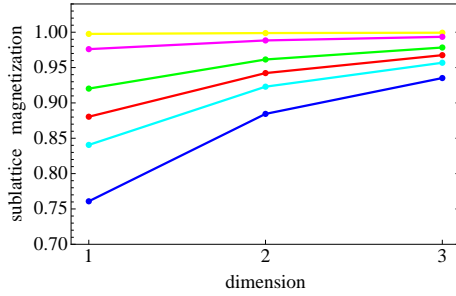


(e) $S = 5$

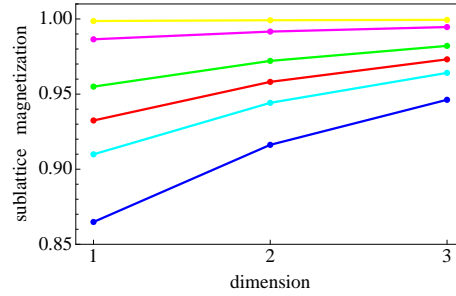
Figure 4.7: Dimensional dependence of the normalized ground state sublattice magnetization $M_{T=0}^{\text{sl}}/S$ for different fixed spin quantum numbers S and various $h_2 \geq 0$; the lines are guides to the eyes.



(a) $h_2 = 0.01$



(b) $h_2 = 0.1$



(c) $h_2 = 0.25$

Figure 4.8: Dimensional dependence of the normalized ground state sublattice magnetization $M_{T=0}^{\text{sl}}/S$ for different fixed anisotropy fields $h_2 > 0$ and various spin quantum numbers S ; the lines are guides to the eyes.

From the depicted dependencies $M_{T=0}^{\text{sl}}(h_p, S)$ we can draw the important conclusion that not only large, but also relatively small anisotropy fields profoundly reduce the quantum fluctuations and, thereby, convert the former quantum system into a classical one. The classical description of the SP-STM experiments performed in Hamburg on spin systems under the influence of anisotropy fields ([23]-[31], see also the introductory chapter 1) can hereby fully confirmed by our studies.

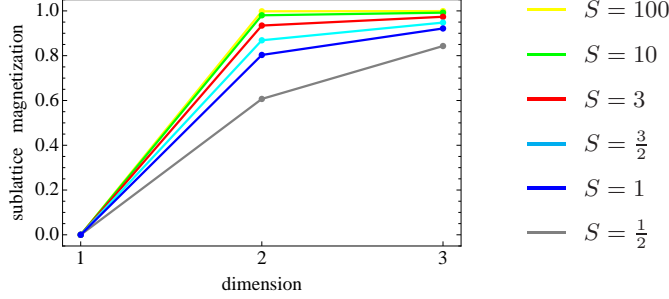


Figure 4.9: Dimensional dependence of the normalized ground state sublattice magnetization $M_{T=0}^{sl}/S$ for the isotropic ($h_2 = 0$) Heisenberg system, shown for various spin quantum numbers S ; the lines are guides to the eyes.

In order to compare higher-order anisotropies containing larger even p , we have again to rescale the fields, which is very straightforward in LSWA: We simply have to remove the already existing prefactors S^{p-2} in (4.88), respectively S_Q^{p-2} in (4.100). At this, we find the behaviour that was already suggested by the energy gap $\Delta \sim \sqrt{p}$ (4.55) in section 4.3.1: Due to the remaining prefactor p in (4.88) and (4.100), we conclude a higher relevance for anisotropies with higher order p , which is consistent with our QMF prediction for small spin quantum numbers in chapter 3. In the end, we are therefore dealing with a typical LSWA paradox: Although the LSWA outcome is derived for large spin quantum numbers, the still involved quantum effects lead to results that are yet valid for small spin quantum numbers. Thereby, we find from (4.88) the prefactors $a_{\text{LSWA}}(p)$ and their rescaled counterparts $\tilde{a}_{\text{LSWA}}(p)$

$$\tilde{a}_{\text{LSWA}}(p) = \frac{a_{\text{LSWA}}(p)}{S^{p-2}} \quad \text{with} \quad a_{\text{LSWA}}(p) = \frac{p S^{p-2}}{2dJ} . \quad (4.110)$$

Consequently, their relevance is characterized by

$$\tilde{a}_{\text{LSWA}}(p') > \tilde{a}_{\text{LSWA}}(p) \quad \text{for even } p' > p , \quad (4.111)$$

which turns out to be independent of S . This finding is thus consistent with the QMF trend for small spin quantum numbers, but lacks to recover the inverse trend for large spin quantum numbers. It has to be regarded as a weakness of the LSWA approach that we do not discover any S -dependence of the higher-order relevance that is manifested in the rescaled prefactors.

Finally, we did not achieve an S -dependent prefactor, but found the same basic behaviour for all even p and gained a consistent hierarchy for small spin quantum numbers.

4.5 Staggered and Uniform Fields

We may study now the different effects induced by staggered and uniform fields, with even as well as odd p , which beautifully reveal the nature of the quantum fluctuations related to the singlet formations presented in the introductory paragraph 1.5 on toy models. The fully aligned FM shows no sensitivity to any fields, except for its magnetization orientation for odd p . AFMs, on the other hand, can be profoundly and differently influenced by certain classes of fields.

4.5.1 Uniform Magnetic Field

The consequences of a uniform field with even p have already been discussed in the course of this chapter. In order to contrast these previous findings, we study the consequences of the fields

$$-h_{p'} \left[\sum_{i \in A} (S_i^z)^{p'} + \sum_{j \in B} (S_j^z)^{p'} \right] \quad \text{with } p' \text{ odd}, \quad (4.112)$$

especially the case of the uniform magnetic field $p' = 1$. For the sake of clarification, we denote the odd order in this section by p' .

In the Kubo-Manousakis scheme, the field terms (4.112) are, in contrast to (4.48), approximated by

$$+ h_{p'} p' S^{p'-1} \left[\sum_{i \in A} n_i^A - \sum_{j \in B} n_j^B \right], \quad (4.113)$$

and we get the provisional Hamiltonian

$$\begin{aligned} H_{\text{LSWA}}(h_{p'}) &= -dJS^2N + 2dJS \sum_{\mathbf{q}} \gamma_{\mathbf{q}} \left[a_{\mathbf{q}} b_{\mathbf{q}} + a_{\mathbf{q}}^\dagger b_{\mathbf{q}}^\dagger \right] \\ &\quad + 2dJS \left(1 + h_{p'} \frac{p' S^{p'-2}}{2dJ} \right) \sum_{\mathbf{q}} a_{\mathbf{q}}^\dagger a_{\mathbf{q}} \\ &\quad + 2dJS \left(1 - h_{p'} \frac{p' S^{p'-2}}{2dJ} \right) \sum_{\mathbf{q}} b_{\mathbf{q}}^\dagger b_{\mathbf{q}}, \end{aligned} \quad (4.114)$$

which differs from the p -even case (4.50) in the sign of the term $\sim h_{p'} b_{\mathbf{q}}^\dagger b_{\mathbf{q}}$. The subsequent Bogoliubov transformation (4.15)-(4.16) elucidates the consequences of this sign change: The diagonalized final Hamiltonian for odd p' reads

$$H_{\text{LSWA}}(h_{p'}) = H_{\text{LSWA}}^{\text{isotropic}} + h_{p'} p' S^{p'-1} \sum_{\mathbf{q}} \left[n_{\mathbf{q}}^\alpha - n_{\mathbf{q}}^\beta \right], \quad (4.115)$$

with $H_{\text{LSWA}}^{\text{isotropic}}$ referring to the isotropic Hamiltonian (4.18).

To recover the corresponding result in Anderson's scheme, we have to alter the procedure we refer to as method II: The application of the semiclassical approximation formula (4.24) to the odd- p' -fields yields the Hamiltonian

$$\begin{aligned}
 H_{\text{LSWA}}(h_{p'}) &= -dJS(S+1)N + 2dJS \sum_{\mathbf{q}} \gamma_{\mathbf{q}} \left[Q_{\mathbf{q}} R_{\mathbf{q}} - P_{\mathbf{q}} S_{\mathbf{q}} \right] \\
 &+ dJS \left(1 + h_{p'} \frac{p' S_Q^{p'-2}}{2dJ} \right) \sum_{\mathbf{q}} \left[Q_{\mathbf{q}}^2 + P_{\mathbf{q}}^2 \right] \\
 &+ dJS \left(1 - h_{p'} \frac{p' S_Q^{p'-2}}{2dJ} \right) \sum_{\mathbf{q}} \left[R_{\mathbf{q}}^2 + S_{\mathbf{q}}^2 \right], \quad (4.116)
 \end{aligned}$$

which contains, as before, an additional sign compared to the case of even p (4.61). Since the previously used transformation (4.29)-(4.30) would leave the two harmonic oscillators still coupled to each other, via terms $\sim h_{p'} x_{\mathbf{q}}^1 x_{\mathbf{q}}^2$ and $\sim h_{p'} p_{\mathbf{q}}^1 p_{\mathbf{q}}^2$, we have to introduce an alternate transformation in order to decouple the oscillators. At this point, we benefit from our parallel treatment of two approximative schemes: In the manner of the Kubo-Manousakis method, we perform the adequate Bogoliubov transformation

$$\tilde{Q}_{\mathbf{q}} = Q_{\mathbf{q}} \cosh \tilde{\theta}_{\mathbf{q}} + R_{\mathbf{q}} \sinh \tilde{\theta}_{\mathbf{q}}, \quad \tilde{P}_{\mathbf{q}} = P_{\mathbf{q}} \cosh \tilde{\theta}_{\mathbf{q}} - S_{\mathbf{q}} \sinh \tilde{\theta}_{\mathbf{q}}, \quad (4.117)$$

$$\tilde{R}_{\mathbf{q}} = R_{\mathbf{q}} \cosh \tilde{\theta}_{\mathbf{q}} + Q_{\mathbf{q}} \sinh \tilde{\theta}_{\mathbf{q}}, \quad \tilde{S}_{\mathbf{q}} = S_{\mathbf{q}} \cosh \tilde{\theta}_{\mathbf{q}} - P_{\mathbf{q}} \sinh \tilde{\theta}_{\mathbf{q}}. \quad (4.118)$$

Due to the skilful choice of the signs, the new operator pairs $\{\tilde{Q}_{\mathbf{q}}, \tilde{P}_{\mathbf{q}}\}$ and $\{\tilde{R}_{\mathbf{q}}, \tilde{S}_{\mathbf{q}}\}$ represent two distinct sets of position and momentum operators with

$$\left[\tilde{Q}_{\mathbf{q}}, \tilde{P}_{\mathbf{q}} \right] = i, \quad \left[\tilde{R}_{\mathbf{q}}, \tilde{S}_{\mathbf{q}} \right] = i, \quad (4.119)$$

and all of the mixed commutators vanishing.

The additionally introduced parameters $\tilde{\theta}_{\mathbf{q}}$ are determined by the diagonalization condition, which reads

$$\tanh[2\tilde{\theta}_{\mathbf{q}}] = \gamma_{\mathbf{q}}. \quad (4.120)$$

With its use we yield the diagonalized final Hamiltonian

$$H_{\text{LSWA}}(h_{p'}) = H_{\text{LSWA}}^{\text{isotropic}} + h_{p'} p' S S_Q^{p'-2} \sum_{\mathbf{q}} \left[n_{\mathbf{q}}^1 - n_{\mathbf{q}}^2 \right], \quad (4.121)$$

with $H_{\text{LSWA}}^{\text{isotropic}}$ denoting the isotropic Hamiltonian (4.33). For large $S \gg 1$, as throughout this chapter, the result (4.121) by Anderson's method turns consistently into the result (4.115) gained by the Kubo-Manousakis scheme.

Both results, (4.115) and (4.121), clearly signify that small fields $h_{p'}$ have no effect on the ground state properties of the AFM. As long as the ground state is still represented by $\langle n_{\mathbf{q}}^{\alpha/\beta} \rangle_0 = 0$, respectively $\langle n_{\mathbf{q}}^{1/2} \rangle_0 = 0$, the fields are

obviously too weak to induce any changes. Consequently, the sublattice magnetization stays at its isotropic value (4.87).

This puzzling behaviour is explained by the emergence of singlets [94]: Due to their uniform shape, the odd-order fields strengthen the alignment on one sublattice, but weaken it on the other sublattice at the same time, which we schematically depicted in fig. 4.10 and 4.11.



Figure 4.10: Schematic depiction of the possible AFM ground state configurations



Figure 4.11: Possible ground state configurations of the AFM influenced by a small uniform magnetic field

At this, the direction of the alignment on a given sublattice remains unspecified, as we illustrated by the subfigures (a) and (b): The presence of singlets induces superpositions of the spin configurations and links thereby the sublattices. As a consequence, the field-induced additional alignments in (a) and (b) cancel each other. Therefore, we recover consistently that singlet formations prevent changes of the AFM ground state by small magnetic fields and their higher-order counterparts with odd p' .

We support this picture by considering the toy model

$$H = +J \mathbf{S}_1 \cdot \mathbf{S}_2 - h_1 (S_1^z + S_2^z) , \quad (4.122)$$

which consists of two $S = \frac{1}{2}$ -spins influenced by the magnetic field h_1 . To avoid a double-counting of J , we impose open boundary conditions. From the corresponding energy eigenvalues $E = +J \left[\frac{S_{\text{tot}}(S_{\text{tot}}+1)}{2} - \frac{3}{4} \right] - h_1 m_{S_{\text{tot}}}$, with $m_{S_{\text{tot}}} \in \{-1, 0, +1\}$, we can identify the unaffected singlet $\{S_{\text{tot}}=0, m_{S_{\text{tot}}}=0\}$ as the perpetuated ground state for fields $|h_1| < J$. Large fields $|h_1| > J$, whose absolute value surpasses the value of the coupling constant, on the other hand, establish the according triplet state as the new ground state and enforce thereby the ferromagnetic ordering along the preferred direction.

4.5.2 Staggered Magnetic Field

We can circumvent the foregoing cancellation effect by considering a staggered field $\tilde{h}_{p'}$, whose preferred alignment alters according to the sublattices:

$$- \tilde{h}_{p'} \sum_{i \in A} (S_i^z)^{p'} + \tilde{h}_{p'} \sum_{j \in B} (S_j^z)^{p'} \quad \text{with } p' \text{ odd.} \quad (4.123)$$

Therefore, the alignments on both of the sublattices are enhanced, and we circumvent the cancellation effect of the foregoing paragraph. Accordingly, we expect a resulting net effect on the magnetization.

In both LSWA schemes, we effectively find the same modification rule

$$\gamma_{\mathbf{q}} \rightarrow \frac{\gamma_{\mathbf{q}}}{1 + \tilde{h}_{p'} \frac{p' S^{p'-2}}{2dJ}} \quad \text{for } S \gg 1, \quad (4.124)$$

and get indeed a shifted magnetization:

$$M_{T=0}^{\text{sl}}(\tilde{h}_{p'}) = S + \frac{1}{2} - \frac{1}{N} \sum_{\mathbf{q}} \left[1 - \frac{\gamma_{\mathbf{q}}^2}{\left(1 + \tilde{h}_{p'} \frac{p' S^{p'-2}}{2dJ}\right)^2} \right]^{-1/2}. \quad (4.125)$$

4.5.3 Fields on a Single Sublattice

We may further illustrate that the distinct sublattices of the AFM are inextricably linked to each other by corresponding singlet formations: For this purpose, we study fields

$$- h'_p \sum_{i \in A} (S_i^z)^p, \quad (4.126)$$

which are solely defined on a single sublattice. For both p even and odd, we find in both approximation schemes the modification rule

$$\gamma_{\mathbf{q}} \rightarrow \frac{\gamma_{\mathbf{q}}}{1 + h'_p \frac{p S^{p-2}}{4dJ}} \quad \text{for } S \gg 1, \quad (4.127)$$

and get, thereby, the resulting sublattice magnetization

$$M_{T=0}^{\text{sl}}(h'_p) = S + \frac{1}{2} - \frac{1}{N} \sum_{\mathbf{q}} \left[1 - \frac{\gamma_{\mathbf{q}}^2}{\left(1 + h'_p \frac{p S^{p-2}}{4dJ}\right)^2} \right]^{-1/2}. \quad (4.128)$$

For odd p , we consequently find a net effect on the magnetization due to the perturbed symmetry between the two sublattices, which permits the cancellation effect of the second last paragraph.

For even p , on the other hand, we find a resultant magnetization shift, which is equally distributed on both sublattices and takes on half of its former value

compared to (4.88): $h_p \rightarrow \frac{h'_p}{2}$. For the complementary field $-h'_p \sum_{j \in B} (S_j^z)^p$, which is defined only on sublattice B , we recovered the identical outcome, which leads us to the following conclusion: Although this anisotropy field is defined only on one sublattice, the entire system develops a homogeneously distributed magnetization shift, which strongly underlines the singlet-caused intertwining of the sublattices.

4.6 Anisotropy Susceptibility

This section will contain further key results, which strengthen the main message of the second last section. Based on the results for the anisotropic sublattice magnetization, we aim to elucidate the drastic effects that arise with emerging anisotropy fields.

As illustrated in fig.4.5-4.8, we observe a rapid change of $M_{T=0}^{\text{sl}}$ that is induced by relatively small anisotropy fields. Now we quantify this sensitivity by representing the slope of this shifting. For this purpose, we introduce the corresponding derivative

$$\chi_{h_p} = \frac{\partial M_{T=0}^{\text{sl}}}{\partial h_p}, \quad (4.129)$$

which we want to refer to as anisotropy susceptibility.

We emphatically want to point out that the definition (4.129) exclusively incorporates quantum effects: The ferromagnetic, respectively classical counterpart is given by

$$\chi_{h_p}^{\text{classical}} = \frac{\partial M_{T=0}}{\partial h_p} = \frac{\partial S}{\partial h_p} = 0. \quad (4.130)$$

As a consequence, the anisotropy susceptibility describes explicitly the reduction of quantum fluctuations. Therefore, the quantity (4.129) is of uttermost importance for our investigations.

From the analytical point of view, we extract from (4.88), respectively (4.100), the dominant behaviour of χ_{h_p} for $h_p \ll 1$ and $|\mathbf{q}| \ll 1$ in d dimensions:

$$1d: \quad \chi_{h_p}^{1d} \sim 1/h_p, \quad (4.131)$$

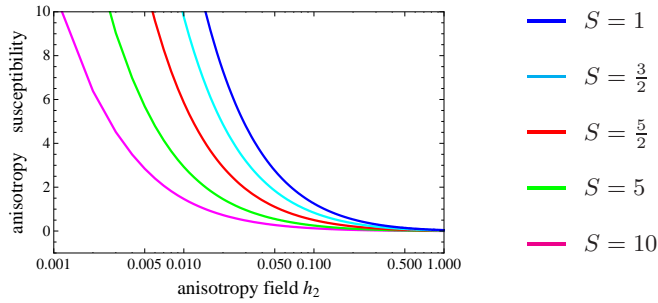
$$2d: \quad \chi_{h_p}^{2d} \sim 1/\sqrt{h_p}, \quad (4.132)$$

$$3d: \quad \chi_{h_p}^{3d} \sim -\ln(h_p). \quad (4.133)$$

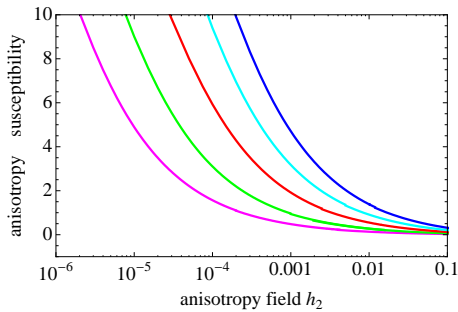
The numerically determined behaviour for the entire range of h_2 is shown in fig. 4.12. As before, we restrict the depiction to the case $p=2$ in order to keep the set of illustrations limited.

In the end, the divergence for $h_p \rightarrow 0$ in all of the dimensions impressively demonstrates the enormously strong suppression of quantum fluctuations by even tiny anisotropy fields.

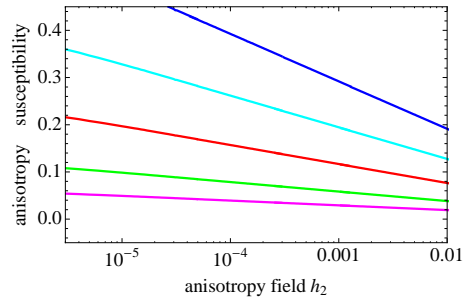
Therefore, we can strengthen our previous statement concerning the classical modelling of the Hamburg SP-STM experiments on spin systems under the influence of anisotropy fields [23]-[31]: The mere existence of finite anisotropy fields is accompanied by the intense reduction of quantum fluctuations, which drives the original quantum system rapidly towards a classical one. This finding, thereby, further confirms the validity of the classical description not only for large, but also for relatively small anisotropies.



(a) $d = 1$



(b) $d = 2$



(c) $d = 3$

Figure 4.12: Anisotropy susceptibility χ_{h_2} (4.129) in one, two and three dimensions for various spin quantum numbers S , scaled logarithmically.

4.7 Retrospect and Outlook

In this chapter we elucidated how the presence of anisotropy fields affects the sublattice magnetization of the AFM at $T=0$. For this purpose, we made use of the Linear Spin Wave Approximation (LSWA) in two different approaches: Despite the differing approximation techniques, all of the results obtained by these distinct methods turned out to be consistent in the LSWA regime. For a start, we presented in section 4.2 the LSWA treatments for isotropic Heisenberg systems in detail. Based on this detailed description, we could extend these procedures in section 4.3 to the inclusion of the vital anisotropy fields. The subsequent results for the ground state sublattice magnetization were presented in section 4.4. The exhibited graphical illustrations clearly underline the main message of this thesis: Besides the classical limits for $S \gg 1$ and $h_p \gg 1$, we could show the emergence of classical trends that are provided by the combined increase of h_p and S . The anisotropy susceptibility, introduced and discussed in section 4.6, supplemented this trend and revealed the extreme sensitivity of quantum fluctuations to the presence of relatively small and even tiny anisotropy fields: This conclusion generally confirms the classical modelling of recently published SP-STM experiments that were performed at the Department of Physics at the University of Hamburg [23]-[31].

The repeated comparison to FMs contrasted the completely aligned FM ground state with the typical quantum corrections in the AFM ground state, which reduce or even completely destroy its staggered long range order. Furthermore, the comparison to peculiar effects by special fields in section 4.5 revealed the characteristic singlet formations in the AFM as the source of the quantum fluctuations.

In the coming chapter we will confirm and refine these results with the use of the more sophisticated Random Phase Approximation (RPA).

At the close of this chapter, we want to discuss possible improvements and extensions: A straightforward extension of the presented LSWA treatment could deal with finite temperatures $T > 0$. The corresponding investigation would, nevertheless, demand a new comprehensive study taking into account the new parameter T for a widespread range combined with the emergence of thermal criticality, but could further reveal the combined influence of thermal and quantum fluctuations. Besides this extension of the parameter space, further general improvements of the exposed LSWA technique would be desirable, but would demand a completely new, more sophisticated setup: On the one hand, the wish arises to yield the S -dependent prefactors of the h_p -shift in order to clarify the relevance of higher-order anisotropies for general S . A more general treatment, on the other hand, could also include the easy-plane case $h_p < 0$, which would in turn require the calculation of all the expectation values $\langle S^\alpha \rangle$ with $\alpha \in \{x, y, z\}$.

Chapter 5

Random Phase Approximation

The Random Phase Approximation (RPA) represents an analytical theory that is a vital ingredient of this thesis: The RPA approach will act as the bridging theory that refers back to the Linear Spin Wave Approximation (LSWA) for large spin quantum numbers, but, at the same time, offers strong analytical predictions for the Quantum Monte Carlo (QMC) results presented in the next chapter. We will, on the one hand, deal with the improvement and comparison of the LSWA results for the sublattice magnetization at $T=0$ and, on the other hand, determine the critical temperatures of anisotropic systems, which we will use again in the chapter on QMC.

5.1 Overview

We refine our LSWA results and successfully refer to them by making use of the Random Phase Approximation (RPA) [99, 100], which is a powerful analytical Green's function (GF) technique. Based on the Tyablikov decoupling scheme [101, 102], the corresponding RPA treatment improves the LSWA results quantitatively.

Although we have to deal with certain shortcomings, the RPA theory offers distinguished advantages: In contrast to all of the other techniques used in this thesis, RPA enables us to calculate the ground state sublattice magnetization as well as the critical temperature. Furthermore, RPA acquires analytically the desired dimensional dependencies for critical temperatures and successfully complies with the Mermin-Wagner theorem [8].

There exist several related Green's function techniques, sometimes called RPA as well. These use different or extended decoupling schemes, for example the Anderson-Callen decoupling [100]. Especially the presence of anisotropy fields gave rise to new decoupling procedures [103, 104, 105] and still remains a challenging task. Although these ideas have been touched upon decades ago, recently published studies [53, 54, 55, 56, 57], based on RPA and related Green's function techniques, highlight their renewed interest. In order to keep our issues neatly arranged, we adopt the decoupling scheme that is as simple as possible [100, 106] and remains closely related to the original Tyablikov decoupling. Therefore, we refer throughout this thesis to RPA as Tyablikov decoupling pro-

cedures, for isotropic as well as for anisotropic systems.

As before in LSWA, we need to fix the order p of the anisotropy fields by $p \leq 2S$ right at the beginning.

5.2 Technical Preparations: Green's Functions and their Properties

In order to keep an overview on the technical issues, we start by outlining the Green's functions (GFs) and their properties we will use later on [107]. The essential ingredient to the RPA approach is the retarded GF

$$G_{ij}^{\text{ret}}(t, t') = G_{ij}^{\text{ret}}(t - t') = \langle\langle S_i^+(t); S_j^-(t') \rangle\rangle^{\text{ret}} \quad (5.1)$$

$$= -i \Theta(t - t') \langle [S_i^+(t), S_j^-(t')] \rangle. \quad (5.2)$$

We will particularly make use of its energy representation

$$G_{ij}^{\text{ret}}(E) = \langle\langle S_i^+; S_j^- \rangle\rangle_E^{\text{ret}} = \int_{-\infty}^{+\infty} d(t - t') G_{ij}^{\text{ret}}(t - t') \exp[iE(t - t')]. \quad (5.3)$$

The Heisenberg's equation of motion, rewritten in energy space, results in the equation of motion (EoM) for $G_{ij}^{\text{ret}}(E)$

$$E \cdot G_{ij}^{\text{ret}}(E) = \langle [S_i^+, S_j^-] \rangle + \langle\langle [S_i^+, H]; S_j^- \rangle\rangle_E^{\text{ret}}, \quad (5.4)$$

with H representing the corresponding Hamiltonian we wish to investigate.

We will further make use of the spectral representation of the retarded GF

$$G_{ij}^{\text{ret}}(E) = \int_{-\infty}^{+\infty} dE' \frac{S_{ij}(E')}{E - E' + i0^+}, \quad (5.5)$$

with $S_{ij}(E)$ denoting the spectral density and $+i0^+$ signifying the required boundary condition for the retarded version of the GF. Since we are dealing exclusively with retarded GFs, we may, for the sake of simplicity, omit this boundary condition in the following. Applying Dirac's identity

$$\frac{1}{x - x_0 + i0^+} = \mathcal{P} \left(\frac{1}{x - x_0} \right) - i\pi \delta(x - x_0), \quad (5.6)$$

with \mathcal{P} denoting the principal value, we can relate the spectral density to the singularities of the GF:

$$S_{ij}(E) = -\frac{1}{\pi} \text{Im} [G_{ij}^{\text{ret}}(E)]. \quad (5.7)$$

Finally, we will link the spectral density $S_{ij}(E)$ to the correlation function $\langle S_j^- S_i^+ \rangle$ via the spectral theorem for equal times:

$$\langle S_j^- S_i^+ \rangle = \int_{-\infty}^{+\infty} dE \frac{S_{ij}(E)}{\exp[\beta E] - 1} \quad \text{with } \beta = \frac{1}{T}. \quad (5.8)$$

For the sake of a simplified notation, we will omit in the following the sub- and superscripts ‘ret’ and ‘E’:

$$G_{ij} = G_{ij}^{\text{ret}}(E) = \langle\langle S_i^+; S_j^- \rangle\rangle_E^{\text{ret}} = \langle\langle S_i^+; S_j^- \rangle\rangle. \quad (5.9)$$

The coming section outlines the physical issues that require the use of these Green’s functions.

5.3 Isotropic Systems

To depict the basic approximation scheme, we will start by outlining the RPA method for isotropic systems [58, 107]. We first give a detailed description of the treatment for the ferromagnet [107] and subsequently implement the required extensions for the antiferromagnet [58].

5.3.1 Ferromagnet

To begin with, we outline the RPA technique in detail for the FM Hamiltonian

$$H = - \sum_{\langle ij \rangle} J_{ij} \mathbf{S}_i \cdot \mathbf{S}_j = - \sum_{\langle ij \rangle} J_{ij} \left[S_i^z S_j^z + \frac{1}{2} (S_i^+ S_j^- + S_i^- S_j^+) \right]. \quad (5.10)$$

We start with the easiest case of $S = 1/2$ and transfer the presented scheme to larger spin quantum numbers later on. To motivate the use of the GFs, we use the identity

$$S_i^- S_i^+ = S(S+1) - S_i^z - (S_i^z)^2, \quad (5.11)$$

which allows for $S = 1/2$ ($\rightarrow (S_i^z)^2 = 1/4 \forall i$) to express the magnetization by the expectation value $\langle S_i^- S_i^+ \rangle$:

$$M = \frac{1}{N} \sum_i \langle S_i^z \rangle = S - \frac{1}{N} \sum_i \langle S_i^- S_i^+ \rangle. \quad (5.12)$$

Since we are dealing with a homogeneous system, we can set

$$M = \langle S_i^z \rangle = S - \langle S_i^- S_i^+ \rangle \quad \forall i. \quad (5.13)$$

The GF comes now into play: The yet missing calculation of $\langle S_i^- S_i^+ \rangle$ is performed with the use of the spectral theorem (5.8), whose spectral density is linked via (5.5) and (5.7) to the two-spin GF

$$G_{ij} = \langle\langle S_i^+; S_j^- \rangle\rangle \quad (5.14)$$

we defined in (5.3) and (5.9).

Its EoM (5.4) reads for the isotropic Hamiltonian (5.10):

$$E \cdot G_{ij} = 2M \delta_{ij} + \sum_k J_{ki} \left[\langle\langle S_i^+ S_k^z; S_j^- \rangle\rangle - \langle\langle S_k^+ S_i^z; S_j^- \rangle\rangle \right], \quad (5.15)$$

with $J_{ki} = J$ for the lattice sites k being nearest neighbours of the sites i , and zero otherwise.

Sighting this EoM, we observe the well-known phenomenon of an induced hierarchy of higher-order GFs: The EoM for the two-spin GF contains the three-spin GFs $\langle\langle S_i^+ S_k^z; S_j^- \rangle\rangle$ and $\langle\langle S_k^+ S_i^z; S_j^- \rangle\rangle$. Their corresponding EoMs consequently contain four-spin GFs, and so on. Therefore, the need for a suitable approximation scheme arises, which interrupts the series of GFs of increasing orders. For this purpose, several interruption schemes have been developed (see e.g. [99, 100]). Among all these, we will adopt the Tyablikov decoupling [101, 102] representing the most direct interruption scheme: It reduces the three-spin GFs in (5.15) directly to two-spin GFs and keeps, therefore, the overall appearance of GFs limited to two-spin GFs. This reduction is achieved by the application of the Hartree-Fock decoupling

$$AB \rightarrow A\langle B \rangle + \langle A \rangle B - \langle A \rangle \langle B \rangle \quad \text{for the operators } A \text{ and } B, \quad (5.16)$$

which translates into

$$\begin{aligned} \langle\langle S_a^+ S_b^z; S_j^- \rangle\rangle &\rightarrow \langle S_a^+ \rangle \langle\langle S_b^z; S_j^- \rangle\rangle + \langle S_b^z \rangle \langle\langle S_a^+; S_j^- \rangle\rangle = M G_{aj} \quad (5.17) \\ &\forall \text{ pairwise different } a, b, \end{aligned}$$

due to $\langle S_i^\pm \rangle = 0 \quad \forall i$. The resulting EoM reads

$$[E - J_0 M] G_{ij} = 2M \delta_{ij} - M \sum_k J_{ki} G_{kj}, \quad (5.18)$$

$$\text{with } J_0 = \sum_k J_{ki} \quad \forall i. \quad (5.19)$$

Although (5.16) reminds us of the Mean Field approach used in chapter 2 and 3, there is an important difference to this GF technique named RPA: Whereas the former MF approximation operates on the level of the Hamiltonian, thereby consequently neglecting fluctuations in a very coarse manner, the latter RPA approach still takes into account the two-spin correlations and operates, therefore, on a higher and more precise level. This sophistication is the reason for the successful compliance of the RPA method with the Mermin-Wagner theorem [8, 58], which we will point out later on by investigating the dimensional dependence of the critical temperature.

In order to yield a unique index for the GFs involved in (5.18), we introduce the Fourier transformation

$$S_i^+ = \frac{1}{\sqrt{N}} \sum_{\mathbf{q}} S_{\mathbf{q}}^+ \exp[+i\mathbf{q}\mathbf{r}_i], \quad (5.20)$$

$$S_i^- = \frac{1}{\sqrt{N}} \sum_{\mathbf{q}} S_{\mathbf{q}}^- \exp[-i\mathbf{q}\mathbf{r}_i], \quad (5.21)$$

$$G_{ij} = \frac{1}{N} \sum_{\mathbf{q}} G_{\mathbf{q}} \exp[+i\mathbf{q}(\mathbf{r}_i - \mathbf{r}_j)], \quad (5.22)$$

and the coupling constant $J_{\mathbf{q}}$ in Fourier space:

$$J_{\mathbf{q}} = \frac{1}{N} \sum_{i,j} J_{ij} \exp[-i\mathbf{q}(\mathbf{r}_i - \mathbf{r}_j)] . \quad (5.23)$$

With the use of (5.22)-(5.23), we gain from (5.18) the solution for the GF

$$G_{\mathbf{q}} = \frac{2M}{E - E_{\mathbf{q}}} \quad \text{with} \quad E_{\mathbf{q}} = M[J_0 - J_{\mathbf{q}}] , \quad (5.24)$$

where we may add $+i0^+$ in the denominator to fulfill the boundary condition for retarded GFs. The application of (5.6)-(5.7) enables us to extract the spectral density in Fourier space:

$$S_{\mathbf{q}} = 2M \delta(E - E_{\mathbf{q}}) . \quad (5.25)$$

By inserting this Fourier transform of S_{ij} into the spectral theorem (5.8), we find for the required correlation function

$$\langle S_i^- S_i^+ \rangle = \frac{1}{N} \sum_{\mathbf{q}} \frac{2M}{\exp[\beta E_{\mathbf{q}}] - 1} \quad \forall i , \quad (5.26)$$

and yield, with (5.13), the final formula for the magnetization

$$M = S \left[1 + \frac{2}{N} \sum_{\mathbf{q}} \frac{1}{\exp[\beta E_{\mathbf{q}}] - 1} \right]^{-1} \quad \text{for} \quad S = \frac{1}{2} , \quad (5.27)$$

with $E_{\mathbf{q}}$ defined in (5.24). Since the excitation energies $E_{\mathbf{q}}$ contain themselves the magnetization M , the formula (5.27) represents a self-consistent equation for the determination of M .

At $T=0$ ($\beta \rightarrow \infty$), we obtain

$$M_{T=0} = \frac{1}{2} \quad \text{for} \quad S = \frac{1}{2} , \quad (5.28)$$

and conclude a completely saturated alignment for the FM ground state, as we found before with the use of the LSWA approach.

In order to determine the critical temperature T_C , we take a look at the limit

$$T \lesssim T_C \quad \text{resp.} \quad M \gtrsim 0 . \quad (5.29)$$

Therefore, the excitation energies $E_{\mathbf{q}} \sim M$ become themselves small quantities:

$$E_{\mathbf{q}} \ll 1 \quad \text{resp.} \quad \beta E_{\mathbf{q}} \approx \beta_C E_{\mathbf{q}} \ll 1 \quad \text{with} \quad \beta_C = \frac{1}{T_C} . \quad (5.30)$$

As a consequence, we can explicitly expose the dominant M -dependence for $M \gtrsim 0$ for $S = \frac{1}{2}$:

$$M \approx S \left[1 + \frac{2}{N} \sum_{\mathbf{q}} \frac{1}{\beta_C E_{\mathbf{q}}} \right]^{-1} \approx M \beta_C \left[\frac{4}{N} \sum_{\mathbf{q}} \frac{1}{J_0 - J_{\mathbf{q}}} \right]^{-1} . \quad (5.31)$$

At this point, it becomes apparent why we imposed the important limit condition (5.29) to start from an ordered phase at low temperatures: Due to $M \gtrsim 0$ we may cancel the magnetization M on both sides of the equation (5.31) and achieve the resulting critical temperature

$$T_C^{\text{RPA}} = \left[\frac{4}{N} \sum_{\mathbf{q}} \frac{1}{J_0 - J_{\mathbf{q}}} \right]^{-1} \quad \text{for } S = \frac{1}{2}. \quad (5.32)$$

We will discuss the consequences later on, after we have derived the final equations for the general case of arbitrary S .

In the following we present the basic idea how to extend these previous considerations to the case $S > \frac{1}{2}$. In particular, we have to deal for $S > \frac{1}{2}$ with all of the expectation values

$$\langle (S_i^z)^n \rangle \quad n = 1, \dots, 2S. \quad (5.33)$$

According to the reduction formula (1.10)

$$\prod_{m=-S}^{+S} (S_i^z - m) = 0 \quad \forall i, \quad (5.34)$$

$n = 2S$ represents the highest non-reducible power of the expectation values $\langle (S_i^z)^n \rangle$. All of the expectation values with higher orders $n > 2S$, on the contrary, can be reduced to orders $n \leq 2S$. Therefore, we could restrict our considerations in the case $S = \frac{1}{2}$ to $\langle S_i^z \rangle$.

In order to determine those remaining $2S$ expectation values (5.33), we rewrite (5.11) for $n = 0, \dots, 2S - 1$:

$$\langle (S_i^z)^n S_i^- S_i^+ \rangle = S(S+1) \langle (S_i^z)^n \rangle - \langle (S_i^z)^{n+1} \rangle - \langle (S_i^z)^{n+2} \rangle. \quad (5.35)$$

Sighting the structure of this set of equations with $n = 0, \dots, 2S - 1$, we find that (5.34) and (5.35) represent together $2S + 1$ equations for the determination of the $2S + 1$ expectation values $\langle (S_i^z)^n \rangle_{n=1, \dots, 2S+1}$ involved in (5.35).

Therefore, we yet need to calculate the $2S$ correlation functions in (5.35)

$$\langle (S_i^z)^n S_i^- S_i^+ \rangle \quad n = 0, \dots, 2S - 1. \quad (5.36)$$

Now the GFs come into play: In order to determine these correlations functions, we introduce the set of GFs

$$G_{ij}^{(n)} = \left\langle \left\langle S_i^+; (S_j^z)^n S_j^- \right\rangle \right\rangle_E^{\text{ret}} \quad n = 0, \dots, 2S - 1. \quad (5.37)$$

Their $2S$ EoMs for the isotropic FM Hamiltonian (5.10),

$$E \cdot G_{ij}^{(n)} = \left\langle \left[S_i^+, (S_j^z)^n S_j^- \right] \right\rangle + \left\langle \left\langle [S_i^+, H]; (S_j^z)^n S_j^- \right\rangle \right\rangle_E^{\text{ret}}, \quad (5.38)$$

read explicitly

$$E \cdot G_{ij}^{(n)} = \sum_k J_{ki} \left[\left\langle \left\langle S_i^+ S_k^z ; (S_j^z)^n S_j^- \right\rangle \right\rangle - \left\langle \left\langle S_k^+ S_i^z ; (S_j^z)^n S_j^- \right\rangle \right\rangle \right] + \left\langle [S_i^+, (S_j^z)^n S_j^-] \right\rangle \quad \text{with } n = 0, \dots, 2S - 1. \quad (5.39)$$

Performing the Tyablikov decoupling via (5.16),

$$\left\langle \left\langle S_i^+ S_k^z ; (S_j^z)^n S_j^- \right\rangle \right\rangle \rightarrow M G_{ij}^{(n)}, \quad \left\langle \left\langle S_k^+ S_i^z ; (S_j^z)^n S_j^- \right\rangle \right\rangle \rightarrow M G_{kj}^{(n)}, \quad (5.40)$$

yields the $2S$ EoMs on the RPA level

$$[E - J_0 M] G_{ij}^{(n)} = \left\langle [S_i^+, (S_j^z)^n S_j^-] \right\rangle - M \sum_k J_{ki} G_{kj}^{(n)}, \quad (5.41)$$

whose corresponding solutions in Fourier space read

$$G_{\mathbf{q}}^{(n)} = \frac{\Sigma^{(n)}}{E - E_{\mathbf{q}} + i0^+} \quad n = 0, \dots, 2S - 1, \quad (5.42)$$

with $E_{\mathbf{q}}$ defined before in (5.24) and the inhomogeneities

$$\Sigma^{(n)} = \left\langle [S^+, (S^z)^n S^-] \right\rangle = \left\langle [S_i^+, (S_i^z)^n S_i^-] \right\rangle \quad \forall i. \quad (5.43)$$

For $n = 0$ we consistently recover (5.24) with $\Sigma^{(0)} = 2\langle S^z \rangle = 2M$.

Compared to the $S = \frac{1}{2}$ -result (5.24), we observe that only the inhomogeneity has changed and that the basic functional structure remains unaltered. Due to this preserved structure, we can adopt our previous strategy: From (5.42)-(5.43), we extract the according spectral densities

$$S_{\mathbf{q}}^{(n)} = \Sigma^{(n)} \delta(E - E_{\mathbf{q}}), \quad (5.44)$$

and find with the use of the corresponding spectral theorem:

$$\left\langle (S_i^z)^n S_i^- S_i^+ \right\rangle = \left\langle [S_i^+, (S_i^z)^n S_i^-] \right\rangle \cdot \Phi \quad (5.45)$$

$$\text{with } \Phi = \frac{1}{N} \sum_{\mathbf{q}} \frac{1}{\exp[\beta E_{\mathbf{q}}] - 1}. \quad (5.46)$$

At that, the case $n = 0$ is consistently linked to (5.26).

The combination of (5.34)-(5.35) and (5.45)-(5.46), with known $E_{\mathbf{q}}$ (5.24), allows now to determine all the expectation values $\langle (S_i^z)^n \rangle_{n=1, \dots, 2S+1}$, and especially the magnetization $M = \langle S_i^z \rangle \forall i$. The corresponding final expression for the magnetization for general S has been skilfully derived by Callen [99]:

$$M = \frac{(S - \Phi)(1 + \Phi)^{2S+1} + (1 + S + \Phi)\Phi^{2S+1}}{(1 + \Phi)^{2S+1} - \Phi^{2S+1}}. \quad (5.47)$$

By rewriting (5.46), with the use of (5.7), as

$$\Phi = -\frac{1}{2\pi M} \int_{-\infty}^{+\infty} dE \frac{\text{Im}[G]}{\exp[\beta E] - 1}, \quad (5.48)$$

$$\text{with } \text{Im}[G] = \text{Im}[G_{ii}] \quad \forall i \quad \text{and} \quad G_{ii} = G_{ii}^{(0)} = G_{ii}^{\text{ret}}(E),$$

we can relate the calculation of the magnetization (5.47) directly to the GF $G_{ij} = \langle\langle S_i^+; S_j^- \rangle\rangle$, which we used right at the beginning of this section. Therefore, we can simplify our further calculations by restricting our considerations to the $n = 0$ - GF, whose index we may omit again in the following.

In the remaining part of this section, we will discuss the results for the ground state magnetization $M_{T=0}(S)$ and for the critical temperature $T_C(S)$ for general spin quantum numbers S .

At $T = 0$, we find, due to $\Phi \xrightarrow{T \rightarrow 0} 0$, from (5.47) the ground state magnetization

$$M_{T=0}(S) = S \quad \text{for general } S, \quad (5.49)$$

which is completely saturated and coincides with the maximal classical value. This finding fully concords with the corresponding LSWA result (4.103).

In order to determine the critical temperature for general S , we consider again the limits (5.29)-(5.30) and find as a consequence

$$\Phi \approx \frac{1}{N} \sum_{\mathbf{q}} \frac{1}{\beta_C E_{\mathbf{q}}} = \frac{1}{N} \sum_{\mathbf{q}} \frac{1}{\beta_C M [J_0 - J_{\mathbf{q}}]} \gg 1. \quad (5.50)$$

Expanding the Callen equation (5.47) in powers of $\frac{1}{\Phi} \ll 1$, the expression for the magnetization reduces in the critical region to

$$M = \frac{S(S+1)}{3} \frac{1}{\Phi} + \mathcal{O}\left[\frac{1}{\Phi^2}\right]. \quad (5.51)$$

Combining (5.50) and (5.51), we yield the final expression for the critical temperature of the isotropic FM

$$T_C^{\text{RPA}} = \frac{S(S+1)}{3} \left[\frac{1}{N} \sum_{\mathbf{q}} \frac{1}{J_0 - J_{\mathbf{q}}} \right]^{-1} \quad \text{for general } S. \quad (5.52)$$

For $S = \frac{1}{2}$ we consistently recover (5.32).

Rewriting the Fourier transformed couplings (5.19) and (5.23) as

$$J_0 = zJ, \quad J_{\mathbf{q}} = zJ \gamma_{\mathbf{q}}, \quad (5.53)$$

$$\text{with } J = \begin{cases} J_{ij} & \forall i, j \text{ being nearest neighbours,} \\ 0 & \text{otherwise,} \end{cases} \quad (5.54)$$

$$\text{using } \gamma_{\mathbf{q}} = \frac{1}{d} \sum_{i=1}^d \cos(q_i), \quad (5.55)$$

as defined before in (4.14), we gain the explicit expression

$$T_C^{\text{RPA}} = S(S+1) \frac{zJ}{3} \left[\frac{1}{N} \sum_{\mathbf{q}} \frac{1}{1-\gamma_{\mathbf{q}}} \right]^{-1} \quad (5.56)$$

for simple lattices (simple cubic, square lattice and chain).

Beholding (5.56), we recognize that the last factor contains all the improvements of the RPA approach compared to the MF results

$$T_C^{\text{CMF}} = \frac{zJ}{3} S^2 \quad \text{for classical spins of length } S, \quad (5.57)$$

$$T_C^{\text{QMF}} = S(S+1) \frac{zJ}{3} \quad \text{for quantum spins,} \quad (5.58)$$

found in chapter 2 and 3.

By studying the dimensional dependency of the critical temperature T_C^{RPA} (5.56), we successfully recover the Mermin-Wagner theorem [8]: Taking into account the thermodynamical limit, we replace the sums involved in (5.56) by the integrals

$$\frac{1}{N} \sum_{\mathbf{q}} \dots \rightarrow \frac{1}{(2\pi)^d} \left(\prod_{i=1}^d \int_{-\pi}^{+\pi} dq_i \right) \dots \quad (5.59)$$

At the critical point we make further use of the long-wavelength approximation and find the following behaviour for $q = |\mathbf{q}| \ll 1$:

$$\frac{1}{T_C} \sim \int d^d q \frac{1}{q^2} \sim \int dq q^{d-3}. \quad (5.60)$$

This well-known integral diverges for all dimensions $d \leq 2$, but converges for dimensions $d > 2$. Therefore, we conclude for the critical temperatures:

$$T_C^{\text{RPA}} = 0 \quad \text{in } d \leq 2, \quad T_C^{\text{RPA}} > 0 \quad \text{in } d > 2. \quad (5.61)$$

This compliance with the Mermin-Wagner theorem represents an impressive feature of the analytical RPA method.

In three dimensions we explicitly obtain

$$T_C^{3d} = 2JS(S+1) \left[\frac{1}{(2\pi)^3} \iiint_{-\pi}^{+\pi} \frac{dq_x dq_y dq_z}{1 - \frac{1}{3}(\cos q_x + \cos q_y + \cos q_z)} \right]^{-1}, \quad (5.62)$$

with the resulting numerical value

$$T_C^{3d} \approx 1.319 JS(S+1). \quad (5.63)$$

Compared to high-precision QMC simulations and sophisticated high-temperature expansions [108], the value of (5.63) lies between the corresponding values for $S = \frac{1}{2}$ and $S \rightarrow \infty$ and represents therefore quite a good estimate. We will

pick up again the detailed S -dependence of T_C later on in the next chapter. At this, as we can read from (5.62)-(5.63), we yet have to state that T_C^{RPA} contains only a trivial S -dependence $\sim S(S+1)$. Nevertheless, RPA represents a cogent theory that extends the concepts of MF and LSWA and improves the results on the analytical level.

At the close of this derivation for the FM, we add a note on the denotation of RPA: Throughout this thesis, we will use the Tyablikov decoupling [101, 102] and refer to it as the RPA technique. Nevertheless, there exist more sophisticated techniques, which are sometimes called RPA as well; one famous example is the Anderson-Callen decoupling scheme [99, 100]: This scheme contains additional correction terms, but turns out to yield in the end worse results than the original Tyablikov method for small spin quantum numbers S despite the additional effort, as reviewed by Ecker et al. [109] and commented by Callen himself in his original article [99].

5.3.2 Antiferromagnet

In this paragraph, we will outline the appropriately modified RPA procedure for the isotropic AFM Hamiltonian

$$H = + \sum_{\langle nm \rangle} J_{n,m} \mathbf{S}_n \cdot \mathbf{S}_m . \quad (5.64)$$

The underlying lattice can be divided into two sublattices A and B with $n \in A$ and $m \in B$, according to the emergence of the staggered magnetization with alternately reversed spin directions in the low-temperature region. Due to this bipartite lattice structure, four different Green's functions G_{n,n_0}^{AA} , G_{m,n_0}^{BA} , G_{n,m_0}^{AB} , G_{m,m_0}^{BB} appear, with $\{n, n_0\} \in A$ and $\{m, m_0\} \in B$ and the upper indices denoting the respective sublattices. It will be sufficient to focus on the set of the two Green's functions $\{G_{n,n_0}^{AA}, G_{m,n_0}^{BA}\}$, since the other set $\{G_{n,m_0}^{AB}, G_{m,m_0}^{BB}\}$ yields identical results.

The EoMs for G_{n,n_0}^{AA} and G_{m,n_0}^{BA} read

$$E \cdot G_{n,n_0}^{AA} = \langle [S_n^+, S_{n_0}^-] \rangle + \langle \langle [S_n^+, H]; S_{n_0}^- \rangle \rangle \quad (5.65)$$

$$= 2 \delta_{n,n_0} \langle S_{n_0}^z \rangle + \sum_{m \in B} J_{n,m} \left[\langle \langle S_n^z S_m^+; S_{n_0}^- \rangle \rangle - \langle \langle S_n^+ S_m^z; S_{n_0}^- \rangle \rangle \right], \quad (5.66)$$

$$E \cdot G_{m,n_0}^{BA} = \langle [S_m^+, S_{n_0}^-] \rangle + \langle \langle [S_m^+, H]; S_{n_0}^- \rangle \rangle \quad (5.67)$$

$$= \sum_{n \in A} J_{n,m} \left[\langle \langle S_m^z S_n^+; S_{n_0}^- \rangle \rangle - \langle \langle S_m^+ S_n^z; S_{n_0}^- \rangle \rangle \right]. \quad (5.68)$$

Taking into account the sublattice structure of the AFM, we can directly identify the sublattice magnetization (4.79):

$$M^{\text{sl}} = \begin{cases} + \langle S_n^z \rangle & \forall n \in A, \\ - \langle S_m^z \rangle & \forall m \in B. \end{cases} \quad (5.69)$$

The Tyablikov decoupling

$$\langle\langle S_n^z S_m^+; S_{n_0}^- \rangle\rangle \rightarrow M^{\text{sl}} G_{m,n_0}^{BA}, \quad \langle\langle S_n^+ S_m^z; S_{n_0}^- \rangle\rangle \rightarrow -M^{\text{sl}} G_{n,n_0}^{AA}, \quad (5.70)$$

$$\langle\langle S_m^+ S_n^z; S_{n_0}^- \rangle\rangle \rightarrow M^{\text{sl}} G_{m,n_0}^{BA}, \quad \langle\langle S_m^z S_n^+; S_{n_0}^- \rangle\rangle \rightarrow -M^{\text{sl}} G_{n,n_0}^{AA}, \quad (5.71)$$

removes the appearance of higher-order Green's functions and leaves two coupled equations of motion for G_{n,n_0}^{AA} and G_{m,n_0}^{BA} . The resulting EoMs on the RPA level read

$$\left[E - J_0 M^{\text{sl}} \right] G_{n,n_0}^{AA} = 2 M^{\text{sl}} \delta_{n,n_0} + M^{\text{sl}} \sum_{m \in B} J_{m,n} G_{m,n_0}^{BA}, \quad (5.72)$$

$$\left[E + J_0 M^{\text{sl}} \right] G_{m,n_0}^{BA} = -M^{\text{sl}} \sum_{n \in A} J_{m,n} G_{n,n_0}^{AA}. \quad (5.73)$$

Performing the Fourier transformations,

$$G_{n,n_0}^{AA} = \frac{2}{N} \sum_{\mathbf{q}} G_{\mathbf{q}}^{AA} \exp[+i\mathbf{q}(\mathbf{r}_n - \mathbf{r}_{n_0})], \quad (5.74)$$

$$G_{m,n_0}^{BA} = \frac{2}{N} \sum_{\mathbf{q}} G_{\mathbf{q}}^{BA} \exp[+i\mathbf{q}(\mathbf{r}_m - \mathbf{r}_{n_0})], \quad (5.75)$$

$$\text{and } J_{\mathbf{q}} = \frac{2}{N} \sum_{n,m} J_{n,m} \exp[-i\mathbf{q}(\mathbf{r}_n - \mathbf{r}_m)], \quad (5.76)$$

with $\sum_{\mathbf{q}} = \frac{N}{2}$ due to the sublattice structure, enables us to decouple the EoMs (5.72)-(5.73) according to [58]:

$$G_{\mathbf{q}}^{AA} = \frac{M^{\text{sl}}}{2\varepsilon_{\mathbf{q}}} \left[\frac{2\varepsilon_{\mathbf{q}} + \varepsilon_{\mathbf{q}}^- + \varepsilon_{\mathbf{q}}^+}{E - \varepsilon_{\mathbf{q}}} + \frac{2\varepsilon_{\mathbf{q}} - \varepsilon_{\mathbf{q}}^- - \varepsilon_{\mathbf{q}}^+}{E + \varepsilon_{\mathbf{q}}} \right], \quad (5.77)$$

$$G_{\mathbf{q}}^{BA} = -\frac{J_{\mathbf{q}} (M^{\text{sl}})^2}{\varepsilon_{\mathbf{q}}} \left[\frac{1}{E - \varepsilon_{\mathbf{q}}} - \frac{1}{E + \varepsilon_{\mathbf{q}}} \right], \quad (5.78)$$

$$\text{with } \varepsilon_{\mathbf{q}}^- = M^{\text{sl}} [J_0 - J_{\mathbf{q}}] \stackrel{(5.53)}{=} 2dJM^{\text{sl}} [1 - \gamma_{\mathbf{q}}], \quad (5.79)$$

$$\varepsilon_{\mathbf{q}}^+ = M^{\text{sl}} [J_0 + J_{\mathbf{q}}] \stackrel{(5.53)}{=} 2dJM^{\text{sl}} [1 + \gamma_{\mathbf{q}}], \quad (5.80)$$

$$\varepsilon_{\mathbf{q}}^2 = \varepsilon_{\mathbf{q}}^- \varepsilon_{\mathbf{q}}^+, \quad (5.81)$$

and $\gamma_{\mathbf{q}}$ defined in (4.14). Please note that Yablonskiy [58] presented a wrong sign in the equation corresponding to (5.78), which can be ruled out in a straightforward way.

Besides the alternating character of the staggered magnetization, we are dealing with a clean and homogeneous system as suggested by (5.69). Therefore, we may focus our following considerations on the sublattice A and the GF $G_{\mathbf{q}}^{AA}$

(we additionally checked the calculation on sublattice B and found the identical outcome). With the use of the corresponding spectral density

$$S_{\mathbf{q}}^{AA} = -\frac{1}{\pi} \text{Im} [G_{\mathbf{q}}^{AA}] \quad (5.82)$$

$$= \frac{M^{\text{sl}}}{2\varepsilon_{\mathbf{q}}} \left[(2\varepsilon_{\mathbf{q}} + \varepsilon_{\mathbf{q}}^- + \varepsilon_{\mathbf{q}}^+) \delta(E - \varepsilon_{\mathbf{q}}) + (2\varepsilon_{\mathbf{q}} - \varepsilon_{\mathbf{q}}^- - \varepsilon_{\mathbf{q}}^+) \delta(E + \varepsilon_{\mathbf{q}}) \right], \quad (5.83)$$

we can rewrite the spectral theorem

$$\langle S_{n_0}^- S_{n_0}^+ \rangle = \int_{-\infty}^{+\infty} dE \frac{S_{n_0, n_0}^{AA}}{\exp[\beta E] - 1} = 2 M^{\text{sl}} \Phi^{\text{AFM}} \quad \forall n_0 \quad (5.84)$$

with the use of

$$\Phi^{\text{AFM}} = -\frac{1}{2\pi M^{\text{sl}}} \int_{-\infty}^{+\infty} dE \frac{\text{Im} [G_{n_0, n_0}^{AA}]}{\exp[\beta E] - 1} \quad \forall n_0 \quad (5.85)$$

$$= \frac{1}{N} \sum_{\mathbf{q}} \left[\frac{\varepsilon_{\mathbf{q}}^- + \varepsilon_{\mathbf{q}}^+}{2\varepsilon_{\mathbf{q}}} \coth \left[\frac{\beta \varepsilon_{\mathbf{q}}}{2} \right] - 1 \right]. \quad (5.86)$$

For $S = \frac{1}{2}$, we can extract the resulting sublattice magnetization M^{sl} via $\langle S_{n_0}^- S_{n_0}^+ \rangle = S - M^{\text{sl}}$. The extension to larger spin quantum numbers $S > \frac{1}{2}$ is achieved in a similar way as for the FM by considering expectation values of the kind $\langle (S_{n_0}^z)^l S_{n_0}^- S_{n_0}^+ \rangle$ with $l = 0, \dots, 2S - 1$: In the end, we yield the AFM Callen equation for general spin quantum numbers S [58, 99]

$$M^{\text{sl}} = \frac{(S - \Phi^{\text{AFM}})(1 + \Phi^{\text{AFM}})^{2S+1} + (1 + S + \Phi^{\text{AFM}})(\Phi^{\text{AFM}})^{2S+1}}{(1 + \Phi^{\text{AFM}})^{2S+1} - (\Phi^{\text{AFM}})^{2S+1}}, \quad (5.87)$$

with Φ^{AFM} defined above by (5.85) and (5.86).

In (5.87) we have chosen the original representation according to Callen [99], which is more asthetical and practical than Yablonskiy's renewed version [58]: The quantity Φ^{AFM} can be directly related to the quantum corrections as we will point out later.

In order to determine the critical temperature of the isotropic AFM, we take a look at the limits

$$T \lesssim T_C^{\text{AFM}} \quad \text{resp.} \quad M^{\text{sl}} \gtrsim 0, \quad (5.88)$$

and can consequently reduce (5.86), with the use of (5.79)-(5.81), to

$$\Phi^{\text{AFM}} \approx \frac{T_C^{\text{AFM}}}{N} \sum_{\mathbf{q}} \frac{\varepsilon_{\mathbf{q}}^- + \varepsilon_{\mathbf{q}}^+}{\varepsilon_{\mathbf{q}}^2} = \frac{T_C^{\text{AFM}}}{dJM^{\text{sl}}} \frac{1}{N} \sum_{\mathbf{q}} \frac{1}{1 - \gamma_{\mathbf{q}}^2} \gg 1. \quad (5.89)$$

Due to the condition $\Phi^{\text{AFM}} \gg 1$, we can approximate the AFM Callen equation (5.87) itself by

$$M^{\text{sl}} \approx \frac{S(S+1)}{3} \frac{1}{\Phi^{\text{AFM}}}, \quad (5.90)$$

and obtain by combining (5.89) and (5.90)

$$T_C^{\text{AFM}} = \frac{zJ}{6} S(S+1) \left[\frac{1}{N} \sum_{\mathbf{q}} \frac{1}{1-\gamma_{\mathbf{q}}^2} \right]^{-1}. \quad (5.91)$$

In order to compare (5.91) with the critical temperature of the FM (5.56), we have to bear in mind that the sum $\sum_{\mathbf{q}}$ of the AFM runs over the magnetic Brillouin zone, which represents half of the original Brillouin zone, whereas the sum $\sum'_{\mathbf{q}}$ of the FM runs over the crystallographic Brillouin zone coincident with the original full Brillouin zone. With the use of the identity [58]

$$2 \cdot \sum_{\mathbf{q}} \frac{1}{1-\gamma_{\mathbf{q}}^2} = \sum'_{\mathbf{q}} \frac{1}{1-\gamma_{\mathbf{q}}}, \quad (5.92)$$

the critical temperature of the AFM turns out to be identical with that of the FM. By replacing the sums in (5.91) by integrals in the thermodynamical limit,

$$\frac{1}{N} \sum_{\mathbf{q}} \dots \longrightarrow \frac{1}{2} \frac{1}{(2\pi)^d} \left(\prod_{i=1}^d \int_{-\pi}^{+\pi} dq_i \right) \dots, \quad (5.93)$$

we consistently find vanishing critical temperatures in one and two dimensions, and the numerical value in three dimensions

$$T_C^{\text{AFM}} \approx 1.319 J S(S+1) \stackrel{(5.63)}{=} T_C^{\text{FM}} \quad (5.94)$$

on a simple cubic lattice with $z = 2d = 6$.

Therefore, we cannot distinguish FMs and AFMs by looking at the critical temperatures on the RPA level.

Nonetheless, the ground state sublattice magnetization of the AFM is still influenced by quantum fluctuations. The resulting quantum corrections are, thereby, directly related to $\Phi_{T=0}^{\text{AFM}} > 0$: Whereas $\Phi_{T=0} = 0$ leads to $M_{T=0} = S$ in the FM case, the emergence of a finite $\Phi_{T=0}^{\text{AFM}} > 0$ gives rise to a deviation from the maximal classical value S , which subsequently reduces the sublattice magnetization $M_{T=0}^{\text{sl}}$. From the explicit expressions

$$\Phi_{T=0}^{\text{AFM}} = \frac{1}{N} \sum_{\mathbf{q}} \left[\frac{\varepsilon_{\mathbf{q}}^- + \varepsilon_{\mathbf{q}}^+}{2\varepsilon_{\mathbf{q}}} - 1 \right] = \frac{1}{N} \sum_{\mathbf{q}} \left[\frac{1}{\sqrt{1-\gamma_{\mathbf{q}}^2}} - 1 \right] \quad (5.95)$$

$$= \frac{1}{2(2\pi)^d} \left(\prod_{i=1}^d \int_{-\pi}^{+\pi} dq_i \right) \left[\frac{1}{\sqrt{1 - \frac{4}{z^2} (\sum_{i=1}^d \cos q_i)^2}} - 1 \right], \quad (5.96)$$

we obtain the numerical values

$$d = 1 : \quad \Phi_{T=0}^{\text{AFM}} \rightarrow \infty , \quad (5.97)$$

$$d = 2 : \quad \Phi_{T=0}^{\text{AFM}} \approx 0.197 , \quad (5.98)$$

$$d = 3 : \quad \Phi_{T=0}^{\text{AFM}} \approx 0.078 . \quad (5.99)$$

At this, the RPA technique can successfully repair the incorrect LSWA behaviour in one dimension (4.109), which led to $M_{T=0}^{\text{sl}} \rightarrow -\infty$ and had to be reinterpreted as a vanishing sublattice magnetization: The combination of (5.90) and (5.97) yields directly $M_{T=0}^{\text{sl}} = 0$.

In two and three dimensions, we get, as an example, for $S = \frac{1}{2}$

$$d = 2 : \quad M^{\text{sl}} \approx 0.359 , \quad (5.100)$$

$$d = 3 : \quad M^{\text{sl}} \approx 0.432 . \quad (5.101)$$

Please note that Yablonskiy's article [58] contains a rounding error in the last digit in the equation corresponding to (5.100). A more detailed graphical overview for various S will be given in section 5.5.2.

At this point, we can refer back to our LSWA results in chapter 4: For large spin quantum numbers $S \gg 1$, we can approximate the AFM Callen equation (5.87) by $M^{\text{sl}} = S - \Phi^{\text{AFM}}$ and, thus, reduce the equation for the sublattice magnetization to the simpler formula

$$M_{T=0}^{\text{sl}} = S - \frac{1}{N} \sum_{\mathbf{q}} \left[\frac{1}{\sqrt{1 - \gamma_{\mathbf{q}}^2}} - 1 \right] , \quad (5.102)$$

which is consistent with the according LSWA result (4.87).

In two and three dimensions, we get from (5.102) the explicit quantum corrections for $S \gg 1$

$$d = 2 : \quad M^{\text{sl}} \approx S - 0.197 , \quad (5.103)$$

$$d = 3 : \quad M^{\text{sl}} \approx S - 0.078 , \quad (5.104)$$

which concord with the LSWA values given in [59, 91]. In this additional approximation for large spin quantum numbers, we can directly identify $\Phi_{T=0}^{\text{AFM}}$ as the corresponding (LSWA) quantum correction.

5.4 Consequences for Magnetic Fields

Before we investigate the consequences of anisotropy fields, we start with the study of magnetic fields ($p = 1$), which highlight the characteristic differences between FMs and AFMs.

5.4.1 Ferromagnet

We consider a magnetic field h_1 of the kind

$$H = - \sum_{\langle ij \rangle} J_{ij} \mathbf{S}_i \cdot \mathbf{S}_j - h_1 \sum_i S_i^z. \quad (5.105)$$

We will follow the established RPA strategy and highlight the changes that are induced by the presence of h_1 . The EoM includes, as a consequence, an additional term $\sim h_1 G_{ij}$,

$$E \cdot G_{ij} = 2M \delta_{ij} + h_1 G_{ij} + \sum_k J_{ki} \left[\langle \langle S_i^+ S_k^z; S_j^- \rangle \rangle - \langle \langle S_k^+ S_i^z; S_j^- \rangle \rangle \right], \quad (5.106)$$

and reads after the Tyablikov decoupling (5.17):

$$[E - h_1 - J_0 M] G_{ij} = 2M \delta_{ij} - M \sum_k J_{ki} G_{kj}. \quad (5.107)$$

The functional structure (5.24) of the GF in Fourier space remains unaltered

$$G_{\mathbf{q}} = \frac{2M}{E - E_{\mathbf{q}}}, \quad (5.108)$$

but the involved excitation energies $E_{\mathbf{q}}$ are shifted by h_1 :

$$E_{\mathbf{q}} = h_1 + M[J_0 - J_{\mathbf{q}}]. \quad (5.109)$$

Due to the preserved algebraic structure of (5.108), we can adopt all of the previous general equations for the spectral density, magnetization, etc., as long as we bear in mind to insert the excitation energies (5.109).

As a result, the ground state magnetization remains fully aligned, $M_{T=0} = S$, for $h_1 > 0$, respectively $M_{T=0} = -S$ for corresponding negative h_1 by preferring the opposite alignment.

5.4.2 Antiferromagnet

For the AFM, we may study uniform as well as staggered magnetic fields: Their different resulting effects will underline the singlet character of the AFM quantum fluctuations and confirm the corresponding outcome found previously (section 4.5) with the use of the LSWA approach.

The uniform magnetic field h_1 prefers the same spin orientation on both sublattices:

$$H = + \sum_{\langle nm \rangle} J_{n,m} \mathbf{S}_n \cdot \mathbf{S}_m - h_1 \left[\sum_{n \in A} S_n^z + \sum_{m \in B} S_m^z \right] \quad (5.110)$$

The corresponding EoMs on the RPA level read

$$\left[E - h_1 - J_0 M^{\text{sl}} \right] G_{n,n_0}^{AA} = 2 M^{\text{sl}} \delta_{n,n_0} + M^{\text{sl}} \sum_{m \in B} J_{m,n} G_{m,n_0}^{BA} , \quad (5.111)$$

$$\left[E - h_1 + J_0 M^{\text{sl}} \right] G_{m,n_0}^{BA} = - M^{\text{sl}} \sum_{n \in A} J_{m,n} G_{n,n_0}^{AA} . \quad (5.112)$$

As a consequence, the poles of the GFs (5.77) and (5.78) are shifted by h_1 ,

$$G_{\mathbf{q}}^{AA} = \frac{M^{\text{sl}}}{2\varepsilon_{\mathbf{q}}} \left[\frac{2\varepsilon_{\mathbf{q}} + \varepsilon_{\mathbf{q}}^- + \varepsilon_{\mathbf{q}}^+}{E - h_1 - \varepsilon_{\mathbf{q}}} + \frac{2\varepsilon_{\mathbf{q}} - \varepsilon_{\mathbf{q}}^- - \varepsilon_{\mathbf{q}}^+}{E - h_1 + \varepsilon_{\mathbf{q}}} \right] , \quad (5.113)$$

$$G_{\mathbf{q}}^{BA} = - \frac{J_{\mathbf{q}} (M^{\text{sl}})^2}{\varepsilon_{\mathbf{q}}} \left[\frac{1}{E - h_1 - \varepsilon_{\mathbf{q}}} - \frac{1}{E - h_1 + \varepsilon_{\mathbf{q}}} \right] , \quad (5.114)$$

whereas the definitions (5.79)-(5.81) of $\varepsilon_{\mathbf{q}}^-$, $\varepsilon_{\mathbf{q}}^+$ and $\varepsilon_{\mathbf{q}}$ remain unmodified.

In order to investigate the effect of the uniform field h_1 , we make use of the spectral theorem (5.84) and extract $\Phi_{T=0}^{\text{AFM}}$: For $T \rightarrow 0$ ($\beta \rightarrow \infty$), we recover for $h_1 \ll 1$ the isotropic result

$$\Phi_{T=0}^{\text{AFM}} = \frac{1}{N} \sum_{\mathbf{q}} \left[\frac{1}{\sqrt{1 - \gamma_{\mathbf{q}}^2}} - 1 \right] . \quad (5.115)$$

Therefore, no change of the ground state sublattice magnetization $M_{T=0}^{\text{sl}}$ is induced by the presence of a small uniform magnetic field h_1 , as we could explain in paragraph 4.5.1 by taking into account the underlying singlet states.

The staggered magnetic field \tilde{h}_1 ,

$$H = + \sum_{\langle nm \rangle} J_{n,m} \mathbf{S}_n \cdot \mathbf{S}_m - \tilde{h}_1 \sum_{n \in A} S_n^z + \tilde{h}_1 \sum_{m \in B} S_m^z , \quad (5.116)$$

on the contrary, prefers alternating spin orientations according to the sublattice structure and leads to modified signs in the EoMs:

$$\left[E - \tilde{h}_1 - J_0 M^{\text{sl}} \right] G_{n,n_0}^{AA} = 2 M^{\text{sl}} \delta_{n,n_0} + M^{\text{sl}} \sum_{m \in B} J_{m,n} G_{m,n_0}^{BA} , \quad (5.117)$$

$$\left[E + \tilde{h}_1 + J_0 M^{\text{sl}} \right] G_{m,n_0}^{BA} = - M^{\text{sl}} \sum_{n \in A} J_{m,n} G_{n,n_0}^{AA} . \quad (5.118)$$

As a consequence, the staggered field \tilde{h}_1 leaves the functional form of (5.77) and (5.78) unchanged, but modifies $\varepsilon_{\mathbf{q}}^-$, $\varepsilon_{\mathbf{q}}^+$ and $\varepsilon_{\mathbf{q}}$:

$$\varepsilon_{\mathbf{q}}^- = M^{\text{sl}} [J_0 - J_{\mathbf{q}}] + \tilde{h}_1 = 2dJM^{\text{sl}} [1 - \gamma_{\mathbf{q}}] + \tilde{h}_1, \quad (5.119)$$

$$\varepsilon_{\mathbf{q}}^+ = M^{\text{sl}} [J_0 + J_{\mathbf{q}}] + \tilde{h}_1 = 2dJM^{\text{sl}} [1 + \gamma_{\mathbf{q}}] + \tilde{h}_1, \quad (5.120)$$

$$\varepsilon_{\mathbf{q}}^2 = \varepsilon_{\mathbf{q}}^- \varepsilon_{\mathbf{q}}^+. \quad (5.121)$$

Due to the preserved functional form of (5.77)-(5.78), we may directly adopt (5.86), which explicitly reads at $T = 0$ after inserting (5.119)-(5.121):

$$\Phi_{T=0}^{\text{AFM}} = \frac{1}{N} \sum_{\mathbf{q}} \left[\left(1 - \frac{\gamma_{\mathbf{q}}^2}{\left(1 + \frac{\tilde{h}_1}{2dJM^{\text{sl}}}\right)^2} \right)^{-1/2} - 1 \right]. \quad (5.122)$$

Combined with the Callen formula (5.87), we acquire an implicate equation determining the sublattice magnetization M^{sl} . Assuming an ordered state for large S , we may further approximate (5.122) by reducing M^{sl} to the constant S . In combination with the approximated Callen equation $M^{\text{sl}} \approx S - \Phi^{\text{AFM}}$ for $S \gg 1$, we consistently reach the LSWA regime and recover the LSWA result (4.125) for $p' = 1$.

Thereby, we confirm the resulting effect on the sublattice magnetization that is induced by the staggered field \tilde{h}_1 . Its adapted substructure prevents the singlet-caused cancellation effect exhibited by a small uniform field h_1 .

For a magnetic field h'_1 that is solely defined on one of the sublattices,

$$- h'_1 \sum_{n \in A} S_n^z, \quad (5.123)$$

we correspondingly find the result (5.122) with the substituted field $\tilde{h}_1 \rightarrow \frac{h'_1}{2}$, which is homogeneously spread over both sublattices A and B . With the same approximation scheme for large spin quantum numbers $S \gg 1$ as before, we consistently recover the LSWA result (4.128) for $p' = 1$. This finding further confirms the singlet-based mutual influence of the intertwined sublattices.

5.5 Modifications for Quadratic Anisotropy Fields

We study now the treatment and the outcome of quadratic anisotropy fields ($p = 2$) on the RPA level. The corresponding Hamiltonian reads

$$H = \pm \sum_{\langle ij \rangle} J_{ij} \mathbf{S}_i \cdot \mathbf{S}_j - h_2 \sum_i (S_i^z)^2, \quad (5.124)$$

with the upper sign referring to the AFM and the lower one to the FM.

As we will point out in this paragraph, the RPA treatment of anisotropy fields is beset by several difficulties. As a consequence, the presence of anisotropy fields gave rise to a variety of new decoupling procedures [103, 104, 105]. Although these techniques have been introduced decades ago, recent studies [53, 54, 55, 56, 57], which are based on RPA and related Green's function techniques, emphasize the renewed interest in such investigations. In order to keep our issues manageable, we adopt the Narath decoupling scheme [100, 106], which is as simple as possible and closely related to the original Tyablikov decoupling. Thus, we further refer to the RPA technique as Tyablikov-like decoupling procedures. Although we cannot remove the existing shortcomings, we gain precious analytical expressions describing the changes that are induced by small anisotropy fields and, thereby, elucidate the rise of classical trends in anisotropic spin systems.

Since we have to fix the anisotropy order $p \leq 2S$ right at the beginning, we have to assume spin quantum numbers $S \geq 1$ for quadratic fields.

We start by outlining the modifications for the FM and discuss the modified outcome, especially the critical temperature that is shifted due to the presence of the fields h_2 . Subsequently, we present the corresponding modifications for the AFM and focus on the ground state sublattice magnetization.

5.5.1 Ferromagnet

The EoM for the FM Hamiltonian (5.124) contains now additional terms representing higher-order GFs:

$$\begin{aligned} E \cdot G_{ij} &= 2M \delta_{ij} + \sum_k J_{ki} \left[\langle \langle S_i^+ S_k^z; S_j^- \rangle \rangle - \langle \langle S_k^+ S_i^z; S_j^- \rangle \rangle \right] \\ &+ h_2 \left[\langle \langle S_i^z S_i^+; S_j^- \rangle \rangle + \langle \langle S_i^+ S_i^z; S_j^- \rangle \rangle \right]. \end{aligned} \quad (5.125)$$

Therefore, an appropriate decoupling scheme is required in order to avoid the occurrence of multiple-spin GFs, which would induce a complete hierarchy of coupled higher-order GFs. For this purpose, we adopt the decoupling procedure according to Narath [106], which has originally been mentioned by Anderson and Callen themselves: In their original article [100] they presented the following decoupling rule and referred to it as ‘‘semi-molecular-field approximation’’:

$$\langle \langle S_i^z S_i^+; S_j^- \rangle \rangle \rightarrow \langle S_i^z \rangle G_{ij} = M G_{ij}, \quad (5.126)$$

$$\langle \langle S_i^+ S_i^z; S_j^- \rangle \rangle \rightarrow \langle S_i^z \rangle G_{ij} = M G_{ij}. \quad (5.127)$$

Thereby, we pointedly neglect the occurrence of identical indices in the GFs (5.126)-(5.127), which explains the origin of Anderson's and Callen's naming. The choice of this approximation scheme will lead to well-known shortcomings for large anisotropy fields [104], but will yield reasonable and valuable results for small anisotropy fields, which we will both point out in the following. Please note that this dilemma arises solely due to the presence of anisotropy fields; in the isotropic case we had not to deal with this problem since the condition

$J_{kk} = 0$ guaranteed distinct indices in (5.15). Since we primarily aim, according to our previous results, to elucidate the behaviour for small anisotropy fields, we congruently decided to pursue the Narath decoupling.

With the use of the Narath decoupling (5.126)-(5.127), the additional anisotropy terms in (5.125) are reduced to expressions $\sim h_2 M G_{ij}$:

$$[E - J_0 M - 2h_2 M] G_{ij} = 2M\delta_{ij} - M \sum_k J_{ki} G_{kj}. \quad (5.128)$$

As a consequence, the functional form (5.24) of the resulting GF $G_{\mathbf{q}}$ remains unchanged, but the excitation energies are shifted $\sim h_2 M$:

$$G_{\mathbf{q}} = \frac{2M}{E - E_{\mathbf{q}}}, \quad (5.129)$$

$$\text{with } E_{\mathbf{q}} = M[J_0 - J_{\mathbf{q}} + 2h_2] = 2dJM \left[1 - \gamma_{\mathbf{q}} + \frac{h_2}{dJ} \right]. \quad (5.130)$$

From this point of view, the anisotropy field h_2 causes a change of the effective coupling $J_0 \rightarrow J_0 + 2h_2$, and we consistently recover for $h_2 = 0$ the isotropic excitation energy $E_{\mathbf{q}}$ in (5.24).

Due to the preserved algebraic structure, we can directly adopt the previously derived formulae (5.46)-(5.47). From $\Phi_{T=0} = 0$, we correspondingly recover the unchangedly complete saturation of the FM ground state magnetization:

$$M \xrightarrow{T \rightarrow 0} S. \quad (5.131)$$

The critical temperature, on the contrary, is profoundly influenced by the anisotropy fields h_2 : By inserting the anisotropic excitation energies (5.130) into the preserved functional forms of (5.50)-(5.51), we yield the resulting critical temperature

$$T_C(h_2) = \frac{S(S+1)}{3} \left[\frac{1}{N} \sum_{\mathbf{q}} \frac{1}{J_0 - J_{\mathbf{q}} + 2h_2} \right]^{-1} \quad (5.132)$$

$$\stackrel{(5.53)}{=} \frac{zJ}{3} S(S+1) \left[\frac{1}{N} \sum_{\mathbf{q}} \frac{1}{1 - \gamma_{\mathbf{q}} + \frac{h_2}{dJ}} \right]^{-1} \quad (5.133)$$

$$\stackrel{(5.55),(5.59)}{=} \frac{zJ}{3} S(S+1) \left[\frac{1}{(2\pi)^d} \left(\prod_{i=1}^d \int_{-\pi}^{+\pi} dq_i \right) \frac{1}{1 - \frac{1}{d} \sum_{i=1}^d \cos q_i + \frac{h_2}{dJ}} \right]^{-1}. \quad (5.134)$$

The study of the critical temperature (5.132)-(5.134) elucidates now the ramifications induced by the inclusion of h_2 : On the one hand, we consistently recover for $h_2 = 0$ the critical temperature (5.52),(5.56) of the isotropic reference system. For $h_2 > 0$, on the other hand, we explicitly observe the expected shift towards increasing values of T_C , which is depicted in fig. 5.1.

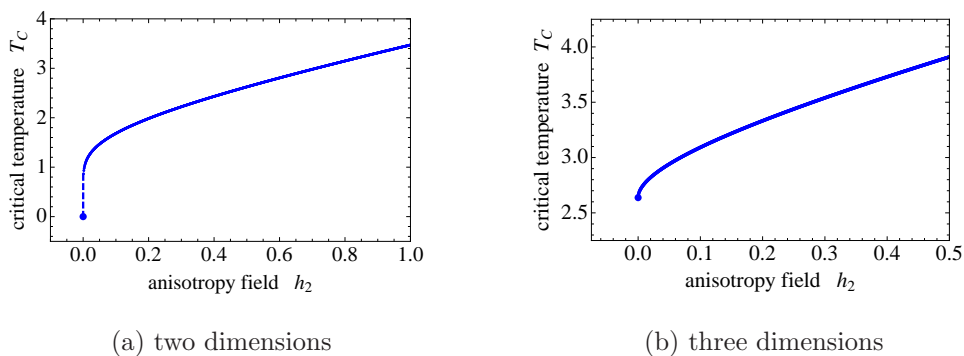


Figure 5.1: Critical temperatures $T_C(h_2)$ of the Heisenberg model (5.124) with quadratic anisotropy fields in two (a) and three (b) dimensions; the values are calculated by the corresponding integrals (5.134).

At this point, the RPA analysis enables us to study the h_2 -dependence in detail: In the long-wavelength approximation $|\mathbf{q}| \ll 1$, we can extract the dominant behaviour of (5.134) for small anisotropy fields $h_2 \ll 1$; these analytical predictions represent important key results that describe the sensitivity to emerging small fields h_2 .

In two dimensions we successfully recover the logarithmic behaviour

$$T_C^{2d} = \frac{a J S(S+1)}{\ln\left[1 + b \frac{J}{h_2}\right]} \quad \text{for } h_2 \ll 1, \quad (5.135)$$

with $a = \frac{4\pi}{3}$ and the numerically determined factor $b = 4.93$. A similar result was found by the related Anderson-Callen decoupling [53, 100]. From (5.135), we find again $T_C^{2d} \rightarrow 0$ for $h_2 \rightarrow 0$, which underlines the compliance with the Mermin-Wagner theorem [8].

In three dimensions we extract for $h_2 \ll 1$ and $|\mathbf{q}| \ll 1$ the dominant behaviour

$$T_C^{3d} = \frac{J S(S+1)}{u - v \sqrt{\frac{h_2}{J}} \arctan\left[w \sqrt{\frac{J}{h_2}}\right]} \quad \text{for } h_2 \ll 1, \quad (5.136)$$

with $\{u, v, w\}$ representing numerical constants: $\{u = 0.48, v = 0.21, w = 2.22\}$. We will use (5.135) and (5.136) again in chapter 6 as fit functions for our Quantum Monte Carlo data. For that purpose, we will change $\{a, b\}$ and $\{u, v, w\}$ to adjustable fit parameters.

For large anisotropy fields $h_2 \gg 1$, on the contrary, we have to face the limitations that come along with the Narath decoupling: For $h_2 \rightarrow \infty$, respectively

$\frac{h_2}{J} \rightarrow \infty$, we recover from (5.132)-(5.134) the well-known $T_C \rightarrow \infty$ - problem [104]:

$$\lim_{h_2 \rightarrow \infty} T_C(h_2) \rightarrow \infty. \quad (5.137)$$

This misleading trend, which is clearly depicted in fig.5.1 as well, can be explained by the appearance of h_2 as an effective coupling ($J_0 \rightarrow J_0 + 2h_2$). Therefore, $h_2 \rightarrow \infty$ as well as $J \rightarrow \infty$ lead to an ordered system at all temperatures.

As a consequence, we have to restrict our analytical predictions on the RPA level to small anisotropy fields.

There have been several proposals for modified decoupling schemes [105]: In fact, some of them removed the divergence for large anisotropy fields, but failed in turn to recover the isotropic value for T_C [105]. Since we are mainly interested in the parameter region for small anisotropies around the isotropic point in the phase diagram, we have consequently chosen the presented RPA procedure by Narath [100, 106].

5.5.2 Antiferromagnet

For the AFM Heisenberg model with quadratic anisotropy fields

$$H = + \sum_{\langle nm \rangle} J_{n,m} \mathbf{S}_n \cdot \mathbf{S}_m - h_2 \left[\sum_{n \in A} (S_n^z)^2 + \sum_{m \in B} (S_m^z)^2 \right], \quad (5.138)$$

we find, as for the FM, additional terms in the EoMs containing higher GFs:

$$\begin{aligned} E \cdot G_{n,n_0}^{AA} &= 2 M^{\text{sl}} \delta_{n,n_0} + \sum_{m \in B} J_{n,m} \left[\langle \langle S_n^z S_m^+; S_{n_0}^- \rangle \rangle - \langle \langle S_n^+ S_m^z; S_{n_0}^- \rangle \rangle \right] \\ &+ h_2 \left[\langle \langle S_n^z S_n^+; S_{n_0}^- \rangle \rangle + \langle \langle S_n^+ S_n^z; S_{n_0}^- \rangle \rangle \right], \end{aligned} \quad (5.139)$$

$$\begin{aligned} E \cdot G_{m,n_0}^{BA} &= \sum_{n \in A} J_{n,m} \left[\langle \langle S_m^z S_n^+; S_{n_0}^- \rangle \rangle - \langle \langle S_m^+ S_n^z; S_{n_0}^- \rangle \rangle \right] \\ &+ h_2 \left[\langle \langle S_m^z S_m^+; S_{n_0}^- \rangle \rangle + \langle \langle S_m^+ S_m^z; S_{n_0}^- \rangle \rangle \right]. \end{aligned} \quad (5.140)$$

Again, we have to find an appropriate decoupling procedure to reduce the higher GFs in (5.139)-(5.140) to two-spin-GFs. As for the FM, we adopt the Narath decoupling scheme [106], which Anderson and Callen originally referred to as “semi-molecular-field approximation” [100]. Its application to the AFM reads

$$\langle \langle S_n^z S_n^+; S_{n_0}^- \rangle \rangle \rightarrow M^{\text{sl}} G_{n,n_0}^{AA}, \quad \langle \langle S_n^+ S_n^z; S_{n_0}^- \rangle \rangle \rightarrow M^{\text{sl}} G_{n,n_0}^{AA}, \quad (5.141)$$

$$\langle \langle S_m^z S_m^+; S_{n_0}^- \rangle \rangle \rightarrow -M^{\text{sl}} G_{m,n_0}^{BA}, \quad \langle \langle S_m^+ S_m^z; S_{n_0}^- \rangle \rangle \rightarrow -M^{\text{sl}} G_{m,n_0}^{BA}. \quad (5.142)$$

Although we neglect hereby, again, the occurrence of identical indices, this approach provides several advantages for the AFM as well as for the FM, as

pointed out in the foregoing paragraph. Together with the previous Tyablikov procedure (5.70)-(5.71), the reduced EoMs read

$$\left[E - M^{\text{sl}}(J_0 + 2h_2) \right] G_{n,n_0}^{AA} = 2 M^{\text{sl}} \delta_{n,n_0} + M^{\text{sl}} \sum_{m \in B} J_{m,n} G_{m,n_0}^{BA}, \quad (5.143)$$

$$\left[E + M^{\text{sl}}(J_0 + 2h_2) \right] G_{m,n_0}^{BA} = - M^{\text{sl}} \sum_{n \in A} J_{m,n} G_{n,n_0}^{AA}. \quad (5.144)$$

Therefore, the presence of the anisotropy field h_2 acts, again, as an effective coupling according to the shift $J_0 \rightarrow J_0 + 2h_2$.

As a consequence, the functional forms of the decoupled GFs $G_{\mathbf{q}}^{AA}$ (5.77) and $G_{\mathbf{q}}^{BA}$ (5.78) remain unchanged, whereas the energies $\varepsilon_{\mathbf{q}}^-$ and $\varepsilon_{\mathbf{q}}^+$ contain shifts $\sim h_2 M^{\text{sl}}$:

$$\varepsilon_{\mathbf{q}}^- = M^{\text{sl}} \left[J_0 - J_{\mathbf{q}} + 2h_2 \right] = 2dJM^{\text{sl}} \left[1 - \gamma_{\mathbf{q}} + \frac{h_2}{dJ} \right], \quad (5.145)$$

$$\varepsilon_{\mathbf{q}}^+ = M^{\text{sl}} \left[J_0 + J_{\mathbf{q}} + 2h_2 \right] = 2dJM^{\text{sl}} \left[1 + \gamma_{\mathbf{q}} + \frac{h_2}{dJ} \right], \quad (5.146)$$

$$\varepsilon_{\mathbf{q}}^2 = \varepsilon_{\mathbf{q}}^- \varepsilon_{\mathbf{q}}^+. \quad (5.147)$$

Due to the preserved functional form of $G_{\mathbf{q}}^{AA}$ (5.77) and $G_{\mathbf{q}}^{BA}$ (5.78), we can pursue to determine the critical temperature as in section 5.3.2: In the limits

$$T \lesssim T_C^{\text{AFM}} \quad M^{\text{sl}} \gtrsim 0, \quad (5.148)$$

we can further on uphold the conditions $\varepsilon_{\mathbf{q}}^-, \varepsilon_{\mathbf{q}}^+, \varepsilon_{\mathbf{q}} \ll 1$ for finite h_2 due to $\varepsilon_{\mathbf{q}}^-, \varepsilon_{\mathbf{q}}^+, \varepsilon_{\mathbf{q}} \sim M^{\text{sl}}$. Thus, we can approximate Φ^{AFM} (5.89) as before by

$$\Phi^{\text{AFM}} \approx \frac{T_C^{\text{AFM}}}{N} \sum_{\mathbf{q}} \frac{\varepsilon_{\mathbf{q}}^- + \varepsilon_{\mathbf{q}}^+}{\varepsilon_{\mathbf{q}}^2} \gg 1, \quad (5.149)$$

which translates, by inserting (5.145)-(5.147), into

$$\Phi^{\text{AFM}} \approx \frac{T_C^{\text{AFM}}}{dJM^{\text{sl}}} \frac{1}{N} \sum_{\mathbf{q}} \frac{1 + \frac{h_2}{dJ}}{\left(1 + \frac{h_2}{dJ}\right)^2 - \gamma_{\mathbf{q}}^2} \gg 1. \quad (5.150)$$

The condition $\Phi^{\text{AFM}} \gg 1$ allows the further use of the approximated Callen equation (5.90): By combining (5.90) and (5.150), we can cancel M^{sl} on both sides of the resulting formula and finally yield, thereby, the h_2 -dependent critical temperature

$$T_C^{\text{AFM}}(h_2) = \frac{zJ}{6} S(S+1) \left[\frac{1}{N} \sum_{\mathbf{q}} \frac{1 + \frac{h_2}{dJ}}{\left(1 + \frac{h_2}{dJ}\right)^2 - \gamma_{\mathbf{q}}^2} \right]^{-1}. \quad (5.151)$$

From (5.151), we can identify the correct trend of rising critical temperatures for increasing values of the anisotropy fields:

$$T_C^{\text{AFM}}(h_2 > 0) > T_C^{\text{AFM}}(h_2 = 0) \quad \text{in } d = 2, 3. \quad (5.152)$$

Thereby, this critical temperature for the AFM (5.151) turns out to be numerically identical with the previous FM result (5.132)-(5.134). Thus, we can extend the former statement that was well established for isotropic systems [58]: The RPA technique is not capable of distinguishing the critical temperatures of FMs and AFMs, neither for isotropic nor for anisotropic systems. As a consequence, we can directly adopt the long-wavelength behaviour in two (5.135) and three (5.136) dimensions and can use these formulae as fit functions for our QMC simulations on AFMs.

The ground state sublattice magnetization $M_{T=0}^{\text{sl}}$, on the contrary, exhibits profound differences to the completely saturated FM magnetization $M_{T=0} = S$: Quantum fluctuations consequently reduce $M_{T=0}^{\text{sl}}$ and cause deviations from the maximal classical value S . In order to determine the quantum corrections to $M_{T=0}^{\text{sl}}$, we need to calculate $\Phi_{T=0}^{\text{AFM}}$ and can make further use of the general formula in (5.95) since the functional forms of the GFs remain unchanged. By inserting the shifted energies $\varepsilon_{\mathbf{q}}^-, \varepsilon_{\mathbf{q}}^+, \varepsilon_{\mathbf{q}}$ (5.145)-(5.147) in (5.95), we get

$$\Phi_{T=0}^{\text{AFM}} = \frac{1}{N} \sum_{\mathbf{q}} \left[\left(1 - \frac{\gamma_{\mathbf{q}}^2}{\left(1 + \frac{h_2}{dJ}\right)^2} \right)^{-1/2} - 1 \right]. \quad (5.153)$$

Combined with the Callen equation (5.87), we yield the ground state sublattice magnetization $M_{T=0}^{\text{sl}}(h_2, S, d)$, which depends on the anisotropy fields h_2 , the spin quantum number S and the dimension d . The final outcome in the thermodynamical limit (5.93) is presented in fig.5.2-5.5 and shows these dependencies over a widespread parameter range. In order to compare these new findings with those of the foregoing chapter, the figures contain our previous LSWA results as well.

Since RPA and LSWA deal with different approximations for the quantum corrections, thereby estimating their amount differently, their diminished difference for increasing h_2 and S underlines the suppression of quantum fluctuations.

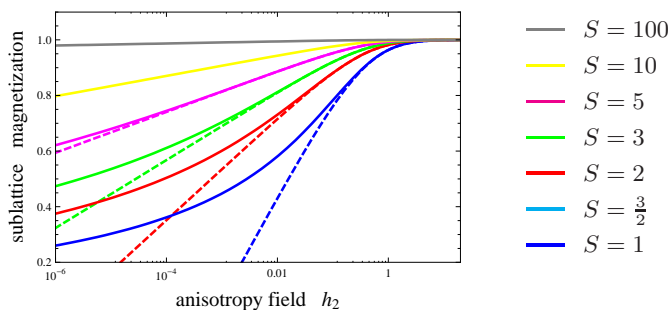
Thereby, these RPA results can be directly linked to those from the LSWA approach: For large spin quantum numbers $S \gg 1$, we can approximate the AFM Callen equation (5.87) by

$$M_{T=0}^{\text{sl}} \approx S - \Phi_{T=0}^{\text{AFM}}, \quad (5.154)$$

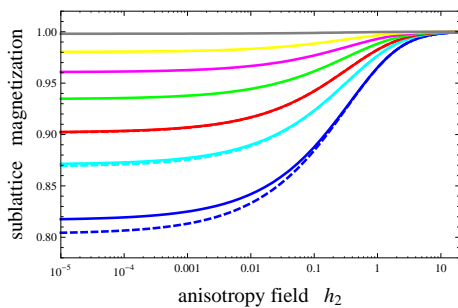
which subsequently reduces the formula for the resulting sublattice magnetization to

$$M_{T=0}^{\text{sl}}(h_2) \approx S - \frac{1}{N} \sum_{\mathbf{q}} \left[\left(1 - \frac{\gamma_{\mathbf{q}}^2}{\left(1 + \frac{h_2}{dJ}\right)^2} \right)^{-1/2} - 1 \right]. \quad (5.155)$$

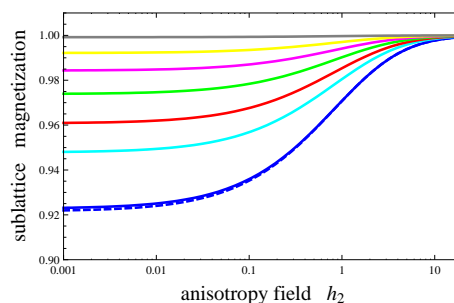
This approximative result is well-known from the last chapter: (5.155) turns out to be identical with our previous LSWA result (4.88) for $p = 2$. Thus, our RPA results consistently refer back to our LSWA formulae for $S \gg 1$.



(a) $d = 1$



(b) $d = 2$



(c) $d = 3$

Figure 5.2: Normalized ground state sublattice magnetization $M_{T=0}^{\text{sl}}/S$ in one, two and three dimensions for various spin quantum numbers S , in RPA (solid curves) and LSWA (dashed curves), scaled logarithmically; if there is no dashed curve, it coincides with the solid one.

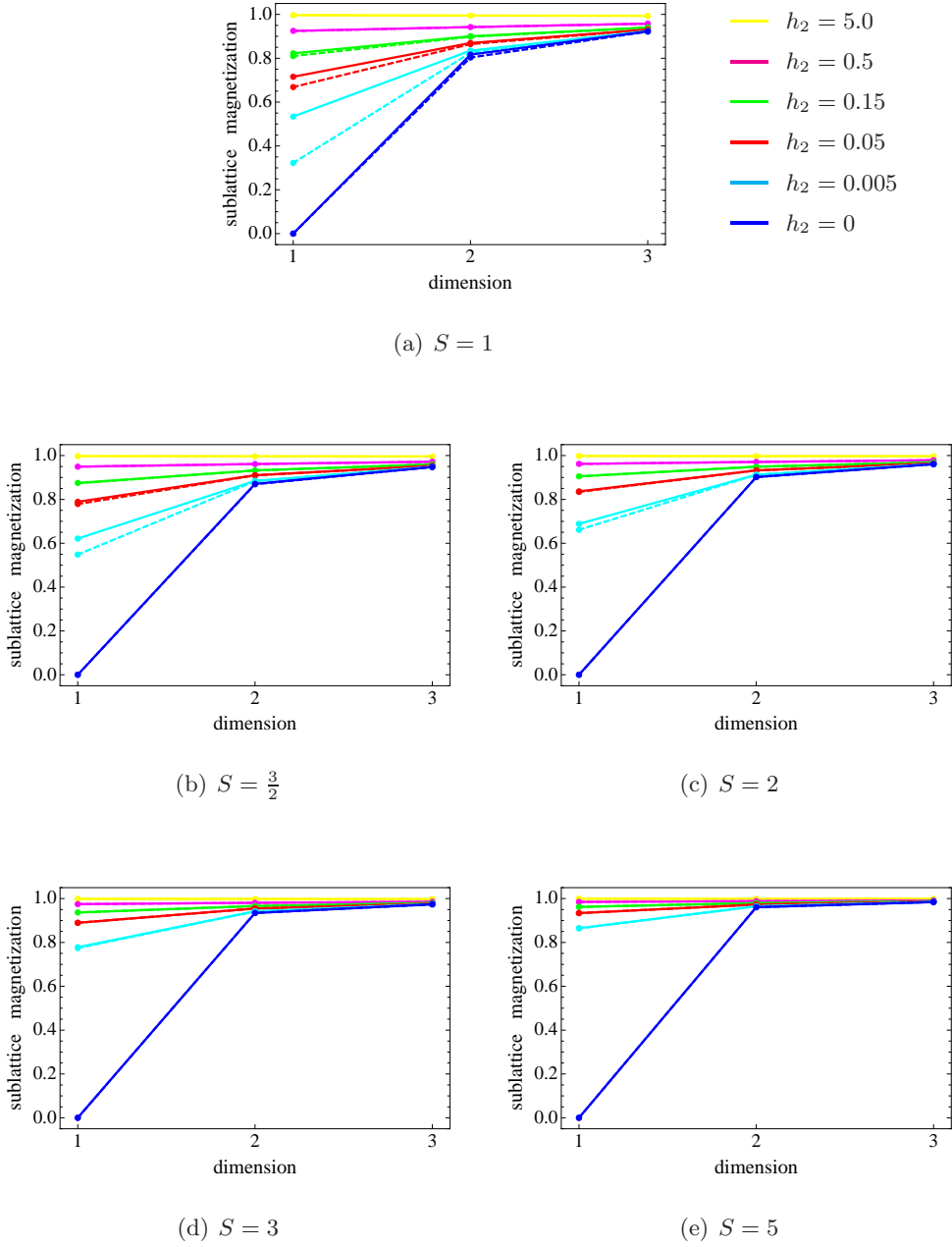


Figure 5.3: Dimensional dependence of the normalized ground state sublattice magnetization $M_{T=0}^{\text{sl}}/S$ for different fixed spin quantum numbers S and various $h_2 \geq 0$, in RPA (solid lines) and LSWA (dashed lines); the lines are guides to the eyes; if there is no dashed line, it coincides with the solid one.

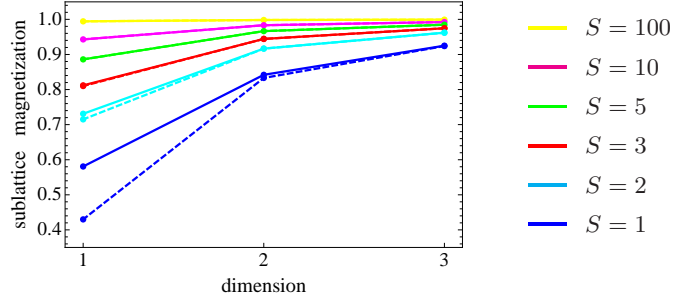
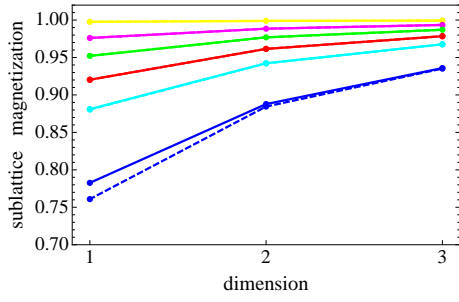
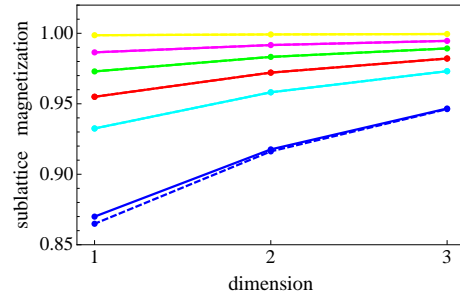

 (a) $h_2 = 0.01$

 (b) $h_2 = 0.1$

 (c) $h_2 = 0.25$

Figure 5.4: Dimensional dependence of the normalized ground state sublattice magnetization $M_{T=0}^{\text{sl}}/S$ for different fixed anisotropy fields $h_2 > 0$ and various spin quantum numbers S in RPA (solid lines) and LSWA (dashed lines); the lines are guides to the eyes; if there is no dashed line, it coincides with the solid one.

The refinement and improvement due to the RPA approach can be highlighted by the $h_2 \rightarrow 0$ - behaviour in one dimension: In the LSWA method, we had to face with the trend $M_{T=0}^{\text{sl}} \xrightarrow{h_2 \rightarrow 0} -\infty$, which had to be reinterpreted as an infinitely strong quantum correction that leads to the vanishing of the long range order. On the RPA level, on the contrary, we can repair this incorrect limit: In the long-wavelength approximation we yield for small h_2

$$\Phi_{T=0}^{\text{AFM}} \sim \ln \left[\frac{J}{h_2} \right] \xrightarrow{h_2 \rightarrow 0} +\infty, \quad (5.156)$$

which leads, with (5.90), directly to the correct limit

$$M_{T=0}^{\text{sl}} \sim \frac{1}{\ln \left[\frac{J}{h_2} \right]} \xrightarrow{h_2 \rightarrow 0} 0. \quad (5.157)$$

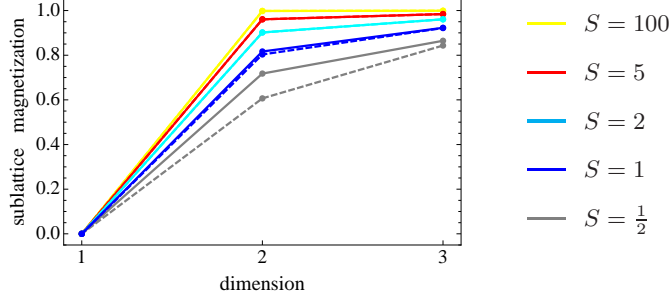


Figure 5.5: Dimensional dependence of the normalized ground state sublattice magnetization $M_{T=0}^{\text{sl}}/S$ for the isotropic ($h_2 = 0$) Heisenberg system, shown for various spin quantum numbers S in RPA (solid lines) and LSWA (dashed lines); the lines are guides to the eyes; if there is no dashed line, it coincides with the solid one.

As before, the figures 5.2-5.4 demonstrate the strong sensitivity to increasing anisotropy fields h_2 and rising spin quantum numbers S . Thereby, we can adopt the observation of the foregoing chapter: For large parameter values $h_2 \rightarrow \infty$ and $S \rightarrow \infty$ we consistently recover the classical limit $M_{T=0}^{\text{sl}} \rightarrow S$, which suppresses all of the quantum effects and corrections. From the fig. 5.2-5.4, we further confirm the important observation that the quantum fluctuations are most profoundly influenced by relatively small anisotropy fields. In order to quantify this key result, we use again the anisotropy susceptibility

$$\chi_{h_p} = \frac{\partial M_{T=0}^{\text{sl}}}{\partial h_p}, \quad (5.158)$$

which is depicted in fig. 5.6 and compared to the LSWA results from chapter 4. We emphasize again that the anisotropy susceptibility is exclusively sensitive to quantum fluctuations due to its vanishing classical version (4.130). From the RPA result (5.155) we can extract the dominant behaviour of χ_{h_p} for $h_p \rightarrow 0$: The anisotropy susceptibility diverges according to

$$1d: \quad \chi_{h_p}^{1d} \sim 1/h_p, \quad (5.159)$$

$$2d: \quad \chi_{h_p}^{2d} \sim 1/\sqrt{h_p}, \quad (5.160)$$

$$3d: \quad \chi_{h_p}^{3d} \sim -\ln(h_p), \quad (5.161)$$

which concurs with the dominant behaviour (4.131)-(4.133) found in LSWA. This confirmed finding strongly underlines the rapid suppression of quantum fluctuations by relatively small and even tiny anisotropy fields. The repeated observation of this phenomenon by various analytical techniques further validates the classical modelling of the SP-STM measurements of magnetic samples that are influenced by anisotropy fields [23]-[31].

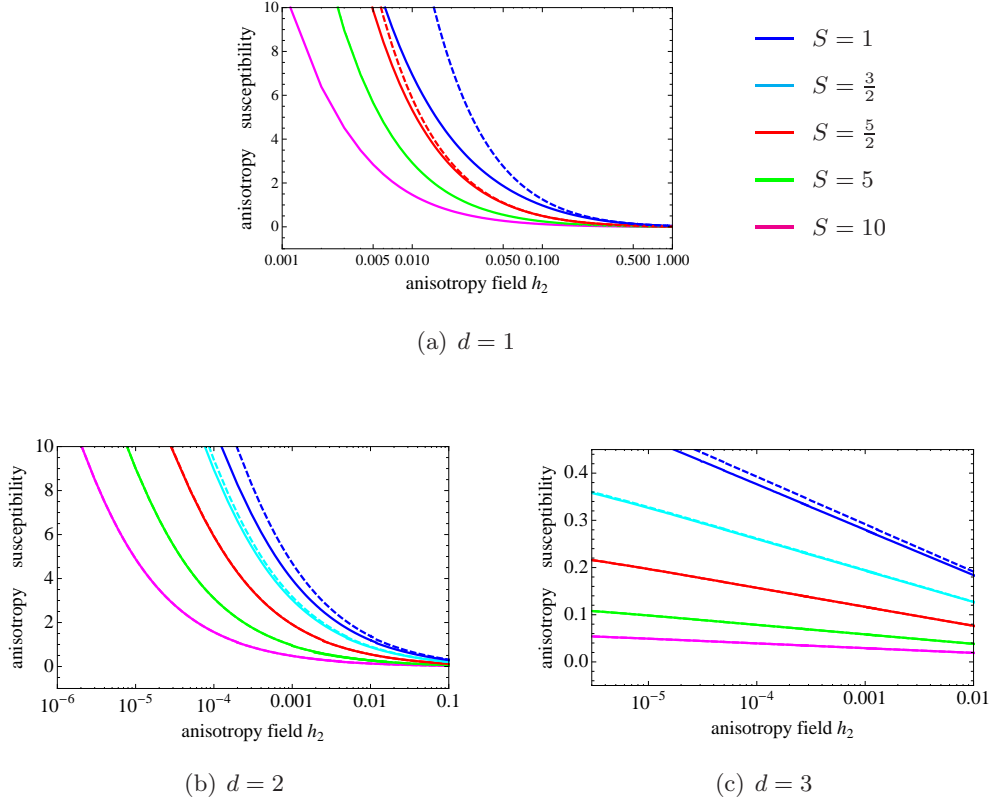


Figure 5.6: Anisotropy susceptibility χ_{h_2} (5.158) in one, two and three dimensions for various spin quantum numbers S in RPA (solid curves) and LSWA (dashed curves), scaled logarithmically; if there is no dashed curve, it coincides with the solid one.

We want to close this paragraph on anisotropy fields in the AFM by considering the field h'_2 that is solely defined on one of the sublattices:

$$H = + \sum_{\langle nm \rangle} J_{n,m} \mathbf{S}_n \cdot \mathbf{S}_m - h'_2 \sum_{n \in A} (S_n^z)^2. \quad (5.162)$$

The application of the Tyablikov (5.70)-(5.71) and Narath (5.141)-(5.142) decoupling schemes reduce the EoMs to

$$\left[E - M^{\text{sl}} (J_0 + 2h'_2) \right] G_{n,n_0}^{AA} = 2 M^{\text{sl}} \delta_{n,n_0} + M^{\text{sl}} \sum_{m \in B} J_{m,n} G_{m,n_0}^{BA}, \quad (5.163)$$

$$\left[E + M^{\text{sl}} J_0 \right] G_{m,n_0}^{BA} = - M^{\text{sl}} \sum_{n \in A} J_{m,n} G_{n,n_0}^{AA}. \quad (5.164)$$

Due to their non-symmetric structure, both the energies $\varepsilon_{\mathbf{q}}^-, \varepsilon_{\mathbf{q}}^+, \varepsilon_{\mathbf{q}}$ and the GFs

$G_{\mathbf{q}}^{AA}, G_{\mathbf{q}}^{BA}$ change in Fourier space:

$$G_{\mathbf{q}}^{AA} = \frac{M^{\text{sl}}}{2\varepsilon_{\mathbf{q}}} \left[\frac{2\varepsilon_{\mathbf{q}} + \varepsilon_{\mathbf{q}}^- + \varepsilon_{\mathbf{q}}^+}{E - h'_2 M^{\text{sl}} - \varepsilon_{\mathbf{q}}} + \frac{2\varepsilon_{\mathbf{q}} - \varepsilon_{\mathbf{q}}^- - \varepsilon_{\mathbf{q}}^+}{E - h'_2 M^{\text{sl}} + \varepsilon_{\mathbf{q}}} \right], \quad (5.165)$$

$$G_{\mathbf{q}}^{BA} = -\frac{J_{\mathbf{q}} (M^{\text{sl}})^2}{\varepsilon_{\mathbf{q}}} \left[\frac{1}{E - h'_2 M^{\text{sl}} - \varepsilon_{\mathbf{q}}} - \frac{1}{E - h'_2 M^{\text{sl}} + \varepsilon_{\mathbf{q}}} \right], \quad (5.166)$$

$$\text{with } \varepsilon_{\mathbf{q}}^- = M^{\text{sl}} [J_0 - J_{\mathbf{q}} + h'_2] \stackrel{(5.53)}{=} 2dJM^{\text{sl}} \left[1 - \gamma_{\mathbf{q}} + \frac{h'_2}{2dJ} \right], \quad (5.167)$$

$$\varepsilon_{\mathbf{q}}^+ = M^{\text{sl}} [J_0 + J_{\mathbf{q}} + h'_2] \stackrel{(5.53)}{=} 2dJM^{\text{sl}} \left[1 + \gamma_{\mathbf{q}} + \frac{h'_2}{2dJ} \right], \quad (5.168)$$

$$\varepsilon_{\mathbf{q}}^2 = \varepsilon_{\mathbf{q}}^- \varepsilon_{\mathbf{q}}^+. \quad (5.169)$$

From the spectral theorem (5.84) we extract for small h'_2 at $T = 0$

$$\Phi_{T=0}^{\text{AFM}} = \frac{1}{N} \sum_{\mathbf{q}} \left[\left(1 - \frac{\gamma_{\mathbf{q}}^2}{\left(1 + \frac{h'_2}{2dJ}\right)^2} \right)^{-1/2} - 1 \right], \quad (5.170)$$

and recover, by comparison to (5.153), our former RPA result with the substitution $h_2 \rightarrow \frac{h'_2}{2}$. The ground state sublattice magnetization $M_{T=0}^{\text{sl}}$ is subsequently determined by the Callen equation (5.87), which can be reduced for large spin quantum numbers to

$$M_{T=0}^{\text{sl}} \approx S - \frac{1}{N} \sum_{\mathbf{q}} \left[\left(1 - \frac{\gamma_{\mathbf{q}}^2}{\left(1 + \frac{h'_2}{2dJ}\right)^2} \right)^{-1/2} - 1 \right] \quad \text{for } S \gg 1. \quad (5.171)$$

The latter resulting formula consistently concords with our previous result (4.128) found by the corresponding LSWA treatment in section 4.5.3. Thus, we could again successfully lead back our RPA findings to our former LSWA results and validate them in the limit of large S .

Applying the limits $T \xrightarrow{\leq} T_C^{\text{AFM}}$ and $M^{\text{sl}} \xrightarrow{\geq} 0$, we can further on uphold the condition $\Phi^{\text{AFM}} \gg 1$ and find, with the use of (5.90), the critical temperature for small h'_2

$$T_C^{\text{AFM}}(h'_2) = \frac{zJ}{6} S(S+1) \left[\frac{1}{N} \sum_{\mathbf{q}} \frac{1}{1 + \frac{h'_2}{dJ} - \gamma_{\mathbf{q}}^2} \right]^{-1}, \quad (5.172)$$

whose dominant order is again related to the symmetrically defined field h_2 in (5.151) by the substitution $h_2 \rightarrow \frac{h'_2}{2}$.

In the end, we can confirm the physical outcome found by the LSWA approach

in section 4.5.3: Although the anisotropy field h'_2 is merely defined on one of the sublattices, it induces a homogeneous effect on both of the sublattices. This finding further underlines the intertwining of the sublattices and supports, thereby, the picture of the singlet states characterizing the AFM quantum fluctuations.

5.6 Higher-Order Anisotropy Fields

The determination of the relevance of higher-order fields (h_p with $p \geq 3$) on the RPA level is beset by some difficulties, which we will explain in the following. For the sake of simplicity, we will restrict ourselves to the FM case, but the following considerations apply in a slightly modified manner as well for the AFM.

Considering the FM Heisenberg Hamiltonian with the higher-order anisotropy fields h_p ,

$$H = - \sum_{\langle ij \rangle} J_{ij} \mathbf{S}_i \cdot \mathbf{S}_j - h_p \sum_i (S_i^z)^p \quad \text{with } p \in \{3, 4, 5, 6\}, \quad (5.173)$$

the EoMs (5.4) consequently contain additional terms $\sim h_p$ with the following higher-order GFs exhibiting all of the permutations of the S_i^+ -operator and $p-1$ S_i^z -operators for a given p :

$$\begin{aligned} \underline{p=3}: \quad & + h_3 \left[\langle\langle (S_i^z)^2 S_i^+; S_j^- \rangle\rangle + \langle\langle S_i^z S_i^+ S_i^z; S_j^- \rangle\rangle \right. \\ & \left. + \langle\langle S_i^+ (S_i^z)^2; S_j^- \rangle\rangle \right], \end{aligned} \quad (5.174)$$

$$\begin{aligned} \underline{p=4}: \quad & + h_4 \left[\langle\langle (S_i^z)^3 S_i^+; S_j^- \rangle\rangle + \langle\langle (S_i^z)^2 S_i^+ S_i^z; S_j^- \rangle\rangle \right. \\ & \left. + \langle\langle S_i^z S_i^+ (S_i^z)^2; S_j^- \rangle\rangle + \langle\langle S_i^+ (S_i^z)^3; S_j^- \rangle\rangle \right], \end{aligned} \quad (5.175)$$

$$\begin{aligned} \underline{p=5}: \quad & + h_5 \left[\langle\langle (S_i^z)^4 S_i^+; S_j^- \rangle\rangle + \langle\langle (S_i^z)^3 S_i^+ S_i^z; S_j^- \rangle\rangle \right. \\ & + \langle\langle (S_i^z)^2 S_i^+ (S_i^z)^2; S_j^- \rangle\rangle + \langle\langle S_i^z S_i^+ (S_i^z)^3; S_j^- \rangle\rangle \\ & \left. + \langle\langle S_i^+ (S_i^z)^4; S_j^- \rangle\rangle \right], \end{aligned} \quad (5.176)$$

$$\begin{aligned} \underline{p=6}: \quad & + h_6 \left[\langle\langle (S_i^z)^5 S_i^+; S_j^- \rangle\rangle + \langle\langle (S_i^z)^4 S_i^+ S_i^z; S_j^- \rangle\rangle \right. \\ & + \langle\langle (S_i^z)^3 S_i^+ (S_i^z)^2; S_j^- \rangle\rangle + \langle\langle (S_i^z)^2 S_i^+ (S_i^z)^3; S_j^- \rangle\rangle \\ & \left. + \langle\langle S_i^z S_i^+ (S_i^z)^4; S_j^- \rangle\rangle + \langle\langle S_i^+ (S_i^z)^5; S_j^- \rangle\rangle \right]. \end{aligned} \quad (5.177)$$

Unfortunately, this appearance of several S_i^z -operators represents a source of complications since the Narath decoupling scheme (5.126)-(5.127) remains, as a consequence, no longer unambiguous for the higher-order GFs in (5.174)-(5.177): In the isotropic and $p \leq 2$ - case, we had merely to deal with three-spin GFs and we could simply apply the Hartree-Fock-decoupling rule (5.16)

for the first two operators. For the multiple-spin GFs in (5.174)-(5.177), on the contrary, it is not uniquely determined how to proceed since there exist several possible decoupling procedures: We could, for example, always extract the first two operators and afterwards the remaining ones, or could simply extract the highest power of S_i^z or think of even more exotic scheme rules. For the multiple spin operators in (5.174)-(5.177) there exists, unfortunately, no general Wick's theorem containing an arbitrary number of S^+ - and S^z - operators, which would fix the scheme unambiguously.

We performed a variety of sensible decoupling procedures that reduce the multiple -spin GFs to two-spin-GFs and found, as a result, quite different prefactors c_p for the resulting anisotropy terms $c_p h_p M G_{ij}$ with even p ($c_2 = 2$). These prefactors describe in conclusion the relevance of the higher-order anisotropies according to

$$T_C = \frac{zJ}{3} S(S+1) \left[\frac{1}{N} \sum_{\mathbf{q}} \frac{1}{1 - \gamma_{\mathbf{q}} + \frac{c_p h_p}{2dJ}} \right]^{-1}. \quad (5.178)$$

As before, we rescale the fields by $c_p \rightarrow \tilde{c}_p/S^{p-2}$, thereby leaving $1 - \gamma_{\mathbf{q}} + \tilde{c}_p h_p/2dJS^{p-2}$ as the argument of the denominator in (5.178).

Eventually, we cannot unambiguously determine these prefactors and the resultant relevance of the higher-order fields on the RPA level: Some decoupling schemes predict a higher relevance for higher p and some of them vice versa. As a solution to our dilemma, we could indeed apply certain decoupling procedures for specified ranges of the spin quantum number S and could thereby reproduce our QMF predictions from chapter 3. Nevertheless, we want to emphasize that such conclusions represent no genuine RPA results, but can be achieved by including the external physical input of the supplementary QMF theory.

In the end, we can at least make further use of the long-wavelength behaviour found in (5.135) and (5.136): Since the change of the numerical factors leaves their functional forms unaltered, we find the general trends

$$T_C^{2d}(h_p) = \frac{aJS(S+1)}{\ln\left[1 + b\frac{J}{h_p}\right]} \quad \text{for } h_p \ll 1, \quad (5.179)$$

$$T_C^{3d}(h_p) = \frac{JS(S+1)}{u - v\sqrt{\frac{h_p}{J}} \arctan\left[w\sqrt{\frac{J}{h_p}}\right]} \quad \text{for } h_p \ll 1, \quad (5.180)$$

with the mostly non-specified parameters $\{a, b\}$ and $\{u, v, w\}$. Thus, we can use them as fit functions with variable fit parameters for our QMC data in chapter 6 for any even p .

A possible way out of the ambiguous decoupling possibilities could be achieved by a completely alternate ansatz, which is a hybrid of the approaches used in the chapters 4 and 5: The Dyson-Maleev transformation [110, 111] offers an alternative mapping onto bosonic operators and is thereby closely related to the

Holstein-Primakoff transformation [92]. In contrast to the latter, the Dyson-Maleev transformation does not use the equally distributed square roots $\sqrt{2S} \cdot \sqrt{1 - n_i/2S}$ for the conversion of S_i^+ and S_i^- , but allocates instead the expression $2S(1 - n_i/2S)$ completely to S_i^+ ; in the FM version this transformation reads

$$S_i^- = a_i^\dagger, \quad S_i^+ = 2S \left(1 - \frac{n_i}{2S}\right) a_i, \quad (5.181)$$

$$S_i^z = S - n_i, \quad \text{with } n_i = a_i^\dagger a_i. \quad (5.182)$$

The price you have to pay in turn is the loss of hermiticity for the involved Hamiltonian due to $(S_i^-)^\dagger \neq S_i^+$. Anyway, the following treatment offers again the existence of Wick's theorem: A subsequent Hartree-Fock decoupling could be based on Wick's theorem for boson operators and would render the sought prefactors unambiguous. Nevertheless, its corresponding treatment would require a completely new and more sophisticated workout right from the beginning.

5.7 Retrospect and Outlook

In this chapter we further refined our results on the suppression of quantum fluctuations by anisotropy fields:

Based on the RPA Green's function technique, we elucidated the impact of anisotropy fields on the critical temperatures: In the long wavelength regime, we could extract the analytical behaviours (5.135)-(5.136) and (5.179)-(5.180). We will make explicit use of these formulae in the following chapter in order to mutually validate our results from different approaches.

Thereby, any differences between the FM and AFM critical temperatures turned out to be absent on the RPA level; this restriction will be removed in the coming chapter on Quantum Monte Carlo simulations.

The results for the AFM ground state sublattice magnetization, which exhibits the typical quantum fluctuations, could be improved and further underlined the extreme sensitivity to relatively small anisotropy fields h_p : The results for the sublattice magnetization are summarized and illustrated in fig. 5.2-5.4, together with the LSWA results of the last chapter in order to highlight the improvements of the RPA technique. The anisotropy susceptibility, which highlights this sensitivity to anisotropy fields h_p in fig. 5.6, exposed for $h_p \rightarrow 0$ the divergent trends (5.159)-(5.161); the latter turned out to be concordant with the results of chapter 4: This confirmed finding firmly reveals the fast suppression of quantum fluctuations that is induced by the presence of even tiny anisotropy fields.

For higher-order fields ($p \geq 3$), we consistently found the same principal trends; nevertheless, we could not, due to the ambiguity of the decoupling procedure, reveal the precise prefactors that determine the relevance of these higher-order fields. A more sophisticated ansatz, like e.g. the Dyson-Maleev transformation, could render the decoupling scheme unambiguous and detect their relevance, but would require a modified treatment right from the beginning.

Extended studies could further include thermal excitations at $T > 0$ and elucidate the interplay of quantum and thermal fluctuations including their suppression by the presence of anisotropy fields.

All in all, the outcome of the RPA technique bridges the foregoing and following chapters: The calculation of the sublattice magnetization refers back to the LSWA results, whereas the determined critical temperatures will be connected to the QMC simulation results.

The following chapter on Quantum Monte Carlo simulations will present the vital numerical counterpart to the analytical studies we presented up to here, and will achieve important and quantitatively improved results.

Chapter 6

Quantum Monte Carlo

In the course of this chapter we will refine our previous results by performing numerical Quantum Monte Carlo (QMC) simulations. The outcome will provide quantitatively improved phase diagrams and further substantiate our findings on the suppression of quantum fluctuations. Furthermore, the QMC technique enables us to extract the differences between AFM and FM models. Their detailed comparison will underline the main message of this thesis that quantum effects can be profoundly reduced by the presence of anisotropy fields.

In the following introduction, we will outline the features of the ALPS package and explain how to use them in practice. After having presented several successful benchmarks, we will expose our refined results exhibiting the influence of anisotropy fields on the critical temperatures of various systems.

6.1 Introduction to ALPS

For our QMC simulations we made use of the software package ALPS [112], which stands for “Algorithms and Libraries for Physics Simulations” and is provided by the ALPS community (please visit the ALPS homepage [113] for further information). ALPS offers modern and state-of-the-art QMC algorithms, which are periodically updated and extended by new features. Our simulations are based on the version 1.3, which has been released at the end of 2007.

The great advantage of the ALPS package, besides its modern algorithms, is marked by the variable C++ implementation of different models, underlying lattices and applied algorithms. This feature allows to investigate a wide class of models on various lattices by several algorithms, which can all be specified by relatively simple input files based on XML (eXtensible Markup Language).

6.1.1 Handling and Features

Due to the modern C++ implementation, the ALPS user may focus his attention on the choice of appropriate simulation parameters, which are specified in the input file. Fig. 6.1 shows such a typical input file in text format. The first lines specify the concrete model and its underlying lattice. Thereby, the

parameter L represents, throughout this thesis, the linear extent $L = N^{1/d}$ of the system, with N denoting the total number of lattices sites in d dimensions. We set all the nearest-neighbour coupling constants J to unity ($|J| = 1$); as a consequence, the resulting critical temperatures will be given in units of $|J|$. The sign of J in the input file discriminates between the FM and AFM: In the quantum case, $J > 0$ corresponds to the AFM and $J < 0$ to the FM (for the classical algorithms vice versa). The parameter `THERMALIZATION` corresponds to the initial update steps, which are not comprised in the final average values, in order to generate configurations sufficiently thermalized for the subsequent numerical measurements. The amount of main simulation steps, which are taken into account for the calculation of the resulting output data, is tuned by the parameter `SWEEPS`. For more detailed information and tutorials, please visit the ALPS homepage [113].

```
LATTICE="simple cubic lattice"
MODEL="spin"
LATTICE_LIBRARY="./lattices.xml"
MODEL_LIBRARY="./models.xml"
local_S=3/2
L=10
J=-1
THERMALIZATION=500000
SWEEPS=2500000
{T=5.0;}
{T=5.1;}
{T=5.2;}
{T=5.3;}
{T=5.4;}
{T=5.5;}
{T=5.6;}
{T=5.7;}
{T=5.8;}
{T=5.9;}
{T=6.0;}
```

Figure 6.1: Typical input file in text format; the specified system is the isotropic ferromagnetic three-dimensional $S = \frac{3}{2}$ - Heisenberg model on a simple cubic lattice consisting of 10^3 lattice sites.

In all of the performed simulations we successfully applied the rule-of-thumb of allocating 20% of the total number of simulation steps to the thermalization. The convergence of the final data was checked by an implemented binning analysis, respectively jackknife analysis. We usually performed about three million sweeps and raised their amount if necessary; especially the data points in the critical region (due to the phenomenon of critical slowing down) and in the low

temperature region (due to the SSE representation, which stands for Stochastic Series Expansion and corresponds to the expansion in the inverse temperature and, therefore, to a high-temperature expansion) required more elaborate simulation runs.

The input file can be written as a simple text file (`parameter`) and is subsequently converted into the corresponding XML file (`parameter.in.xml`) by the provided XML converter. Please note that all the model and lattice specifications used in the input files are precedingly defined in the underlying files `models.xml` and `lattices.xml`. Required modifications and extensions can be directly defined in those files. The selected algorithm (see below) runs the simulation based on the specified input parameters and collects all the resulting numerical measurements in the corresponding output file (`parameter.out.xml`), which can be further analysed. Fig. 6.2 depicts the typical schedule of a QMC simulation referring to [114, 115].

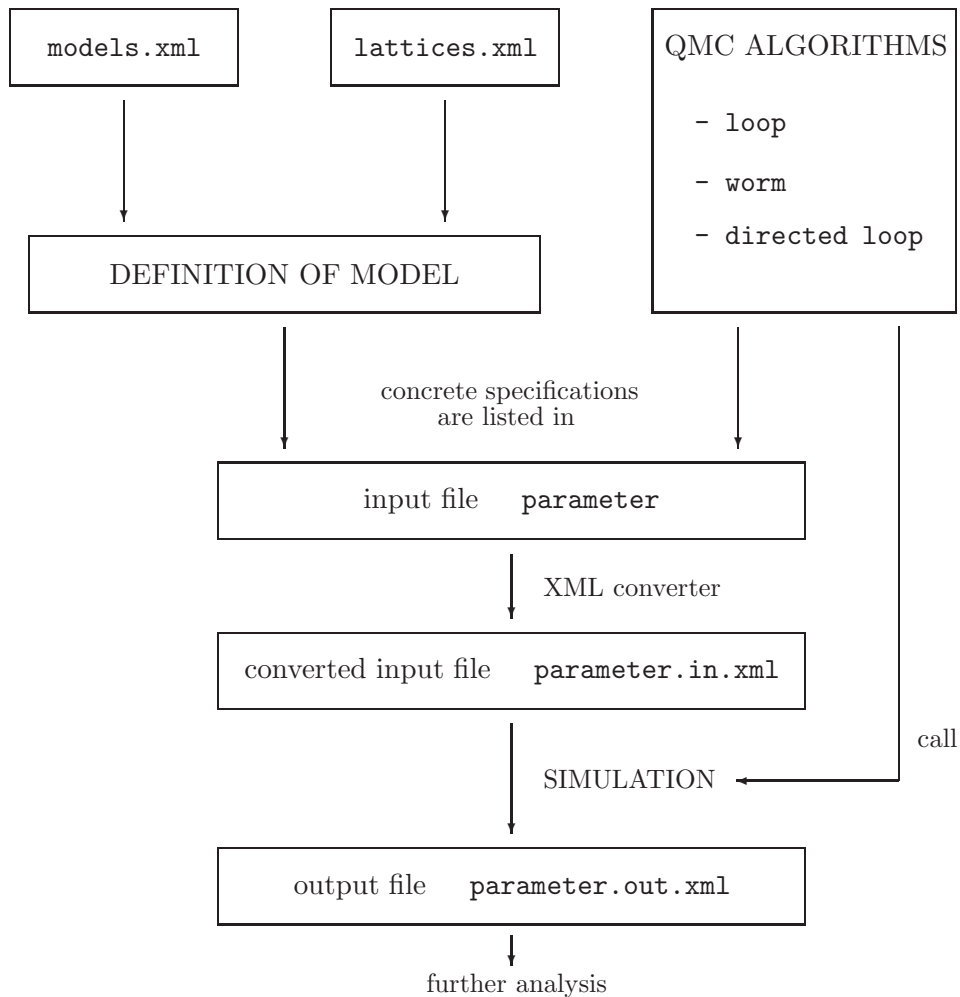


Figure 6.2: Scheme of ALPS ingredients, according to [114, 115].

6.1.2 Overview of the Algorithms

In order to highlight the modern status of the algorithms provided by the ALPS package, we will shortly, but illustratively describe and review them.

For classical systems the ALPS package offers two update methods: The original local update (`UPDATE="local"`) runs with single spin-flip procedures and risks to be stuck in certain spin configurations. The improved cluster update (`UPDATE="cluster"`) removes the resulting shortcomings by flipping entire clusters of spins and yields, as a consequence, a better convergence and more reliable results.

In the case of quantum systems we have to deal with an additional imaginary time axis and, therefore, with world lines on the space-time structure. There exist several techniques in order to update these world lines. All of the modern QMC algorithms, described in the following, provide non-local updates and a cluster-like flipping in space-time: The `loop` algorithm [116, 117] decomposes the world lines into loops and performs loop-flips in order to create new world line configurations. Despite its non-local character, the `loop` algorithm is beset by the problem of frozen configurations for several classes of problems. These freezing problems have been overcome by the invention of the `worm` [118] algorithm: A mobile worm's head, which is connected to its tail, moves in space-time and updates the world lines on the fly. The advantages of both methods are combined in the `directed loop` algorithm [119, 120], which represents a hybrid of the `worm` and `loop` algorithm: It equips the worm's head's motion with a direction and avoids thereby unnecessary movements, especially the occurrence of repeated "bounce" moves that jump forth and back between two points in space-time. As a consequence, these clever worm's head movements result in a more efficient use of the CPU time. For certain classes of problems, this `directed loop` algorithm automatically reduces to the non-local loop-update of the `loop` algorithm, which explains the origin of its name. A detailed overview on these QMC algorithms has been given in [121].

We mainly made use of the `directed loop` algorithm in the SSE representation (Stochastic Series Expansion), which proved to show the best performance for our investigated systems. On occasion, we checked our `directed loop` results with the `loop` code.

Besides these Monte Carlo algorithms, ALPS also offers diagonalization procedures: The full diagonalization procedure `fulldiag` and the Lanczos algorithm `sparsediag` that is suited for sparse matrices. Occasionally, we used the `fulldiag` algorithm on very small systems in order to test the conformance with the results gained by the QMC algorithms.

6.2 Simulation Setups and Benchmarks

We performed our simulations on a small Linux cluster consisting of six processors. Although the CPU time on these machines is limited, we achieved impressive results by studying relatively small systems. In order to validate our procedures, we performed several benchmarks for isotropic systems with our typical set of parameters that constitute successful tests for our subsequent

simulations.

6.2.1 Literature Values for Benchmarking

As a reference point to our benchmarks we choose the high-precision results of Oitmaa and Zheng [108] gained by high-temperature series expansions up to the 14th order. Their results are summarized in table 6.1. We will use this synopsis later on for a detailed comparison of the FM and AFM. At this, we will elucidate the trend of higher critical temperatures for the AFM and present illustrative explanations for this behaviour in paragraph 6.5.

	$S = \frac{1}{2}$	$S = 1$	$S = \frac{3}{2}$	$S \rightarrow \infty$
T_C^{FM}	0.839(1)	2.599(1)	5.13(8)	$\rightarrow \infty$
$\frac{T_C^{\text{FM}}}{S(S+1)}$	1.119(2)	1.2994(5)	1.37(2)	$\rightarrow 1.4429$
T_C^{AFM}	0.944(2)	2.735(1)	5.26(3)	$\rightarrow \infty$
$\frac{T_C^{\text{AFM}}}{S(S+1)}$	1.259(2)	1.3676(7)	1.404(7)	$\rightarrow 1.4429$
$\frac{T_C^{\text{AFM}} - T_C^{\text{FM}}}{S(S+1)}$	0.140(4)	0.0682(12)	0.034(32)	$\rightarrow 0$

Table 6.1: Numerical literature values for the critical temperatures of three-dimensional Heisenberg ferro- and antiferromagnets on a simple cubic lattice, gained by high-temperature series expansions [108].

Our following benchmarks will persuasively agree with these literature values.

6.2.2 Procedures and Analyses

Before we start presenting results, we point out our typically performed analyses: In order to include finite size effects and to find the critical temperature T_C of the infinite system, we applied the crossing Binder cumulants method [122]. Thereby, the Binder cumulant represents the reduced fourth order cumulant

$$U_4 = 1 - \frac{\langle M^4 \rangle}{3 \langle M^2 \rangle^2} \text{ for FMs, resp. } U_4 = 1 - \frac{\langle (M^{\text{sl}})^4 \rangle}{3 \langle (M^{\text{sl}})^2 \rangle^2} \text{ for AFMs, (6.1)}$$

with $\langle \dots \rangle$ denoting the Monte Carlo averages. The intersection points of the Binder cumulants $U_4(L, T)$ at different system sizes L^d yield eventually the critical temperature T_C of the infinite system [122]. Alternatively, we could make use of the second cumulant $U_2 = \langle M^2 \rangle / \langle |M| \rangle^2$. In practice, for a second order phase transition, a small triangle to a low scale will appear [123]. From our corresponding numerical measurements we consistently extracted this property

of the Binder cumulants, respectively of the second cumulants. In three dimensions, we usually compared simulation runs for system sizes of 216, 512 and 1000 spins. If necessary, we raised the system sizes accordingly. The resulting errors were estimated by the variations of the intersection points: Besides the small triangle that appears due to the required differing system sizes (with the main value given by the largest systems), we took into account the variations due to different interpolation schemes: We used cubic splines (usually depicted on the left-hand side) as well as straight lines (depicted on the right-hand side) in order to interpolate our measured points in various ways. Thereby, the main values have been taken from the intersections of the cubic splines, which offer appropriately smooth curve shapes. The linear interpolation has been used to employ a more elaborate error analysis: The final errors of T_C guarantee the separation of the straight lines including the error bars of the measured points.

6.2.3 $S = \frac{1}{2}$ - Heisenberg Model in Three Dimensions

For the simulation of quantum Heisenberg models we made, throughout this thesis, use of the `directed loop` algorithm. Since isotropic two-dimensional Heisenberg systems exhibit no finite critical temperature, we consequently restricted our benchmarks to the case of three dimensions. From the output data for the three-dimensional $S = \frac{1}{2}$ - model we extracted the specific heat curves for the FM and AFM, which are shown in fig. 6.3. Their shapes concord with the expectations for a second order phase transition reproduced by a finite system.

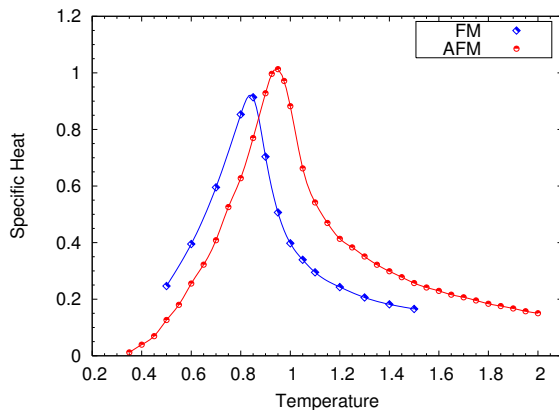


Figure 6.3: Specific heat of the $10 \times 10 \times 10$ simple cubic $S = \frac{1}{2}$ - Heisenberg model; the curves are guides to the eyes.

The application of the crossing Binder cumulant method, depicted in fig.6.4-6.5, yields the critical temperatures

$$\text{FM: } T_C = 0.833(11) , \quad (6.2)$$

$$\text{AFM: } T_C = 0.941(8) , \quad (6.3)$$

which agree very well with the literature values in table 6.1 and [124, 125, 126].

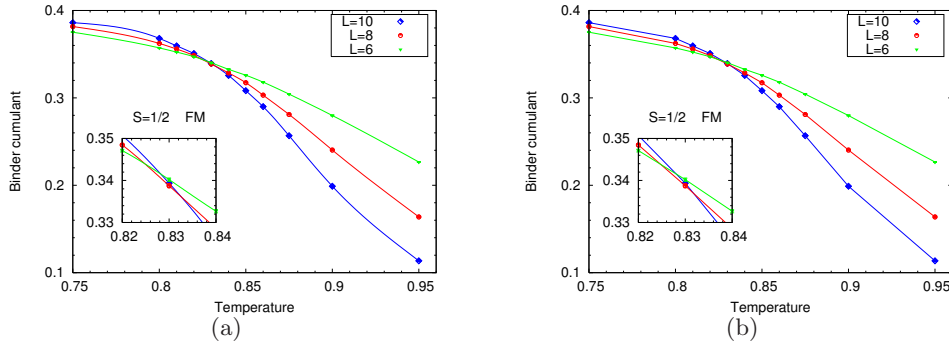


Figure 6.4: Crossing Binder cumulants $U_4(L, T)$ of the simple cubic $S = \frac{1}{2}$ - Heisenberg FM for $L \in \{6, 8, 10\}$, with L^3 denoting the total system size; the data points are interpolated by cubic splines in (a) and lines in (b).

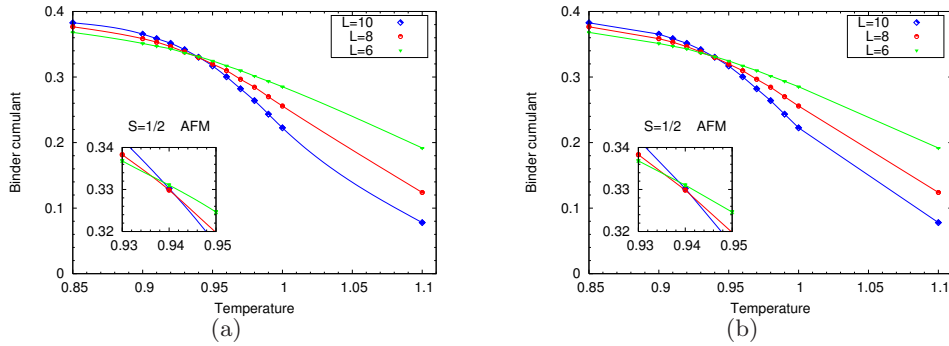


Figure 6.5: Crossing Binder cumulants $U_4(L, T)$ of the simple cubic $S = \frac{1}{2}$ - Heisenberg AFM for $L \in \{6, 8, 10\}$, with L^3 denoting the total system size; the data points are interpolated by cubic splines in (a) and lines in (b).

Please note that anisotropy fields have no effect on these critical temperatures, since the fields $(S_i^z)^2$ represent just the trivial constants $\frac{1}{4}$ for $S = \frac{1}{2}$ - systems.

Further benchmarks for quantum systems with higher spin quantum numbers $S > \frac{1}{2}$ are embedded in the following sections dealing with the presence of irreducible anisotropy fields.

6.2.4 Classical Heisenberg Model in Three Dimensions

In order to recover the classical limit $S \rightarrow \infty$, we performed a classical Monte Carlo simulation of the three-dimensional Heisenberg model using the cluster version of the classical algorithm `spinmc`. The accordingly intersecting cumulants $U_2(L, T)$ are depicted in fig. 6.6. Their different interpolation schemes

yield

$$T_C = 1.440(10) . \quad (6.4)$$

The error is smaller than 1% and coincides very well with the literature value of $T_C = 1.4429$ [108, 127, 128].

This classical value represents an important asymptotic reference point for the convergence of T_C^{FM} and T_C^{AFM} .

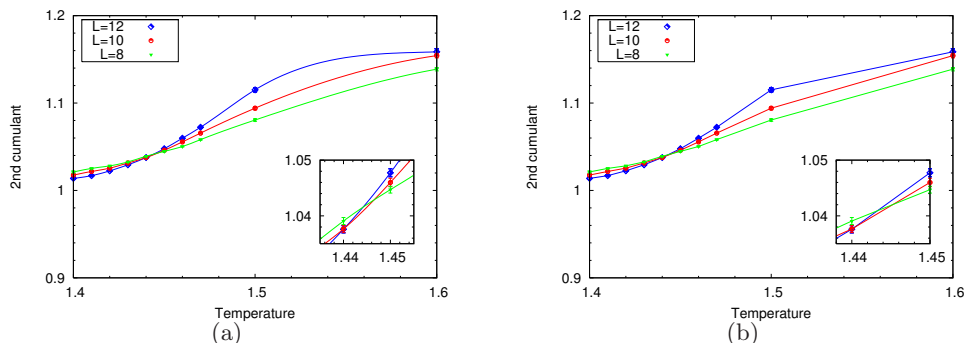


Figure 6.6: Crossing second cumulants $U_2(L, T)$ of the simple cubic classical Heisenberg model for $L \in \{8, 10, 12\}$, with L^3 denoting the total system size; the data points are interpolated by cubic splines in (a) and lines in (b).

6.2.5 Ising Model in Three Dimensions

Beyond the classical Heisenberg model, we can study the Ising model, which represents another important classical model: Since the presence of anisotropy fields renders our models Ising-like, it is worthwhile to study this simulation benchmark. From the different crossing points due to various system sizes and interpolations in fig.6.7 we gain the critical temperature of the three-dimensional Ising model

$$T_C^{3d\text{-Ising}} = 4.509(13) , \quad (6.5)$$

which concords with the high-precision results in [129]. This Ising value will represent an important limit for large anisotropy fields $h_p \gg 1$ with even p .

6.2.6 Ising Model in Two Dimensions

Due to its discrete symmetry, the Ising model circumvents the Mermin-Wagner theorem [8] and exhibits a finite critical temperature in two spatial dimensions. From the different intersections of $U_2(L, T)$ with $L \in \{16, 24, 32\}$, shown in fig.6.8, we extract the critical temperature

$$T_C^{2d\text{-Ising}} = 2.271(11) , \quad (6.6)$$

which concords very well with the famous value $T_C = 2.269$ gained by the Onsager solution [18, 19, 64]. This value will represent the according limit for the anisotropic two-dimensional Heisenberg model we will study in section 6.8.

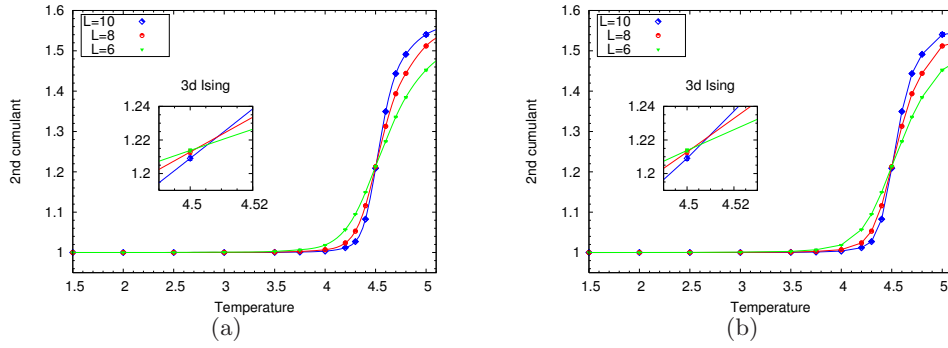


Figure 6.7: Crossing second cumulants $U_2(L, T)$ of the simple cubic Ising model for $L \in \{6, 8, 10\}$, with L^3 denoting the total system size; the data points are interpolated by cubic splines in (a) and lines in (b).

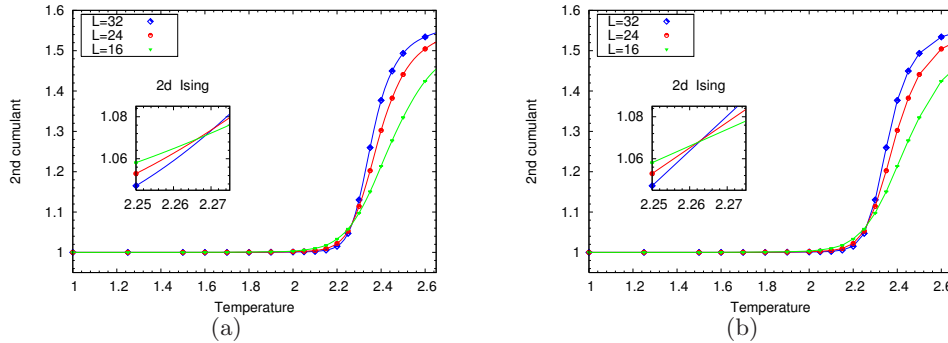


Figure 6.8: Crossing second cumulants $U_2(L, T)$ of the square lattice Ising model for $L \in \{16, 24, 32\}$, with L^2 denoting the total system size; the data points are interpolated by cubic splines in (a) and lines in (b).

6.3 Numerical Results for the $S = 1$ - Heisenberg FM

After these successful benchmarks, we turn towards simulations of quantum systems with anisotropy fields and, therefore, higher spin quantum numbers $S > \frac{1}{2}$. The following numerical outcome will represent main results of this thesis that strongly underline our previous findings: We will mainly focus on three-dimensional systems in the following sections 6.3-6.7, but will also present QMC results on two-dimensional systems in section 6.8.

We start with the $S = 1$ -Heisenberg FM in three dimensions and performed simulations for various values of the quadratic anisotropy field h_2 with the use of the `directed loop` algorithm according to our outlined procedure. The numerical results are given in table 6.2 and fig. 6.9-6.11. If no error bars are indicated (without any additional comment), the numerical errors are smaller than the size of the symbols. The `loop` algorithm yielded in benchmark tests

the same results within the error range (for $h_2 = 0$ and $h_2 \neq 0$). Additionally, the exact diagonalization (using the `fulldiag` algorithm) applied to small systems was fully consistent.

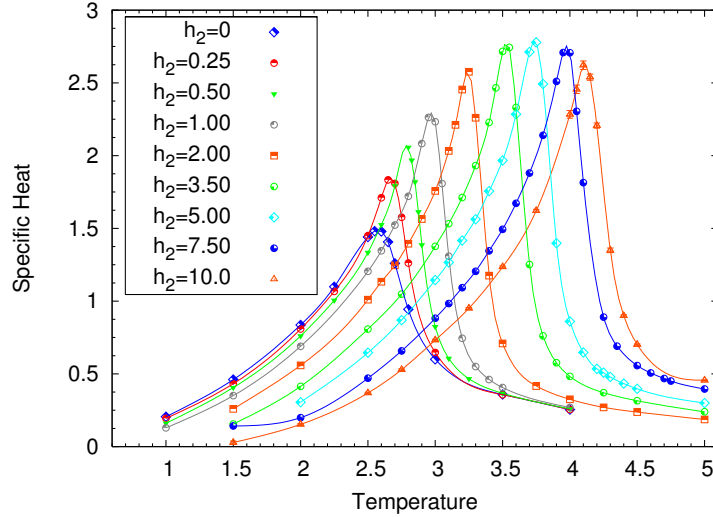


Figure 6.9: Specific heat of the $10 \times 10 \times 10$ simple cubic $S = 1$ - Heisenberg FM for various anisotropy fields $h_2 \geq 0$; the curves are guides to the eyes.

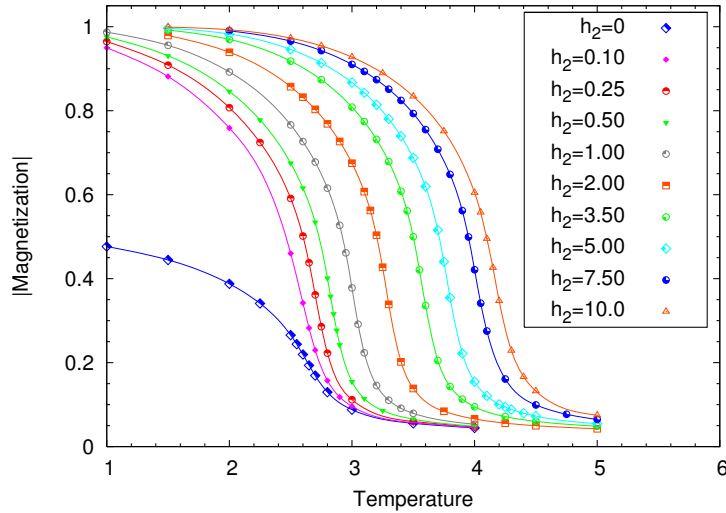


Figure 6.10: Magnetization of the $10 \times 10 \times 10$ simple cubic $S = 1$ - Heisenberg FM for various anisotropy fields $h_2 \geq 0$; the curves are guides to the eyes; the inflection points coincide with the maxima of the specific heat.

The change of T_C towards larger values is illustrated by the shift of the peaks of the specific heat C_V in fig. 6.9 and the shift of the inflection points of the magnetization in fig. 6.10. The following table 6.2 shows the resulting data for the critical temperatures $T_C(h_2)$. Their final errors are throughout smaller than 1%. The value for the isotropic system ($h_2 = 0$) is fully concordant with the literature value in table 6.1, which was gained by a 12th order expansion series [108]. All the diagrams showing the intersections of the Binder cumulants have been transferred to the appendix A in order to focus the reader's attention to the numerical results and their conclusions. We additionally checked the crossing points of the 2nd cumulants for the isotropic system, which yielded $T_C = 2.585(28)$ and are fully consistent with both the literature value and the Binder Cumulant method.

h_2	T_C
0	2.584(22)
0.1	2.708(18)
0.25	2.779(21)
0.5	2.883(16)
1.0	3.051(9)
2.0	3.325(10)
3.5	3.621(16)
5.0	3.823(10)
7.5	4.058(16)
10.0	4.201(17)

Table 6.2: Critical temperatures of the simple cubic $S=1$ - Heisenberg FM for various anisotropy fields $h_2 \geq 0$.

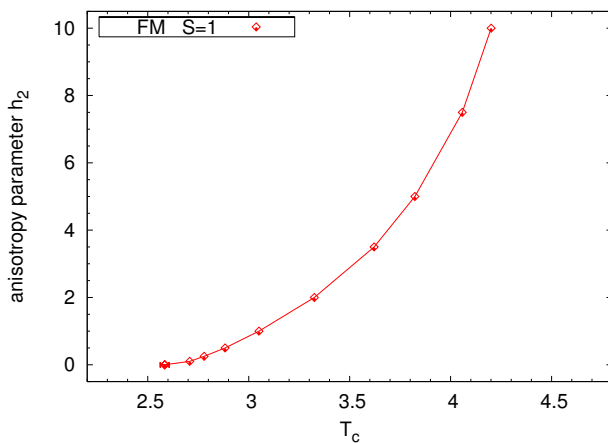


Figure 6.11: Phase diagram h_2 vs. T_C of the simple cubic $S=1$ - Heisenberg FM; the lines are guides to the eyes.

The corresponding phase diagram h_2 vs. T_C is plotted in fig. 6.11. The ever increasing slope with rising anisotropy fields accords with our expectations based on the previous chapters and highlights the final precision reached in this calculation. As a consequence, these numerical measurements confirm the rapid changes of T_C that are induced by relatively small anisotropy fields.

For large anisotropy fields ($h_2 = 10.0$), we consistently reach more than 90% of the corresponding Ising value ($T_C^{3d\text{-Ising}} \sim 4.51$ in units of J). This convergence towards an Ising-like system affirms the classical limit for $h_2 \gg 1$ for increasing fields h_2 associated with the suppression of quantum fluctuations.

6.4 Numerical Results for the $S=1$ - AFM

For the AFM we performed accordingly modified simulations for the same set of anisotropy field values. Thereby, the AFM turned out to be less convergent than the FM and, consequently, we had to raise the number of sweeps. The resulting data and phase diagram are shown in table 6.3 and fig. 6.12. The corresponding Binder cumulants are depicted in the appendix section A.2.

h_2	T_C
0	2.735(1)
0.1	2.851(22)
0.25	2.925(18)
0.5	3.016(21)
1.0	3.175(17)
2.0	3.444(12)
3.5	3.725(12)
5.0	3.928(6)
7.5	4.167(21)
10.0	4.315(28)

Table 6.3: Critical temperatures of the simple cubic $S=1$ - Heisenberg AFM for various anisotropy fields $h_2 \geq 0$; the isotropic value ($h_2 = 0$) is taken from the literature [108].

For the isotropic system we found the intersection points in the range $T_C = 2.73(1)$ fully agreeing with data from the literature [108]. Due to strong numerical fluctuations of the measured points, a more detailed error analysis was not possible for the isotropic system and we have resorted to the literature value. The remaining final errors in this calculation are smaller than 1%.

In fig. 6.12 we find the same principal shape of the curves as before for the FM case and consistently approach the Ising limit ($T_C^{3d\text{-Ising}} \sim 4.51$) for large anisotropy fields $h_2 \gg 1$. Therefore, we consistently recover the same content-related conclusions as for the FM case, which proves the final precision we reached in our simulations.

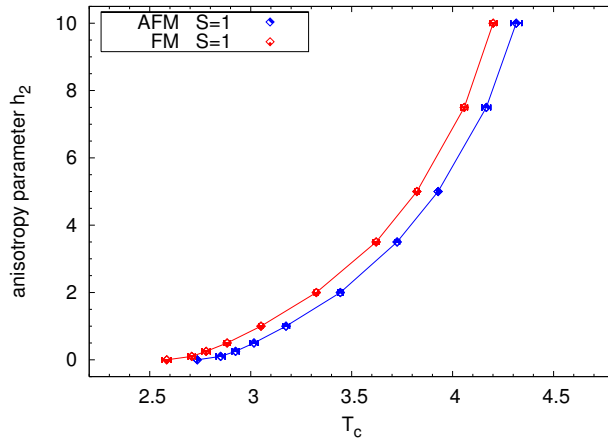


Figure 6.12: Phase diagram h_2 vs. T_C of the simple cubic $S = 1$ - Heisenberg AFM and FM; the lines are guides to the eyes.

In order to compare the numerical results for the FM and AFM, we added the FM results of the foregoing paragraph 6.3 in fig. 6.12. We will now take a closer look at the difference between T_C^{AFM} and T_C^{FM} .

6.5 Comparison of FM and AFM

It is well-known since decades that the Heisenberg AFM turns out to show a higher critical temperature than its FM counterpart [130, 131, 132]. This behaviour seems, at first glance, to be counter-intuitive due to the stronger quantum fluctuations in the AFM we extracted at $T=0$. Although it has been well established by high-temperature expansions that the difference $T_C^{\text{AFM}} - T_C^{\text{FM}}$ scales according to $\sim 1/S(S+1)$ [130, 131, 132], no physical reasons have been given in the corresponding articles in order to explain this surprising behaviour. With the use of a toy model and the spin wave dispersion, we show how to identify entropic effects at $T>0$ as the origin of the higher AFM critical temperature and make up for a convincing explanation.

As a final result, we elucidate the effects of anisotropy fields on the equalization of T_C^{AFM} and T_C^{FM} accompanied by the suppression of quantum fluctuations.

6.5.1 FM vs. AFM I - Entropy vs. Quantum Fluctuations

In contrast to the ground state sublattice magnetization $M_{T=0}^{\text{sl}}$ solely influenced by quantum fluctuations, we have now to deal with thermal effects at $T > 0$, which give rise to entropic effects. In order to estimate the impact of the latter, we study the entropy of a small toy model consisting of two quantum spins with $S = \frac{1}{2}$, which we also made use of in the introductory chapter. For this toy model the Hamiltonian reads

$$H = \pm 2J \mathbf{S}_1 \cdot \mathbf{S}_2 = \pm J \left[S_{\text{tot}}(S_{\text{tot}} + 1) - \frac{3}{2} \right], \quad (6.7)$$

with $S_{\text{tot}} \in \{0, 1\}$ denoting the total spin of the system. We imposed periodic boundary conditions in (6.7) and the upper sign refers to the AFM and the lower one to the FM.

The entropy for this model reads

$$S = \ln \left[\exp \left[\pm \frac{3J}{2T} \right] + 3 \exp \left[\mp \frac{1J}{2T} \right] \right] \pm \frac{3J}{2T} \frac{\exp \left[\mp \frac{1J}{2T} \right] - \exp \left[\pm \frac{3J}{2T} \right]}{\exp \left[\pm \frac{3J}{2T} \right] + 3 \exp \left[\mp \frac{1J}{2T} \right]}. \quad (6.8)$$

Again, the upper sign refers to the AFM and the lower one to the FM. From the plot of (6.8) in fig. 6.13, we clearly identify a larger entropy for the FM at all temperatures $T < \infty$. As a consequence, we would expect a larger critical temperature for the AFM.

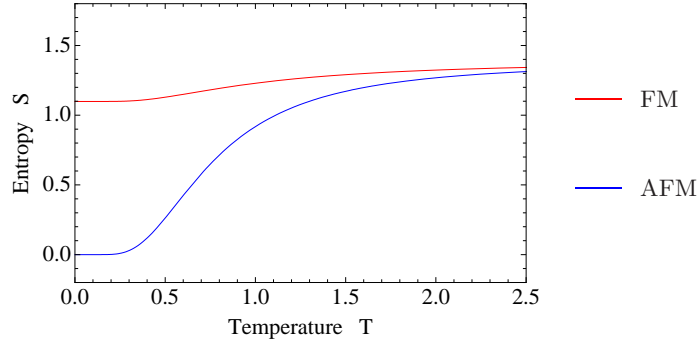


Figure 6.13: Comparison of the FM and AFM entropy (6.8) of the toy model (6.7); J has been set to unity.

For $T \rightarrow \infty$ we find $S \rightarrow \ln(4)$, for the FM as well as for the AFM, since all four orientation configurations become equilibrated. For $T \rightarrow 0$, on the contrary, we extract

$$S^{\text{AFM}} \xrightarrow{T \rightarrow 0} 0, \quad S^{\text{FM}} \xrightarrow{T \rightarrow 0} \ln(3). \quad (6.9)$$

This behaviour can be explained by the degeneracy of the FM ground state given by the three triplet states with $S_{\text{tot}} = 1$ and $m_{S_{\text{tot}}} \in \{-1, 0, 1\}$ (for the corresponding $S = 1$ - model we find a similar picture with a fivefold degeneracy at $T = 0$). The AFM, on the contrary, exhibits a non-degenerate ground state since the possible configurations are yet incorporated into the preferred singlet state. According to the third law of thermodynamics, the ground state for quantum systems should be unique due to the spontaneous symmetry breaking in the thermodynamical limit [60]. In order to model this unique ground state, we lift this degeneracy by hand and, for this purpose, switch on a small magnetic field $h_1 \neq 0$. The corresponding Hamiltonian

$$H = \pm 2J \mathbf{S}_1 \cdot \mathbf{S}_2 - h_1 (S_1^z + S_2^z) \quad (6.10)$$

leads to the entropy

$$\begin{aligned}
 S &= \ln \left[\exp \left[\pm \frac{3J}{2T} \right] + \exp \left[\mp \frac{1J}{2T} \right] \cdot \left(1 + 2 \cosh \left[\frac{h_1}{T} \right] \right) \right] \\
 &\mp \frac{J}{T} \frac{\frac{3}{2} \exp \left[\pm \frac{3J}{2T} \right] - \frac{1}{2} \exp \left[\mp \frac{1J}{2T} \right] \cdot \left(1 + 2 \cosh \left[\frac{h_1}{T} \right] \right)}{\exp \left[\pm \frac{3J}{2T} \right] + \exp \left[\mp \frac{1J}{2T} \right] \cdot \left(1 + 2 \cosh \left[\frac{h_1}{T} \right] \right)} \\
 &- 2 \frac{h_1}{T} \frac{\exp \left[\mp \frac{1J}{2T} \right] \cdot \sinh \left[\frac{h_1}{T} \right]}{\exp \left[\pm \frac{3J}{2T} \right] + \exp \left[\mp \frac{1J}{2T} \right] \cdot \left(1 + 2 \cosh \left[\frac{h_1}{T} \right] \right)}, \quad (6.11)
 \end{aligned}$$

which is depicted for various h_1 in fig. 6.14 and 6.15. From these figures and (6.11), we clearly extract, for the AFM as well as for the FM, the correct limit $S \rightarrow 0$ for $T \rightarrow 0$.

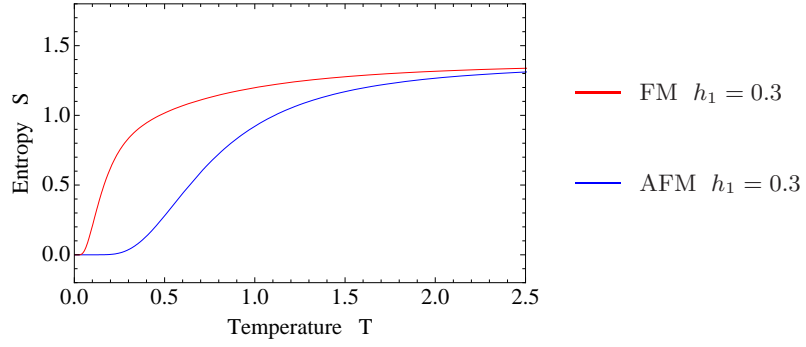


Figure 6.14: Comparison of the FM and AFM entropy (6.11) of the toy model (6.10) for $h_1 = 0.3$; J has been set to unity.

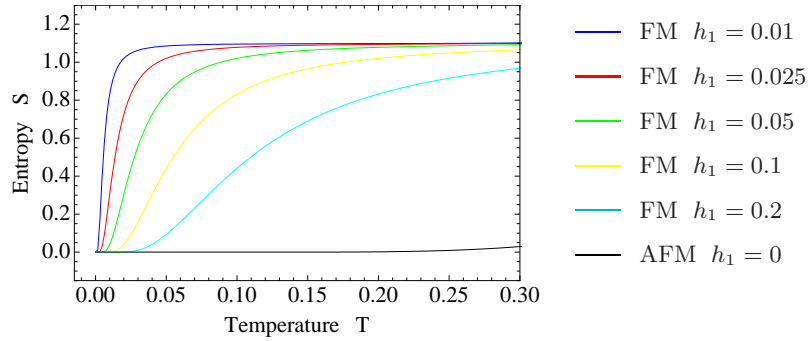


Figure 6.15: Comparison of the FM and AFM entropy (6.11) of the toy model (6.10) for various h_1 ; J has been set to unity.

Nonetheless, the main message of this paragraph remains principally unchanged: As a final result, we state that the entropy of the FM remains larger than for the AFM at all temperatures $0 < T < \infty$, which consequently results in a larger critical temperature of the AFM.

Therefore, we identify entropic effects as the physical origin of $T_C^{\text{AFM}} > T_C^{\text{FM}}$.

6.5.2 FM vs. AFM II - Spin Wave Dispersion

Besides this toy model, we can build an alternative explanation upon the spin wave picture. Since the significant energy scale for excitations is given by the spin wave energies according to $E = E_0 + \sum_{\mathbf{q}} \omega_{\mathbf{q}} \langle n_{\mathbf{q}} \rangle$, with $\langle \dots \rangle$ denoting the average according to the Bose-Einstein distribution, we will take a closer look at the different dispersion relations for the FM and AFM [93, 94]:

$$\omega_{\mathbf{q}} \sim \begin{cases} |\mathbf{q}|^2 & \text{for the FM,} \\ |\mathbf{q}| & \text{for the AFM.} \end{cases} \quad (6.12)$$

Therefore, we find at the critical point for $|\mathbf{q}| \rightarrow 0$ generally larger excitation energies for the AFM, which suggests that the AFM is more stabilized against thermal fluctuations than the FM.

This suggestion can be further concretized by considering the density of states $D(\omega)$; referring to the systems investigated in the foregoing paragraphs, we will outline the three-dimensional case: Due to $N(\omega) \sim |\mathbf{q}|^3$ states in a sphere of radius $|\mathbf{q}|$ with $dN \sim |\mathbf{q}|^2 dq \sim D(\omega) d\omega$, we find with (6.12) the following differing densities of states for the FM and AFM:

$$D(\omega) \sim \begin{cases} \sqrt{\omega} & \text{for the FM,} \\ \omega^2 & \text{for the AFM.} \end{cases} \quad (6.13)$$

The lower density of states for the AFM at the critical point in the long wavelength limit ($|\mathbf{q}| \rightarrow 0$) emphatically underlines the picture that the AFM is less excitable than the FM and is, therefore, effectively stronger stabilized against fluctuations, which consequently results in a higher critical temperature for the AFM.

The following paragraphs will deal with the possibilities to reduce these differences between the critical temperatures of the FM and AFM.

6.5.3 Reducing $T_C^{\text{AFM}} - T_C^{\text{FM}}$ by Anisotropy Fields

Comparing the FM and AFM results for $S = 1$ in table 6.2-6.4, we observe a decreasing difference between T_C^{AFM} and T_C^{FM} with increasing anisotropy fields. This observation indicates that both systems are made more classical by an increasing anisotropy field, thereby reducing quantum fluctuations. Unfortunately, the error bars are too large to find the shape of the decaying quantum fluctuations. At least, we can find following result: Using high-precision results from the literature for $h_2 = 0$ [108], the difference $T_C^{\text{AFM}} - T_C^{\text{FM}}$ becomes, for

$h_2 = 3.5$ and $h_2 = 5.0$, smaller than its isotropic difference including the error bars (for larger anisotropy fields the simulations become more elaborate, which leads to larger errors again and, therefore, results in an overlapping of the error bars). This finding is a clear indication of reduced quantum fluctuations for sufficiently high anisotropy fields since the system becomes more classical.

h_2	$T_C^{\text{AFM}} - T_C^{\text{FM}}$
0	0.136 ± 0.002
0.1	0.143 ± 0.040
0.25	0.146 ± 0.039
0.5	0.133 ± 0.037
1.0	0.124 ± 0.026
2.0	0.119 ± 0.022
3.5	0.104 ± 0.028
5.0	0.105 ± 0.016
7.5	0.109 ± 0.037
10.0	0.114 ± 0.045

Table 6.4: Differences of the critical temperatures of the FM and AFM $S=1$ - Heisenberg model on a simple cubic lattice for various anisotropy fields $h_2 \geq 0$; the isotropic value ($h_2 = 0$) is taken from the literature [108].

6.5.4 Reducing $T_C^{\text{AFM}} - T_C^{\text{FM}}$ by Large Spin Quantum Numbers

Another possibility to decrease the difference between the FM and AFM critical temperatures in the isotropic system is given by the enlargement of the spin quantum number S : The convergence towards the unique classical value $T_C = 1.4429$ (see table 6.1 and paragraph 6.2.4) is depicted in fig. 6.16. Thereby, we replaced the literature value for $T_C^{\text{FM}}/S(S+1)$ for $S = \frac{3}{2}$ by our own simulation result 1.360(11) of the coming paragraph, which proved to show a smaller error bar.

As a consequence, the most profound changes, i.e. the steepest slopes of these differences, occur in the region of smallest S , as pointed out in fig. 6.17. From these diminished differences, we may conclude that increasing spin quantum numbers consequently suppress quantum fluctuations and render the original quantum system more and more classical. These effects especially come to light for systems starting at small S and exhibiting strong quantum character. Therefore, we recover in our simulations the fascinating interplay of the spin quantum number S and the anisotropy fields h_p , which both represent a classical limit for large values and consequently conceal the quantum character of spin systems with rising values.

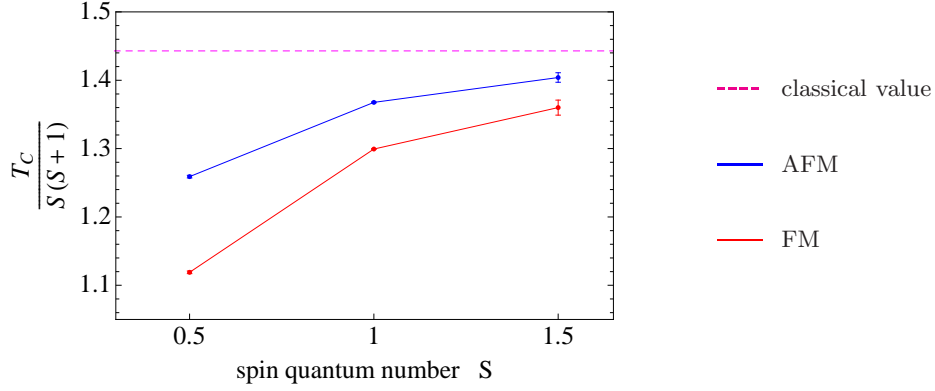


Figure 6.16: Comparison of the rescaled critical temperatures $\frac{T_C}{S(S+1)}$ of the FM and AFM for various spin quantum numbers S ; the lines are guides to the eyes.

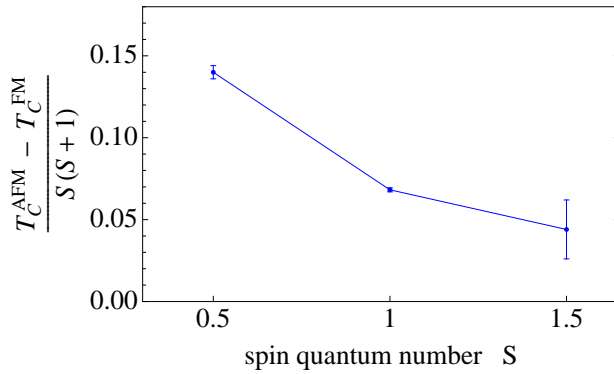


Figure 6.17: Difference of the rescaled critical temperatures of the FM and AFM for various spin quantum numbers S ; the lines are guides to the eyes.

6.6 Numerical Results for $S = \frac{3}{2}$

We successfully extended our simulations to the case $S = \frac{3}{2}$. The following results will clearly confirm and underline our previous numerical measurements and their according conclusions.

6.6.1 $S = \frac{3}{2}$ - FM

The following table 6.5 shows the resulting data for the $S = \frac{3}{2}$ - Heisenberg FM, which are plotted in fig. 6.18. The isotropic value agrees perfectly with the value from the literature, which was obtained by a 9th order expansion series

[108]. Our error turns out to be even smaller than in this reference. All the final errors in this calculation are again smaller than 1%.

h_2	T_C
0	5.099(39)
0.25	5.498(40)
0.5	5.734(20)
1.0	6.135(19)
2.0	6.783(23)
3.5	7.509(19)
5.0	8.043(11)
7.5	8.719(37)
10.0	9.166(23)
12.5	9.475(54)

Table 6.5: Critical temperatures of the simple cubic $S = \frac{3}{2}$ - Heisenberg FM for various anisotropy fields $h_2 \geq 0$.

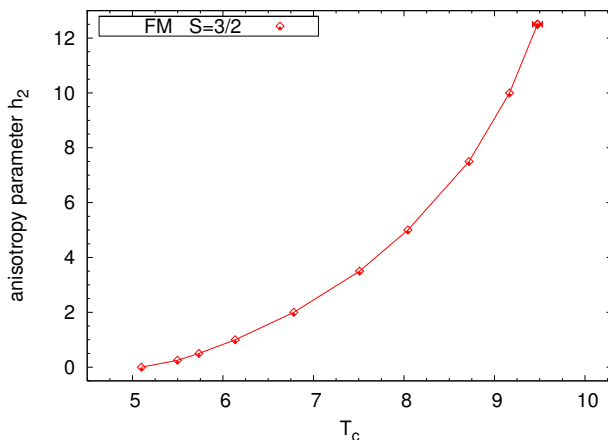


Figure 6.18: Phase diagram h_2 vs. T_C of the simple cubic $S = \frac{3}{2}$ - Heisenberg FM; the lines are guides to the eyes.

The ever increasing slope with rising anisotropy fields shows again the finally reached precision and demonstrates the classical trend of anisotropic spin systems. Consistently, more than 90% of the Ising value are reached for large anisotropy fields $h_2 \gg 1$ ($h_2 = 12.5$). The Ising value for $S = \frac{3}{2}$ is given by $T_C^{3d\text{-Ising}} \sim 4.51 \cdot S^2 \sim 10.15$ (in units of $|J|$). Please note that the rescaling changes from $S(S+1)$ in the pure quantum case ($h_2 = 0$) to S^2 in the classical limit ($h_2 \gg 1$), which further demonstrates the conversion towards a system with classical properties. This finding strengthens our main message that quantum fluctuations are strongly influenced and suppressed by anisotropy fields.

6.6.2 $S = \frac{3}{2}$ - AFM

For the $S = \frac{3}{2}$ - AFM we found the same principal behaviour: Based on table 6.6 we plotted in fig.6.19 the corresponding phase diagram together with its FM counterpart. The isotropic value agrees perfectly with the data from the literature [108], and for $h_2 = 12.5$ about 95% of the Ising value have been consistently reached ($T_C^{3d\text{-Ising}} \sim 10.15$).

h_2	T_C
0	5.226(47)
0.25	5.639(49)
0.5	5.872(30)
1.0	6.281(12)
2.0	6.911(15)
3.5	7.622(10)
5.0	8.162(33)
7.5	8.834(26)
10.0	9.284(36)
12.5	9.596(53)

Table 6.6: Critical temperatures of the simple cubic $S = \frac{3}{2}$ - Heisenberg AFM for various anisotropy fields $h_2 \geq 0$.

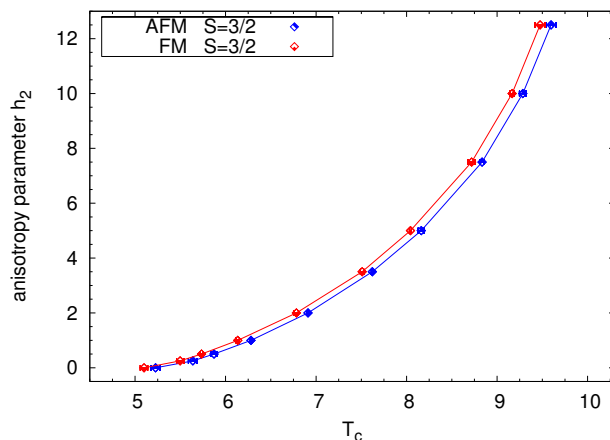


Figure 6.19: Phase diagram h_2 vs. T_C of the simple cubic $S = \frac{3}{2}$ - Heisenberg FM and AFM; the lines are guides to the eyes.

Unfortunately, we cannot extract the convergence between T_C^{AFM} and T_C^{FM} from the numerical data in table 6.5 and 6.6, as we did before for $S = 1$: The error bars are finally too large to draw such conclusions. For the isotropic system, as an example, we found $T_C^{\text{AFM}} - T_C^{\text{FM}} = 0.127 \pm 0.086$ (literature value

[108]: 0.13 ± 0.11), which highlights the problem of underlying large error bars. Therefore, we will skip a comparison of FM and AFM for larger spin quantum numbers S in the following.

6.7 Numerical Results for the $S = 2$ - FM

In order to investigate higher-order, but irreducible anisotropy fields, we performed QMC simulations for the $S = 2$ - Heisenberg FM

$$H = - \sum_{\langle ij \rangle} J_{ij} \mathbf{S}_i \cdot \mathbf{S}_j - h_p \sum_i (S_i^z)^p \quad \text{with } p \in \{2, 4\} \quad \text{for } S = 2. \quad (6.14)$$

As a consequence, we may study and elucidate the relevance of these higher-order fields. The outcome will fully confirm our previous analytical predictions for small spin quantum numbers.

6.7.1 $p = 2$: Quadratic Fields

The QMC simulations for the $S = 2$ - Heisenberg FM, influenced by quadratic fields ($p = 2$), are shown in table 6.7 and depicted in fig. 6.20. We found a consistent shape of the curves and reached consequently more than 90% of the corresponding Ising value ($T_C^{3d\text{-Ising}} \sim 18.0$) for large anisotropy fields $h_2 \gg 1$.

h_2	T_C
0	8.310(76)
0.1	8.734(53)
0.25	8.999(61)
0.5	9.410(40)
1.0	10.119(18)
2.0	11.252(40)
3.5	12.558(49)
5.0	13.534(73)
7.5	14.830(64)
10.0	15.755(81)
12.5	16.447(105)

Table 6.7: Critical temperatures of the simple cubic $S = 2$ - Heisenberg FM for various quadratic anisotropy fields $h_2 \geq 0$.

6.7.2 $p = 4$: Quartic Fields

In order to compare the results for $p = 2$ and $p = 4$, we have to rescale the quartic fields h_4 appropriately by S^2 :

$$h_4 = \frac{h_2}{S^2}. \quad (6.15)$$

The corresponding numerical results for the comparable set of h_4 are shown in table 6.8. The concluding phase diagram is depicted in fig. 6.20.

h_4	T_C
0	8.310(76)
0.025	8.748(57)
0.0625	9.055(53)
0.125	9.498(36)
0.25	10.256(23)
0.5	11.489(18)
0.875	12.905(38)
1.25	13.998(61)
1.875	15.292(38)
2.5	16.240(76)
3.125	16.875(154)

Table 6.8: Critical temperatures of the simple cubic $S = 2$ - Heisenberg AFM for various quartic anisotropy fields $h_4 \geq 0$.

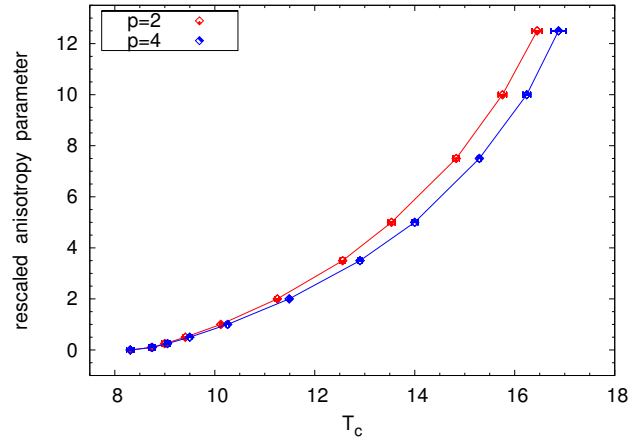


Figure 6.20: Phase diagram h_p vs. T_C of the simple cubic $S=2$ - Heisenberg FM for quadratic ($p = 2$) and quartic ($p = 4$) anisotropy fields h_p ; the lines are guides to the eyes.

From the tables 6.7-6.8 and fig. 6.20 we can conclude

$$T_C(h_4 = h_2/S^2) > T_C(h_2) \quad \text{for } h_2 \geq 0.5. \quad (6.16)$$

This finding fully concurs with the result of our Quantum Mean Field study for small spin quantum numbers S in chapter 3. Since we have started from the same isotropic value for T_C , the error bars are overlapping for small anisotropy fields, but for $h_2 \geq 0.5$ their separation is guaranteed.

As a consequence and a final result, we can successfully confirm by reliable QMC simulations that higher-order anisotropy fields ($p > 2$) exhibit a larger relevance for small spin quantum numbers S .

6.8 Numerical Results for Two-Dimensional Systems

In this section we present QMC results on the $S = 1$ - Heisenberg model in two spatial dimensions on a square lattice: We will compare the critical temperatures of the FM and AFM for various values of the quadratic anisotropy field h_2 . Since very small anisotropy fields induce large finite size effects [54], the determination of critical temperatures $T_C(h_2)$ in the presence of small fields demands in turn the simulation of correspondingly large system sizes: An illustrative warning for $h_2 = 0.01$ is given in [54]. Therefore, we will restrict ourselves to values of the anisotropy field down to $h_2 = 0.1$. We extracted the critical temperatures, as described before, via the intersection points of the Binder cumulants $U_4(L, T)$. In two dimensions we usually used the three distinct linear extents $L \in \{16, 24, 32\}$, with L^2 denoting the total number of spin sites. The correspondingly intersecting Binder cumulants are documented in appendix A.7 - A.8.

6.8.1 $S = 1$ - FM in Two Dimensions

The resulting critical temperatures of the two-dimensional $S = 1$ - Heisenberg FM are summarized in table 6.9 and illustrated in fig. 6.21. Our determined critical temperature for $h_2 = 1.5$ concords very well with the QMC value, which is shown as an example in [54]. However, the authors in [54] did not investigate the whole parameter range, but mainly presented the feasibility of a corresponding QMC approach and, thus, limited themselves to illustrative examples [54]. The expected ever increasing slope over the whole parameter range in fig. 6.21 highlights the final precision we reached in our numerical simulations. For large anisotropy fields we consistently reach over 90% of the corresponding Ising value $T_C^{2d\text{-Ising}} = 2.269$ given by Onsager's famous solution of the two-dimensional Ising model [18, 19, 64].

h_2	T_C
0	0
0.1	1.116(26)
0.25	1.239(11)
0.5	1.375(6)
0.75	1.473(6)
1.0	1.555(6)
1.5	1.675(9)
2.0	1.760(11)
3.5	1.964(14)
5.0	2.078(12)

Table 6.9: Critical temperatures of the square lattice $S = 1$ - Heisenberg FM for various anisotropy fields $h_2 \geq 0$.

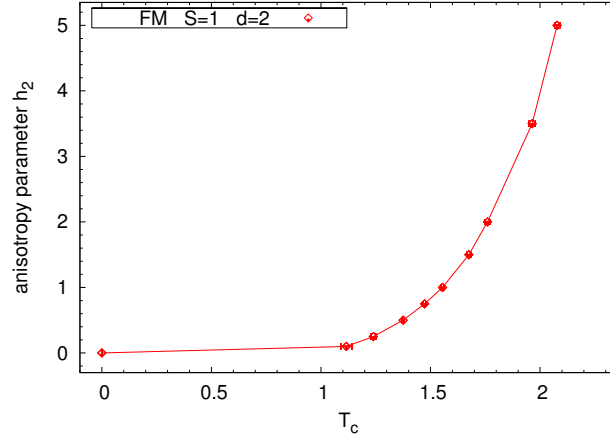


Figure 6.21: Phase diagram h_2 vs. T_C of the square lattice $S = 1$ - Heisenberg FM; the lines are guides to the eyes.

From the non-existence of any intersection points of the Binder cumulants $U_4(L, T)$ for the isotropic system in fig. 6.22, which are usually typical for second order phase transitions, we deduce, in concordance with the Mermin-Wagner theorem, the non-existence of a finite critical temperature in two dimensions: $T_C = 0$.

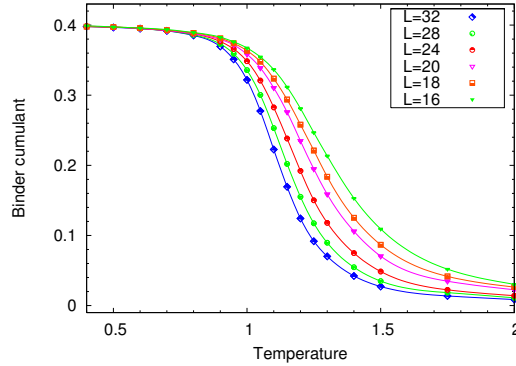


Figure 6.22: Binder cumulants $U_4(L, T)$ of the isotropic $S = 1$ - Heisenberg FM for various linear extents $L \in \{16, 18, 20, 24, 28, 32\}$, with L^2 denoting the total number of lattice sites; the curves are guides to the eyes.

Assuming the scaling behaviour

$$U_4\left(\frac{L_1}{\xi(T_1)}\right) = U_4\left(\frac{L_2}{\xi(T_2)}\right) \quad (6.17)$$

for different linear extents L_i and different temperatures T_i , we can furthermore

confirm the shape of the correlation length [133]

$$\xi(T) \sim \exp \left[+ \frac{a}{T} \right] \quad (6.18)$$

with the numerical constant $a = 5.77 \pm 0.43$; the error is given by the standard deviation of the results given by all of the pairs of L_i and T_i depicted in fig. 6.22 in the temperature region $T \in [1.0, 1.3]$; we choose the latter temperature region, since it exhibits a clear separation of the curves.

6.8.2 $S = 1$ - AFM in Two Dimensions

The numerical results for the $S = 1$ - AFM are shown in table 6.10. The numerical data for the isotropic ($h_2 = 0$) AFM are, as usual, very slowly convergent. Nevertheless, we did not recognize the typical intersection behaviour of the Binder cumulants, which is expected for second order transitions at finite temperatures. Thus, we can conclude from the Mermin-Wagner theorem that the critical temperature vanishes ($T_C = 0$) for the isotropic system.

h_2	T_C
0	0
0.1	1.208(27)
0.25	1.327(12)
0.5	1.461(8)
0.75	1.563(8)
1.0	1.639(14)
1.5	1.763(14)
2.0	1.863(9)
3.5	2.059(11)
5.0	2.159(48)

Table 6.10: Critical temperatures of the square lattice $S = 1$ - Heisenberg AFM for various anisotropy fields $h_2 \geq 0$.

The AFM phase diagram h_2 vs. T_C is depicted in fig. 6.23, together with the FM results. From our numerical measurements we clearly find the behaviour

$$T_C^{\text{AFM}}(h_2) \geq T_C^{\text{FM}}(h_2) \quad \forall h_2 \geq 0, \quad (6.19)$$

which we could explain in section 6.5. Therefore, our numerical study on two-dimensional systems persuasively complements our previous investigations and findings.

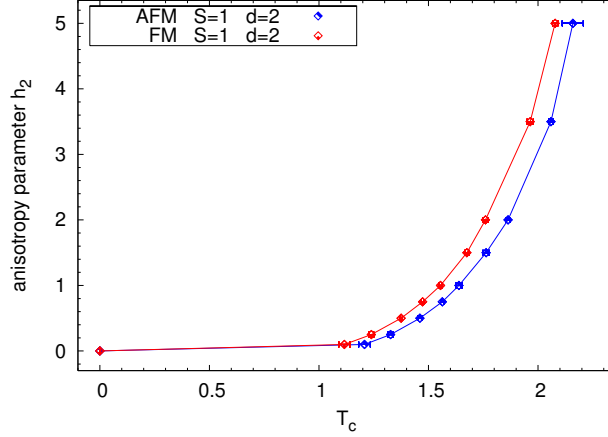


Figure 6.23: Phase diagram h_2 vs. T_C of the square lattice $S = 1$ - Heisenberg FM and AFM; the lines are guides to the eyes.

6.9 Comparison to the Analytical RPA Results

In order to mutually validate our numerical QMC results with the outcome of an analytical theory, we fitted our numerical measurement points with the $T_C(h_p)$ -behaviour (5.179)-(5.180) found by the RPA technique:

$$T_C^{2d}(h_p) = \frac{a J S(S+1)}{\ln\left[1 + b \frac{J}{h_p}\right]}, \quad (6.20)$$

$$T_C^{3d}(h_p) = \frac{J S(S+1)}{u - v \sqrt{\frac{h_p}{J}} \arctan\left[w \sqrt{\frac{J}{h_p}}\right]}. \quad (6.21)$$

Thereby, we changed $\{a, b\}$ and $\{u, v, w\}$ to variable fit parameters used for the following fits (with J set to one).

Due to the $T_C(h_p \rightarrow \infty) \rightarrow \infty$ - problem [104], which consequently causes deviations for larger values of the anisotropy fields, we had to restrict the fitting procedure to small fields h_p . The resulting fits in fig. 6.24 - 6.27 show a brilliant coincidence with our simulated data points and represent a strong confirmation of our employed techniques.

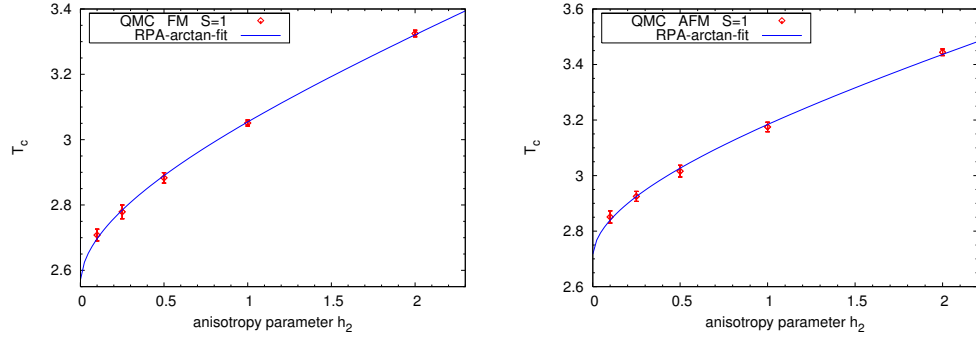


Figure 6.24: Fitting our three-dimensional QMC data for $S=1$ with the function (6.21); the resulting fit parameters are $\{u = 0.78, v = 0.08, w = 2.29 \cdot 10^7\}$ for the FM on the left-hand side and $\{u = 0.74, v = 0.07, w = 2.14 \cdot 10^7\}$ for the AFM on the right-hand side; the large values for the parameter w have only a slight impact due to the asymptotic behaviour of arctan.

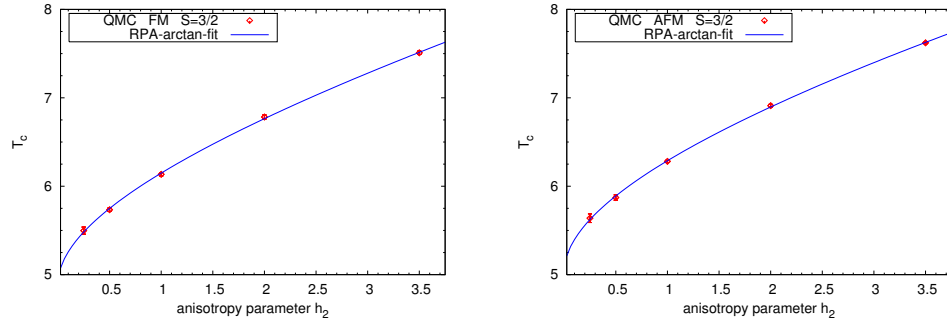


Figure 6.25: Fitting our three-dimensional QMC data for $S = \frac{3}{2}$ with the function (6.21); the resulting fit parameters are $\{u = 0.77, v = 0.11, w = 6.82\}$ for the FM on the left-hand side and $\{u = 0.75, v = 0.11, w = 6.50\}$ for the AFM on the right-hand side.

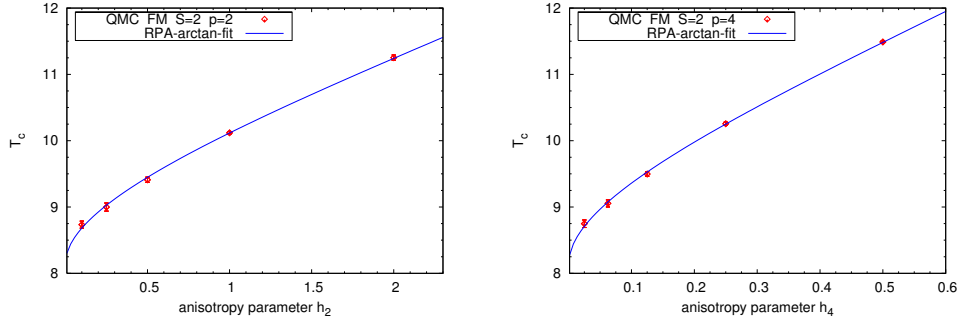


Figure 6.26: Fitting our three-dimensional QMC data for $S=2$ with the function (6.21); the resulting fit parameters are $\{u = 0.74, v = 0.09, w = 1.37 \cdot 10^7\}$ for $p = 2$ on the left-hand side and $\{u = 0.74, v = 0.19, w = 1.57 \cdot 10^4\}$ for $p = 4$ on the right-hand side; the large values for the parameter w have only a slight impact due to the asymptotic behaviour of arctan.

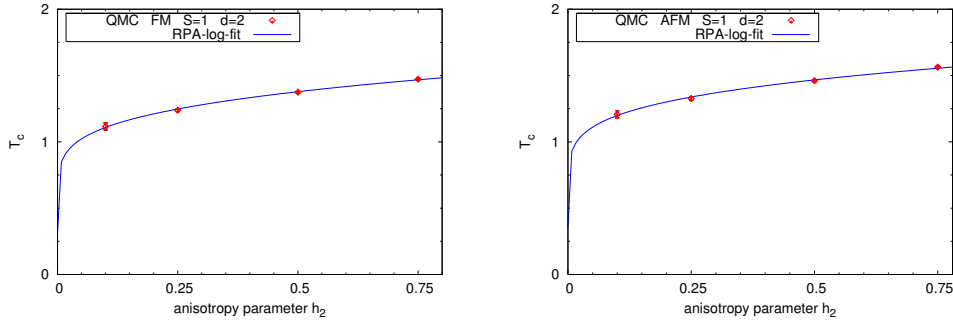


Figure 6.27: Fitting our two-dimensional QMC data for $S=1$ with the function (6.20); the resulting fit parameters are $\{a = 4.57, b = 376.61\}$ for the FM on the left-hand side and $\{a = 5.27, b = 656.78\}$ for the AFM on the right-hand side.

6.10 Retrospect and Outlook

In the course of this chapter we successfully performed Quantum Monte Carlo simulations for various Heisenberg systems: In three dimensions, we investigated the influence of quadratic ($p = 2$) anisotropy fields for FMs and AFMs with the spin quantum numbers $S = 1$ and $S = \frac{3}{2}$. We further studied quadratic ($p = 2$) and quartic ($p = 4$) anisotropy fields for $S = 2$ - FMs in three dimensions. Additionally, we analysed for $S = 1$ the effects of quadratic anisotropy fields on two-dimensional FMs and AFMs.

As a consequence, we could highlight and further elucidate the phenomenon that anisotropy fields profoundly suppress quantum fluctuations; several issues clarify the conversion of the original quantum systems into systems exhibiting classical properties:

- For large anisotropy fields we consistently recovered the classical Ising limits $T_C^{3d\text{-Ising}} \sim 4.51 \cdot S^2$ and $T_C^{2d\text{-Ising}} \sim 2.27 \cdot S^2$ (in units of J).
- The rescaling of the critical temperatures is altered: It changes from the quantum rescaling $S(S + 1)$ for the isotropic ($h_p = 0$) case towards the classical rescaling S^2 for large anisotropy fields $h_p \gg 1$.
- For all parameter sets we found principally identical phase diagrams: The shape of the curves with the ever increasing slope in the fig. 6.12, 6.19, 6.20 and 6.23 manifests the most profound suppression of quantum fluctuations by relatively small anisotropy fields. This finding concords with our previous results concerning the sensitivity to anisotropy fields.
- The difference between the critical temperatures for AFMs and FMs, originating from quantum effects, is diminished by increasing anisotropy fields. For the three-dimensional $S = 1$ - model we could numerically substantiate this trend of convergence.

Furthermore, we could mutually validate our results from different theories: We successfully fitted our QMC simulation data with the analytical functions $T_C(h_p)$ gained by the RPA approach. The resulting fits are shown in paragraph 6.9.

In addition, we could further elucidate the relevance of higher-order anisotropy fields ($p > 2$) and could, thereby, fully affirm our analytical quantum mean field predictions from chapter 3: Higher-order anisotropies exhibit a larger relevance for small spin quantum numbers S , which has been demonstrated by stronger shifts of the critical temperatures.

Subsequent studies could extend these investigations towards larger spin quantum numbers S and higher orders p of the anisotropies, but would in turn require more elaborate simulation setups.

Further studies could as well deal with disordered systems containing diluted impurity spins. Their investigation would reveal the fascinating interplay of disorder and anisotropy fields and their combined effects on the suppression of quantum fluctuations. We pick up this topic in the coming chapter that provides a detailed and concretized outlook for disordered systems.

Chapter 7

Outlook: Extension to Disordered Systems

In the foregoing chapters we considered clean and homogeneous systems. Their lattice sites were all occupied by spins without exception. We will now open the way for subsequent studies based on this thesis treating disordered systems on diluted lattices. Such further investigations could offer lucrative outcomes, but have to deal with several difficulties, as Sandvik pointed out in a recent publication [134]:

“Systems with a finite concentration of impurities are much more difficult to treat, both analytically and numerically.”

7.1 Dilution - Motivation for Ongoing Research

The study of disordered systems offers the possibility to investigate an additional intriguing parameter: The dilution of the spins on a given lattice is expected to influence the prevailing quantum fluctuations in a profound manner.

In order to elucidate this fascinating influence, the primarily interesting quantity for FMs is the magnetization M representing the average of the local magnetizations $\langle S_i^z \rangle$

$$M = \frac{1}{N_{\text{imp}}} \sum_{i=1}^{N_{\text{imp}}} \langle S_i^z \rangle, \quad (7.1)$$

with N_{imp} denoting the number of impurity sites (occupied sites). Alternatively, one could study the magnetization \overline{M} of the entire lattice, which consists of occupied and empty lattice sites,

$$\overline{M} = \frac{1}{N_{\text{tot}}} \sum_{i=1}^{N_{\text{imp}}} \langle S_i^z \rangle = \frac{N_{\text{imp}}}{N_{\text{tot}}} M, \quad (7.2)$$

with N_{tot} denoting the total number of lattice sites (occupied and non-occupied). The latter quantity is measured in most of the corresponding experiments, which operate on a broad spatial resolution scale. Based on the magnetization, further important quantities can be derived, especially the critical temperature that depends now on the impurity concentration $x = N_{\text{imp}}/N_{\text{tot}}$.

In order to motivate further studies on this issue, we will demonstrate the use of ALPS for QMC simulations on depleted lattices and outline the analytical and numerical implementation of the disordered FM on the RPA level. In the end we will give a promising outlook to disordered AFMs. These topics have been initiated in the course of this thesis and their research is going on with our collaboration partner G. Bouzerar from CNRS in Grenoble, France.

7.2 Monte Carlo on Diluted Lattices

The ALPS community [113] steadily upgrades their algorithms and codes and periodically publishes new releases. At the end of 2007, the ALPS community released the important version ALPS 1.3 [112]. This extended simulation package especially provides the modification of the dilution on a given lattice via the input parameters `DEPLETION` and `DEPLETION_SEED`. The parameter `DEPLETION`, ranging from 0 to 1, allows to tune the probability of the occupation of each lattice site. The input parameter `DEPLETION_SEED` further allows to fix the random numbers generated by the algorithms.

We performed a detailed benchmark with the use of the classical algorithm `spinmc` applying cluster updates: We compared the specific heat C_V of the three-dimensional Ising model for various depletion probabilities, tuned by the parameter `DEPLETION`, and averaged the outcome over $N_c = 10$ distinct disorder configurations induced by different values for the `DEPLETION_SEED`. The average over the N_c distinct disorder configurations, $C_V^{(i)}(T)$, $i = 1, \dots, N_c$, is thereby taken arithmetically for each numerical temperature measurement:

$$\langle C_V(T) \rangle_{\text{av}} = \frac{1}{N_c} \sum_{i=1}^{N_c} C_V^{(i)}(T). \quad (7.3)$$

Its standard deviation is accordingly given by

$$\sigma = \sqrt{\frac{1}{N_c - 1} \sum_{i=1}^{N_c} \left(C_V^{(i)}(T) - \langle C_V(T) \rangle_{\text{av}} \right)^2}. \quad (7.4)$$

By sighting this outcome for the specific heat in fig. 7.1, we can consistently recover the following properties with increasing dilution [129]:

- shift of the peak towards lower (critical) temperatures
- reduction of the peak height
- smeared out peak width (e.g. FWHM)

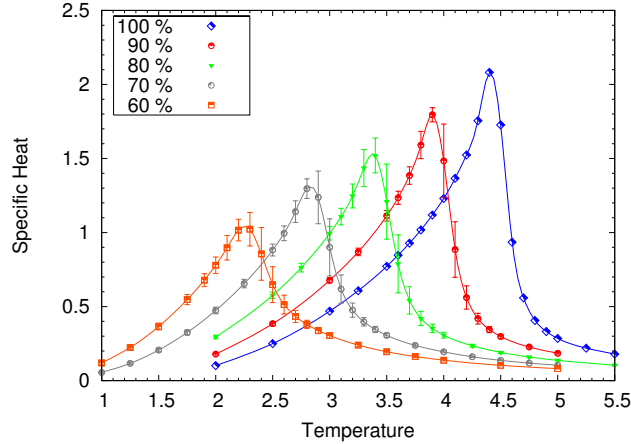


Figure 7.1: Specific heat of the $12 \times 12 \times 12$ simple cubic Ising model for different dilution probabilities (100% refer to the clean system); each curve is averaged over $N_c = 10$ disorder configurations, including the standard deviation σ .

The according benchmark on the QMC level looks also quite promising: With the use of the `directed loop` algorithm [119, 120] we simulated the three-dimensional $S = \frac{1}{2}$ Heisenberg model for single disorder configurations with various depletion probabilities. From the results, depicted in fig. 7.2, we can extract the same consistent conclusions as for the classical Monte Carlo simulations.

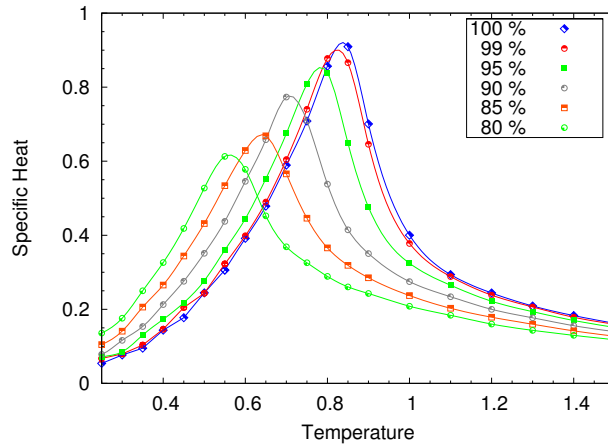


Figure 7.2: Specific heat of the $10 \times 10 \times 10$ simple cubic $S = \frac{1}{2}$ -Heisenberg model for different dilution probabilities (100% refer to the clean system); each curve was simulated for a single disorder configuration.

These studies can be further intensified in the future provided that sufficient CPU time will be available.

7.3 Self-Consistent Local RPA for Disordered Systems

In the previous chapter 5 we presented the RPA method for clean and homogeneous systems. We will now outline the generalization to disordered ferromagnets. We will refer to this generalization as Self-Consistent Local RPA (SC-LRPA) according to G. Bouzerar [135]-[139], who invented and explored this technique and successfully applied it to studies on diluted semiconductors. Thereby, the SC-LRPA approach provides several advantages: It combines semi-analytical expressions with a high-speed numerical performance: The SC-LRPA method proved to be three orders of magnitude faster than corresponding Monte Carlo benchmarks [137].

We will start with the outline of the principal idea on the analytical level and will subsequently elucidate its numerical implementation.

7.3.1 Basic Idea

In order to solve the disordered system, we have to determine the average of the local magnetic moments

$$M = \frac{1}{N_{\text{imp}}} \sum_{i=1}^{N_{\text{imp}}} \langle S_i^z \rangle \quad (7.5)$$

$$= S - \frac{1}{N_{\text{imp}}} \sum_{i=1}^{N_{\text{imp}}} \langle S_i^- S_i^+ \rangle \quad \text{for } S = \frac{1}{2}, \quad (7.6)$$

for N_{imp} occupied lattice sites. At this, we have to keep the indices in the local expectation values $\langle S_i^z \rangle$ and should bear in mind that in general

$$\langle S_i^z \rangle \neq \langle S_j^z \rangle \quad \text{for } i \neq j. \quad (7.7)$$

Nonetheless, we can uphold main parts of our previous strategy: In order to determine the yet missing expectation values for $S = \frac{1}{2}$,

$$\langle S_i^- S_i^+ \rangle \quad i = 1, \dots, N_{\text{imp}}, \quad (7.8)$$

we still use the GFs

$$G_{ij} = G_{ij}^{\text{ret}}(E) = \langle \langle S_i^+; S_j^- \rangle \rangle. \quad (7.9)$$

Their corresponding EoMs read

$$E \cdot G_{ij} = 2 \langle S_i^z \rangle \delta_{ij} + \sum_k J_{ki} \left[\langle \langle S_i^+ S_k^z; S_j^- \rangle \rangle - \langle \langle S_k^+ S_i^z; S_j^- \rangle \rangle \right], \quad (7.10)$$

where we have to keep all of the indices. Bearing the latter in mind, we apply the Tyablikov decoupling (5.16)-(5.17) and get the reductions

$$\langle \langle S_i^+ S_k^z; S_j^- \rangle \rangle \rightarrow \langle S_k^z \rangle G_{ij}, \quad \langle \langle S_k^+ S_i^z; S_j^- \rangle \rangle \rightarrow \langle S_i^z \rangle G_{kj}, \quad (7.11)$$

which lead to the RPA EoMs for the GFs

$$\left[E - \sum_k J_{ki} \langle S_k^z \rangle \right] G_{ij} = 2 \langle S_i^z \rangle \delta_{ij} - \langle S_i^z \rangle \sum_k J_{ki} G_{kj}. \quad (7.12)$$

Sighting this set of EoMs and comparing it to the clean case (5.18), we realize that the principal structure of the EoMs remains preserved. Therefore, we may abbreviate the further procedure by observing the important difference between the clean and the disordered system: On the one hand, the solution of the clean and homogeneous system required only the knowledge of a single $\langle S_i^z \rangle = \langle S^z \rangle$ for an arbitrary lattice site i . As a consequence, we could restrict our resulting considerations to a single GF $G = G_{ii}$ and a single $\Phi = \Phi_i$ for arbitrary i .

The disordered system, on the other hand, demands now the determination of the local magnetization $\langle S_i^z \rangle$ for each impurity site $i = 1, \dots, N_{\text{imp}}$. Thus, we finally need to consider N_{imp} distinct resulting GFs G_{ii} and N_{imp} distinct Φ_i .

The generalization to the case $S > \frac{1}{2}$ is also straightforward and parallel to our previous treatment, so we finally yield for the local magnetization for general S :

$$\langle S_i^z \rangle = \frac{(S - \Phi_i)(1 + \Phi_i)^{2S+1} + (1 + S + \Phi_i)\Phi_i^{2S+1}}{(1 + \Phi_i)^{2S+1} - \Phi_i^{2S+1}}, \quad (7.13)$$

$$\text{with } \Phi_i = -\frac{1}{2\pi \langle S_i^z \rangle} \int_{-\infty}^{+\infty} dE \frac{\text{Im}[G_{ii}]}{\exp[\beta E] - 1}, \quad (7.14)$$

$$\text{and } G_{ii} = G_{ii}^{\text{ret}}(E) = \langle \langle S_i^+; S_i^- \rangle \rangle \quad \text{for } i = 1, \dots, N_{\text{imp}}. \quad (7.15)$$

Please keep in mind that the dependence on the nearest-neighbour local magnetizations is centralized in G_{ii} and that we have therefore to deal with a set of coupled equations.

In order to generalize the determination of the critical temperature T_C for disordered systems, we introduce the local auxiliary variables

$$\lambda_i = \lim_{T \rightarrow T_C} \frac{\langle S_i^z \rangle}{M} \quad i = 1, \dots, N_{\text{imp}}, \quad (7.16)$$

and make use of the properties

$$\lim_{T \rightarrow T_C} M = 0, \quad \text{but } \lim_{T \rightarrow T_C} \lambda_i \neq 0. \quad (7.17)$$

The starting point is the limit of the averaged magnetization

$$\lim_{T \rightarrow T_C} M = \frac{1}{N_{\text{imp}}} \sum_{i=1}^{N_{\text{imp}}} \lim_{T \rightarrow T_C} \langle S_i^z \rangle. \quad (7.18)$$

By approximating the local Callen equation (7.13) for $\Phi_i \xrightarrow{T \rightarrow T_C} \infty$,

$$\lim_{T \rightarrow T_C} \langle S_i^z \rangle = \frac{S(S+1)}{3} \frac{1}{\lim_{T \rightarrow T_C} \Phi_i}, \quad (7.19)$$

and rewriting Φ_i with the use of the auxiliary variables (7.16),

$$\lim_{T \rightarrow T_C} \Phi_i = -\frac{1}{\lim_{T \rightarrow T_C} M} \frac{1}{2\pi\lambda_i} \int_{-\infty}^{+\infty} dE \frac{\text{Im}[G_{ii}]}{\beta_C E}, \quad (7.20)$$

we can cancel $\lim_{T \rightarrow T_C} M$ on both sides of the equation

$$\cancel{\lim_{T \rightarrow T_C} M} = \frac{S(S+1)}{3 N_{\text{imp}}} \cancel{\lim_{T \rightarrow T_C} M} \sum_{i=1}^{N_{\text{imp}}} \left[-\frac{1}{2\pi\lambda_i} \int_{-\infty}^{+\infty} dE \frac{\text{Im}[G_{ii}]}{\beta_C E} \right]^{-1}, \quad (7.21)$$

and gain the resulting formulae for the calculation of T_C :

$$T_C = \frac{S(S+1)}{3 N_{\text{imp}}} \sum_{i=1}^{N_{\text{imp}}} \frac{1}{F_i} \quad (7.22)$$

$$\text{with } F_i = -\frac{1}{2\pi\lambda_i} \int_{-\infty}^{+\infty} dE \frac{\text{Im}[G_{ii}]}{E}. \quad (7.23)$$

Based on these equations, the following section depicts the development of the concrete code realization.

7.3.2 Code Implementation

In order to face the coupled equations in (7.12), we rewrite these EoMs with the use of $N_{\text{imp}} \times N_{\text{imp}}$ matrices:

$$\left[E \cdot \mathbf{1} - \mathbf{H}^{\text{eff}} \right] \mathbf{G} = \mathbf{D}, \quad (7.24)$$

$$\text{with } (\mathbf{D})_{ij} = 2 \langle S_i^z \rangle \delta_{ij}, \quad (7.25)$$

$$(\mathbf{G})_{ij} = G_{ij}, \quad (7.26)$$

$$(\mathbf{H}^{\text{eff}})_{ij} = -\langle S_i^z \rangle J_{ij} + \delta_{ij} \sum_k \langle S_k^z \rangle J_{kj}, \quad (7.27)$$

and $\mathbf{1}$ denoting the $N_{\text{imp}} \times N_{\text{imp}}$ unit matrix.

Via matrix inversion we recast (7.24),

$$\mathbf{G} = \left[E \cdot \mathbf{1} - \mathbf{H}^{\text{eff}} \right]^{-1} \mathbf{D}, \quad (7.28)$$

and gain the rewritten GF

$$G_{ij} = \left\langle i \left| \left[E \cdot \mathbf{1} - \mathbf{H}^{\text{eff}} \right]^{-1} \mathbf{D} \right| j \right\rangle. \quad (7.29)$$

The basic idea is now to diagonalize the involved Hamiltonian matrix \mathbf{H}^{eff} . For that purpose, we insert the corresponding left and right eigenvectors

$$\left\{ \langle \psi_\alpha^L | \right\}, \quad \left\{ | \psi_\alpha^R \rangle \right\}, \quad \alpha = 1, \dots, N_{\text{imp}}, \quad (7.30)$$

$$\text{with} \quad \sum_{\alpha=1}^{N_{\text{imp}}} | \psi_\alpha^R \rangle \langle \psi_\alpha^L | = \mathbf{1}. \quad (7.31)$$

Since the Hamiltonian matrix \mathbf{H}^{eff} is real, but non-symmetric in general, we have to take special care of the eigenstates and have to distinguish left $\{ \langle \psi_\alpha^L | \}$ and right eigenvectors $\{ | \psi_\alpha^R \rangle \}$ associated with the corresponding eigenvalues

$$\{ E_\alpha \}, \quad \alpha = 1, \dots, N_{\text{imp}}, \quad (7.32)$$

$$\text{defined by} \quad \mathbf{H}^{\text{eff}} | \psi_\alpha^R \rangle = E_\alpha | \psi_\alpha^R \rangle \quad (7.33)$$

$$\text{and} \quad \langle \psi_\alpha^L | \mathbf{H}^{\text{eff}} = E_\alpha \langle \psi_\alpha^L |, \quad \text{resp.} \quad (\mathbf{H}^{\text{eff}})^T | \psi_\alpha^L \rangle = E_\alpha | \psi_\alpha^L \rangle, \quad (7.34)$$

with $(\mathbf{H}^{\text{eff}})^T$ denoting the transposed of \mathbf{H}^{eff} .

Inserting the identity (7.31) in (7.29),

$$G_{ij} = \sum_{\alpha=1}^{N_{\text{imp}}} \langle i | [E \cdot \mathbf{1} - \mathbf{H}^{\text{eff}}]^{-1} | \psi_\alpha^R \rangle \langle \psi_\alpha^L | \mathbf{D} | j \rangle, \quad (7.35)$$

enables us to express the GFs G_{ij} completely by the eigenstates (7.30), their corresponding eigenvalues (7.32) and the local magnetizations $\{ \langle S_i^z \rangle \}$:

$$G_{ij} = 2 \langle S_j^z \rangle \sum_{\alpha=1}^{N_{\text{imp}}} \frac{\langle i | \psi_\alpha^R \rangle \langle \psi_\alpha^L | j \rangle}{E - E_\alpha}. \quad (7.36)$$

Using this result and the connection (7.14) to the essential quantities Φ_i , we can express the latter in the same way:

$$\Phi_i = \sum_{\alpha=1}^{N_{\text{imp}}} \frac{\langle i | \psi_\alpha^R \rangle \langle \psi_\alpha^L | j \rangle}{\exp[\beta E_\alpha] - 1}. \quad (7.37)$$

Combining this set of derived equations with the local Callen equation (7.13), we have now a procedure at our hand to determine self-consistently all the local magnetizations $\langle S_i^z \rangle$. This self-consistent procedure, which has to be performed numerically, is depicted in fig. 7.3. The corresponding input parameters are the couplings J_{ij} , the temperature T and the spin quantum number S .

For the determination of the critical temperature we adopt a similar scheme, but have to bear in mind to deal with the auxiliary variables defined in (7.16),

$$\{ \lambda_i \} \quad i = 1, \dots, N_{\text{imp}}. \quad (7.38)$$

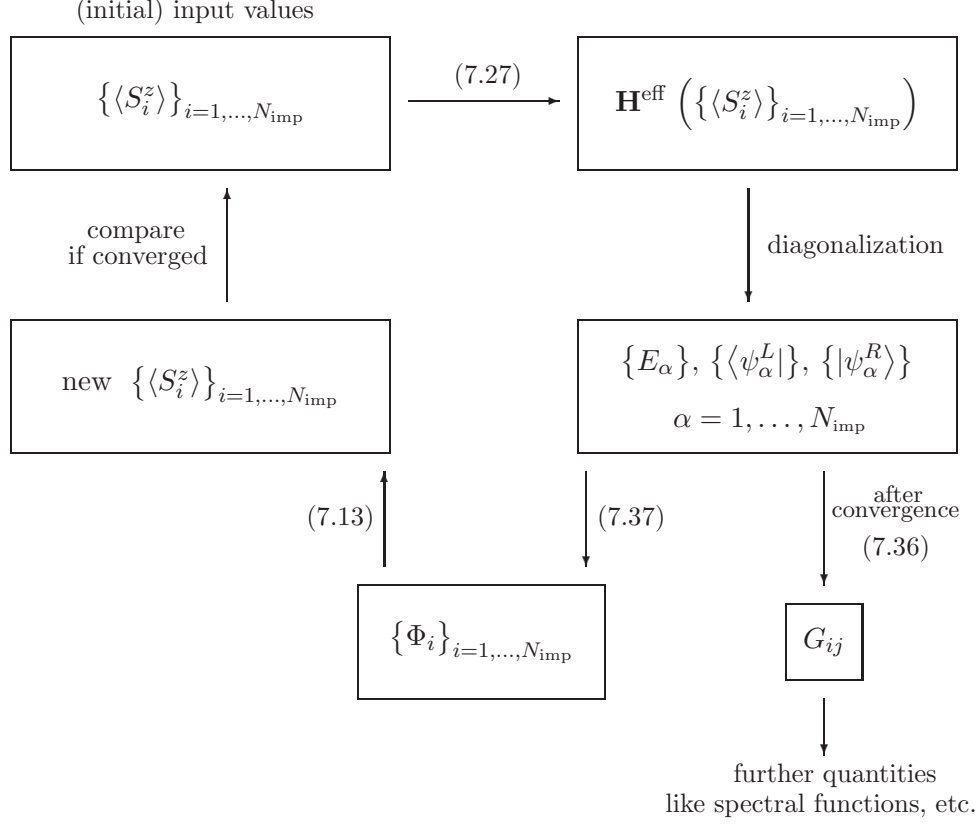


Figure 7.3: Numerical procedure for the calculation of the local magnetizations $\{\langle S_i^z \rangle\}_{i=1, \dots, N_{\text{imp}}}$.

Due to

$$\frac{1}{M} \mathbf{H}^{\text{eff}}(\{\langle S_i^z \rangle\}) = \mathbf{H}^{\text{eff}}(\{\lambda_i\}) \quad \text{and} \quad \frac{1}{M} \mathbf{D}(\{\langle S_i^z \rangle\}) = \mathbf{D}(\{\lambda_i\}) \quad (7.39)$$

in the limit $T \rightarrow T_C$, we may perform the substitutions

$$\langle S_i^z \rangle \rightarrow \lambda_i \quad \text{and} \quad E_{(\alpha)} \rightarrow E'_{(\alpha)} = \frac{E_{(\alpha)}}{M}. \quad (7.40)$$

As a consequence, we replace all the local magnetization variables by λ_i and recast the set $\{F_i\}$ by the corresponding eigenvalues E'_α and eigenstates (7.30):

$$F_i = \sum_{\alpha=1}^{N_{\text{imp}}} \frac{\langle i | \psi_\alpha^R \rangle \langle \psi_\alpha^L | j \rangle}{E'_\alpha}. \quad (7.41)$$

Making use of (7.22) and the relation between F_i and λ_i ,

$$\lambda_i = \frac{S(S+1)}{3} \beta_C \frac{1}{F_i}, \quad (7.42)$$

we have now a self-consistent procedure for determining T_C at our disposal. The complete scheme is depicted in fig. 7.4. The corresponding input parameters are the couplings J_{ij} and the spin quantum number S .

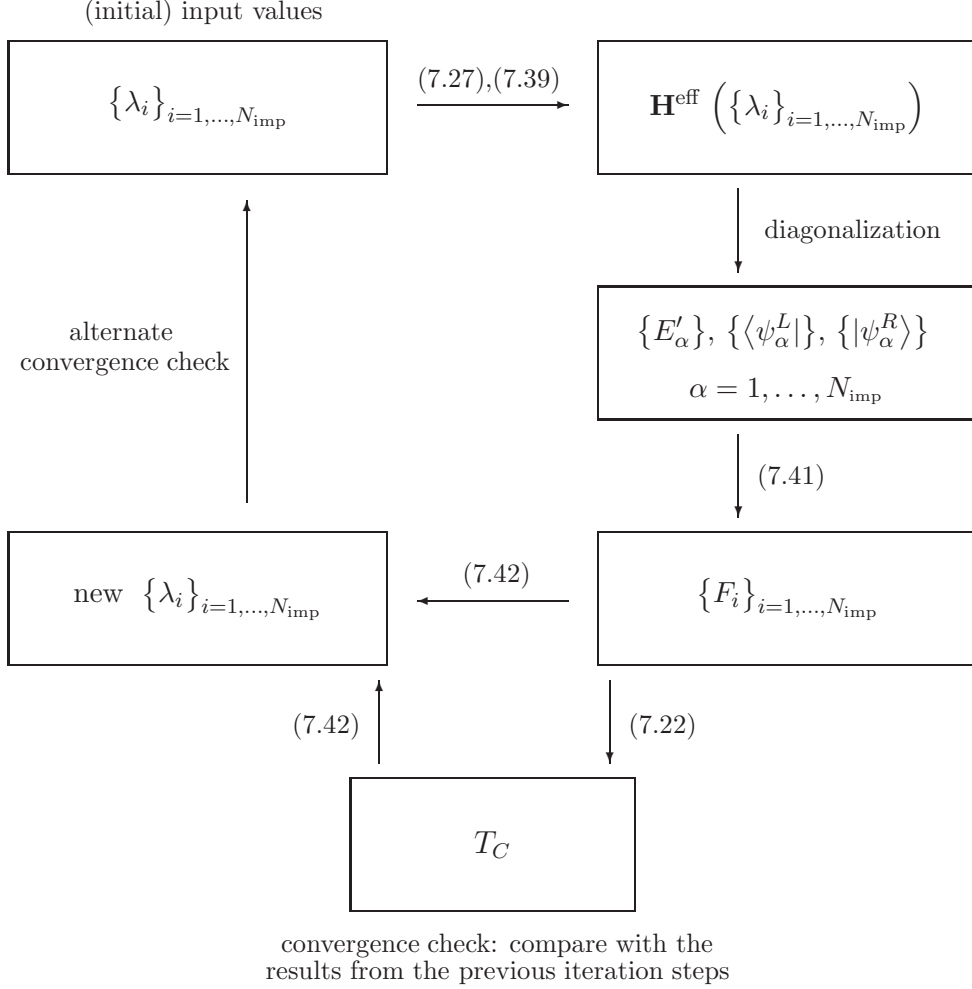


Figure 7.4: Numerical procedure for the calculation of the critical temperature.

We add an important note on the absence of the Goldstone modes in finite systems: Infinite systems show the phenomenon of spontaneous symmetry breaking [20] and consequently exhibit the presence of Goldstone modes. For our numerical studies, on the contrary, we have to restrict ourselves to finite systems. As a consequence, we unavoidably break the symmetry explicitly by hand, which leaves the corresponding Goldstone modes as unphysical artefacts. Therefore, we have to take special care of removing these unphysical Goldstone modes in our codes.

7.3.3 Successful Benchmarks

The self-consistent procedures, derived in the previous section and depicted in fig. 7.3 and 7.4, have been implemented in a C++ code. Hereby, we imported the LAPACK routine DGEEV that provides the calculation of left and right eigenvectors required for our procedures. Our codes will be made available to every-

one interested in its further development (please contact bvogt@physnet.uni-hamburg.de). This code has been written for disordered ferromagnets with variable dilution parameters. As impressive benchmarks we checked the outcome for the clean limit, i.e. each of the lattice sites is occupied by a spin.

In fig. 7.5-7.8 we show the results for the magnetization for various spin quantum numbers gained by the code based on the scheme in fig. 7.3. The shape of these magnetization curves consistently complies with the expectations for second order phase transitions.

The modified code for the critical temperature based on the scheme in fig. 7.4 yields the numerical results presented in fig. 7.9 and 7.10.

Fig. 7.9 shows the critical temperatures of the two-dimensional $S = \frac{1}{2}$ - Heisenberg model for various lattice sizes. The numerical study of the two-dimensional isotropic Heisenberg model is thereby beset by some difficulties: It is well-known that the critical temperature of the two-dimensional system tends to zero in the thermodynamical limit [8]; in order to perform this thermodynamical limit, we apply an appropriate fit procedure: We make use of the fit function

$$f^{2d}(N) = \frac{a}{\ln[N]} \quad \text{with the variable fit parameter } a, \quad (7.43)$$

which performs very well, as depicted in fig. 7.9. This finding consistently leads to a vanishing critical temperature for $N \rightarrow \infty$, thereby rendering this test successful.

Fig. 7.10 presents the critical temperatures of the three-dimensional $S = 1$ - Heisenberg model for different lattice sizes. In order to extract the critical temperature in the thermodynamical limit, we use again a fit procedure. The appropriate fit function

$$f^{3d}(L) = a + \frac{b}{L} + \frac{c}{L^2} + \frac{d}{L^3} + \frac{e}{L^4} + \frac{f}{L^5}, \quad (7.44)$$

$$\text{with the linear extent } L = N^{1/3},$$

yields $a = 2.64$, and, after proper rescaling by $S(S+1)$,

$$T_C^{3d}(N \rightarrow \infty) = 1.32 \pm 0.01 \quad \text{in units of } J, \quad (7.45)$$

which is in excellent agreement with our analytically derived result (5.63). The error is given by the convergence criterion applied in the underlying code.

These successful benchmarks for the clean system open the way for further studies extended to the investigation on diluted systems.

- $S = \frac{1}{2}$

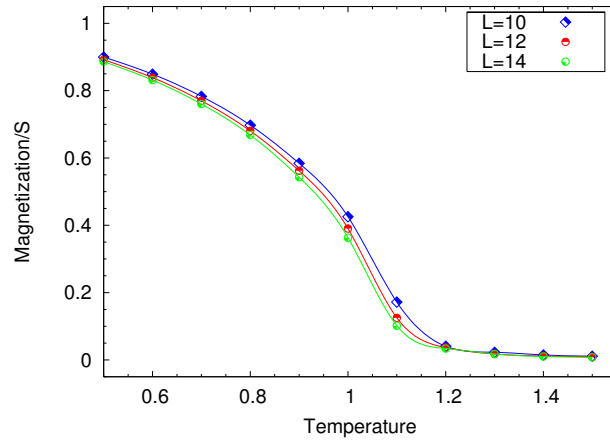


Figure 7.5: Normalized magnetization M/S of the three-dimensional simple cubic Heisenberg model with spin $S = \frac{1}{2}$ for different system sizes $N = L^3$ (L denotes the linear extent); the temperature is given in units of J .

- $S = 1$

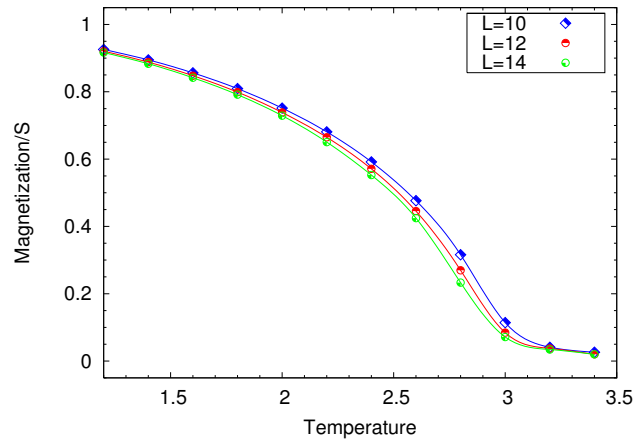


Figure 7.6: Normalized magnetization M/S of the three-dimensional simple cubic Heisenberg model with spin $S = 1$ for different system sizes $N = L^3$ (L denotes the linear extent); the temperature is given in units of J .

- $S = \frac{3}{2}$

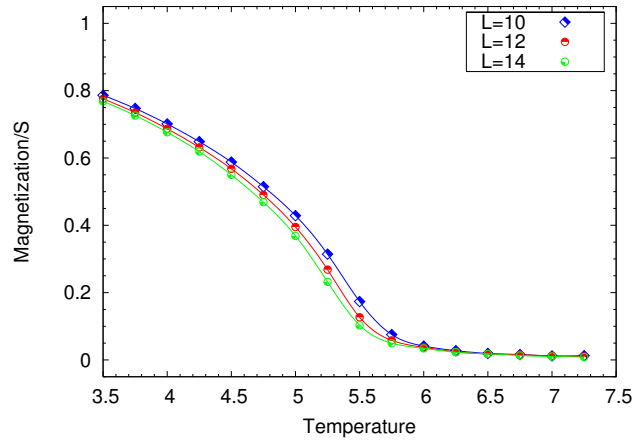


Figure 7.7: Normalized magnetization M/S of the three-dimensional simple cubic Heisenberg model with spin $S = \frac{3}{2}$ for different system sizes $N = L^3$ (L denotes the linear extent); the temperature is given in units of J .

- $S = 10$

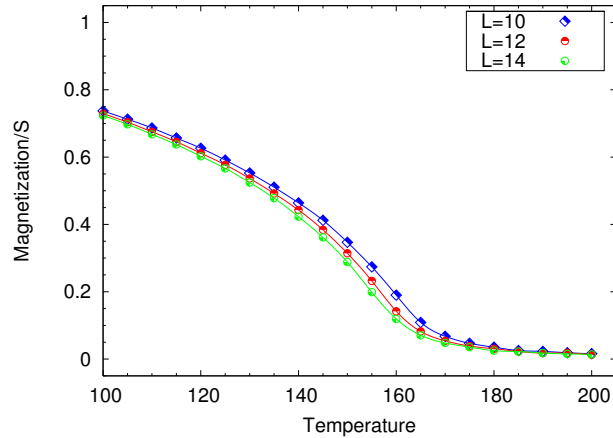


Figure 7.8: Normalized magnetization M/S of the three-dimensional simple cubic Heisenberg model with spin $S = 10$ for different system sizes $N = L^3$ (L denotes the linear extent); the temperature is given in units of J .

- $d = 2$

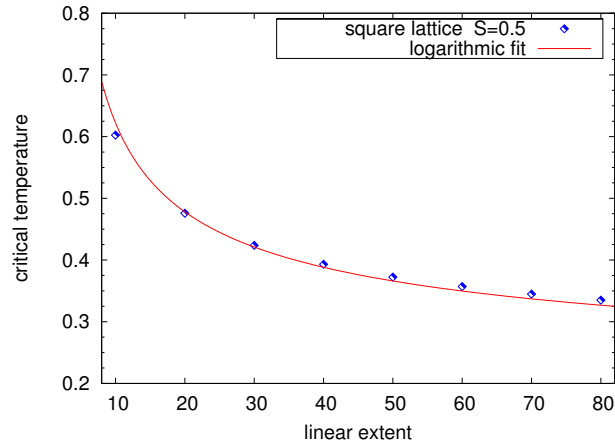


Figure 7.9: Critical temperature in units of J for the two-dimensional square lattice Heisenberg model with spin $S = \frac{1}{2}$ versus the linear extent $L = \sqrt{N}$ of the system, fitted logarithmically with the function (7.43).

- $d = 3$

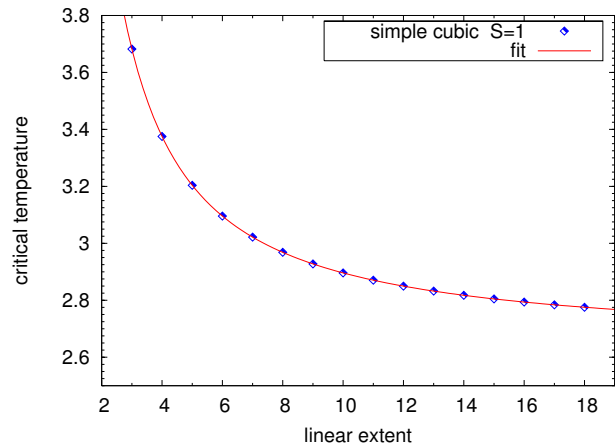


Figure 7.10: Critical temperature in units of J for the three-dimensional simple cubic Heisenberg model with spin $S = 1$ versus the linear extent $L = N^{1/3}$ of the system, fitted with the function (7.44).

7.3.4 Further Prospect

At the close of this chapter, we end with a promising outlook for a further project, which could be directly built upon our previous workout: The AFM, as we pointed out in the course of this thesis, is much stronger affected by quantum fluctuations than the FM. Therefore, the AFM, on the theoretical level as well as in an experimental setup, is a promising system to exhibit a profound dependence of the quantum fluctuations on the dilution ratio $x = N_{\text{imp}}/N_{\text{tot}}$. For this purpose, one should investigate the ground state sublattice magnetization defined in the style of chapter 4,

$$M_{T=0}^{\text{sl}} = \frac{1}{N_A + N_B} \left[\sum_{i \in A}^{N_A} \langle S_i^z \rangle_0 - \sum_{j \in B}^{N_B} \langle S_j^z \rangle_0 \right] = S - \Delta M_{T=0}^{\text{sl}}, \quad (7.46)$$

with N_A and N_B denoting the number of occupied lattice sites on sublattice A and B . Alternatively, one could decide to study the sublattice magnetization of the entire lattice $\overline{M}_{T=0}^{\text{sl}} = M_{T=0}^{\text{sl}} \cdot N_{\text{imp}}/N_{\text{tot}}$ with $N_{\text{imp}} = N_A + N_B$.

Thereby, the quantity $\Delta M_{T=0}^{\text{sl}}$ represents the amount of quantum fluctuations including the additional quantum effects due to the dilution. The study of the quantum correction as a function of the site-dilution,

$$\Delta M_{T=0}^{\text{sl}}(x) \quad \text{with} \quad x = \frac{N_{\text{imp}}}{N_{\text{tot}}}, \quad (7.47)$$

would elucidate the role of the impurity concentration x and its influence on the quantum fluctuations.

This study could be extended to finite temperatures by extracting the specific quantum fluctuations for a given spin quantum number S at $T > 0$ via the difference

$$\frac{\Delta M_Q^{\text{sl}}(S, T)}{S} = \left. \frac{M^{\text{sl}}(S, T)}{S} \right|_{S \rightarrow \infty} - \frac{M^{\text{sl}}(S, T)}{S}. \quad (7.48)$$

This generalized formula is consistently linked to the previous case (7.46) at $T=0$ due to $M^{\text{sl}}(S \rightarrow \infty, T=0) = S$.

Furthermore, one could study the additional interplay with anisotropy fields, which lead to an additional suppression of the quantum fluctuations as we have comprehensively shown in this thesis. From that point of view, two-dimensional anisotropic systems are promising candidates for these phenomena due to their strong quantum fluctuations, which can be profoundly influenced by anisotropy fields at the same time. This has been one of the reasons to study the two-dimensional Heisenberg model with the use of QMC simulations in chapter 6. Future studies on these proposed topics could combine the SC-LRPA approach for AFMs according to [140] with QMC simulations using the ALPS package [112].

Chapter 8

Résumé

In the course of this thesis we thoroughly studied the influence of anisotropy fields

$$- h_p \sum_i (S_i^z)^p \quad \text{with } p \text{ even} \quad (8.1)$$

on the quantum character of Heisenberg ferro- and antiferromagnets. We elucidated in detail the effects that consequently reduce thermal and quantum fluctuations. Thereby, we investigated the interplay of the spin quantum number S and the anisotropy fields h_p , which both represent classical limits for large values. Both parameters further induce classical trends for increasing values, that are too small to find the classical saturation limits, but are large enough to eliminate typical quantum effects. We especially studied the latter phenomenon: We observed the rapid reduction of quantum effects that is unleashed by the presence of relatively small anisotropy fields.

We demonstrated the impact of the anisotropy fields by various theoretical approaches: In chapter 2 we started with a classical Mean Field theory and illustrated the reduction of the thermal spin fluctuations towards an Ising-like behaviour in the easy-axis case $h_p > 0$. We exposed the resulting effects by analytically derived illustrations of the free energy landscapes and quantified the reduction of the fluctuations by the shift of the critical temperatures $T_C(h_p)$. By a careful analysis, we could extract the incipient crossover from the $O(3)$ -symmetry towards the Ising-like Z_2 -symmetry for $h_p > 0$ and found the corresponding crossover temperature located clearly above $T_C(h_p)$.

We extended this Mean Field concept in chapter 3 to a quantum Mean Field approach that includes quantum effects via the quantization of the spin: We consequently found a hierarchy of relevance referring to the order p , which is switched around by tuning the spin quantum number S and consistently linked with the classical Mean Field for large $S \gg 1$. We could explain this change of the hierarchy by taking into account the quantized gaps that are provided by the anisotropy term. We could confirm this behaviour later on by our QMC simulations for $S=2$.

Besides quantum effects that are intermingled with thermal fluctuations, we also focused on pure quantum fluctuations in antiferromagnets by investigating the sublattice magnetization at $T = 0$, whose deviation from its classical value S directly manifests the amount of quantum fluctuations. With the use of the Linear Spin Wave Approximation, we studied in chapter 4 its dependence on the spin quantum number S , the anisotropy field h_p and the dimension d . We successfully found the trend towards a classical system for increasing S and h_p , respectively for a suitable combination of both parameters. Thereby, we studied the outcome for a widespread range of the parameters S and h_p and elucidated their interplay. In order to point out the sensitivity of the sublattice magnetization to the anisotropy fields h_p , we introduced the anisotropy susceptibility as the respective derivative, which strongly supports our picture: The anisotropy susceptibility, which takes into account exclusively quantum effects, diverges for $h_p \rightarrow 0$. This result allows us to strengthen our statement that even tiny fields drive the system towards a classical one by suppressing quantum fluctuations. We subsequently refined these results with the use of the Random Phase Approximation in chapter 5. Furthermore, the RPA technique enabled us to investigate the shifts of the critical temperatures $T_C(h_p)$ for various dimensions in a revised manner that accords with the Mermin-Wagner theorem [8, 58]. We finally confirmed our analytical findings by numerically reliable Quantum Monte Carlo simulations using the software package ALPS [112]. Thereby, we compared the critical temperatures of FMs and AFMs for $S=1$ and proved their convergence for sufficiently large fields h_2 in three dimensions, thereby pointing out the suppression of quantum fluctuations. The maximal slope of $T_C(h_p)$ in the resulting phase diagrams for the smallest h_p , for both FMs and AFMs, demonstrates that the original quantum systems are profoundly driven towards classical systems by relatively small fields. Moreover, we could mutually validate our results by fitting our QMC data with the relations (5.179)-(5.180) we had analytically derived on the RPA level in the long wavelength limit, which yielded perfect concordance for small fields.

As a final result, we proved the extremely high sensitivity of quantum fluctuations to the presence of anisotropy fields: The consequently strong suppression of quantum fluctuations changes the original quantum spin system rapidly into a classical one. This finding emphatically confirms the classical modelling of modern SP-STM experiments performed at the University of Hamburg, which deal with spin systems that are affected by anisotropy fields [23]-[31].

A detailed and concrete outlook for disordered systems is given in chapter 7: Subsequent studies, which deal with the interplay of dilution and anisotropy fields, could be directly based on this thesis. For that purpose, we presented the generalization of the RPA technique to disordered systems based on Bouzerar's publications [135]-[139], which could be combined with the results of Quantum Monte Carlo simulations on depleted lattices. The numerical implementation has been successfully benchmarked and opens the way towards future studies revealing newly composed phenomena.

On that note, we close with the words of one of the pioneering physicists, who explored and inspired the theory of Statistical Physics:

“Statistical mechanics is the bridge between the world of the atom and the world of the object. We live in the latter world but wish, for aesthetic as well as for practical reasons, to understand the former.”

J.L. Lebowitz

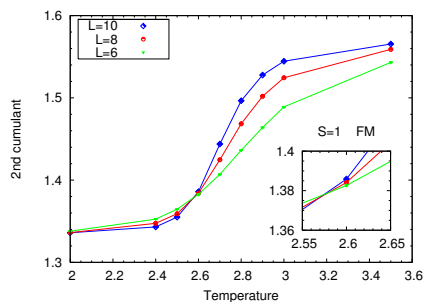
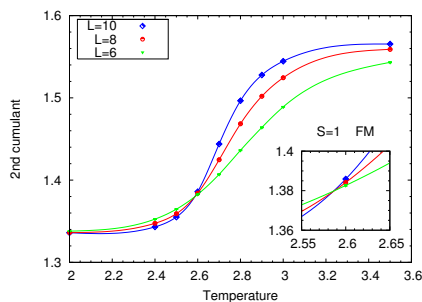
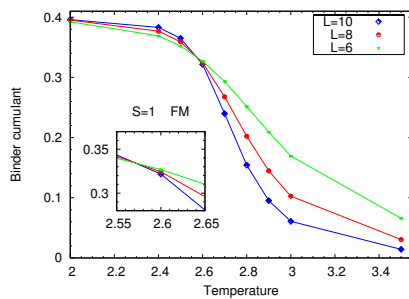
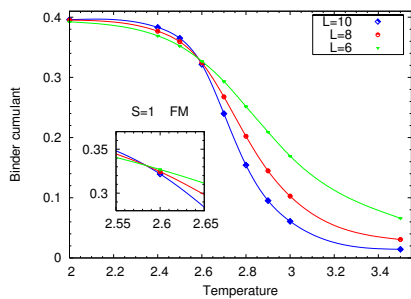
Plenary talk given at the 71st annual meeting of the DPG in Regensburg in 2007 on the occasion of the conferment of the Max Planck medal [141]

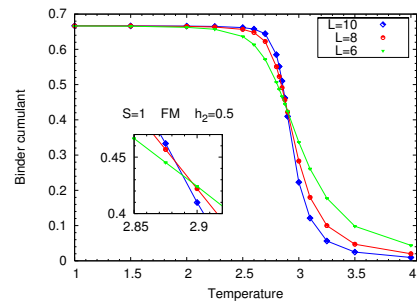
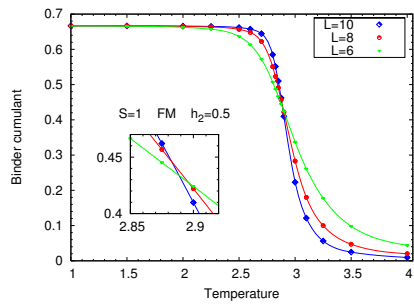
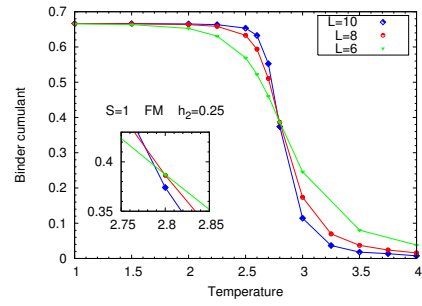
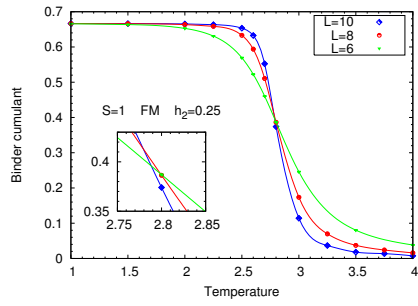
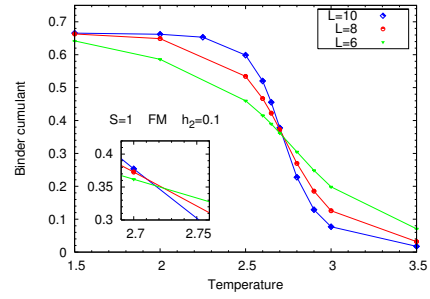
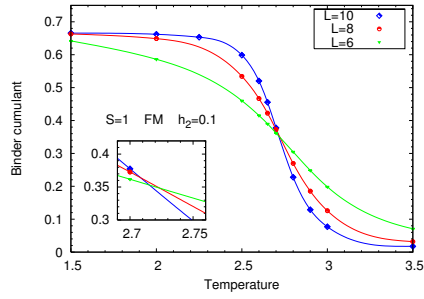
Appendix A

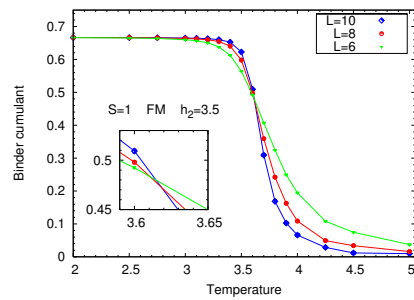
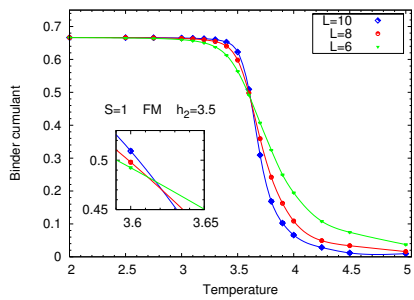
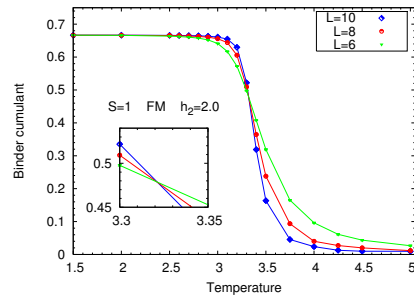
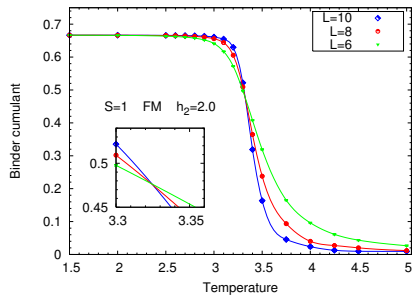
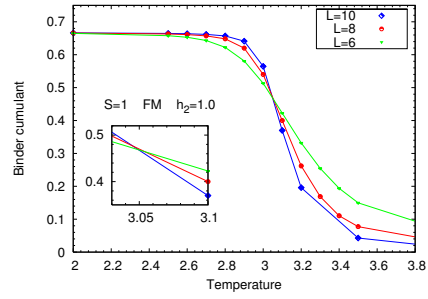
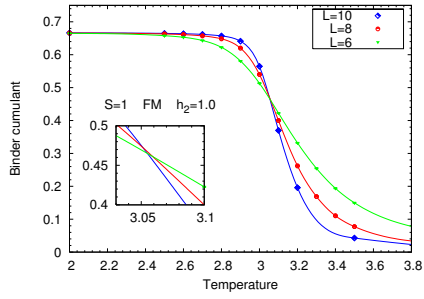
Binder Cumulants

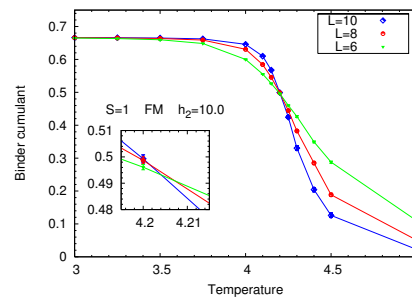
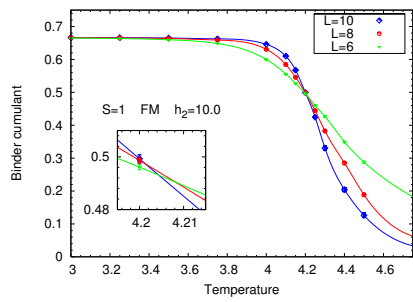
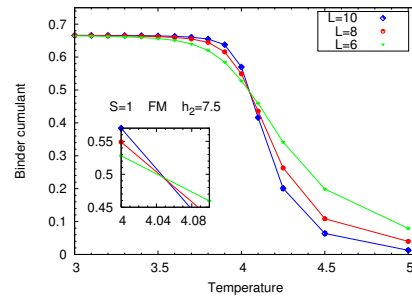
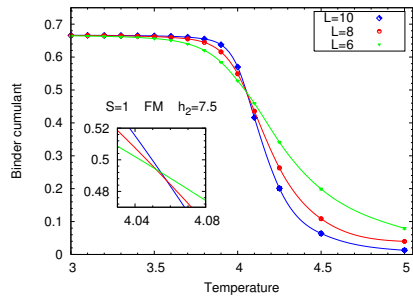
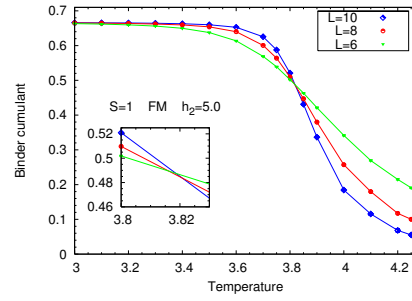
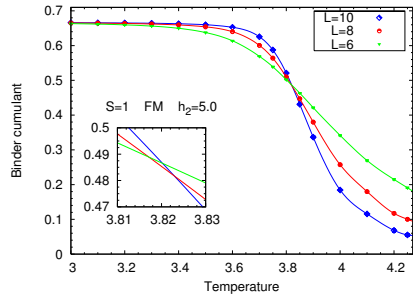
This chapter contains all the figures of intersecting Binder cumulants, which have been left out in the main text in order to focus the reader's attention to the results. The following inset labels describe the value of the spin quantum number S , the kind of magnet (FM/AFM) and the strength of the anisotropy field h_p ; if there is no h_p -value denoted, the system is isotropic ($h_p = 0$). On the left-hand side we depict the interpolation by cubic splines, on the right-hand side the interpolation with lines. The subsections A.1-A.6 refer to three-dimensional systems; the figures for two-dimensional systems are shown in A.7-A.8 and additionally contain "d=2" in their inset labels.

A.1 $S=1$ - Heisenberg FM

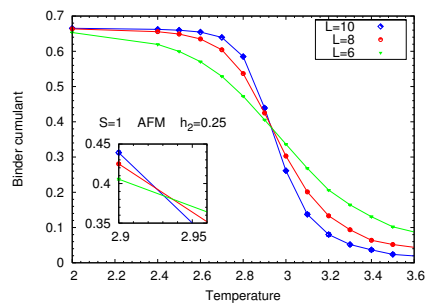
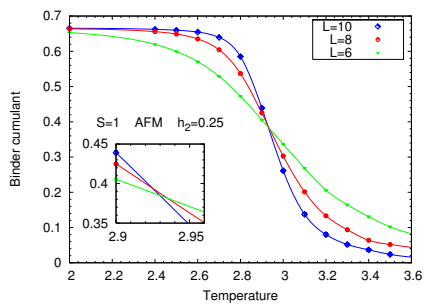
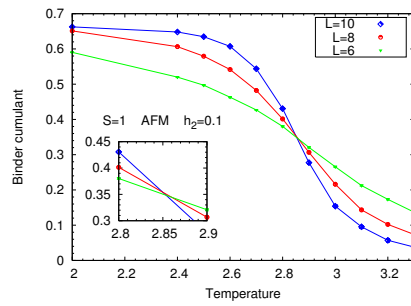
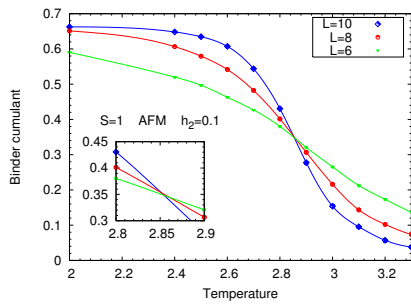
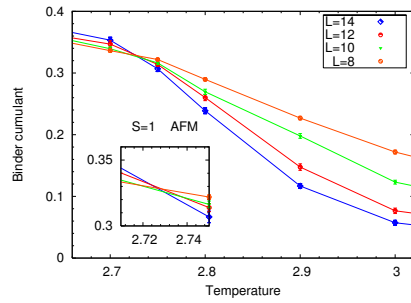
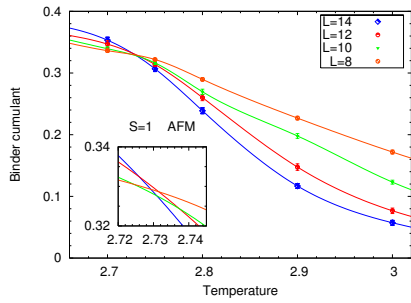


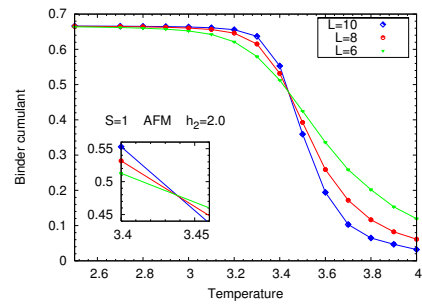
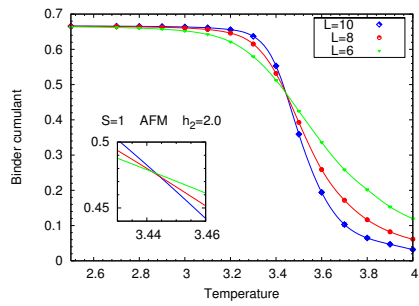
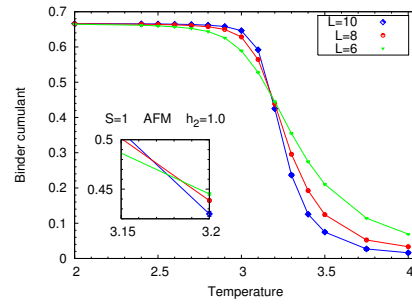
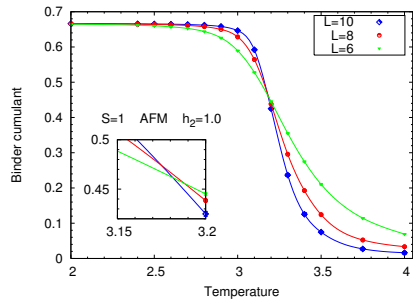
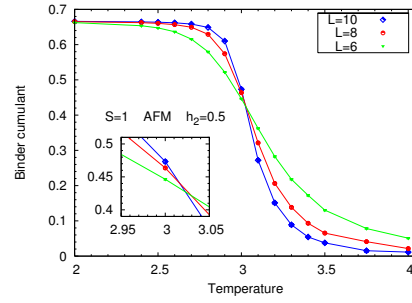
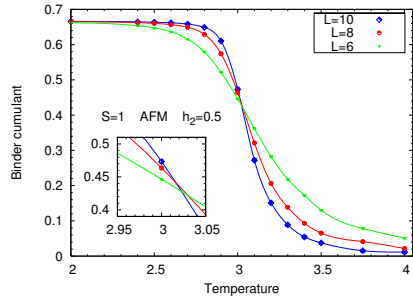


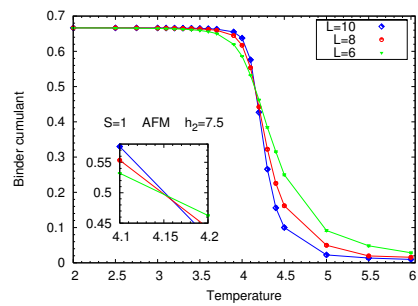
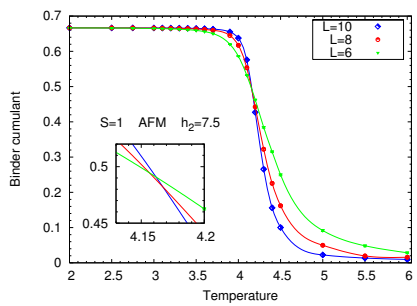
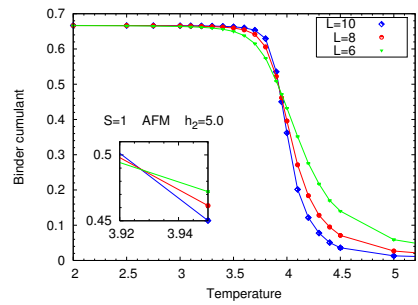
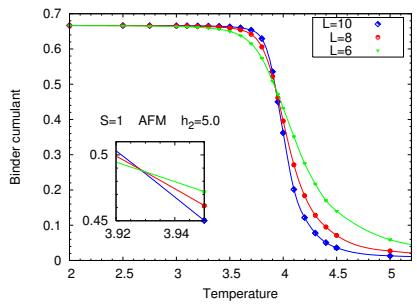
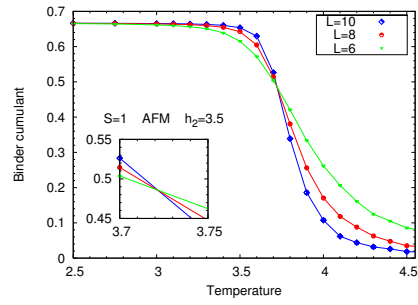
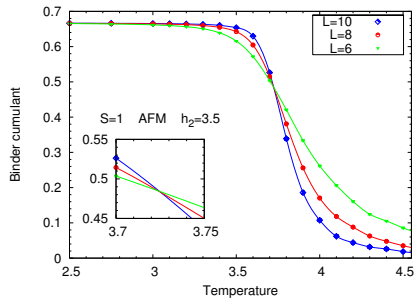


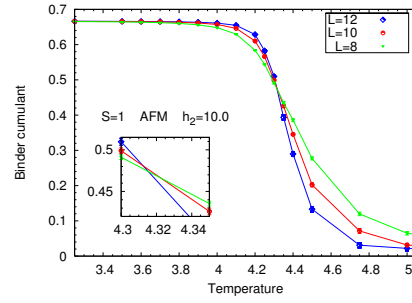
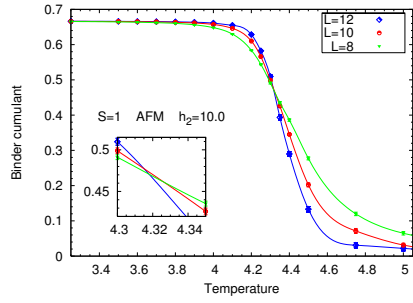


A.2 $S=1$ - Heisenberg AFM

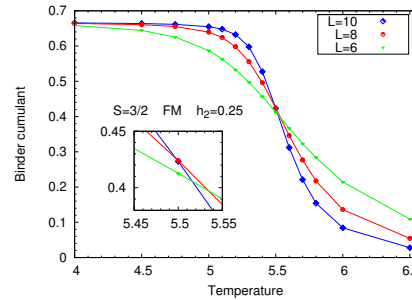
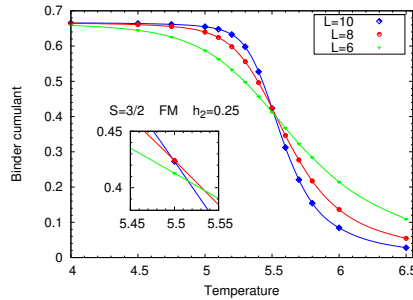
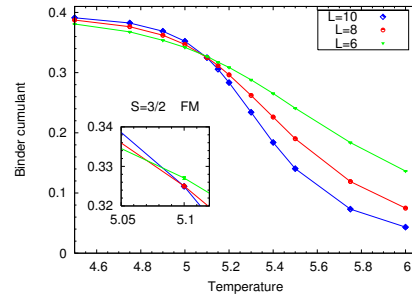
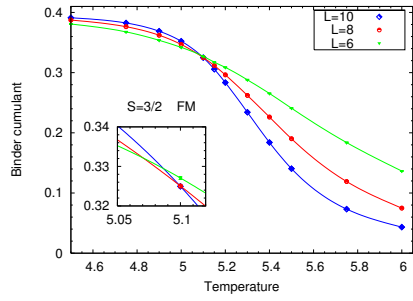




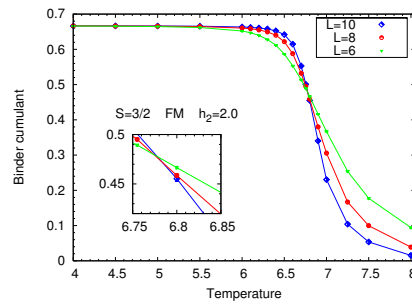
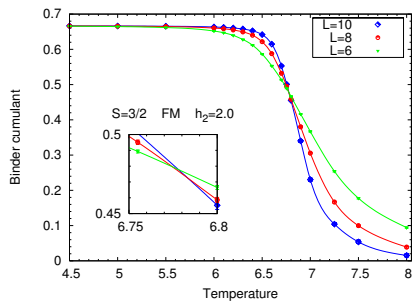
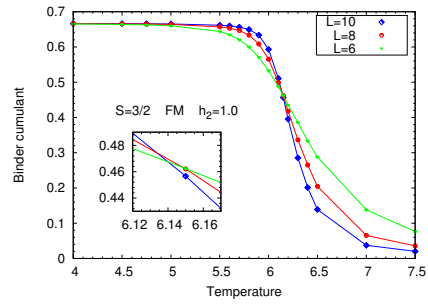
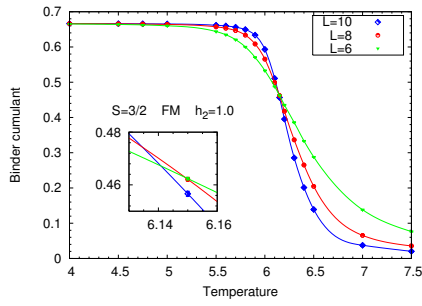
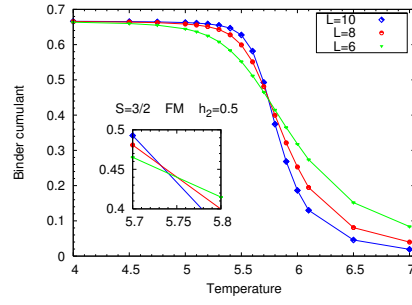
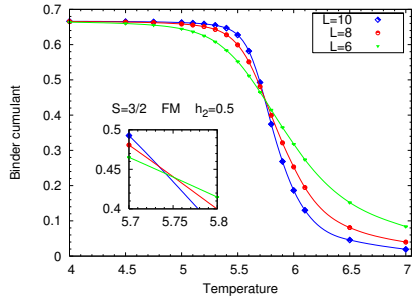


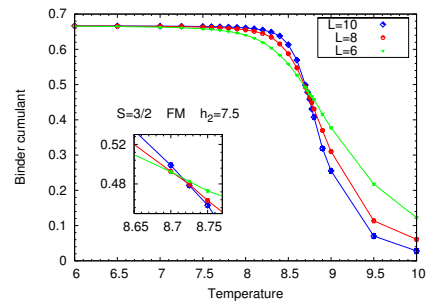
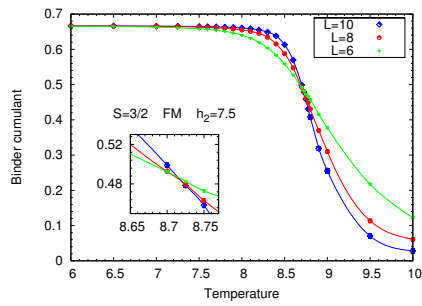
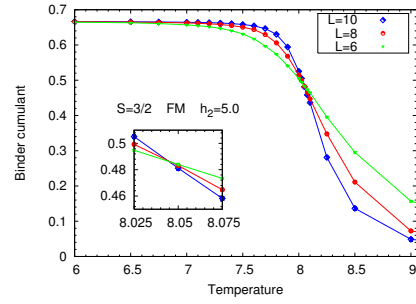
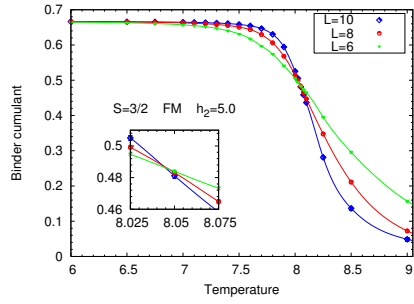
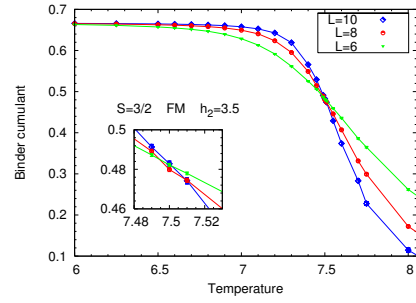
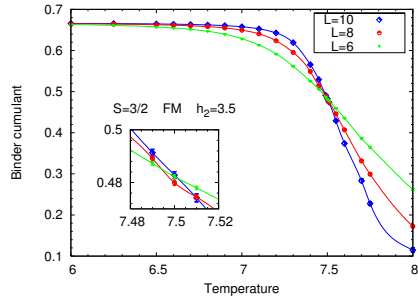


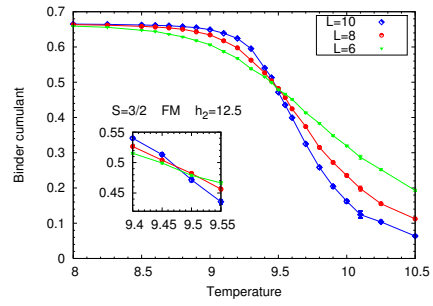
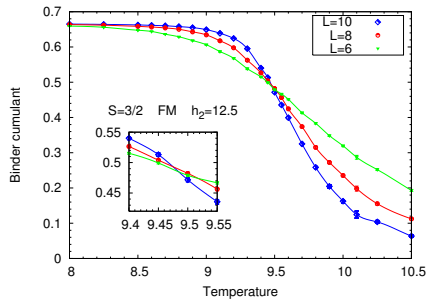
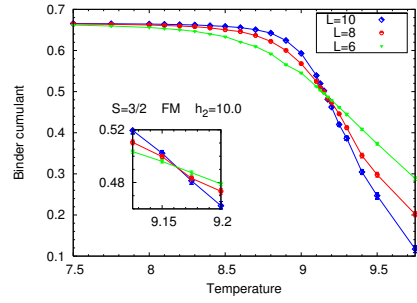
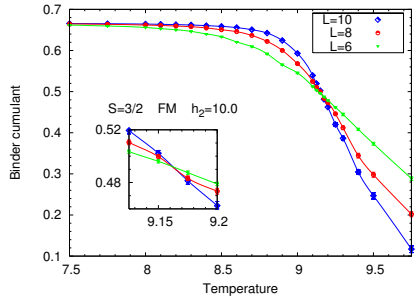
A.3 $S = \frac{3}{2}$ - Heisenberg FM



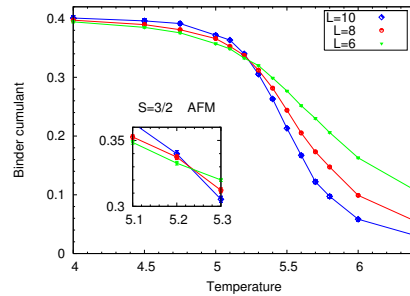
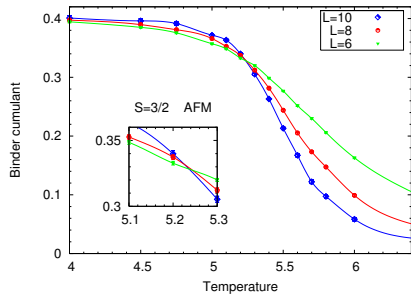
A.3. $S=3/2$ - Heisenberg FM

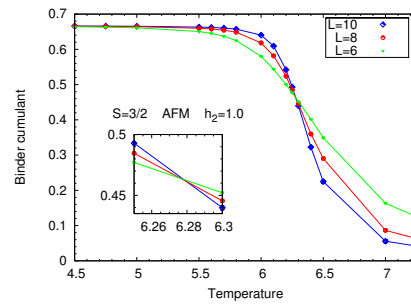
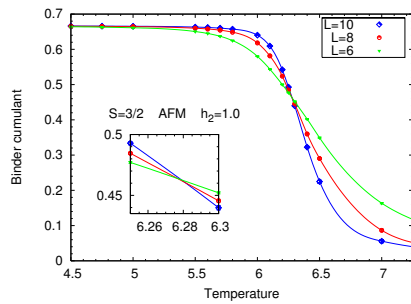
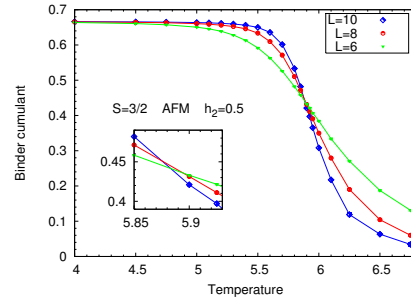
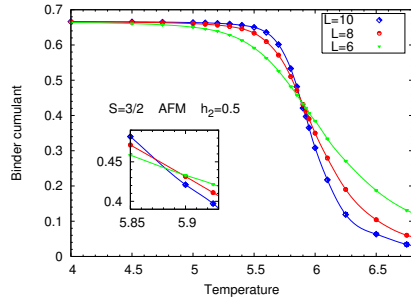
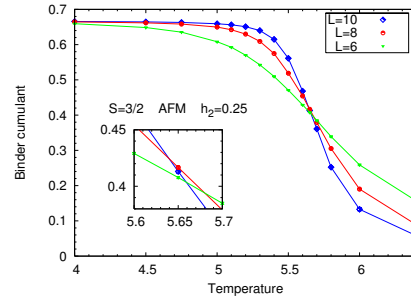
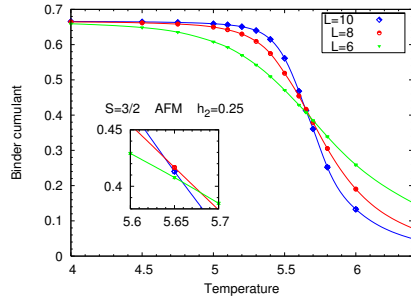




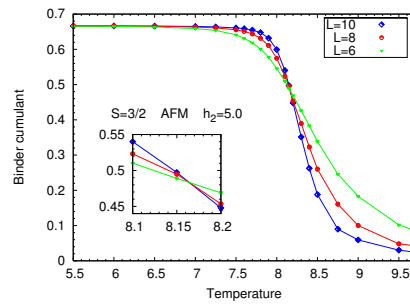
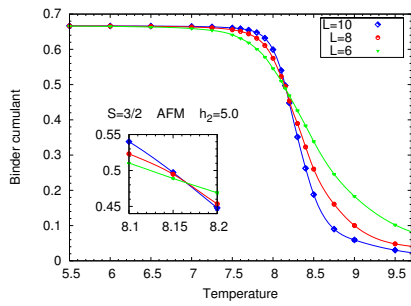
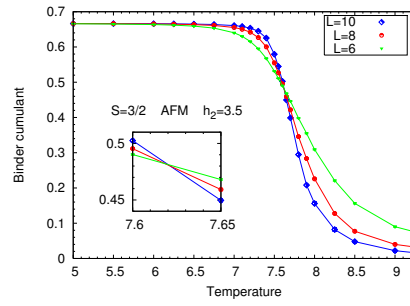
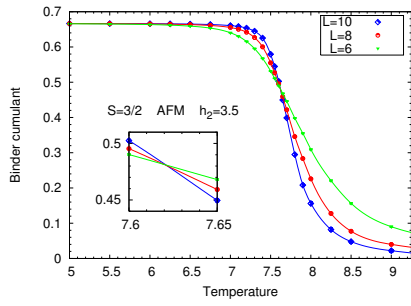
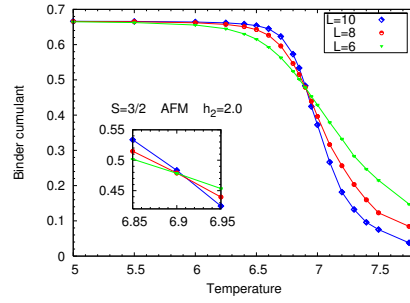
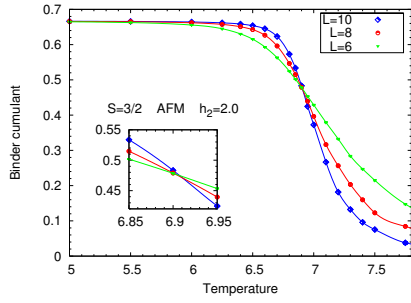


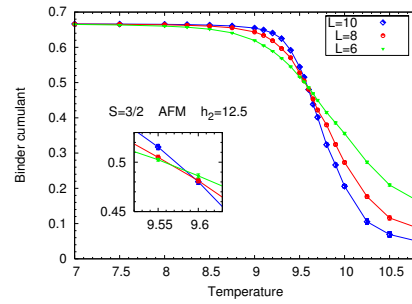
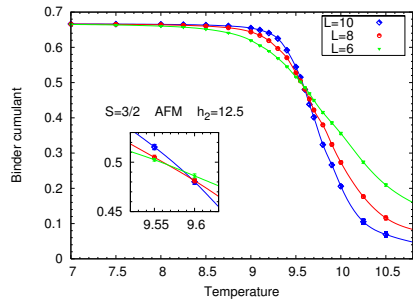
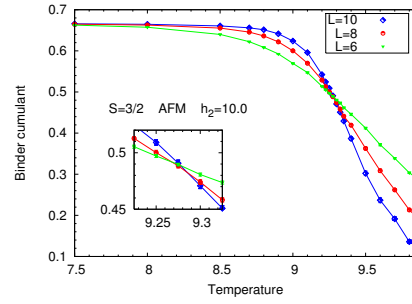
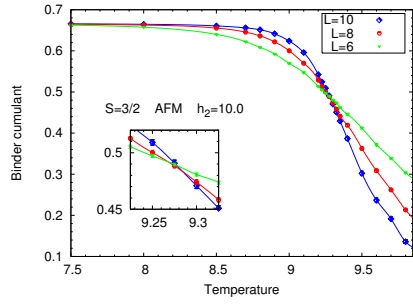
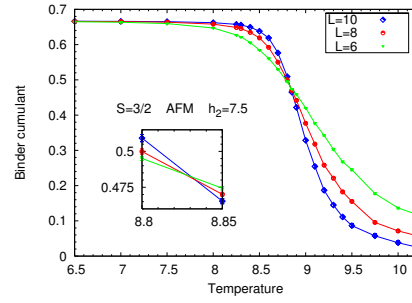
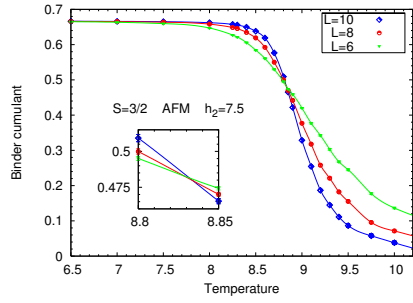
A.4 $S = \frac{3}{2}$ - Heisenberg AFM



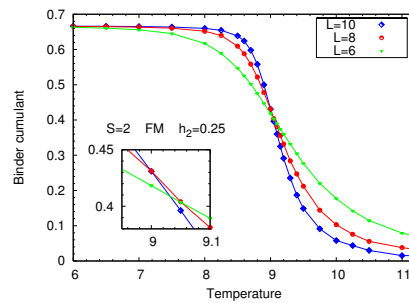
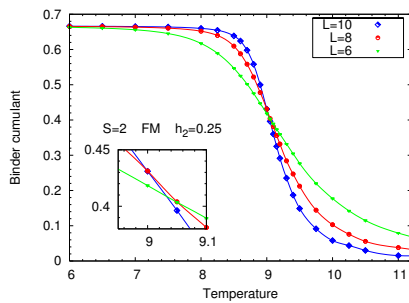
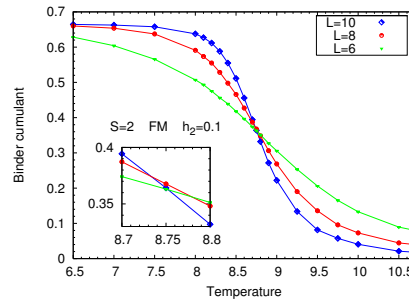
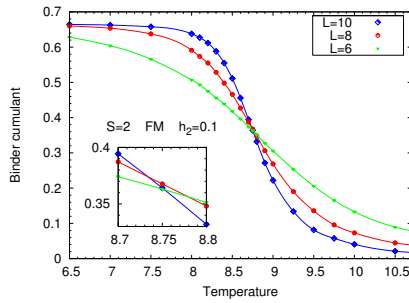
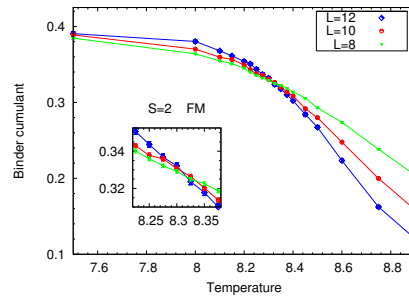
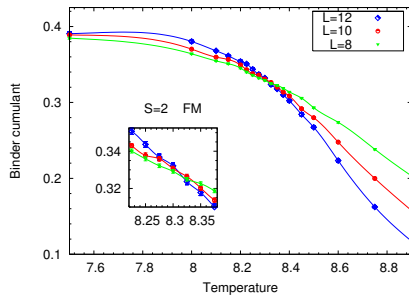


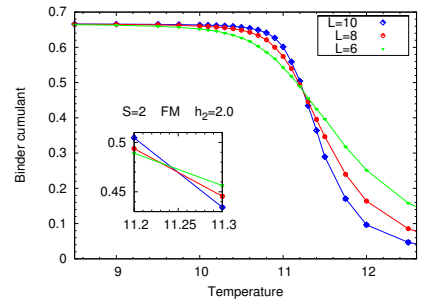
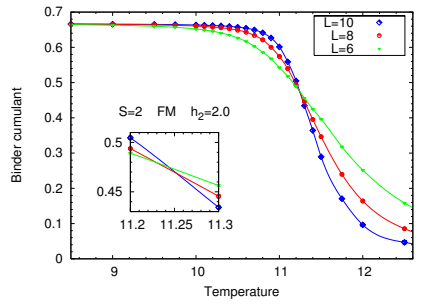
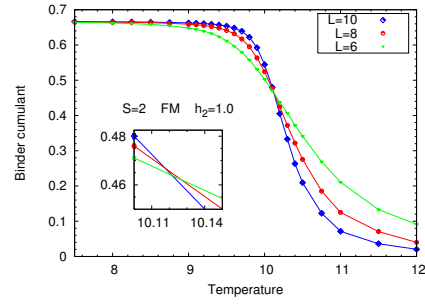
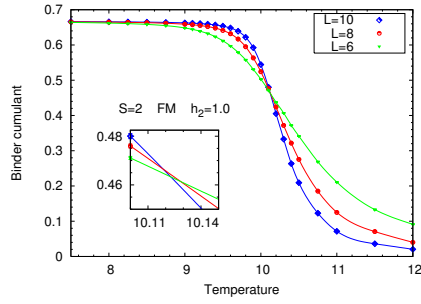
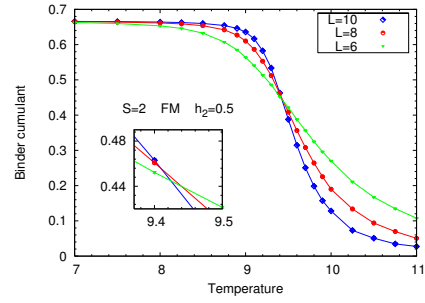
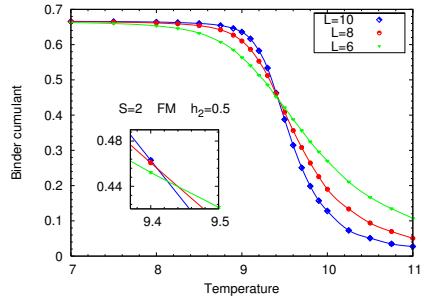
A.4. $S=3/2$ - Heisenberg AFM

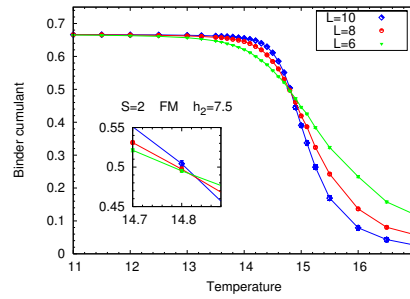
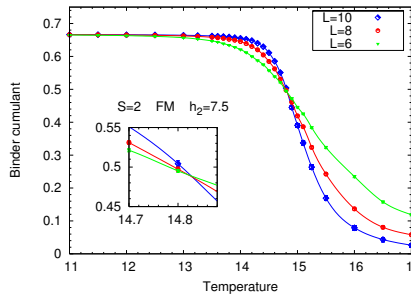
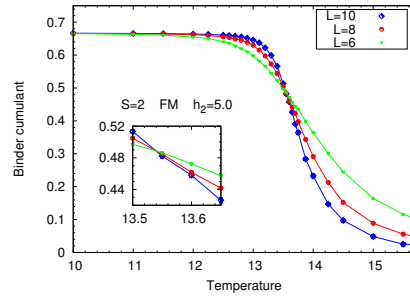
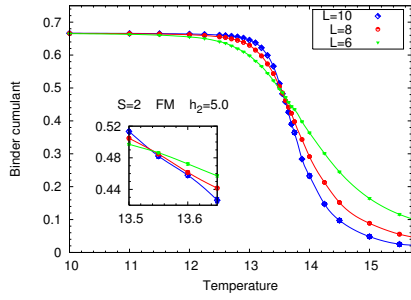
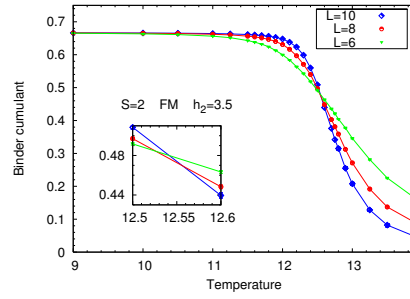
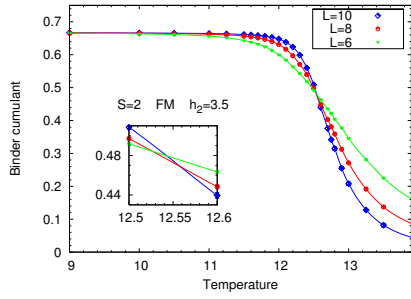


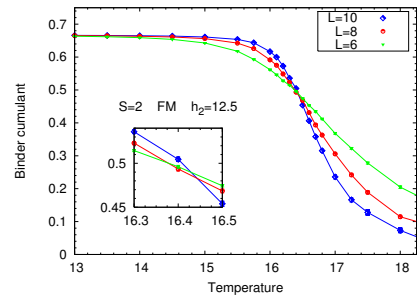
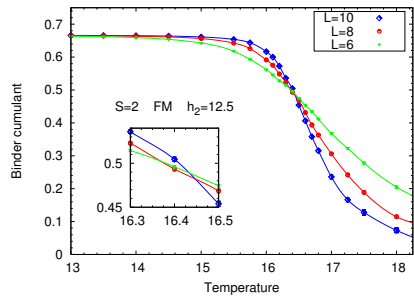
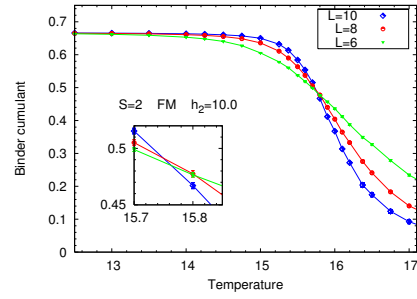
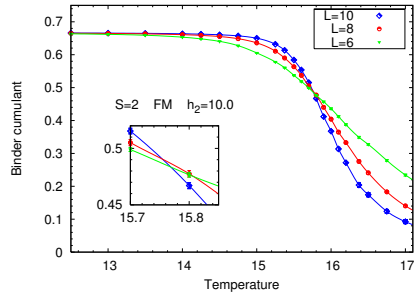


A.5 $S=2$ - Heisenberg FM with $p = 2$

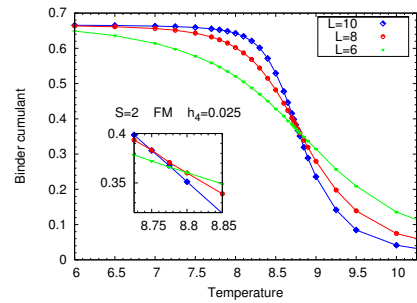
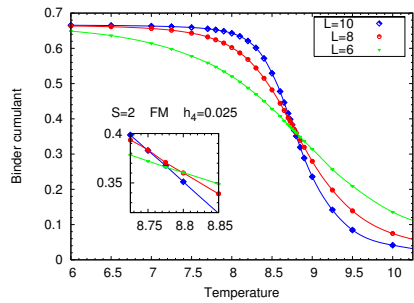




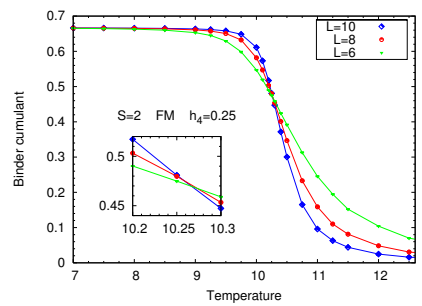
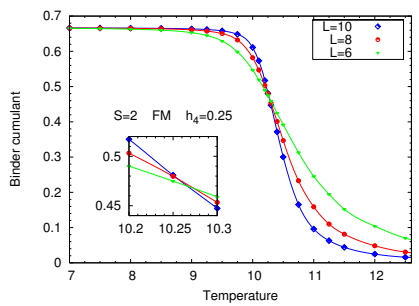
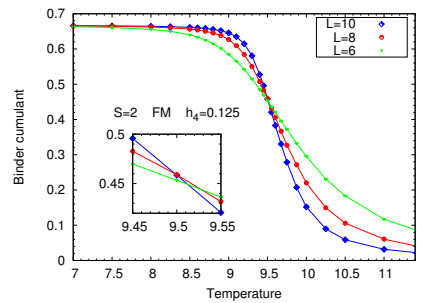
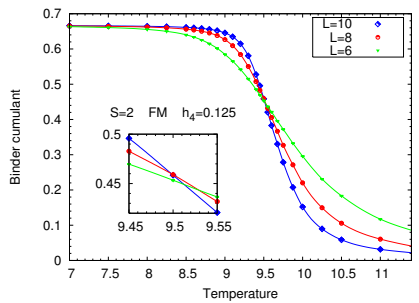
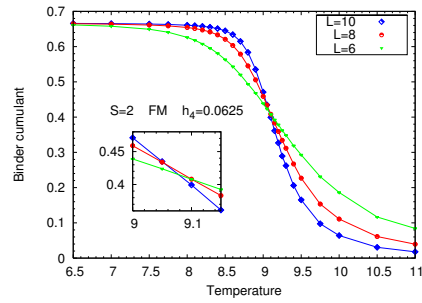
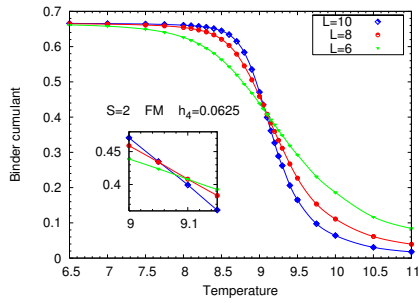


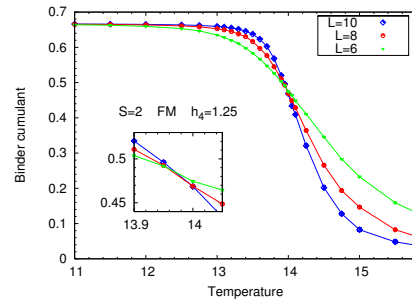
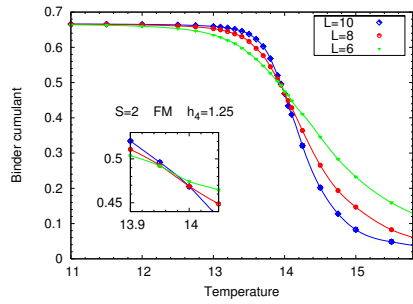
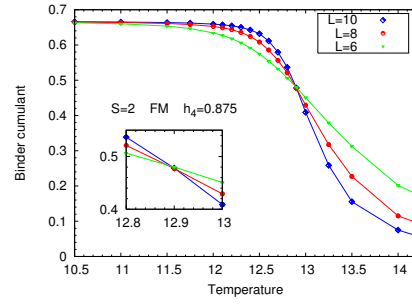
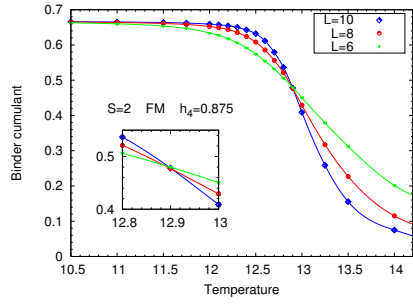
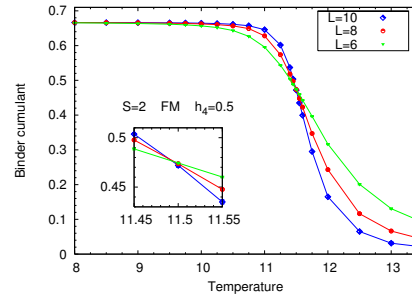
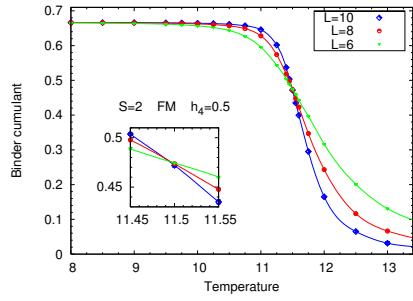


A.6 $S=2$ - Heisenberg FM with $p=4$

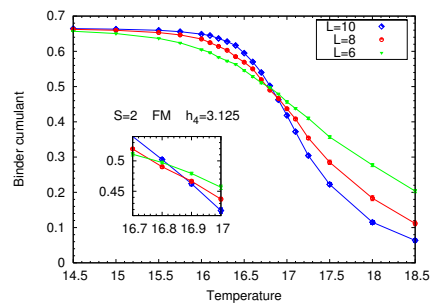
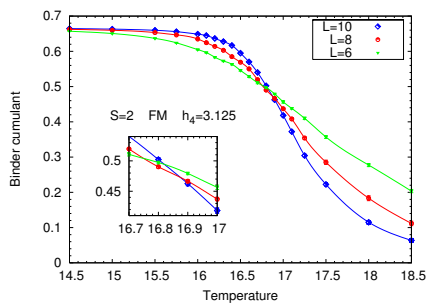
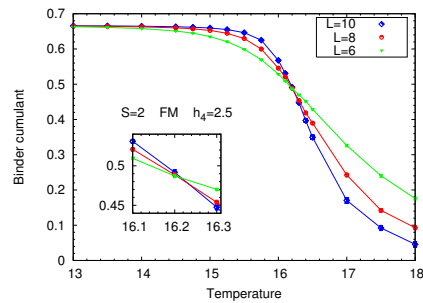
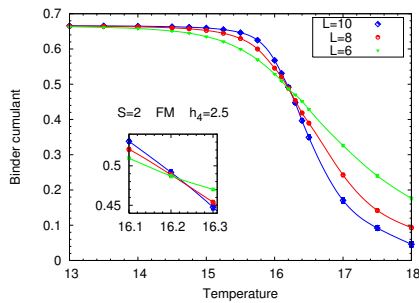
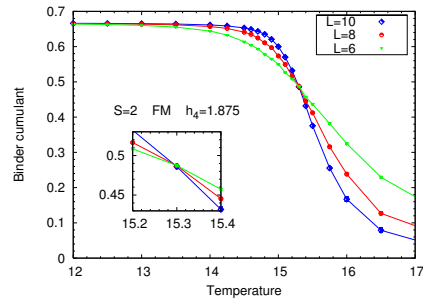
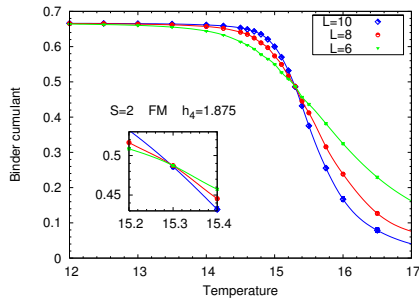


A.6. $S=2$ - Heisenberg FM with $p = 4$

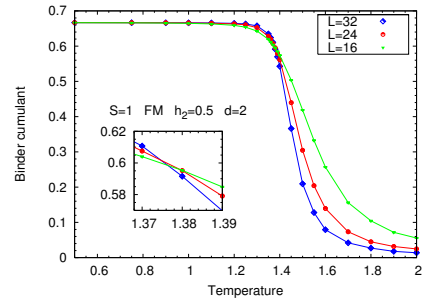
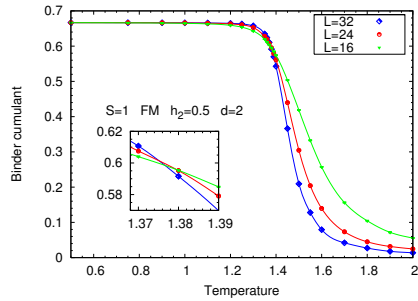
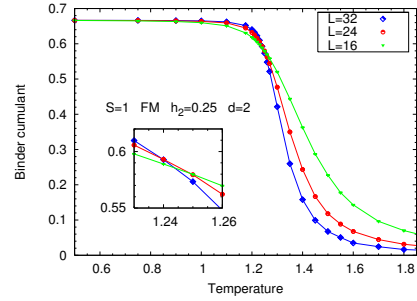
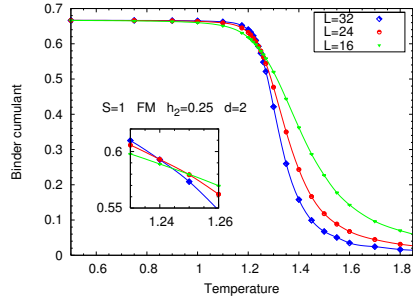
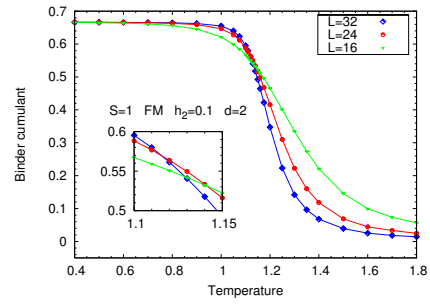
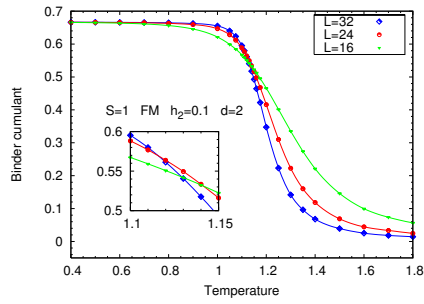


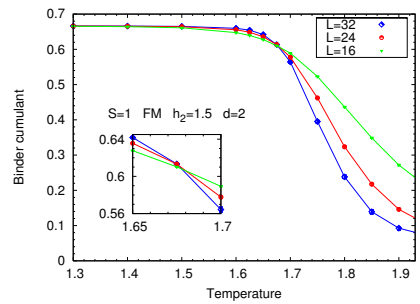
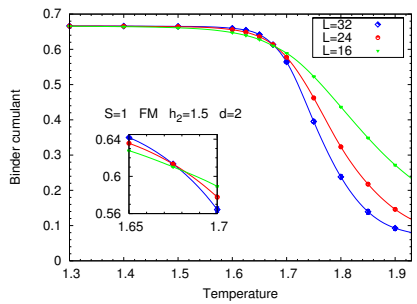
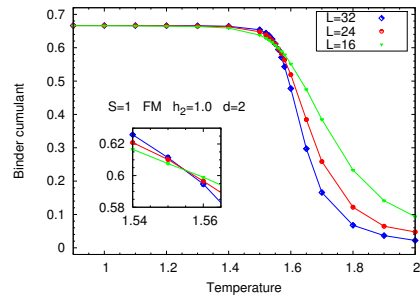
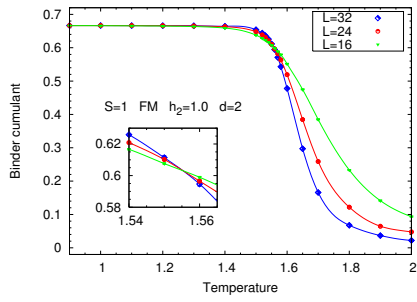
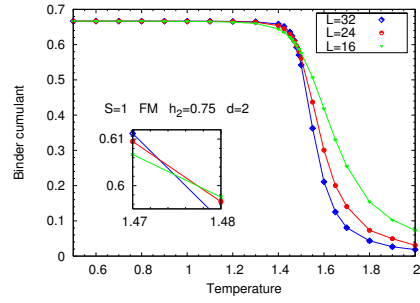
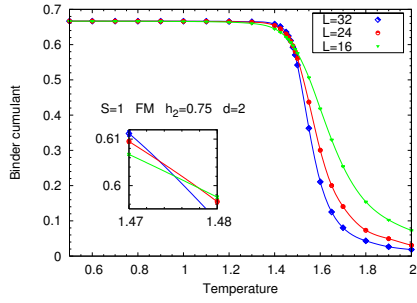


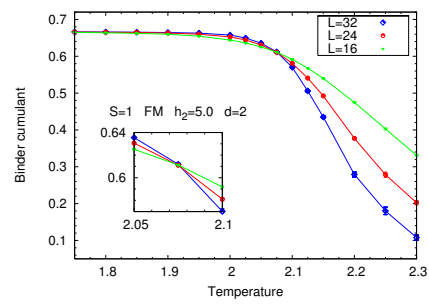
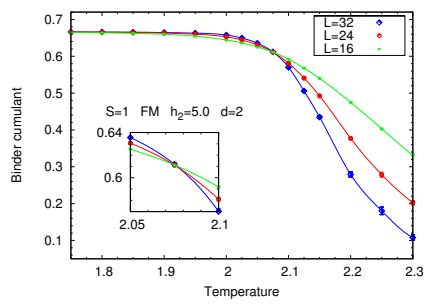
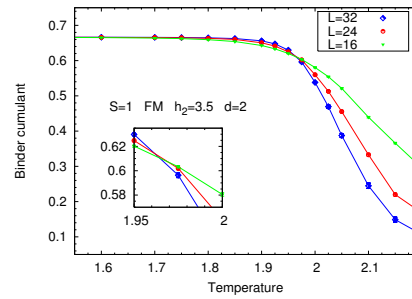
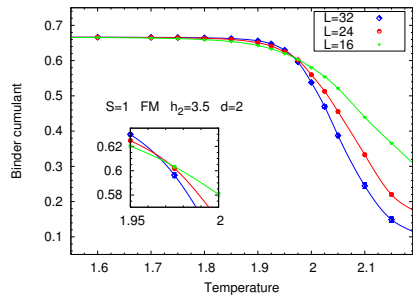
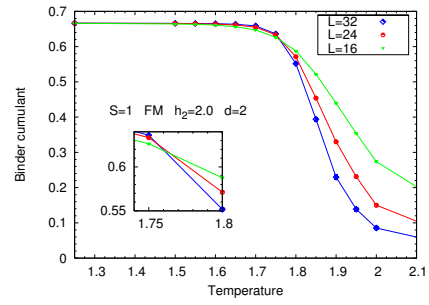
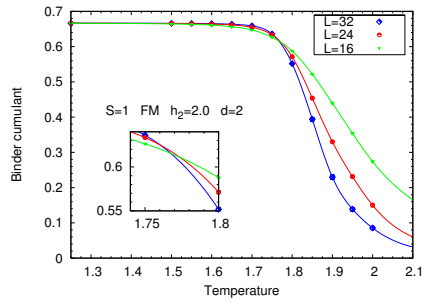
A.6. $S=2$ - Heisenberg FM with $p=4$



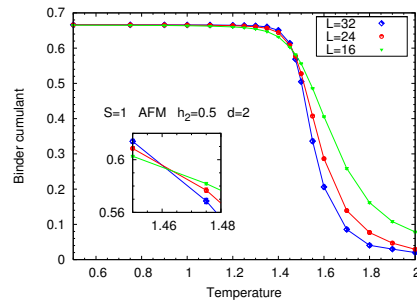
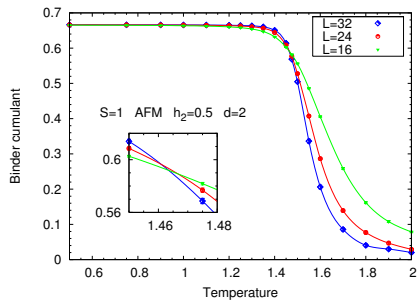
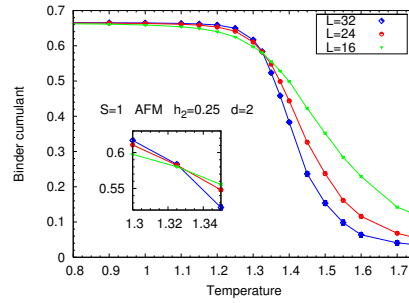
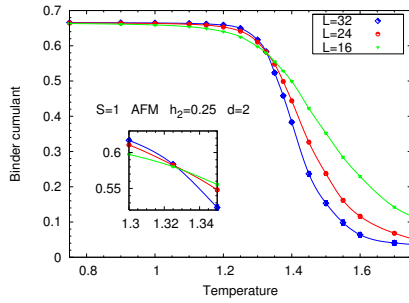
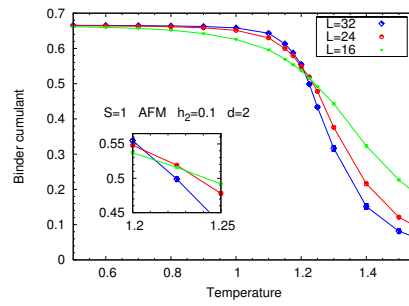
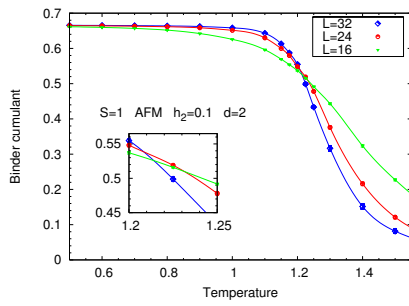
A.7 Two Dimensions: $S=1$ - FM

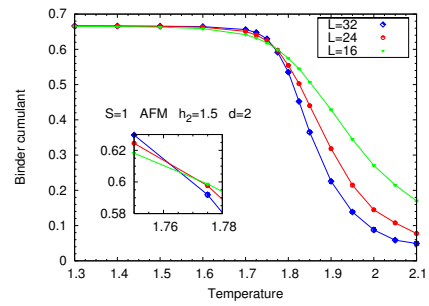
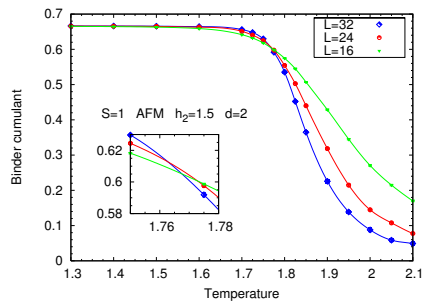
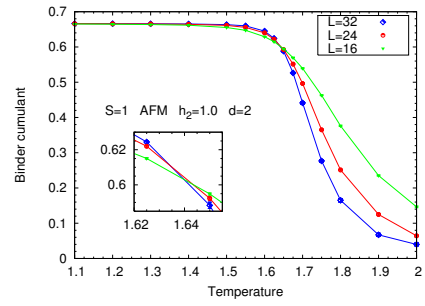
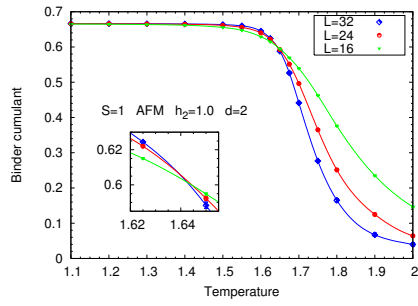
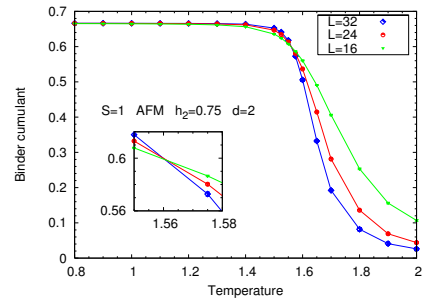
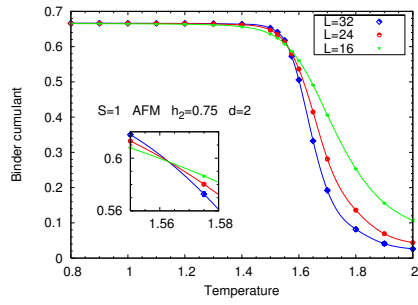


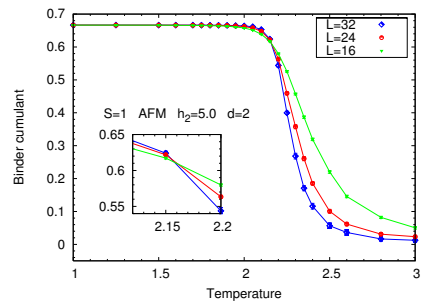
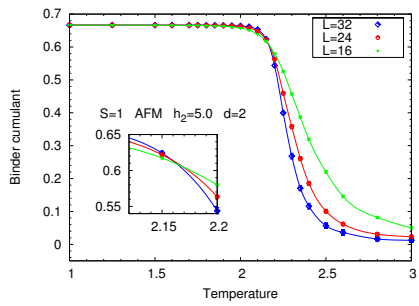
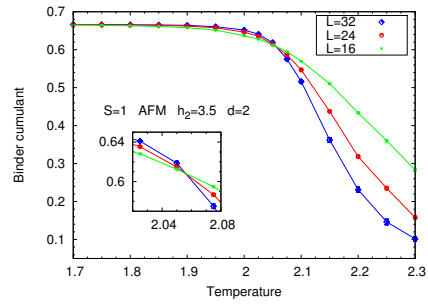
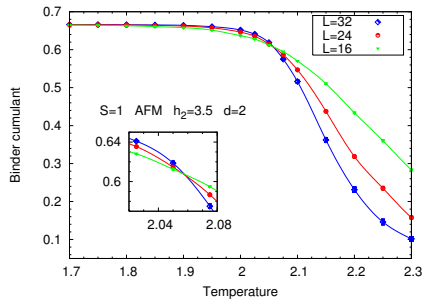
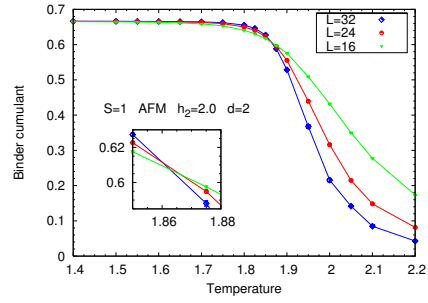
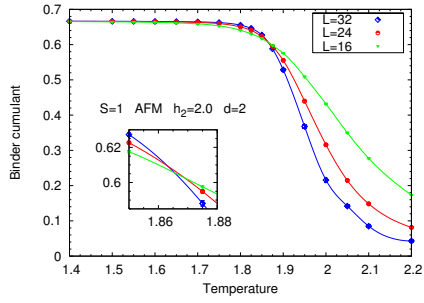




A.8 Two Dimensions: $S=1$ - AFM







Appendix B

List of Abbreviations - Glossary

- AFM Antiferromagnet / antiferromagnetic; prefers the alternating alignment of the spins; the entire lattice can be divided into two distinct sublattices; the corresponding sublattice (staggered) magnetization is influenced by quantum fluctuations even at $T=0$ and represents an essential tool for the extraction of quantum fluctuations.
- ALPS “Algorithms and Libraries for Physics Simulations”; software package providing modern and state-of-the-art QMC algorithms [112].
- CMF Classical Mean Field; analytical technique used in chapter 2; the extended technique including quantum effects is called Quantum Mean Field (QMF).
- EA Easy-axis; preference of a single spin component (usually S^z); the easy-axis case is achieved by $h_p > 0$ in the Hamiltonian (1.8).
- EoM Equation of Motion; refers to Heisenberg’s equation of motion for Green’s functions; the plural form, actually ‘equations of motion’, is abbreviated by EoMs.
- EP Easy-plane; preference of two equitable spin components (usually S^x and S^y) that span an entire plane in spin space; the easy-plane case is achieved by $h_p < 0$ in the Hamiltonian (1.8).

FM	Ferromagnet / ferromagnetic; prefers the uniform alignment of the spins; its technical treatment is less sophisticated than for the AFM; represents an important possibility to compare and contrast with the AFM.
GF	Green's function; basic quantity of the RPA method.
LSWA	Linear Spin Wave Approximation; analytical approximation scheme used in chapter 4; operates in the regime of non-interacting magnons.
MF	Mean Field; approach used in chapter 2 and 3; this collective term for CMF and QMF refers to the general Mean Field idea.
QMC	Quantum Monte Carlo; numerical simulation method including quantum effects; in this thesis, we mainly use the <code>directed loop</code> algorithm provided by the ALPS package.
QMF	Quantum Mean Field; analytical technique used in chapter 3; includes quantum effects in contrast to CMF.
RPA	Random Phase Approximation; analytical Green's function technique applied in chapter 5.
SC-LRPA	Self-Consistent Local RPA; generalization of the RPA technique to disordered systems developed by G. Bouzerar [135]-[139].
SP-STM	Spin-polarized scanning tunneling microscopy; recent overviews are given in [5, 6], including the spectroscopic mode [142], which is also called SP-STs.

Bibliography

- [1] A.J. Schofield, *Science* **315**, 945 (2007)
- [2] W. Demtröder, “Experimentalphysik 2”, 4th edition, Springer (2006)
- [3] W. Gilbert,
“De Magnete, Magneticisque Corporibus, et de Magno Magnete Tellure” (1600)
English translation for the Gilbert Club of London:
“On the Magnet, Magnetick Bodies also, and on the Great Magnet the Earth”, London (1900)
- [4] Official web site of the Nobel Foundation (updated 2009):
http://nobelprize.org/nobel_prizes/physics/laureates/2007/
- [5] R. Wiesendanger, *Europhysics News* **38**, 16 (2007)
- [6] R. Wiesendanger, *G.I.T. Imaging & Microscopy* **02/2007**, 21 (2007)
- [7] W. Heisenberg, *Zeitschrift f. Physik* **49**, 619 (1928)
- [8] N.D. Mermin, H. Wagner, *Phys. Rev. Lett.* **17**, 1133 (1966)
- [9] J.M. Kosterlitz, D.J. Thouless, *J. Phys. C* **5**, L124 (1972)
- [10] J.M. Kosterlitz, D.J. Thouless, *J. Phys. C* **6**, 1181 (1973)
- [11] J.M. Kosterlitz, *J. Phys. C* **7**, 1064 (1974)
- [12] H.E. Stanley, T.A. Kaplan, *Phys. Rev. Lett.* **17**, 913 (1966)
- [13] H.E. Stanley, *Phys. Rev. Lett.* **20**, 589 (1968)
- [14] M.A. Moore, *Phys. Rev. Lett.* **23**, 861 (1969)
- [15] H.W.J. Blöte, W. Guo, H.J. Hilhorst, *Phys. Rev. Lett.* **88**, 047203 (2002)
- [16] E. Ising, “Beitrag zur Theorie des Ferromagnetismus”,
Zeitschrift f. Physik **31**, 253 (1925)
- [17] S. Kobe, “Das Ising-Modell - gestern und heute”,
Physikalische Blätter **54**, 917 (1998)
- [18] L. Onsager, *Phys. Rev.* **65**, 117 (1944)

- [19] B. Kaufman, *Phys. Rev.* **76**, 1232 (1949)
- [20] B. Vogt, “Energieaufspaltung im zweidimensionalen Ising-Modell”, diploma thesis, University of Münster (2003)
available on (updated 2007):
<http://pauli.uni-muenster.de/tp/fileadmin/Arbeiten/vogt.pdf>
- [21] R. Wiesendanger, H.-J. Güntherodt, G. Güntherodt, R.J. Gambino, R. Ruf, *Phys. Rev. Lett.* **65**, 247 (1990)
- [22] R. Wiesendanger, I.V. Shvets, D. Bürgler, G. Tarrach, H.-J. Güntherodt, J.M.D. Coey, S. Gräser, *Science* **255**, 583 (1992)
- [23] F. Meier, L. Zhou, J. Wiebe, R. Wiesendanger, *Science* **320**, 82 (2008)
- [24] A.F. Otte, M. Ternes, K. v. Bergmann, S. Loth, H. Brune, C.P. Lutz, C.F. Hirjibehedin, A.J. Heinrich, *Nature Physics* **4**, 847 (2008)
- [25] C.F. Hirjibehedin, C.-Y. Lin, A.F. Otte, M. Ternes, C.P. Lutz, B.A. Jones, A.J. Heinrich, *Science* **317**, 1199 (2007)
- [26] P. Gambardella, S. Rusponi, M. Veronese, S.S. Dhesi, C. Grazioli, A. Dallmeyer, I. Cabria, R. Zeller, P.H. Dederichs, K. Kern, C. Carbone, H. Brune, *Science* **300**, 1130 (2003)
- [27] K. von Bergmann, M. Bode, A. Kubetzka, O. Pietzsch, E. Y. Vedmedenko, and R. Wiesendanger, *Philosophical Magazine* **88**, 2627 (2008)
- [28] K. von Bergmann, S. Heinze, M. Bode, G. Bihlmayer, S. Blügel, and R. Wiesendanger, *New Journ. Phys.* **9**, 396 (2007)
- [29] M. Bode, E.Y. Vedmedenko, K. von Bergmann, A. Kubetzka, P. Ferriani, S. Heinze, R. Wiesendanger, *Nat. Mat.* **5**, 477 (2006)
- [30] A. Kubetzka, P. Ferriani, M. Bode, S. Heinze, G. Bihlmayer, K. von Bergmann, O. Pietzsch, S. Blügel, R. Wiesendanger, *Phys. Rev. Lett.* **94**, 087204 (2005)
- [31] S. Heinze, M. Bode, A. Kubetzka, O. Pietzsch, X. Nie, S. Blügel, R. Wiesendanger, *Science* **288**, 1805 (2000)
- [32] C. Herring, C. Kittel, *Phys. Rev.* **81**, 869 (1951)
- [33] K. Binder, D.P. Landau, *Phys. Rev. B* **13**, 1140 (1976)
- [34] S. Malyshev, *Comm. Math. Phys.* **40**, 75 (1975)
- [35] J. Fröhlich, E. Lieb, *Phys. Rev. Lett.* **38**, 440 (1977)
- [36] J. Bricmont, J.-R. Fontaine, *Commun. Math. Phys.* **87**, 417 (1982)
- [37] T. Kennedy, *Commun. Math. Phys.* **100**, 447 (1985)

- [38] S.S. Aplesnin, *phys. stat. sol. b* **207**, 491 (1998); *J. Phys.: Condens. Matt.* **10**, 10061 (1998)
- [39] M.E. Gouvea, G.M. Wysin, S.A. Leonel, A.S.T. Pires, T. Kamppeter, F.G. Mertens, *Phys. Rev. B* **59**, 6229 (1999)
- [40] P.A. Serena, N. Garcia, A. Levanyuk, *Phys. Rev. B* **47**, 5027 (1993)
- [41] C. Kawabata, A.R. Bishop, *Solid State Commun.* **42**, 595 (1982)
- [42] F. Dunlop, *J. Stat. Phys.* **41**, 733 (1985)
- [43] H.-Q. Ding, *Phys. Rev. Lett.* **68**, 1927 (1992)
- [44] A. Cuccoli, V. Tognetti, R. Vaia, *Phys. Rev. B* **52**, 10221 (1995)
- [45] A. Cuccoli, T. Roscilde, V. Tognetti, R. Vaia, P. Verrucchi, *Phys. Rev. B* **67**, 104414 (2003)
- [46] H.-Q. Ding, *J. Phys. Condens. Matter* **2**, 7979 (1990)
- [47] A. Cuccoli, T. Roscilde, R. Vaia, P. Verrucchi, *Phys. Rev. Lett.* **90**, 167205 (2003)
- [48] T. Roscilde, A. Cuccoli, P. Verrucchi, *phys. stat. sol. b* **236**, 433 (2003)
- [49] A. Cuccoli, T. Roscilde, V. Tognetti, R. Vaia, P. Verrucchi, *J. Appl. Phys.* **93**, 7637 (2003)
- [50] S.T. Bramwell, P.C.W. Holdsworth, *J. Appl. Phys.* **73**, 6096 (1993)
- [51] M. Heinrich, H.-A. Krug von Nidda, A. Loidl, N. Rogado, R.J. Cava, *Phys. Rev. Lett.* **91**, 137601 (2003)
- [52] K. Takeda, H. Deguchi, T. Hoshiko, K. Yamagata, *J. Phys. Soc. Jpn.* **58**, 3489 (1989)
- [53] C. Timm, P.J. Jensen, *Phys. Rev. B* **62**, 5634 (2000)
- [54] P. Henelius, P. Fröbrich, P.J. Kuntz, C. Timm, P.J. Jensen, *Phys. Rev. B* **66**, 094407 (2002)
- [55] Huai-Yu Wang, Zhen-Hong Dai, P. Fröbrich, P.J. Jensen, P.J. Kuntz, *Phys. Rev. B* **70**, 134424 (2004)
- [56] Huai-Yu Wang, S.U. Jen, Jing-Zhi Yu, *Phys. Rev. B* **73**, 094414 (2006)
- [57] P. Fröbrich, P.J. Kuntz, *Physics Reports* **432**, 223 (2006)
- [58] D.A. Yablonskiy, *Phys. Rev. B* **44**, 4467 (1991)
- [59] R. Kubo, *Phys. Rev.* **87**, 568 (1952)
- [60] W. Nolting, “Grundkurs Theoretische Physik 6: Statistische Physik”, 4th edition, Springer (2002)

- [61] P.M. Chaikin, T.C. Lubensky, “Principles of condensed matter physics”, Cambridge University Press (1995)
- [62] J. Cardy, “Scaling and Renormalization in Statistical Physics”, Cambridge University Press (1996)
- [63] H.E. Stanley,
“Introduction to Phase Transitions and Critical Phenomena”,
Oxford University Press (1971)
- [64] K. Huang, “Statistical Mechanics”, 2nd edition, John Wiley & Sons (1987)
- [65] L. Udvardi, L. Szunyogh, A. Vernes, P. Weinberger,
Philosophical Magazine B **81**, 613 (2001)
- [66] L. Udvardi, R. Kiraly, L. Szunyogh, F. Denat, M.B. Taylor, B.L. Györfly,
B. Ujfalussy, C. Uiberacker, J. Magn. Magn. Mat. **183**, 283 (1998)
- [67] J.V. Jose, L.P. Kadanoff, S. Kirkpatrick, D.R. Nelson,
Phys. Rev. B **16**, 1217 (1977)
- [68] I. Nakayama, T. Tsuneto, Prog. Theor. Phys. **65**, 1246 (1981)
- [69] ISI Web of Knowledge, <http://www.isiknowledge.com>,
Thomson Reuters (2008)
- [70] A.I. Farinas-Sanchez, R. Paredes, B. Berche,
Phys. Rev. E **72**, 031711 (2005)
- [71] RTN Nano Meeting “Fundamentals of Nanoelectronics”,
2nd-7th of September 2007, Portoroz, Slovenia;
book of abstracts available on (updated 2007):
<http://www-fl.ijs.si/portoroz07>
- [72] J. Lou, A.W. Sandvik, L. Balents, Phys. Rev. Lett. **99**, 207203 (2007)
- [73] S. Elitzur, R.B. Pearson, J. Shigemitsu, Phys. Rev. D **19**, 3698 (1979)
- [74] M.S.S. Challa, D.P. Landau, Phys. Rev. B **34**, 1841 (1986)
- [75] R.B. Potts, Proc. Cambridge Philos. Soc. **48**, 106 (1952)
- [76] S. Sachdev, “Quantum Phase Transitions”,
Cambridge University Press (1999)
- [77] J.A. Hertz, Phys. Rev. B **14**, 1165 (1976)
- [78] M. Greiner, O. Mandel, T. Esslinger, T.W. Hänsch, I. Bloch,
Nature **415**, 39 (2002)
- [79] M. Köhl, H. Moritz, T. Stöferle, C. Schori, T. Esslinger,
J. Low Temp. Phys. **138**, 635 (2005)
- [80] I. Bloch, Nature Physics **1**, 23 (2005)

- [81] M.Y. Choi, S.W. Rhee, M. Lee, J. Choi, *Phys. Rev. B* **63**, 094516 (2001)
- [82] M.Y. Choi, *Phys. Rev. B* **48**, 15920 (1993)
- [83] R.M. Bradley, S. Doniach, *Phys. Rev. B* **30**, 1138 (1984)
- [84] C. Rojas, J.V. Jose, *Phys. Rev. B* **54**, 12361 (1996)
- [85] P. Phillips, “Advanced Solid State Physics”, Westview Press (2003)
- [86] H. Kleinert,
“Pfadintegrale in Quantenmechanik, Statistik und Polymerphysik”,
BI-Wissenschaftsverlag (1993)
- [87] P. Gegenwart, T. Westerkamp, C. Krellner, Y. Tokiwa, S. Paschen, C.
Geibel, F. Steglich, E. Abrahams, Q. Si, *Science* **315**, 969 (2007)
- [88] P. Coleman, A.J. Schofield, *Nature* **433**, 226 (2005)
- [89] F. Bloch, *Z. Physik* **61**, 206 (1930)
- [90] P.W. Anderson, *Phys. Rev.* **86**, 694 (1952)
- [91] E. Manousakis, *Rev. Mod. Phys.* **63**, 1 (1991)
- [92] T. Holstein, H. Primakoff, *Phys. Rev.* **58**, 1098 (1940)
- [93] N.W. Ashcroft, N.D. Mermin, “Solid State Physics”, Thomson (1976)
- [94] O. Madelung, “Introduction to Solid-State Theory”,
Springer Series in Solid-State Sciences 2, Springer-Verlag (1978)
- [95] J.J. Rhyne, H. Kaiser, L. Stumpe, J.F. Mitchell, T. McCloskey, A.R.
Chourasia, *J. Magn. Magn. Mat.* **226-230**, 775 (2001)
- [96] H.A. Bethe, *Z. Physik* **21**, 205 (1931)
- [97] G. G. Low, A. Okazaki, R. W. H. Stevenson, K. C. Turberfield,
J. Appl. Phys. **35**, 998 (1964)
- [98] R.N. Sinclair, B.N. Brockhouse, *Phys. Rev.* **120**, 1638 (1960)
- [99] H.B. Callen, *Phys. Rev.* **130**, 890 (1963)
- [100] F.B. Anderson, H.B. Callen, *Phys. Rev.* **136**, A 1068 (1964)
- [101] S.V. Tyablikov, *Ukr. Mat. Zh.* **11**, 287 (1959)
- [102] N.N. Bogoliubov, S.V. Tyablikov, *Dokl. Acad. Nauk. SSSR* **126**, 53
(1959); *Sov. Phys. Dokl.* **4**, 604 (1959)
- [103] M.E. Lines, *Phys. Rev.* **156**, 534 (1967)
- [104] J.F. Devlin, *Phys. Rev. B* **4**, 136 (1971)

- [105] Z. Siming, *J. Phys. Chem. Solids* **47**, 255 (1986)
- [106] A. Narath, *Phys. Rev.* **140**, A 854 (1965)
- [107] W. Nolting, “Grundkurs Theoretische Physik 7: Viel-Teilchen-Theorie”, 6th edition, Springer (2005)
- [108] J. Oitmaa, W.H. Zheng, *J. Phys.: Condens. Matter* **16**, 8653 (2004)
- [109] A. Ecker, P. Fröbrich, P.J. Jensen, P.J. Kuntz, *J. Phys.: Condens. Matter* **11**, 1557 (1999)
- [110] F.J. Dyson, *Phys. Rev.* **102**, 1207 (1956); *Phys. Rev.* **102**, 1230 (1956)
- [111] S.V. Maleev, *Zh. Eksp. Teor. Fiz.* **33**, 1010 (1957); *Sov. Phys. JETP* **64**, 654 (1958)
- [112] A.F. Albuquerque, F. Alet, P. Corboz, P. Dayal, A. Feiguin, S. Fuchs, L. Gamper, E. Gull, S. Gürtler, A. Honecker, R. Igarashi, M. Körner, A. Kozhevnikov, A. Läuchli, S.R. Manmana, M. Matsumoto, I.P. McCulloch, F. Michel, R.M. Noack, G. Pawłowski, L. Pollet, T. Pruschke, U. Schollwöck, S. Todo, S. Trebst, M. Troyer, P. Werner, S. Wessel and for the ALPS collaboration, *J. Magn. Magn. Mat.* **310**, 1187 (2007)
- [113] Homepage of the ALPS project (updated 2008):
http://alps.comp-phys.org/mediawiki-1.9.3/index.php/Main_Page
- [114] S. Todo, talk; published on the ALPS homepage (updated 2009):
<http://alps.comp-phys.org/resources/presentations/psi2006/xml.pdf>
- [115] L. Pollet, talk; published on the ALPS homepage (updated 2009):
http://alps.comp-phys.org/mediawiki-1.9.3/images/7/79/ALPS06_Taiwan.pdf
- [116] H.G. Evertz, G. Lana, and M. Marcu, *Phys. Rev. Lett.* **70**, 875 (1993)
- [117] H.G. Evertz, *Adv. Phys.* **52**, 1 (2003)
- [118] N.V. Prokov’ev, B.V. Svistunov, I.S. Tupitsyn, *Sov. Phys. JETP* **87**, 310 (1998)
- [119] O.F. Syljuasen, A.W. Sandvik, *Phys. Rev. E* **66**, 046701 (2002)
- [120] F. Alet, S. Wessel, M. Troyer, *Phys. Rev. E* **71**, 036706 (2005)
- [121] N. Kawashima, K. Harada, *J. Phys. Soc. Jap.* **73**, 1379 (2004)
- [122] D.P. Landau, K. Binder, “A Guide to Monte Carlo Simulations in Statistical Physics”, 2nd edition, Cambridge University Press (2005)
- [123] V.N. Borodikhin, D.V. Dmitriev, V.V. Prudnikov, *Russian Physics Journal* **47**, 534 (2004)

- [124] A.W. Sandvik, Phys. Rev. Lett. **80**, 5196 (1998)
- [125] Y.C. Chen, H.H. Chen, F. Lee, Phys. Rev. B **43**, 11082 (1991)
- [126] A.J.F. de Souza, M.L. Lyra, Phys. Rev. B **65**, 100405(R) (2002)
- [127] J. Adler, C. Holm, W. Janke, Physica A **201**, 581 (1993)
- [128] K. Chen, A.M. Ferrenberg, D.P. Landau, Phys. Rev. B **48**, 3249 (1993)
- [129] A.K. Murtazaev, I.K. Kamilov, A.B. Babaev, JETP **99**, 1201 (2004)
- [130] G.S. Rushbrooke, P.J. Wood, Mol. Phys. **6**, 409 (1963)
- [131] H.K. Charles Jr., R.I. Joseph, Phys. Rev. Lett. **28**, 823 (1972)
- [132] I.G. Araujo, J.C. Neto, J.R. de Sousa, Physica A **260**, 150 (1998)
- [133] H. Shimahara, S. Takeda, J. Phys. Soc. Jap. **60**, 2394 (1991)
- [134] A.W. Sandvik, Phys. Rev. B **66**, 024418 (2002)
- [135] G. Bouzerar, Europ. Phys. Lett. **79**, 57007 (2007)
- [136] R. Bouzerar, G. Bouzerar, T. Ziman, Phys. Rev. B **73**, 024411 (2006)
- [137] G. Bouzerar, R. Bouzerar, J. Kudrnovsky, T. Ziman, phys. stat. sol. a **203**, 2989 (2006)
- [138] G. Bouzerar, T. Ziman, J. Kudrnovsky, Phys. Rev. B **72**, 125207 (2005)
- [139] G. Bouzerar, T. Ziman, J. Kudrnovsky, Europhys. Lett. **69**, 812 (2005)
- [140] G. Bouzerar, P. Bruno, Phys. Rev. B **66**, 014410 (2002)
- [141] J.L. Lebowitz, “Emergent Phenomena”,
Plenary talk given at the 71st annual meeting of the DPG in Regensburg
on the occasion of the conferment of the Max Planck medal,
Physik Journal **6**, Nr. 8/9, 41 (2007)
- [142] M. Bode, M. Getzlaff, R. Wiesendanger, Phys. Rev. Lett. **81**, 4256 (1998)

Acknowledgements

I would like to thank sincerely my supervisor Prof. Dr. Stefan Kettemann for his guidance and support in the course of this PhD project. I would further like to thank the members of the I. Institute for Theoretical Physics, Prof. Dr. Alexander Lichtenstein and his group, Prof. Dr. Michael Potthoff and his group and especially my colleagues Aleksander Hinz, Christoph Jung and Paul Wenk for their support and ideas. All of them induced a pleasant and motivating atmosphere that gave rise to this thesis. I am especially indebted to Prof. Dr. Georges Bouzerar for his kind hospitality at the CNRS in Grenoble and for introducing me to his RPA technique.

Erklärung gemäß Prüfungsordnung (Promotion)

Hiermit versichere ich, dass ich die vorliegende Dissertation selbständig und nur mit Hilfe der angegebenen Quellen verfasst habe. Des Weiteren gestatte ich die Veröffentlichung dieser Arbeit.

Björn Vogt, Hamburg 2009

